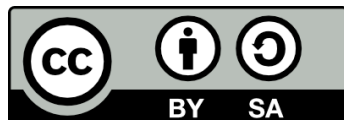




UNIVERSITAT_{DE}
BARCELONA

Developing Advanced Photogrammetric Methods for Automated Rockfall Monitoring

Xabier Blanch Gorriz



Aquesta tesi doctoral està subjecta a la llicència **Reconeixement- Compartigual 4.0. Espanya de Creative Commons.**

Esta tesis doctoral está sujeta a la licencia **Reconocimiento - Compartigual 4.0. España de Creative Commons.**

This doctoral thesis is licensed under the **Creative Commons Attribution-ShareAlike 4.0. Spain License.**



Xabier Blanch Górriz

Developing advanced photogrammetric methods for automated rockfall monitoring

Desenvolupament de mètodes
fotogramètrics avançats per al
monitoratge automàtic de
despreniments de roques

RISKNAT – Grup de Recerca Consolidat en Riscos Naturals
Institut de Recerca Geomodels
Departament de Dinàmica de la Terra i de l'Oceà
Facultat de Ciències de la Terra, Universitat de Barcelona

Developing Advanced Photogrammetric Methods for Automated Rockfall Monitoring

Desenvolupament de mètodes fotogramètrics avançats
per al monitoratge automatitzat de despreniments de
roques

Tesi doctoral presentada per

Xabier Blanch Górriz

per a optar al grau de Doctor per la Universitat de Barcelona sota la supervisió de la **Dra.**

Marta Guinau Sellés i el **Dr. Antonio Abellán Fernández**.

Aquesta tesi s'ha realitzat dins del Programa de Doctorat de Ciències de la Terra (HDK09)
de la Universitat de Barcelona.

Dresden, gener del 2022

Aquesta tesi s'ha realitzat en el Grup de Recerca Consolidat RISKNAT del departament de Dinàmica de la Terra i de l'Oceà de la Facultat de Ciències de la Terra a la Universitat de Barcelona i ha comptat amb el finançament directe del següent ajut predoctoral:

- Ajut de Personal Investigador predoctoral en Formació (APIF-2017) per a doctorands de la Universitat de Barcelona. (2017-2020)

Tanmateix, al llarg de la tesi també han col·laborat en el finançament de la recerca els següents projectes i institucions:

- Projecte “CHARMA. (Caracterización y Control de Movimientos de Masa. Un Reto para la mitigación del Riesgo Geológico).” 2014-2017.
Ref. CGL2013-40828-R. Finançat pel Ministerio de Economía y Competitividad.
- Projecte “Aplicacions Inventari de despreniments de roques i deformacions premonitòries a la muntanya de Montserrat amb LiDAR Terrestre (TLS).” 2017.
Ref. FBG 309453. Finançat per l'Institut Cartogràfic i Geològic de Catalunya
- Projecte “PROMONTEC (Monitoreo, Modelización e Integración de métodos para el Control de Procesos Activos en Montañas)” 2018-2021.
Ref. CGL2017-84720-R. Finançat pel Ministerio de Economía y Competitividad.
- Projecte “Montaje e instalación de sistemas fotogramétricos para el estudio del retroceso del Tajo de San Pedro mediante técnicas 4D.” 2018-2019.
Ref. FBG 310039. Finançat pel Patronato de la Alhambra y Generalife.
- Projecte “Vigilancia y seguimiento de la erosión en el tajo de San Pedro, Granada.” 2020 - 2021. Ref.FBG 310750. Finançat pel Patronato de la Alhambra y Generalife
- Departament de Dinàmica de la Terra i de l'Oceà. Facultat de Ciències de la Terra. Universitat de Barcelona.

Xabier Blanch Górriz, 2022

Contact: xabierblanch@gmail.com

No sirves para ser
ni piedra de un palacio,
ni piedra de una iglesia
ni piedra de una audiencia.

Como tú, piedra aventurera
que tal vez estás hecha
sólo para una honda,
piedra pequeña y ligera...

León Felipe



Com es pot percebre¹, la meva vivència durant la realització d'aquesta tesi doctoral ha transcendit més enllà de l'àmbit professional, ha estat una vivència personal bastant intensa. Aquesta tesi mai hauria estat possible sense el suport tècnic, anímic i moral de molta gent del meu voltant. Tota una riquesa difícil d'aconseguir i que em fa por no saber valorar-la (i agrair-la) com es mereix. Per avançat, moltes gràcies per tot el suport que he rebut. Les pàgines d'aquest manuscrit contenen, d'una manera o d'una altra, tot el suport i ajuda que he rebut al llarg d'aquests anys des de tots els àmbits.

Primer de tot, vull agrair a la Marta Guinau i a l'Antonio Abellán la direcció d'aquesta tesi. A la Marta pel seu guiatge que des de fa anys m'ha ajudat a progressar en l'àmbit de la recerca. Començant pel seu suport amb el Màster, el Grau i finalment el Doctorat. Malgrat tenir horaris vitals radicalment diferents vull agrair-li l'esforç que ha fet per adaptar-se a la meua manera de treballar, vull agrair-li la flexibilitat per tractar amb un "enginyer que ve de la UPC" i la capacitat de crear un vincle que ha permès abordar moltes situacions des de marcs no estrictament professionals. A l'Antonio li vull agrair tot el suport tècnic que he rebut en la primera etapa del doctorat. Vull agrair-li haver-me fet confiança des de l'inici, totes les idees i aportacions que han enriquit (i fonamentat) part del projecte, els contactes que m'ha proporcionat, i les empentes necessàries que m'han permès assolir els objectius. De la segona etapa del doctorat, vull agrair-li el suport personal que m'ha donat, les llargues converses telefòniques i sobretot l'agraïment d'haver obert camí molt abans que jo.

Faig extensiu aquest agraïment a tots els membres del RISKNAT, per totes les ajudes rebudes, el suport científic i totes les converses que configuren el dia a dia d'un investigador en formació. Un agraïment molt sincer a tots aquells companys que de manera proactiva m'han volgut ajudar, m'han resolt dubtes i m'han fet més amena la meua vivència a la facultat. Especialment a tots els companys que m'han ajudat amb les feines de camp i sempre han estat disposats a revisar-me un sistema fotogramètric o a carregar un sac de ciment a Puigcercós! Moltes gràcies per formar part d'aquesta recerca i creure en el que fem els joves.

1. Fa referència a un prefaci que ha estat eliminat de la publicació final d'aquest manuscrit. El document, que no forma part de la tesi, es troba en [català i en castellà en aquest enllaç](#) i en el següent codi QR:



Dins l'àmbit de la facultat, vull agrair molt especialment als encarregats d'efectuar les tasques de neteja. Si la meva recerca té alguna característica és que no ha estat especialment “neta i polida”. Per aquest motiu, un agraïment immens per les tones de silicona, sorra, pedretes, models de gel desfets, llimadures metàl·liques, pintura i paperets que s'han hagut de recollir. De la mateixa manera, agraïment extensiu al personal de la facultat, bidells i punt d'informació perquè de manera desinstitucionalitzada ens ajuden i ens fan més fàcil la nostra vivència a la facultat. Sense anar més lluny, ells continuen sent els únics que em garanteixen poder entrar amb el vehicle a descarregar. Coses tan senzilles però tan difícils d'aconseguir.

Però si aquesta tesi ha acabat sent una realitat, ha estat per l'ajuda (que mai podré agrair prou) de 4 persones que dia rere dia m'han ajudat a sobreviure en aquest absurd món del doctorat. Aquesta tesi ha estat a punt de no-ser durant dues vegades, i sempre s'ha acabat salvant gràcies a ells. Per mi són 4 herois. A més, puc dir amb tranquil·litat que aquesta tesi té part d'ells i ni és mentida ni és una figura retòrica. Ells m'han discutit paràgrafs, figures, estructures i m'han ajudat en l'elaboració d'aquest manuscrit. Per ajudes molt més simples, molts autors firmen articles.

En Pere, el company d'aventures. Relació que ha transcendit més enllà del doctorand. De compartir un spa a Suïssa a haver de baixar de Sant Jeroni de nit i sense frontal. Sempre i a tota hora. Li agraeixo tota l'ajuda que m'ha donat tant en l'àmbit tècnic com emocional, les sortides al camp, les excursions, el suport dels sistemes, totes les converses (i les que ens queden!) i els viatges amb cotxe/furgo. Li agreixo haver-me tret de casa per caminar i desconnectar en els moments de més frustració (i de pas ensenyar-me les contrades). És molt simple, si algú llegeix aquestes línies: en Pere s'ho mereix tot.

En Robert, ai, en Robert! Cap persona m'ha ajudat més a analitzar la meva pròpia tesi que ell. És el director de tesi que tothom hauria de tenir i ningú tindrà. Moltes parts d'aquesta tesi tenen el seu segell de fons. Segurament és la persona amb qui he patit/viscut la tesi de manera més semblant. Ens hem plantejat moltes vegades el perquè de tot el que estàvem fent. La seva contra-crítica i el seu (molt en el fons :D) suport m'ha ajudat a seguir amb la tesi i l'ha enriquida. Sempre en deute per creure que jo no li he pogut tornar amb la mateixa moneda.

L'Octavi, des del primer fins a l'últim dia el meu company de tesi. Des dels primers dies de coneixença fins a l'actualitat, on malgrat la distància, cada dia estem xerrant i compartint sensacions. Vull agrair-li haver estat una guia en el món de la ciència. La sensació d'haver assumit plegats aquest repte. És la persona que més he vist al llarg d'aquests 5 anys i ha estat el meu suport diari tant en aspectes tècnics com epistèmics :D. Sé que estic en deute per tot el que ell ha hagut d'aguantar-me. I amb moltes ganes de continuar compartint espais en un futur! (encara que mai vulgui venir d'excursió).

I finalment la Llanos, l'aire fresc combinat amb l'experiència vital. El toc d'alerta a mitja tesi de què potser no tot s'ho val tant i que cal cuidar-se a un mateix. Agrair-li haver entomat des del primer dia una relació de tu a tu. Ens fotem canya des del primer dia i ja ens coneixerem més endavant. El suport emocional que vam trigar molts mesos a rebre. Agrair-li l'empenta, les energies renovades i la il·lusió per un nou projecte sense perdre de vista la visió crítica, i sempre amb el recordatori de què la prioritat és viure. Encantat de conèixer-te!

Alejándonos de la Universitat de Barcelona quiero trasladar un agradecimiento especial a los compañeros de la Universidad de Granada. Especialmente a José Miguel por confiar en nosotros. Esta energía y esta confianza para apoyar proyectos de jóvenes investigadores debería ser la norma en el campo de la investigación, pero es la excepción. Por este motivo, un agradecimiento inmenso por darnos la oportunidad de ampliar nuestras zonas de estudio y la posibilidad de diseñar sistemas fotogramétricos en la Alhambra de Granada. También de Granada, un agradecimiento muy grande a Cristina por todo el apoyo que me ha dado, tanto técnico como anímico y personal. Ha sido todo un descubrimiento y una persona con la que he podido compartir muchas sensaciones de la tesis (a distancia y presencial). ¡Le deseo lo mejor con su trabajo y espero que nos podamos encontrar de nuevo, próximamente!

I would also like to take this opportunity to express my immense gratitude to all my colleagues at the TU Dresden. Especially to Anette Eltner. Thanks to the months that I spend with her in Dresden during my doctoral stay, this thesis took on a new dimension and everything started to make sense. I thank her for hosting me without having many references and for sharing all her knowledge with me. More recently, I would like to thank her for offering me the opportunity to work with her and be part of her research group.

Finalment, vull agrair al Geoparc Mundial UNESCO Orígens i al Patronato de la Alhambra y Generalife la seva implicació en el projecte de tesi. La seva col·laboració i el seu suport han estat indispensables per instal·lar amb èxit els sistemes fotogramètrics a les zones d'estudi.

Fora dels àmbits universitaris, també vull fer un agraïment especial a tots els companys de l'Institut Montbui. Especialment al Departament de Matemàtiques. Gràcies per la flexibilitat i les facilitats que m'han permès compaginar la tesi doctoral amb la feina de docent a l'institut! Guardo un molt bon record d'aquesta experiència i estic segur que tard o d'hora tornaré a trobar el meu camí en un centre educatiu.

De manera externa a la tesi doctoral vull agrair a totes les persones que m'han acompanyat al llarg d'aquests anys. Han estat anys de gestions emocionals complicades, de reptes i entrebancs on hi ha hagut de tot. S'han desfet relacions en les quals hi creia molt i alhora s'han descobert noves persones i s'han generat nous vincles. De totes elles guardo un record molt gran. Tinc molta estima per a totes aquelles persones que al llarg d'aquests anys m'han fet costat i m'han ajudat a fer front a aquestes dificultats. Segueixin o no al meu costat, s'hagin desfet les relacions o hagin mutat, des dels marges o des de les trinxeres. Amb la consciència d'haver pogut viure uns anys i unes relacions diferents si no hagués fet aquesta tesi i amb la pena de no haver pogut mostrar el meu jo més estable. Unes disculpes i un agraïment. Seguim i seguirem! Moltes gràcies per haver-hi estat o per ser-hi. La lluita sempre continua i ens tornarem a trobar!

Finalment, l'últim agraïment és pels infal·libles. La família en el sentit biològic, però també en el més ampli del terme (la família que tries). Un agraïment a tots aquells que ajuden sense qüestionar. Que parafrasejant n'Ovidi, <<són tendresa i són bastó>>. Que empenyen quan cal empènyer i que són suaus i comprensibles quan s'està al límit (el fràgil art de la tendresa). A tots ells gràcies per fer-me ser com soc, per ser-hi sempre i per acceptar-me en plenitud.

Gràcies per no defallir.

No crec que ningú hagi gaudit, com a tal, del procés de gestació d'aquesta tesi, però com que té pinta que això ja s'acaba, cal intentar estar content! - Una abraçada, i alcem la copa!

Indesinenter.

En els darrers anys, els models fotogramètrics s'han convertit en una eina molt utilitzada en l'àmbit de les geociències gràcies a la seva capacitat per reproduir superfícies naturals. Com a alternativa a altres sistemes com el LiDAR (*Light Detection and Ranging*), la fotogrametria permet obtenir núvols de punts 3D a un cost més baix i amb una corba d'aprenentatge menor. Aquesta combinació ha permès la democratització d'aquesta estratègia de creació de models 3D. Per altra banda, els desprendiments de roca són un dels fenòmens geològics que representen un risc per al conjunt de la societat. És l'afectació natural més abundant en zones muntanyoses i donada la seva gran velocitat, la seva perillositat és molt elevada.

Aquesta tesi doctoral aborda la creació de sistemes fotogramètrics i algorismes de processat per al monitoratge automàtic de desprendiments de roca. Per dur-ho a terme s'han dissenyat **3 sistemes fotogramètrics de càmeres fixes** que s'han instal·lat en **2 zones d'estudi**. A més a més, s'han desenvolupat **3 fluxos de treball diferents**, dos d'ells encarats a obtenir comparacions de models fotogramètrics de major qualitat i un centrat a automatitzar tot el procés de monitoratge amb l'objectiu d'obtenir sistemes automàtics de monitoratge d'alta freqüència temporal.

Per una banda, s'ha dissenyat un sistema fotogramètric de molt baix cost utilitzant càmeres Raspberry, anomenat **RasPi**, instal·lat a la zona d'estudi de **Puigcercós** (Catalunya). Malgrat ser un sistema de molt baix cost i de baixa resolució els resultats obtinguts demostren la seva utilitat per identificar desprendiments i deformació precursora. Per altra banda, s'ha dissenyat un sistema fotogramètric d'alta resolució anomenat **HRCam** també instal·lat a la zona d'estudi de Puigcercós (Catalunya). Aquest sistema utilitza càmeres comercials convencionals i unitats avançades de control. Amb aquest sistema s'han assolit models de gran qualitat que permeten realitzar un millor monitoratge dels desprendiments de roca. Finalment, s'ha dissenyat un tercer sistema fotogramètric de manera similar al sistema HRCam anomenat **DSLR**, instal·lat en una zona de risc real al **Tajo de San Pedro de l'Alhambra** (Granada). Amb aquest sistema s'ha estat duent a terme un monitoratge constant dels desprendiments que afecten aquest escarpament durant els anys de realització d'aquesta tesi doctoral.

Per a poder obtenir comparacions 3D amb la màxima qualitat possible, s'han desenvolupat dos fluxos de treball. El primer, anomenat **PCStacking**, consisteix a realitzar un apilament de models 3D per tal de calcular la mediana de les coordenades Z de cada punt per generar un nou núvol de punts medià. En aquesta tesi es mostra l'aplicació de l'algoritme tant amb núvols de punts sintètics creats ad hoc com amb núvols de punts obtinguts amb el sistema RasPi. En ambdós casos els percentils d'error 25 i 75 de les comparacions 3D s'han reduït de 3,2 cm a 1,4 cm en les proves sintètiques i d'1,5 cm a 0,5 cm en condicions reals.

El segon flux de treball que s'ha desenvolupat s'anomena **MEMI** (*Multi-Epoch and Multi-Imagery*). Aquest flux de treball és capaç d'obtenir comparacions fotogramètriques amb una qualitat superior a les que s'obtenen amb el flux de treball fotogramètric clàssic. La utilització redundat d'imatges de les dues èpoques a comparar permet reduir l'error fins a un factor de 2 en comparació amb l'enfocament clàssic, permetent obtenir una desviació estàndard de la comparació de models 3D d'1,5 cm (en una zona sense cap deformació).

Finalment, el darrer flux de treball que es presenta en aquesta tesi és una **actualització** i una **automatització** del mètode de detecció de despreniments de roca a partir de núvols de punts. L'actualització s'ha realitzat perseguint dos objectius. El primer, traspassar tot el mètode de treball a llicència lliure (tant llenguatge com programari) i el segon, incloure els nous algoritmes i millores desenvolupats en aquesta tesi en el processat fotogramètric. L'automatització del mètode s'ha dut a terme per fer front a la gran quantitat de dades que es generen amb els sistemes fotogramètrics. Per aconseguir-ho, es plantegen estratègies d'aprenentatge automàtic (Machine Learning) que permeten resoldre els aspectes més crítics de l'automatització. Aquest avenç permet automatitzar tots els processos, de tal manera que des de la captura de les imatges que es produeix a la zona d'estudi fins a la l'obtenció dels despreniments, es produeix de manera automàtica gairebé en temps real.

Gràcies a la creació d'aquests sistemes fotogramètrics, dels algoritmes de millora de models 3D i de l'automatització en la identificació de despreniments, aquesta tesi doctoral presenta una proposta sòlida i innovadora en el camp del **monitoratge automàtic de baix cost**. La creació d'aquests sistemes i algoritmes representen un avenç rellevant en l'expansió dels sistemes de monitoratge i alerta que tenen com a objectiu final permetre'ns viure en un món més segur i construir societats més resilents enfront dels riscos geològics.

In recent years, photogrammetric models have become a widely used tool in the field of geosciences thanks to their ability to reproduce natural surfaces. As an alternative to other systems such as LiDAR (Light Detection and Ranging), photogrammetry makes it possible to obtain 3D points clouds at a lower cost and with a shorter learning curve. This combination has allowed the democratization of this 3D modelling strategy. On the other hand, rockfalls are one of the geological phenomena that represent a risk for society. It is the most common natural phenomenon in mountainous areas and, given its great speed, its hazard is very high.

This doctoral thesis deals with the creation of photogrammetric systems and processing algorithms for the automatic monitoring of rockfalls. To this end, **3 fixed camera photogrammetric systems** were designed and installed in **2 study areas**. In addition, **3 different workflows** have been developed, two of which are aimed at obtaining comparisons of higher quality using photogrammetric models and the other focused on automating the entire monitoring process with the aim of obtaining automatic monitoring systems of high temporal frequency.

The photogrammetric **RasPi** system has been designed and installed in the study area of **Puigcercós** (Catalonia). This very low-cost system has been designed using Raspberry cameras. Despite being a very low-cost and low-resolution system, the results obtained demonstrate its ability to identify rockfalls and pre-failure deformation. The **HRCam** photogrammetric system has also been designed and installed in the Puigcercós study area. This system uses commercial cameras and more complex control systems. With this system, higher quality models have been obtained that enable better monitoring of rockfalls. Finally, the **DSLR** system has been designed similarly to the HRCam system but has been installed in a real risk area in the **Tajo de San Pedro in the Alhambra** (Andalusia). With this system, a constant monitoring of the rockfall affecting the Tajo de San Pedro has been carried out during the years of this doctoral thesis.

In order to obtain 3D comparisons with the highest possible quality, two workflows have been developed. The first, called **PCStacking**, consists of stacking 3D models in order to calculate the median of the Z coordinates of each point to generate a new averaged point cloud. This thesis shows the application of the algorithm both with ad hoc created synthetic point clouds and with real point clouds. In both cases, the 25th and 75th percentile errors of the 3D comparisons were reduced from 3.2 cm to 1.4 cm in synthetic tests and from 1.5 cm to 0.5 cm in real conditions.

The second workflow that has been developed is called **MEMI** (Multi-Epoch and Multi-Imagery). This workflow is capable of obtaining photogrammetric comparisons with a higher quality than those obtained with the classical workflow. The redundant use of images from the two periods to be compared reduces the error to a factor of 2 compared to the classical approach, making it possible to obtain a standard deviation of the comparison of 3D models of 1.5 cm (in an area without any deformation).

Finally, the last workflow presented in this thesis is an **update** and **automation** of the method for detecting rockfalls from point clouds. The update has been carried out with two objectives in mind. The first is to transfer the entire working method to free licence (both language and programming), and the second is to include in the processing the new algorithms and improvements that have recently been developed. The automation of the method has been performed to cope with the large amount of data generated by photogrammetric systems. For this purpose, Machine Learning strategies are proposed to solve the most critical aspects of the automation. This advance makes it possible to automate all the processes, so that from the capture of the images produced in the study area to the obtaining of the landslides, it is produced automatically in near-real time.

Thanks to the creation of these photogrammetric systems, the 3D model improvement algorithms and the automation of the rockfall identification workflow, this doctoral thesis presents a solid and innovative proposal in the field of **low-cost automatic monitoring**. The creation of these systems and algorithms constitutes a further step in the expansion of monitoring and early warning systems, whose ultimate goal is to enable us to live in a more secure world and to help make societies more resilient to cope with geological hazards.

List of Tables	15
List of Figures	17
List of QR's	27
List of Acronyms	29
SECTION I INTRODUCTION	
Chapter 1 - General Overview	33
1.1 Structure of the Thesis	33
1.2 Motivation	36
1.3 Objectives	41
1.4 Study areas	42
Chapter 2 - Basic Concepts and Background	49
2.1 Digital Photogrammetry (Structure from Motion)	49
2.2 Photogrammetric Monitoring	56
2.3 Methodological Background (Point Clouds)	59
2.4 Rockfalls	64
2.5 Overview of the Publications	68
SECTION II MATERIALS AND METHODS	
Chapter 3 - Photogrammetric Systems	75
3.1 Brief Disclaimer	75
3.2 General Outlines	75
3.3 RasPi - Photogrammetric System (Puigcercós)	93
3.4 HRCam - Photogrammetric System (Puigcercós)	100
3.5 DSLR - Photogrammetric System (Granada-Alhambra)	105
Chapter 4 - PCStacking Algorithm	113
4.1 Introduction to the research	113
4.2 Materials and Methods	115
Chapter 5 - MEMI Workflow	125
5.1 Introduction of the research	125
5.2 Materials and Methods	125
SECTION III RESULTS AND PARTIAL DISCUSSIONS	
Chapter 6 - Photogrammetric Systems	139
6.1 Results	139
6.2 Partial discussion	150

Chapter 7 - PCStacking Algorithm	155
7.1 Results	155
7.2 Partial discussion	159
Chapter 8 - MEMI Workflow.....	165
8.1 Results	165
8.2 Partial discussion	170
 SECTION IV ROCKFALL MONITORING	
Chapter 9 - Rockfall Monitoring Workflow	179
9.1 Brief background.....	180
9.2 Rockfall detection workflow update.....	183
9.3 Rockfall detection workflow automation.....	188
Chapter 10 - Application Cases.....	205
10.1 Puigcercós I – RasPi System	206
10.2 Puigcercós II – HRCam System	208
10.3 Granada-Alhambra – DSLR System.....	216
Chapter 11 - Brief Considerations	221
11.1 Rockfall monitoring workflow.....	221
11.2 Workflow automation	222
11.3 Application cases.....	224
 SECTION V GLOBAL SUMMARY	
Chapter 12 - Summary of the Discussion.....	227
12.1 Summary of the discussion.....	227
12.2 Global consideration	230
12.3 Further research.....	231
Chapter 13 - Concluding Remarks.....	233
13.1 Photogrammetric Systems	233
13.2 PCStacking (Publication I).....	234
13.3 MEMI Workflow (Publication II).....	234
13.4 Rockfall Monitoring.....	235
 SECTION VI REFERENCES	
Overall References.....	239
 SECTION VII APPENDICES	
Appendix A Scripts and algorithms.....	263
Appendix B Publication I (Remote Sensing)	265
Appendix C Publication II (Remote Sensing)	287

List of Tables



Table I.1. List of selected cases of monitoring strategies associated with different natural phenomena. The different strategies presented can be used for different natural phenomena.	37
Table III.1. Main parameters of the point clouds and M3C2 results obtained in the May 2020 test.	167
Table III.2. Main parameters of the point clouds and M3C2 results obtained in the November 2019 test.	169
Table III.3. Main results obtained in the precision estimation test.	169
Table IV.1. Parameters computed for statistical analysis.	196
Table IV.2. Parameters computed for ML analysis. All these parameters have been calculated twice. Once for the whole set of points forming the cluster and once for the central core of the cluster.	200

List of Figures

F

- Figure I.1.** Structure of the Thesis. Summary of Contents.33
- Figure I.2.** The top 15 research fields with the highest number of publications containing the concept of "digital photogrammetry". The size of the box and the colour is proportional to the number of publications.....39
- Figure I.3.** Visual overview of the specific objectives of the thesis. This graphical distribution helps to understand the linearity and interconnections of the research.....42
- Figure I.4. a)** Situation map in the administrative territorial division of the Generalitat de Catalunya with the Pallars Jussà region in grey and the location of Puigcercós (Inset with the location of Catalunya in the Iberian Peninsula). **b)** Geomorphological context of the study area (the rectangle depicts the area shown in image c). DEM and topographic base from [Institut Cartogràfic i Geològic de Catalunya](#) database. **c)** Image of the Puigcercós cliff and the debris scree, with the ruins of the ancient village of Puigcercós on top of the hill. And **d)** image of the landslide that occurred at the end of the 19th century with the extent delimited by a red line (white square depicts the area shown in image c). From [Google Earth](#) server.43
- Figure I.5. a)** Situation map on the administrative territorial division (comarcas) of the Junta de Andalucía, with the Vega de Granada region in grey (inset with the location of Andalucía in the Iberian Peninsula). **b)** Contextual situation of the study area, with the elements shown in c) delimited. DEM and topographic base from [Instituto Geográfico Nacional](#) database. **c)** [Google Earth](#) image of the Tajo de San Pedro behind the monumental complex of the Alhambra and Generalife. **d)** Frontal image of the Tajo de San Pedro obtained with the DSLR photogrammetric system.47
- Figure I.6.** Schematic workflow of the SfM-MVS process resulting in a dense point cloud from image sets. Reproduced from **Iglhaut et al. (2019)** and distributed under the terms of the Creative Commons Attribution 4.0 International License.51
- Figure I.7. a)** Existing 3D comparison methods between two point clouds PC1 and PC2. **aA:** Simplest cloud-to-cloud distance L_{C2C} . **aB:** Closest point distance to local model distance L_{C2C_H} . **aC:** Cloud-to-mesh (C2M) distance L_{C2M} and **b)** Description of the M3C2 algorithm and the two

user-defined parameters D (normal scale) and d (projection scale). Reproduced with permission of the publisher (certificate available in the **Appendix A – Elsevier Authorisation** and in [this link](#)).63

Figure I.8. DBSCAN Algorithm. **a)** The red and green dots are part of the cluster (they are within the search radius). The blue dot is not part of the cluster. **b)** Clustering result. The grey dots are not part of any cluster. The coloured dots are part of the respective clusters. **a,b)** CC BY-SA 3.0 licence64

Figure I.9. **a)** Schematic representation of a generic rockfall mechanism and the different zones defined in the process. **b)** Rockfall on a coastal escarpment (the twelve apostles, Australia - Creative Commons license). **c)** Rockfall on an anthropic slope that has overcome the defences (Tremp, Catalonia). **d)** Rockfall retained by the installed defences (Tremp, Catalonia). Images **c, d)** have been acquired by the author.66

Figure I.10. Journals with the highest number of publications with the word "structure from motion". In addition, the total citations of the SfM articles are included. The size of the box and the colour reflect the ratio of publications (no citations).....69

Figure II.1. Experiment carried out in the laboratory with ice models **QR 13**, using low-cost cameras. The plot shows the pre-failure deformation of the largest block. It is recommended to visualise the result in the **QR 14** and a similar example in **QR 15**.76

Figure II.2. Representation of the 5 modules that constitute a complete photogrammetric system. Each module shows the main components. The description of the sections **a-j)** is done in the main text and is developed in the following sections of the manuscript. All images/pictograms have been obtained under Creative Common licence or are product images directly obtained from the manufacturer.77

Figure II.3. **a)** Aspect ratio of the most common commercial sensors. CC BY-SA 3.0 Moxfyre. **b)** Evolution in megapixels of the sensors. The different shades of blue roughly divide the different sensor categories. CC BY-SA 3.0 Martin Kraft.....79

Figure II.4. **a)** Sketch showing the projection of a real object on the photographic sensor. The sketch helps to understand the basic concepts of optics inside a photographic camera. The focal length is represented. CC BY-SA 3.0 Moxfyre. **b)** Graphical representation of the different fields of view (represented in angles) obtained for different focal lengths. CC BY-SA 3.0 MrSpyDoS.....80

Figure II.5. Main functions of the advanced control unit. Each block contains its own programming environment and functions. Codes and scripts available in the digital repository of each photogrammetric system. (e.g., Appendix A - HRCam System scripts).....	82
Figure II.6. Diagram of the time sequence of actions carried out by the control unit to transmit and securely store the acquired images to the workstation. There is one direct transmission line and two backups (one temporary and one permanent).	84
Figure II.7. Log file fragment. It shows the status of the HRCam1 system in Puigcercós and the main script outputs. This log is automatically sent to the server after each boot.....	85
Figure II.8. Basic diagram of a general connectivity system. a) Connectivity system installed in Puigcercós. b) Connectivity system installed in Granada-Alhambra. In both systems, the source signal is 4G. Further details are provided in the respective sections	86
Figure II.9. Diagram showing the two power systems designed to supply solar energy to designed systems. Left: DSLR and HRCAM systems. Right: RasPi System.....	91
Figure II.10. Rendering of the RasPi system. Includes the basic elements such as the solar panel, the powerbank, the control unit and the Raspberry Pi Camera.....	94
Figure II.11. Main stages of the development of the RasPi photogrammetric system. Stage 1) Main initial components and scripts. Stage 2) Field intervention to install 2 new systems and introduce connectivity to the systems. Stage 3) Raspberry Pi version upgraded and installation of external Wi-Fi antennas. Stage 4) Current status of the system. (Codes available in the repository: Appendix A – RasPi System scripts).....	94
Figure II.12. a) Locations of the RasPi cameras in Puigcercós. All systems have the same camera and shooting configuration. ICGC base map, no north oriented. b) Frontal image of the Puigcercós cliff with the locations of the RasPi systems.....	95
Figure II.13. Low-cost photogrammetric systems developed ad-hoc for rockfall monitoring on the Puigcercós cliff. a,b) Images of the installation on the Puigcercós cliff. c) Main electronic components (left to right): WittyPi2, Raspberry Pi ZeroW, Raspberry Camera Module v2 and MicroSD card.....	96
Figure II.14. a) Radiation pattern of an omnidirectional antenna similar to those included in Teltonika modems. Used in Granada-Alhambra system. b) Radiation pattern of the sectorial antennas used for the Puigcercós system (MP Antenna, 2019).....	98

Figure II.15. **a)** Schematic map of the location of the Puigcercós connectivity system. [ICGC](#) base map, coordinates in UTM Zone 31N and ETRS89. **b)** Location of the connectivity system. **c)** Location of the 4G antenna, modem and Wi-Fi antennas in the ruined Puigcercós tower. **QR16** shows images of the Puigcercós connectivity device.....99

Figure II.16. Rendering of the HRCam system. Includes the basic elements such as the camera, lense, solar panel, solar charge regulator, AGM battery, releys, DC-DC converters and the control unit. 101

Figure II.17. Main stages of the development of the HRCam photogrammetric system. **Stage 1)** First 3 systems. **Stage 2)** Installation of the lens hood to prevent soiling of glass. **Stage 3)** New script HRCam_UB_v2 with advanced functions **Stage 4)** Harward upgraded. Upper image: MOSFET Switches. Lower image: WittyPi 3 (Both from UUGear). (Codes available in the repository: **Appendix A - HRCam System scripts**)..... 101

Figure II.18. **a)** Map with the locations of the HRCam cameras in Puigcercós. Orange markers show the localization of the Canon cameras and grey markers represent the Sony cameras location. [ICGC](#) base map, no norht oriented. **b)** Frontal image of the Puigcercós cliff with the locations of the HRCam systems..... 103

Figure II.19. Photogrammetric system mounted at Puigcercós. **a)** Internal view of the camera module composed of a camera and the auxiliary control system. **b,c)** Exterior views of a module: **b)** Installation works and **c)** final integration with the environment..... 104

Figure II.20. **a)** Map with the locations of the DSLR cameras in Granada-Alhambra. All systems have the same camera model, but different lenses. [IGN](#) and [ESRI Topo](#) base map. **b)** 3D simulation of the view from the Tajo de San Pedro with the DSLR systems location. [Google Earth](#) model..... 106

Figure II.21. Simulation carried out to obtain the best focal length for each DSLR system. In this case, the figure shows the simulation performed for the DSLR3 located in the bell tower of the church of San Pedro (The location closest to the escarpment). [Google Earth](#) model. 107

Figure II.22. External images of 3 different DSLR systems. **a)** System in the bell tower of the Church of San Pedro (DSLR3). **b)** DSLR2 system installed on the balcony of the Archaeological Museum. **c)** Camera installed in the Zafra Convent (DSLR1). 108

Figure II.23. Main stages of the development of the DSLR photogrammetric system and its scripts (codes available in the repository: **Appendix A - DSLR System Scripts**). The development is similar to that of the HRCam system..... 109

Figure II.24. Location of the 3 connectivity systems installed in Granada-Alhambra. Numbers represent the photogrammetric system. [IGN](#) and [ESRI Topo](#) base map and [Google Maps](#) images. **a)** Global location map. **b)** System located in the Escuela-Hogar. **c)** Systems installed in the Church of San Predro, Zafra Convent and Archaeological Museum. **QR17** (next page) show images of the devices installed in Granada..... 110

Figure II.25. The three steps developed by the Point Cloud Stacking algorithm. **Step 1:** All points are stored in the PC-Stack cloud. **Step 2:** Coordinates system change. **Step 3:** Point averaging on the normal axis..... 116

Figure II.26. Synthetic Point Clouds (Synt-PC). **First row:** Function without error, representing the reference PC (Ref-PC) (Equation (1)). **Rows (2 to 4):** Functions created with errors based on random parameters (Equation (2)). **Columns (left to right):** Error function; sum of Ref-PC + Error function, X cross-section, Y cross-section. Dotted lines correspond to the Ref-PC and continuous lines to the Synt-PC..... 119

Figure II.27. a) X cross-sections of 5 Synt-PC (each colour corresponds to a different Synt-PC), the black line corresponds to the sections of the Ref-PC. **b)** Y cross-sections of 5 Synt-PC (each colour corresponds to a different Synt-PC), the black line corresponds to the sections of the Ref-PC. **c)** Distribution of differences between two Synt-PC computed by M3C2..... 120

Figure II.28. a) X cross-sections of four Photo-PCs generated using five images (each colour corresponds to a different Photo-PC). **b)** Y cross-sections of four Photo-PCs generated using five images (each colour corresponds to a different Photo-PC). **c)** Distribution of differences of two Photo-PCs computed by M3C2. (x) and (y) shows the cross section represented in **a)** and **b)**. 123

Figure II.29. 4D pipeline designed for the automatic analysis of rockfalls in Puigcercós. The colours represent different parts of the process grouped according to their description in the manuscript. 126

Figure II.30. Three different SfM-MVS photogrammetry workflows to calculate multi-temporal point clouds for change detection. The colour shading denotes images obtained at different time epochs. **a)** The classic workflow corresponds to the standard SfM-MVS photogrammetric approach. **b)** The multi-epoch imagery workflow (MESI) adopts the method defined by Feurer and

Vinatier (2018), i.e., joining images from multi-epochs during image matching and bundle adjustment. **c)** The Multi-Epoch Multi-Imagery (MEMI) workflow considers (additionally to b) redundant image bursts from each epoch. 129

Figure II.31. a) Mild MEMI workflow created for the change detection evaluation. **b)** Full MEMI workflow created using all images available. 133

Figure II.32. Pipeline performed to obtain the precision estimation in order to only detect significant changes (consecutive dates analysed). The 4D process illustrated in this figure comprises the classical workflow but the MESI and MEMI workflow has also been evaluated..... 135

Figure III.1. Heat map of the RasPi system operating calendar. The different shades of green indicate the possibility of obtaining photogrammetric models (at least 3 or more images are acquired)..... 140

Figure III.2. Images obtained with each photogrammetric system on 29 November 2019 at 15:45h. **a,b)** Recent images of the RasPi system. The difference between image **a)** and **b)** is the installation of the external Wi-Fi antenna to improve signal reception..... 141

Figure III.3. a) Point cloud of the photogrammetric model. **b)** Detail of the central area of the escarpment. **c)** Depth differences map..... 142

Figure III.4. Heat map of the HRCam system's operating calendar. The different shades of green indicate the possibility of obtaining photogrammetric models (at least 3 or more images are acquired)..... 143

Figure III.5. Images obtained with each HRCam photogrammetric system on 22 April 2019 at 17:47h. **a,b)** Recent image of two HRCam systems..... 144

Figure III.6. a) Point cloud of the photogrammetric model. **b)** Detail of the central area of the escarpment. **c)** Depth differences map..... 145

Figure III.7. Heat map of the DSLR system's operating calendar. The different shades of green indicate the possibility of obtaining photogrammetric models (at least 3 or more images are acquired)..... 146

Figure III.8. Images obtained with each photogrammetric system installed in Granada. Images were taken on 12 July 2019 at 09:17h. **a)** Image of the system installed on the terrace of the Church of San Pedro (DSLR4). The difficulty in installing the system can be seen, as it had to be installed

on raised supports. **b)** System installed in the bell tower of the church (DSLR1), where greater camouflage with the surroundings was required. 148

Figure III.9. a) Point cloud of the photogrammetric model. **b)** Detail of the central area of the escarpment (red inset). **c)** Depth differences map (red inset)..... 149

Figure III.10. Results from the application of the PCStacking algorithm with synthetic data. **a)** Histogram of the differences between the Enh-PC_n and the Ref-PC. Each coloured line represents a different number of Synt-PCs introduced into the PCStacking algorithm. **b)** Boxplot with the errors of the differences obtained in the different comparisons (Enh-PC_n vs. Ref-PC)..... 155

Figure.III.11. a) Evolution of the standard deviation of the comparison Enh-PC_n vs. Ref-PC in the redundancy test. The standard deviation decreased from 4.9 cm to 1.8 cm. A total of 400 Synt-PCs were used to compute this plot. **b)** Number of averaged points according to the search radius (r). Each coloured line represents a different number of Synt-PCs introduced into the PCStacking algorithm. 156

Figure III.12. Results from the application of the PCStacking algorithm to real images. **a)** Histogram of the differences between the Enh-PC_n^{25 feb} and Enh-PC_n^{26 feb}. Each coloured line represents a different number of PCs introduced into the PCStacking algorithm. **b)** Error of the differences obtained in the different comparisons (Enh-PC_n^{25 feb} vs. Enh-PC_n^{26 feb}). 157

Figure III.13. Influence of the search radius (r) on the PCStacking results. **a)** Standard deviation of the Enh-PC_n^{25 feb} vs. Enh-PC_n^{26 feb} comparison. **b)** Comparisons between Enh-PC₁₅^{25 feb} and Enh-PC₁₅^{26 feb} for different search radii (r). 158

Figure III.14. a) Graphic representation of the differences between the models of May 23 and 24, according to the workflow used. The four models are represented using the same colour scale. Zoom detail (inset) of the **b)** classic workflow and the **c)** full MEMI workflow. **d)** Histogram with the M3C2 results. **e)** Error bar plot with the dispersion of the values obtained in each comparison. 166

Figure III.15. a) Graphic representation of the differences between the models of November 8 and 13, according to the workflow used. The three models are represented with the same colour scale. **b)** Histogram with the M3C2 results. **c)** Error bar plot with the dispersion of the values obtained in each comparison. 168

Figure III.16. a) Results obtained from the precision estimation test, considering the distribution of σ_y (depth direction). **b)** Error boxplots of the range of the precision estimations (note the different scale on the y axis). 170

Figure III.17. a) Graphic representation of the differences between the LiDAR data (October 2019) and photogrammetry models (November 2019), according to the workflow used. The three models are represented with the same colour map. The larger red clusters indicate rockfalls that occurred during the comparison period. **b)** Bar plot showing the relative M3C2 standard deviation of the comparisons..... 171

Figure IV.1. Workflow developed by researchers Abellan (2009) and Royán (2015) from the RISKNAT research group. The colour of the box represents a different process or software. 181

Figure IV.2. Update of the rockfall detection workflow. The top row shows how the rockfall detection workflow fits into the general photogrammetric flow developed in this thesis. The bottom row shows the implemented update, with new stages and new programming languages. The colour of the box represents a different process or software. 184

Figure IV.3. Snapshots of the different stages in the rockfall detection process: **a)** Original point cloud. **b)** Result of the M3C2 comparison. Green colours indicate $\text{Diff} \approx 0$, red colours indicate $\text{Diff} > 0$. **c)** In red, points over the threshold ($\text{Diff} > 0.03$). 186

Figure IV.4. Snapshots of the different stages in the rockfall detection process: **a)** Clustering results. Each colour corresponds to one cluster. **b)** Result of manual filtering removing wrong clusters (noise). **c)** One possible outcome: density map..... 187

Figure IV.5. Diagram of the developed **XBGRockfall** automation software. The central element "core" is fed by the i) input data, ii) reference system and iii) processing libraries. The core is in charge of applying the MEMI algorithm, performance of the M3C2 comparisons and, from the strategies described in the automation challenge, identifying the rockfalls. Code available in the repository: **Appendix A - XBGRockfall**. 189

Figure IV.6. Tree diagram with the basic structure of the software. Grante boxes are folders containing the codes and files required for the photogrammetric processing. The light grey folders are the folders generated by the main code for each comparison and contain the files related to the rockfall identification process. (developped in detail **Figure IV.7**)..... 190

Figure IV.7. Tree diagram with the basic structure of the folder that is generated to store each comparison. The whole structure is generated when the software starts up and is unique for each comparison.	191
Figure IV.8. Final proposal of the automatic workflow for the detection of rockfalls. This approach allows an automatic processing from the image acquisition to the calculation of the volume of the rockfall. The colour of the box represents a different process or software.....	199
Figure IV.9. a) Basic diagram of the iterative operation of a machine learning model. b) Schematic of a machine learning model based on Random Forest Classifier algorithm using 3 decision trees.	201
Figure IV.10. a) Explanation of the confusion matrix obtained in a binary classification. The green boxes show the matching between real classification and prediction, the red boxes show the discrepancy between real classification and prediction. b) Best confusion matrix obtained in different tests. The confusion matrix shows an overall classification above 92.6%, which is distributed as shown in the figure.....	203
Figure IV.11. Rockfall identification. DSLR system image showing a capture a) before and b) after a rockfall, and the corresponding photogrammetric models c) before and d) after the rockfall. The QR 24 shows the animated sequence of the 3D models.....	205
Figure IV.12. a) Rockfall identified on 04/04/2019 comparing two photogrammetric models. b) The day before (03/04/2019) there was an earthquake M4.4 45km from the Puigcercós cliff . Map modified from European-Mediterranean Seismological Centre (EMSC). c) Images obtained automatically by the RasPi system. The rockfall has been delimited in white.....	207
Figure IV.13. a) Pre-failure deformation of a large-scale rockfall computed thanks to the daily images obtained with the RasPi system during 6 months. A clear final acceleration phase is identified. b) Schematic illustration of the reference method. c) Images obtained automatically by the RasPi system. The rockfall has been delimited in white. The QR 25 code shows a video of the detached block.	209
Figure IV.14. Large rockfalls identified using the HRCam system and the application of the MEMI algorithm in Puigcercós. The red areas denote the large rockfalls identified. a) The rockfall of 25/04/2019 has an approximate volume of 115 m ³ b) and the rockfall of 26/01/2020 has a volume of approximately 135 m ³	210

Figure IV.15. Rockfalls identified automatically over a period of 32 days. **a)** 29 rockfalls have been identified, the colour code relates the rockfalls on the 3D model to the day of detection in the plot. The size of the rockfalls has been increased in order to display them correctly. **b)** The plot shows the number of daily rockfalls together with the daily rainfall (obtained from [Meteoblue](#) ©)..... 212

Figure IV.16. Pre-failure deformation of a rock block at Puigcercós cliff. The comparison was made between 3D models 50 days apart. It can be seen how the deformation increases with the height of the block, so that a rock toppling movement can be identified. Finally, this block fell on 26/01/2020 (**Figure IV.14**). 213

Figure IV.17. 3D comparison using the classical workflow and the MEMI workflow between 09 November 2019 and 19 January 2020. The same comparison has been rendered twice, but using a different colour/threshold scale; **a)** and **b)** show the comparisons using the classic and MEMI workflows respectively with a threshold value of 30 cm (values below 30 cm are shown in green-yellow); **c)** and **d)** show the comparisons using the respective workflows with a threshold value of 3 cm..... 215

Figure IV.18. Rockfalls identified in the Tajo de San Pedro (Granada). Each colour identifies a different observation period. In total, 135 rockfalls have been identified over 669 days. The size of the rockfall markers has been increased to facilitate their visualisation. 217

Figure IV.19. Visualisation of the rockfall density distribution. The areas with warm colours show a higher concentration in the number of rockfalls during the 462-day observation period. The areas where no landslides are identified can be clearly visualised. These areas correspond to vegetation. A sphere of radius 2 metres has been used to count the number of rock falls per cubic metre. 218

Figure IV.20. Results obtained from the monitoring of rockfalls over a period of 669 days. **a)** Histogram of the distribution of rockfalls. Here we can see that most of the rockfalls are of small magnitude. **b)** Frequency-Magnitude distribution. The equation fitted to the number of rockfalls allows to characterize the behaviour of the Tajo de San Pedro cliff..... 219

Figure IV.21. Result obtained after automatically processing (with Machine Learning algorithm) 68 clusters in the Tajo de San Pedro. Purple colour shows the correctly identified rockfalls. Blue colour shows the wrong clusters correctly identified. Orange dot show a false positive, a cluster identified as a rockfall by the algorithm that is not a rockfall and the colour green identifies the false negatives, clusters identified as wrong clusters but which are rockfalls. 220

QR 1 - Digital gallery of figures (link to Google Drive)	36
QR 2 - Publication chart (LiDAR + Earth Science) (link to Dimensions.ai).....	38
QR 3 - Historical image of Puigcercós (I).....	44
QR 4 - Historical image of Puigcercós (II).....	44
QR 5 - Historical image of Puigcercós (III)	44
QR 6 - Drone video of Puigcercós	44
QR 7 - Historical image of Tajo de San Pedro (I).....	46
QR 8 - Historical image of Tajo de San Pedro (II)	46
QR 9 - Historical image of Tajo de San Pedro (III).....	46
QR 10 - How to classify a landslide (link to British Geological Survey).....	66
QR 11 - Landslide Types and Processes (link to USGS)	66
QR 12 - Remote Sensing Statistics (link to MDPI webpage).....	68
QR 13 - Gallery of the first SfM-MVS experiment (Ice model).....	75
QR 14 - GIF with the result of the experiment, pre-failure deformation (I)	75
QR 15 - GIF with the result of the experiment, pre-failure deformation (II).....	75
QR 16 - Puigcercós connectivity system images (Extra images)	99
QR 17 - Granada connectivity system images (Extra images).....	111
QR 18 - Gallery with the images obtained by the RasPi system.....	139
QR 19 - Link to the 3D viewer. Point Cloud from Puigcercós (RasPi system).....	140
QR 20 - Gallery with the images obtained by the HRCam system.....	143
QR 21 - Link to the 3D viewer. Point Cloud from Puigcercós (HRCam system)	144
QR 22 - Gallery with the images obtained by the DSLR system.....	146
QR 23 - Link to the 3D viewer. Point Cloud from Tajo de San Pedro (DSLR system).....	147
QR 24 - GIF showing the identification of a rockfall from SfM-MVS	206
QR 25 - Drone video of a rockfall in Puigcercós	209

[This link](#) details the licences and conditions of the images and external resources used in the QR codes. For the printed version, scan the following code:



List of Acronyms



2D/3D/4D	Two/Three/Four-dimensional space
4G	Fourth generation of broadband cellular network technology
AC	Alternating current
AGM	Absorbed Glass Mat (Battery)
AI	Artificial Intelligence
API	Application Programming Interface
APS-C	Advanced Photo System type-C
BA	Bundle Adjustment
CANUPO	CAractérisation de NUages de Points
CC BY-SA	Creative Commons Attribution-ShareAlike licence
DBSCAN	Density-Based Spatial Clustering of Applications with Noise
DC	Direct Current
DIC	Digital Image Correlation
DSLR	Digital - Single lens reflex
DTM	Digital Terrain Model
EGU	European Geosciences Union
GCP	Ground Control Points
GNSS	Global Navigation Satellite System
GNU GPL	GNU General Public Licence
GPS	Global Position System
HDR	High Dynamic Resolution
HRCam	High Resolution Cameras System
ICP	Iterative Closest Points
LiDAR	Light Detection and Ranging
LTE	Long Term Evolution signal

LoD	Level of Detection
M3C2	Multiscale Model-to Model Cloud Comparison
MEMI	Multi-Epoch Multi-Imagery
MESI	Multi-Epoch Single-Imagery
ML	Machine Learning
MOSFET	Metal-Oxide-Semiconductor Field-Effect Transistor
MVS	Multi View Stereo
NN	Nearest Neighbour
OS	Operating System
PC	Point Cloud
PCA	Principal Component Analysis
PCStacking	Point Cloud Stacking
PSFL	Python Software Foundation Licence
QR Code	Quick Response Code
RasPi	Raspberry Pi System
RGB	Red, green, blue (Colour model)
RTC	Real Time Clock
SBC	Single-board computer
SCI	Science Citation Index
SfM	Structure from Motion
SfM-MVS	Structure from Motion - Multi View Stereo
SIFT	Scale-Invariant Feature Transform
SNR	Signal-to-Noise Ratio
SSR	Solid State Relay
TLS	Terrestrial Laser Scanner
UAV	Unmanned Aerial Vehicle
USB	Universal Serial Bus

Section I

INTRODUCTION

CHAPTER 01 – GENERAL OVERVIEW

CHAPTER 02 – BASIC CONCEPTS AND BACKGROUND



1.1 Structure of the Thesis

In accordance with the current regulations concerning doctoral theses at the Universitat de Barcelona, as well as with the internal requirements of the Facultat de Ciències de la Terra regarding the deposit of doctoral thesis, this dissertation is presented as a compendium of publications. To include all the sections required by the regulations and to facilitate the understanding and comprehension of the research, the manuscript is divided into **7 sections** and **13 chapters**, as shown in the following structure (**Figure I.1**):

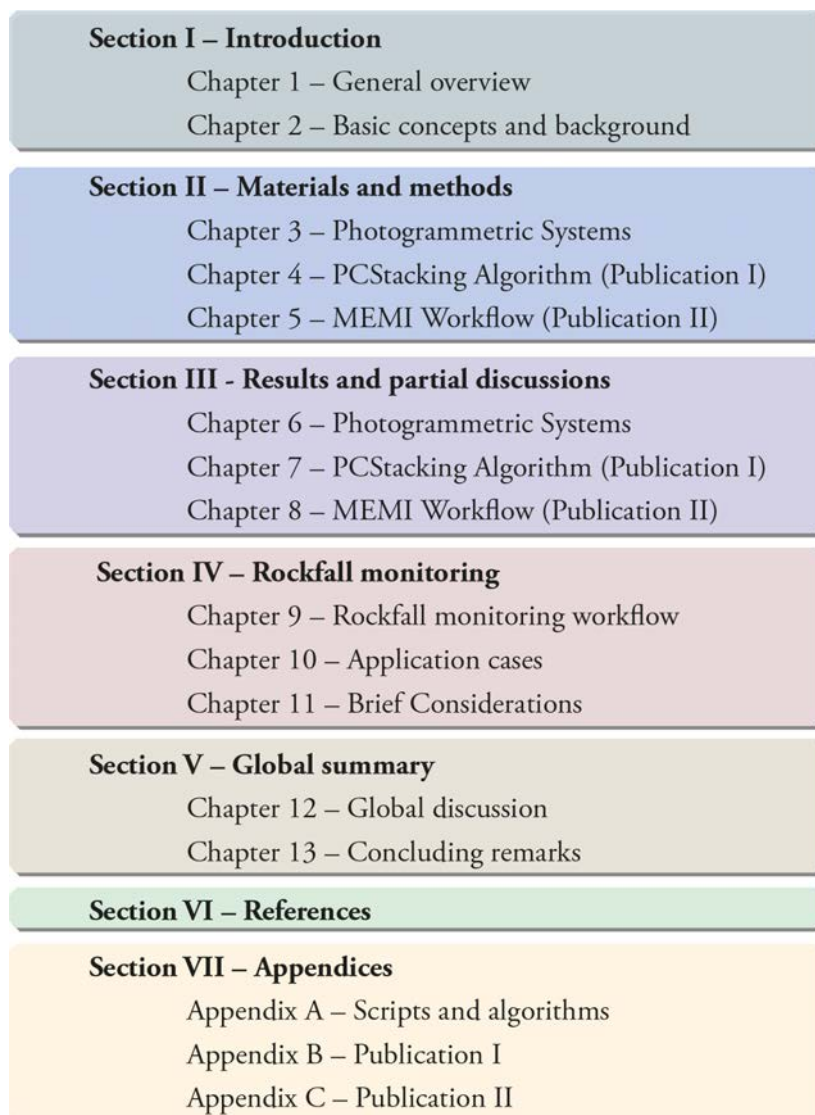


Figure I.1. Structure of the Thesis. Summary of Contents.

The thesis project is introduced in **Section I**, which is divided into two chapters. **Chapter 1** is focused on introducing the reader to the format, motivation, and objectives of the research as well as on describing the study areas. **Chapter 2** introduces the reader to more specific methodological aspects of the work that has been carried out. This second chapter provides basic knowledge for the correct understanding of the subsequent chapters and the justification for the entire research project as well as an outline of the publications.

Due to the technical and methodological nature of the research, **Section II** constitutes the core of the thesis. This section is divided into 3 chapters. The aim of **Chapter 3** is to explain the development (design, creation, and implementation) of the photogrammetric monitoring systems that have been created ad hoc to obtain the data necessary for conducting the research. Subsequently, **Chapter 4** and **Chapter 5** correspond to the methodological part of the papers written during the thesis and published in Remote Sensing journal, indexed in the Science Citation Index (SCI). In accordance with the internal regulations of Earth Science doctoral program of the Earth Sciences Faculty, these articles have been integrated with the same format and design as the rest of the chapters. Compared to the original publications, certain non-essential aspects such as bibliographical references and figures have been modified to make the manuscript more coherent and consistent. In addition, parts of the papers that might be redundant throughout the manuscript of this thesis, such as the description of the study areas or certain parts of their introduction, have been moved or omitted to ensure the continuity of the manuscript. **Appendices B** and **C** contain the original copies of the articles in the format of the publication.

Because this dissertation is presented as a compendium of articles, a section containing the results and discussion concerning the research is mandatory. Thus, **Section III, Chapter 6**, shows the results obtained with photogrammetric systems as well as a brief discussion about them. **Chapters 7** and **Chapter 8** show the results and the partial discussions published in Publication I and II, respectively. These chapters represent the main results of the published content of the thesis and provide a more in-depth discussion of each photogrammetric system and method developed in this research.

Section II and **Section III** encompass the description of the methodological approaches developed to improve photogrammetric models. However, the thesis also addresses the

application of these advances on the field of geosciences. Although this part is not published, the author considers it very important to present all the advances that have been achieved. **Section IV** is devoted to explaining a workflow proposal for the automatic rockfall monitoring and examples of its application. Therefore, **Chapter 9** provides an understanding of how it is possible to develop an automated workflow that integrates all the developments introduced in **Section II**. Subsequently, **Chapter 10** presents case of application in the study areas where rockfall monitoring has been carried out using the systems and the methods developed in this research. Finally, **Chapter 11** provides a brief overview of the method, outlining its opportunities and limitations.

The rockfall monitoring workflow presented in this thesis is of great value and represents a significant advance in the field of geohazard monitoring. Although the publications refer strictly to the photogrammetry method, the case of application in the field of geohazards should be understood as an addendum to the publications. For this reason, **Section IV** should also be considered as results of the research itself. However, in contrast to the methodology shown in the publications, this section does not provide an in-depth analysis of the workflow, nor does it provide any in-depth analysis of the identified rockfalls and their activity.

The author's aim in distinguishing **Section III** from **Section IV** is twofold: i) To highlight the results obtained in the photogrammetric workflow, which has been published and may be useful in numerous fields; and ii) to give specific relevance to the monitoring of rockfalls, which is an essential part of the Research Group in which the thesis has been undertaken.

The aim of **Section V** is to give coherence to all the previous chapters, as well as to integrate the published articles within the research. For this reason, **Chapter 12** provides a global discussion of the research focused on the methodological publications and the rockfall monitoring systems, while **Chapter 13** ends with the conclusions of the research.

Section VI presents the bibliographical references used in the thesis, and **Section VII** shows the different appendices that are added to complement the research. These appendices contain all the scripts and algorithms that have been developed during the research project (**Appendix A**) and both articles published in the original journal format (**Appendix B** and

C). In the printed version of this thesis, the updated articles and the digital repository of algorithms and scripts can be accessed by scanning the respective Quick Response Codes (QR Code). In the digital version, **simply click on these codes** to access, via hyperlink, the respective web pages, and code repositories.

Similarly, throughout the thesis, the main text is complemented by small QR codes located on the outer margin of the page. These codes, which are **scannable in the printed version** and **clickable in the digital version**, provide access to digital resources that are not essential but complement the text.

The following **QR 1** links to the **Figures gallery** where they can be viewed in full resolution. In addition, in the digital version, clicking on each figure opens it directly in full size. In the case of the visualisation of images or pictograms, the authorship or licence is indicated (both in the external resources (QR) and in the Figures of this thesis). If not indicated, they are freely licenced images/pictograms.

Finally, the author considers that open access to knowledge is critical, and that the scientific community is obliged to share knowledge in order to improve our society. For this reason, this manuscript and all scripts are published under the next source licence: [Attribution-ShareAlike 4.0 International \(CC BY-SA 4.0\)](#) / [Free Cultural Works](#). When we share everyone wins.

1.2 Motivation

Natural phenomena monitoring is a field of research that has historically been of great importance to the scientific community in the geosciences (Angeli et al., 2000). From the use of classical surveying instrumentation for observing the movements of large landslides (Gili et al., 2021) to the modern technological solutions currently available for detecting rockfall pre-failure deformations with great precision (Kromer et al., 2018; Royán et al., 2015), the goal of observing and understanding the natural phenomena occurring around us has been ever-present. A better comprehension of natural phenomena directly impacts our ability to manage and mitigate natural hazards, resulting in significant improvements in risk management (Guzzetti et al., 1999).



QR 1

Over the years, monitoring techniques have evolved in parallel with the technological progress of our society. Nowadays, all these techniques cover an infinite number of different technological solutions and allow for a wide range of different monitoring strategies. **Table I.1** shows a few examples of different monitoring strategies applied to different natural phenomena. Nevertheless, many others exist, and the same technique can usually be applied to several natural phenomena, examples of which can be found in Janeras et al. (2015), who show how several techniques can be applied to monitor one specific natural hazard.

Table I.1. List of selected cases of monitoring strategies associated with different natural phenomena. The different strategies presented can be used for different natural phenomena.

Natural event	Monitoring Strategy
Volcanoes	Satellite images (Rothery et al., 1988)
	Thermal sensors (Wooster & Rothery, 1997)
	Geophysics (Grêt et al., 2005)
Landslides	Extensometers (Corominas et al., 2000)
	Inclinometers/Tensiometers (Simeoni & Mongiovì, 2007)
	Interferometry DInSAR (Reyes-Carmona et al., 2020)
	Classical Photogrammetry (Gili et al., 2021)
Snow avalanches	Infrasound (Kogelnig et al., 2011)
	Seismometers (Roig-Lafon, 2021)
Rockfalls	LiDAR (Abellán et al., 2014)
Earthquakes	Gas sensors (Woith et al., 2020)
Debris flows	Ultrasounds (Hürlimann et al., 2011)
	Geophones (Abancó et al., 2012)
Soil erosion	Digital Photogrammetry (Eltner et al., 2017)
Tectonic deformation	GPS (Khazaradze et al., 1999)

From the techniques presented in **Table I.1**, the use of LiDAR (Laser Imaging Detection and Ranging) has contributed to significant advances in the field of geosciences (Petrie & Toth, 2008). The possibility of acquiring high-precision 3D models at long distances from



QR 2

the target and at high speed enables, for example, a considerable improvement in the geometrical characterization of rockfalls (Abellán, 2009) or an increase in the temporal frequency of monitoring of a large landslide (Jaboyedoff et al., 2012). For this reason, over the last 20 years, the number of articles published in indexed journals where the term LiDAR appears in the field of geosciences has been increasing steadily (Abellán et al., 2014; Guzzetti et al., 1999; McKean & Roering, 2004; On et al., 2008; Tarolli, 2014). **QR 2** (in PC web browser) shows an updated chart with with the number of publications containing the word LiDAR in the field of geosciences.

However, despite the many benefits, the use of this technology also has some limitations, such as the high cost of infrastructure acquisition and maintenance, the difficulty of use in remote locations or the high fixed installation costs (Cook, 2017). These limitations make LiDAR incompatible with a massive deployment in the field of natural hazard monitoring (Cook, 2017; Sturzenegger et al., 2007; Wilkinson et al., 2016).

In contrast, digital photogrammetry is a monitoring strategy that overcomes some of the limitations of LiDAR. The capability to create large photogrammetric systems at a very low cost, the possibility to install them easily in remote areas, together with the ability to obtain results with a very low learning curve, have led to the democratization of this monitoring strategy (Eltner & Sofia, 2020; Westoby et al., 2012). In recent years, the large number of publications using point clouds obtained with the digital photogrammetry technique confirm the popularisation of the use of this technique (Anderson et al., 2019).

As an example of this popularisation, point clouds (PC) obtained by photogrammetry are used to analyse and monitor objects and surfaces such as, for example, building structures (Artese et al., 2016; Bartonek & Buday, 2020; Castellazzi et al., 2015; Meidow et al., 2018) or natural surfaces (Eltner et al., 2016; Eltner & Schneider, 2015; Feurer & Vinatier, 2018; Nesbit & Hugenholtz, 2019; Westoby et al., 2012). Thanks to its great versatility and low cost, digital photogrammetry is a monitoring solution that is applied in a multitude of research fields (**Figure I.2**).

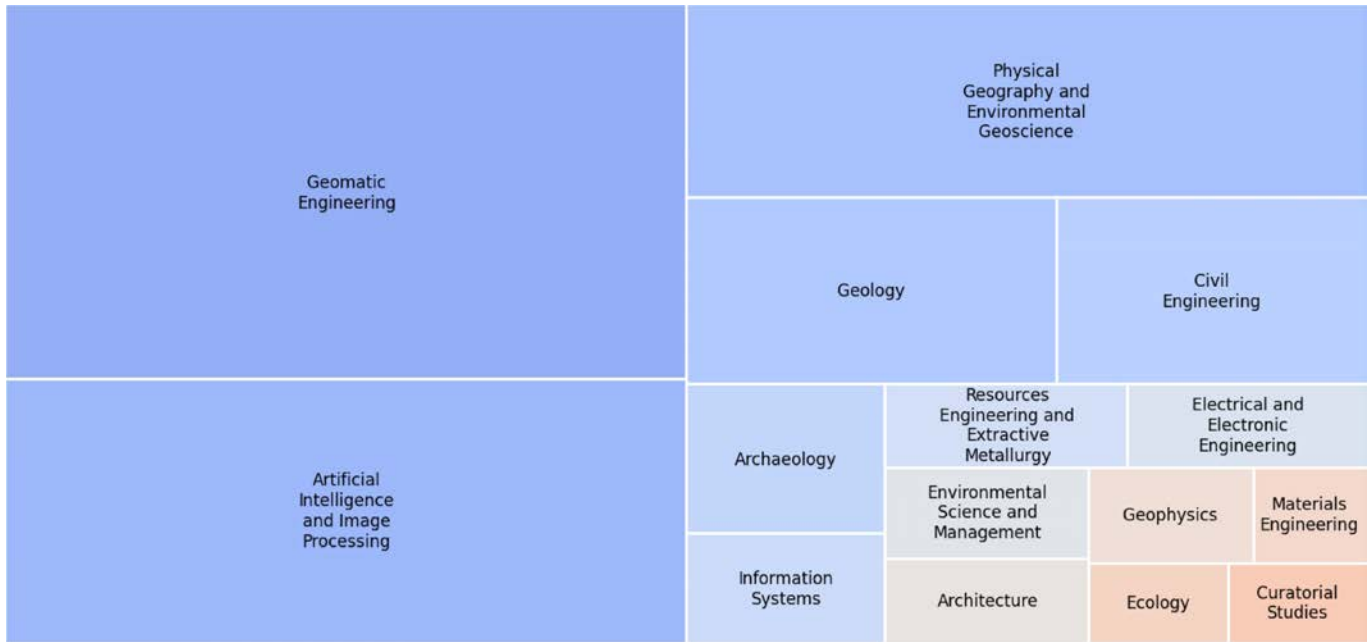


Figure I.2. The top 15 research fields with the highest number of publications containing the concept of "digital photogrammetry". The size of the box and the colour is proportional to the number of publications.

Several studies have shown that the use of photogrammetric techniques does not result in a particular loss of accuracy with respect to LiDAR PCs (Castillo et al., 2012; James & Robson, 2012; Javernick et al., 2014; Kaiser et al., 2014). It should be noted, however, that these studies are mostly based on large-scale or detailed laboratory analyses in which hundreds of photographs and numerous control points were used to generate the models. It is well known that the accuracy of LiDAR data depends mainly on the device used to acquire the data. In contrast, the accuracy of the photogrammetric data depends on many other factors, such as the camera setup, the weather conditions, and the sharpness of the acquired images.

Many publications try to assess accuracies of digital photogrammetry in the geosciences (Brunier et al., 2016; Cook, 2017; James & Quinton, 2014; On et al., 2008; Stumpf et al., 2015). Nowadays, due to advances in the processing techniques of digital photogrammetry and computer vision, photogrammetric results can be compared to LiDAR (Cook & Dietze, 2019; James & Robson, 2012; Rowley et al., 2020; Stumpf et al., 2015). However, these accuracies comparable to LiDAR cannot be generalised, since they depend on the camera used, the number of photographs and the distance and shape of the object. Due to this

limitation, there is a special motivation in the field of photogrammetry to generate further algorithms and workflows (such as those presented in this research) that significantly improve the quality and the accuracy of the process, with the aim of obtaining results similar to those obtained with LiDAR.

Although many geological hazards can benefit from advances in digital photogrammetry, the work presented in this thesis has been carried out in the field of rockfall research. Rockfalls are the most frequent and dangerous event in mountainous areas (Whalley, 1984). They are characterized as being essentially gravitational events triggered at high speed (Hungur et al., 2014) and are therefore highly dangerous. Most rockfalls occur in remote locations and have a localized impact that may not affect society. However, both population growth and climate change affecting triggering factors such as rain (Krautblatter & Moser, 2009) or temperature (Allen & Huggel, 2013) increase our exposure and make us more vulnerable to the impact of rockfalls and other geological and geomorphological hazards (Capes & Teeuw, 2017; Knight et al., 2012; McGuire & Maslin, 2012; Technical, 2010).

The study of rockfalls has been conducted over time and from many different perspectives. Most of the effort is focused on trying i) to predict the rockfalls using mathematical models (Azzoni et al., 1995; Rose & Hungur, 2007); ii) to predict the pre-failure deformations (Kromer et al., 2018; Rosser et al., 2007; Royán et al., 2014); iii) to characterize the rockfalls and their dynamics (Abellán et al., 2006; Derron & Jaboyedoff, 2010; Ferrero et al., 2009; Volkwein et al., 2011); iv) to create inventories (Cataogue et al., 2013; Lato et al., 2013; Malamud et al., 2004), and v) to determine the susceptibility (Copons & Vilaplana, 2008; Gallach, 2012; Gigli et al., 2014; Mazzanti & Brunetti, 2010).

However, the common characteristic in all these studies is the need to create monitoring strategies to obtain the necessary rockfall data. As shown by Janeras et al. (2015), different strategies shown in **Table I.1** can be used for rockfall monitoring, some of the most commonly used being LiDAR (Abellán et al., 2010; Kromer et al., 2015; Teza et al., 2015), seismic sensor (Suriñach et al., 2018; Feng et al., 2020; Walter et al., 2012) or photogrammetry (Buill et al., 2016; Giacomini et al., 2020; Kromer et al., 2019; Kromer et al., 2015). Given the global importance of the study of this phenomenon and the importance of its monitoring,

this thesis focuses on applying all the advances obtained in digital photogrammetry in the field of rockfall monitoring, thereby also obtaining new advances in this area.

The enhanced understanding and better characterization of rockfalls that can be obtained as a result of the improved workflows, together with the automatic monitoring process presented in this dissertation, constitute an essential preliminary step for the creation of early warning systems as well as for improvements in the creation of protection infrastructure, both of which are highly important goals for reducing the impact of this geological hazard on society and thus crucial in the motivation for this research.

1.3 Objectives

The overall objective of this thesis is as follows: to improve the classical workflows used in digital photogrammetry to enhance 3D change detection. This improvement should make it possible to adapt rockfall monitoring workflows to obtain results with a quality and accuracy similar to those obtained by LiDAR. The achievement of this general objective is based on the fulfilment of the following specific objectives:

- i. Design, create and install very low-cost, low-resolution, and solar-powered photogrammetric systems with remote data transmission.
- ii. Design, create and install low-cost, high-resolution, and solar-powered photogrammetric systems with remote data transmission.
- iii. Improve the classical workflow and algorithms used in digital photogrammetry to correct geometric errors in 3D models from low-resolution systems (objective i).
- iv. Improve the classical workflow and algorithms used in digital photogrammetry to enhance change-detection processes obtained by high-resolution photogrammetric systems (objective ii).
- v. Design and develop an automated workflow for the creation of automatic rockfall monitoring systems using the enhanced change-detection process developed (from objectives iii and iv).

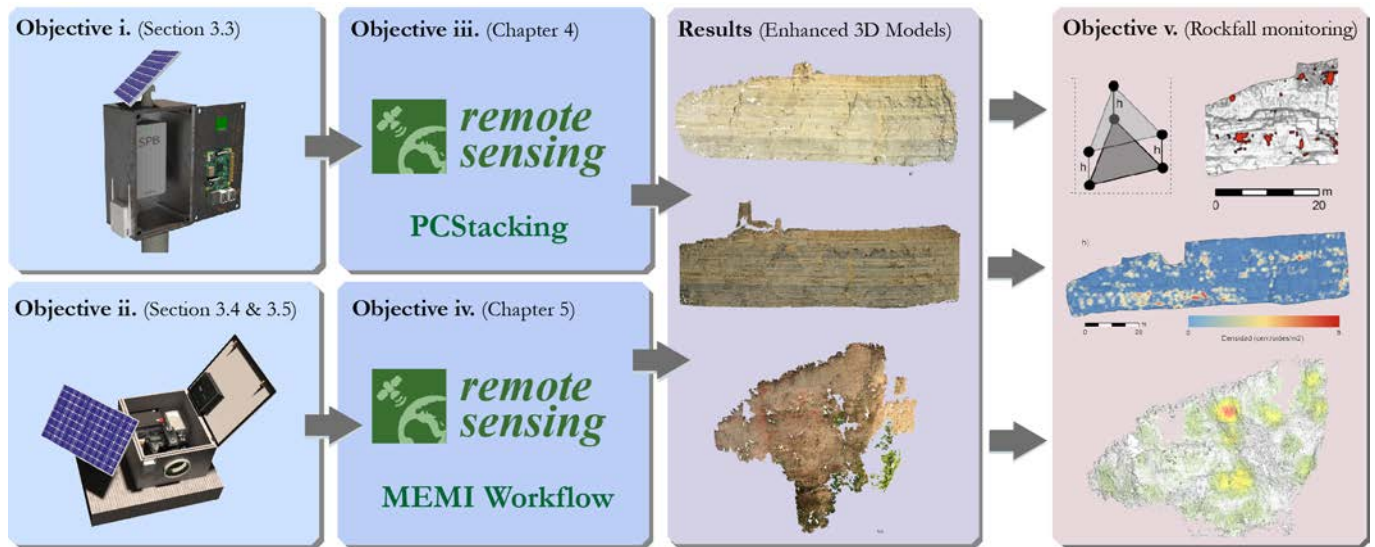


Figure I.3. Visual overview of the specific objectives of the thesis. This graphical distribution helps to understand the linearity and interconnections of the research.

According to the general objective and the specific objectives (i to iv), the research of this thesis is focused on producing an instrumental and algorithmic improvement of the photogrammetric monitoring method, obtaining relevant innovations that allow the characterisation of rockfalls at an unprecedented low-cost and high-temporal frequency (**Figure I.3**).

1.4 Study areas

The development of this thesis has been carried out in two study areas located in Puigcerçós (NE Spain) and Granada (S Spain). These study sites are characterized by relevant rockfall activity (active slopes), as well as the difficulty of accessing the escarpment to install sensors or acquire measurements directly.

1.4.1 Puigcerçós

Location and geological context

The Puigcerçós study area is a rocky cliff called l'Espadat de Puigcerçós. It is located on the mountain where the ruins of the ancient village of Puigcerçós are located (550 m above sea level), located in the Pallars Jussà region (Catalonia, NE Spain) (**Figure I.4a** and **Figure**

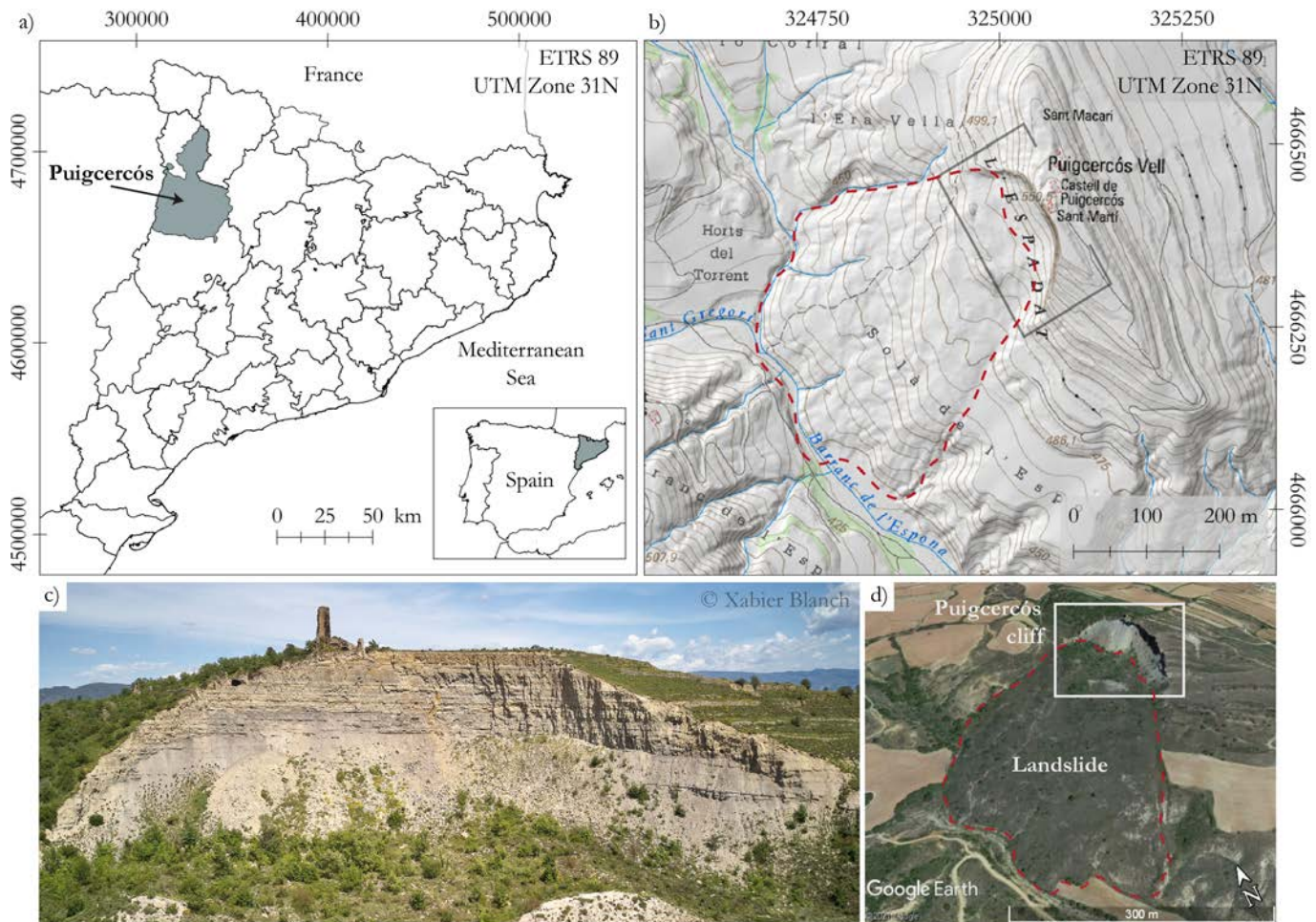


Figure I.4. **a)** Situation map in the administrative territorial division of the Generalitat de Catalunya with the Pallars Jussà region in grey and the location of Puigcercós (Inset with the location of Catalunya in the Iberian Peninsula). **b)** Geomorphological context of the study area (the rectangle depicts the area shown in image c). DEM and topographic base from [Institut Cartogràfic i Geològic de Catalunya](#) database. **c)** Image of the Puigcercós cliff and the debris scree, with the ruins of the ancient village of Puigcercós on top of the hill. And **d)** image of the landslide that occurred at the end of the 19th century with the extent delimited by a red line (white square depicts the area shown in image c). From [Google Earth](#) server.

I.4b). This rock face (123 m long and 27 m high) is the result of a large roto-translational landslide (Hungre et al., 2014) that occurred at the end of the 19th century (Corominas & Alonso, 1984; Vidal, 1881) and caused the replacement of the village in a new location (**Figure I.4c** and **Figure I.4d**). Today, some remains of walls and half a tower of the ancient

castle still exist on the top of the cliff as a reminder of the old village. **QR** codes **3**, **4** and **5** show photographs and sketches of the village before and after the landslide, and **QR 6** links to a current (year 2020) video of the cliff captured by drone in 1080p resolution.



QR 3

Geologically, the Puigcercós escarpment is located in the Tremp Basin, which is embedded between the reliefs that constitute the northern part of the South Pyrenean foreland basins (Cuevas, 1992). The Tremp basin is filled with a sequence of Eocene sedimentary materials. These sequences dip gently toward the north in Puigcercós and alternate in the form of layers of variable thickness of limestone, sandstone, and grey marl.



QR 4

Based on an update of the Varnes classification proposed by Hungr et al. (2014), the main mechanism that cause failures in the Puigcercós cliff is rock toppling, although some detachments may also be controlled by pure rock fall mechanisms. These detachments are conditioned by the intersection of the sub-horizontal stratification with a set of sub-parallel vertical tension cracks in the cliff (Blanchard et al., 2008; Royán, 2015).



QR 5

The ease of access to the area, together with its high rockfall activity and its low risk due to the lack of exposed elements, make it an ideal experimental site in the field of rockfalls. Given its interest in the field of geological hazards and the geological interest of the surroundings, the Puigcercós cliff and its ancient landslide are currently part of the [Orígens UNESCO Global Geopark](#).



QR 6

Background research –Experimental site

Thanks to the good preservation of the cliff, the frequent activity observed and the security with which data can be collected, this area has become a pilot study area of rockfalls for the RISKNAT research group since 2007.

An excellent example of this is the entire development of LiDAR monitoring of rockfalls carried out over the last few years. From the first methodological approach presented by Blanchard et al. (2008) to the present-day, new advances have been developed that have enabled more than a decade of monitoring and methodological evolution (Khazaradze et al., 2019). An example of this evolution are the publications by Abellán et al. (2010) in which they characterise rockfalls and identify pre-failure deformation; Tonini & Abellán (2014),

where new clustering strategies for rockfalls detection with LiDAR are described; Royán et al. (2014 and 2015) where they analyse the possibility of forecasting and predicting rockfall events based on pre-failure deformation. In addition to the aforementioned publications, the doctoral theses of Abellán, 2009 and Royán, 2015 (RISKNAT researchers) have been partially carried out in the Puigcercós study area. Both theses constitute an important advance in the characterization and prediction of rockfalls from LiDAR data.

The study site is an ideal natural laboratory for the development of new techniques, not only for the observation and monitoring of rockfalls, but also landslides (Khazaradze et al., 2019, 2020). Examples are the detection and characterization of rockfalls from seismic data (Suriñach et al., 2018; Telletxea et al., 2021); the use of GNSS data to observe the tension crack evolution at the head of the escarpment and possible displacements of the body of the large landslide (Khazaradze et al., 2017); or the use of advanced photogrammetric systems for the identification of rockfalls (Blanch et al., 2020, 2021). All these integrated techniques enable the RISKNAT research group to make advances in the understanding of the rockfall and landslide phenomena.

1.4.2 Granada-Alhambra

Location and geological context

The Granada-Alhambra study area corresponds to a rocky cliff located on the Sabika hill (790 m above sea level), on which the [Alhambra y Generalife](#) complexes sit. These complexes of historic palaces, gardens, and fortress, declared a World Heritage Site by UNESCO in 1984, are located in the city of Granada (Andalucía, SE Spain) (**Figure I.5a**). This escarpment has a height of 65.5 m and is called Tajo de San Pedro due to its dihedral profile (called Tajo) and its location in front of the Church of San Pedro (**Figure I.5b**).

The beginnings of this dihedral-shaped cut in the Sabika hill are uncertain. Its formation and the regression of the escarpment are mainly produced by erosion and detachments occurring as a consequence of i) the interaction between erosion-scour generated by the Darro river (flowing at the base of the cliff), ii) seismic movements, iii) and water erosion and infiltrations (Azañón et al., 2011; Justo et al., 2009) (**Figure I.5c** and **Figure I.5d**).



QR 7

The first reference demonstrating the presence of Tajo de San Pedro dates from 1520, when the first anthropic refill at the bottom of the escarpment is mentioned. The following **QR** codes complement this information with illustrations and images from the 18th and 19th centuries showing the presence of the Tajo de San Pedro in the past (**QR 7, 8 and 9**).



QR 8

Geologically, the Tajo de San Pedro intersects the dense conglomerates of the Alhambra Formation. This formation, dated between the Upper Pliocene and the Lower Pleistocene, is characterized by being very resistant to compression, but easily rippable (Azañón et al., 2011; Justo et al., 2009). The materials that form the conglomerate of the Alhambra Formation correspond to ancient alluvial fans from the erosion of Sierra Nevada (Azañón et al., 2011; Justo et al., 2009).



QR 9

In the studied escarpment, these conglomerates emerge in a sub-horizontal pattern. Small silty layers, sandy sectors, and a Pleistocene paleosoil level can also be distinguished. In addition, the front face of the Tajo de San Pedro clearly shows the presence of faults, one of which is located on the edge of the dihedral with a 3.5 m gap. (Azañón et al., 2011).

No scientific description of the rockfalls that occur in the Tajo de San Pedro is found in the literature. Even so, from the studies developed in this thesis we may infer that the detachments that occur are mostly controlled by rockfall-type mechanisms, although the largest blocks can be affected by rock toppling mechanisms that quickly evolve to rockfalls (Hungre et al., 2014).

These rockfalls are associated with the degradation of the carbonate cement that fixes the cobbles of the conglomerate and with the opening of tension cracks sub-parallel to the scarp that delimit the blocks.

The presence of a World Heritage Site such as the Alhambra y Generalife just a few metres from the escarpment makes this study site a real geological risk area, both for the more than 6,000,000 tourists who visit the site every year and for the conservation of the Alhambra building itself.

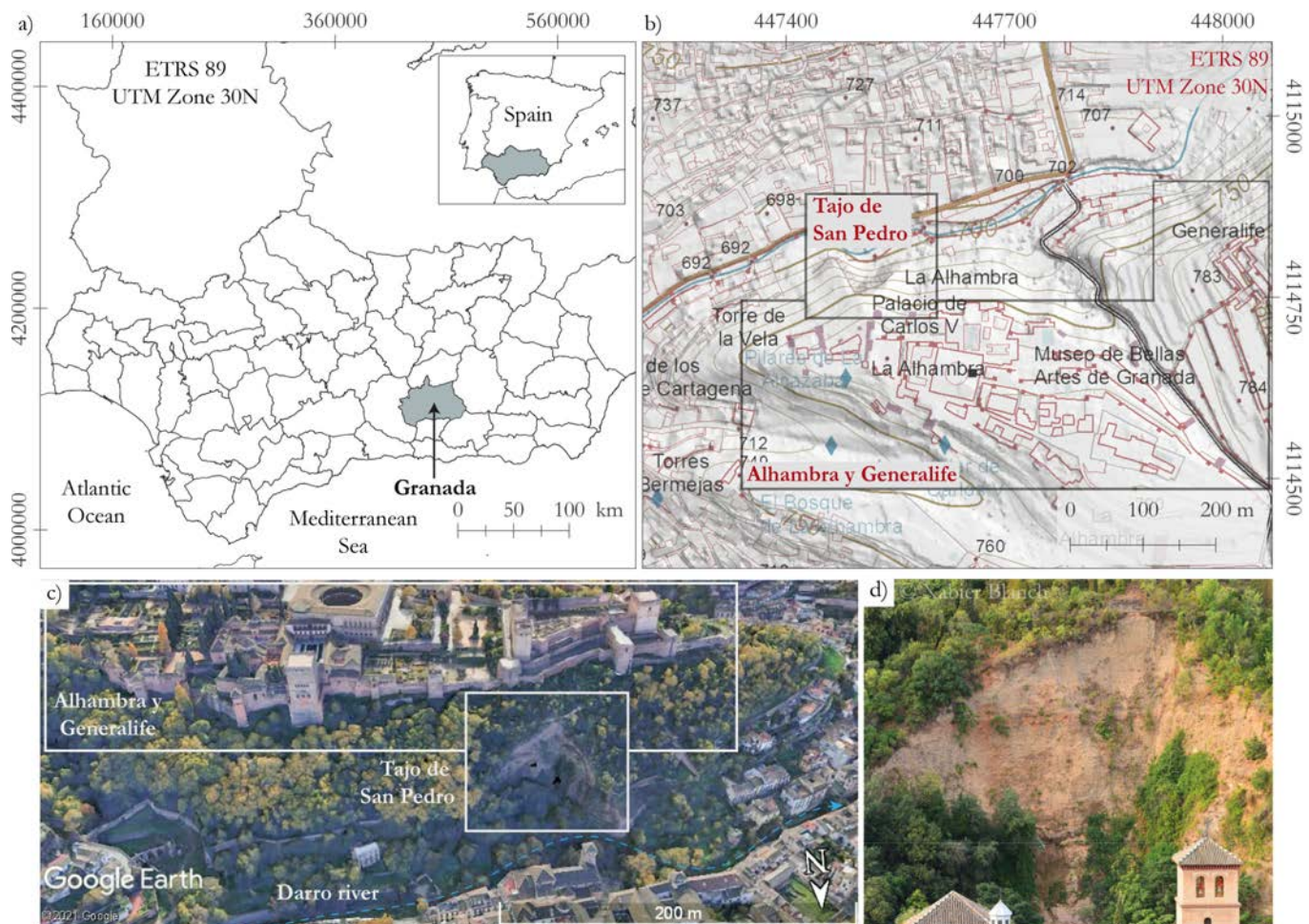


Figure I.5. a) Situation map on the administrative territorial division (comarcas) of the Junta de Andalucía, with the Vega de Granada region in grey (inset with the location of Andalucía in the Iberian Peninsula). b) Contextual situation of the study area, with the elements shown in c) delimited. DEM and topographic base from [Instituto Geográfico Nacional](#) database. c) [Google Earth](#) image of the Tajo de San Pedro behind the monumental complex of the Alhambra and Generalife. d) Frontal image of the Tajo de San Pedro obtained with the DSLR photogrammetric system.

Background research

In contrast to Puigercós, no specific rockfall research has been published in this study area. However, given that there is considerable preoccupation by the managers of the historical complex, various studies commissioned by the Patronato de la Alhambra have been carried out on a private initiative. An example of these studies is the annual monitoring with LiDAR to analyse and characterise the rockfalls that occur in the Tajo de San Pedro. Given the high

interest of the Patronato de la Alhambra in rockfall monitoring, two research projects have been signed during my investigation. One to develop the photogrammetric monitoring system that will be explained in the following chapters, and the other to produce monitoring reports based on the obtained images. Both results are partially shown in this manuscript.

In other fields of research, such as slope engineering or tectonics, publications based on the Tajo de San Pedro can be found. Some examples of this are the publication by Justo et al. (2008 and 2009) where technical aspects of a stabilization project were developed, and the publication of Azañón et al. (2011) where the dynamic behaviour of the faults in the city of Granada is described and characterized, with special interest in the faults affecting the Tajo de San Pedro.

On a more general level, we can find scientific literature oriented to the characterization of the materials of the Alhambra Formation, such as the CEDEX (Centro de Estudios y Experimentación de Obras Públicas) reports (Santos et al., 1994) where a detailed geotechnical characterization of the conglomerates of the Alhambra Formation is carried out, and the publication of Azañón et al. (2004) where a detailed characterization of the faults and geomorphological effects caused by seismicity in the Alhambra is performed out.

The aim of this chapter is to establish the basic concepts and background for understanding the research carried out throughout this thesis. This chapter includes part of the introductions published in the articles. However, to ensure the coherence of the chapter, new parts have been included and the distribution of paragraphs and headings has been modified with respect to those published.

2.1 Digital Photogrammetry (Structure from Motion)

2.1.1 Brief introduction

Digital photogrammetry should be understood as a technological evolution of traditional photogrammetry, since the final purpose is the same. Both methods can be defined as the set of techniques, instrumental and mathematical, that make it possible to obtain three-dimensional coordinates of an object from the two-dimensional information extracted from one or several photographs (Buill et al., 2003).

Although the concept is the same, the use of different technology means that the approaches to each method are radically different. Traditional photogrammetry is based on the application of complex mathematics to analogue or digital images. For example, the application of least squares techniques to calculate the rototranslation matrices needed to obtain the coordinates of homologous points, ensuring collinearity and coplanarity conditions. The resolution of traditional photogrammetry is a complex calculation process that is always carried out by an expert.

On the other hand, digital photogrammetry always uses digital images. The reconstruction process is based on Structure from Motion (SfM) algorithms and Multi View Stereo (MVS). SfM-MVS photogrammetry is the set of techniques used to reconstruct 3D models from unregistered, overlapping image sets. This approach is a low-cost and flexible surveying tool that can be considered as an alternative to techniques such as Light Detection and Ranging (LiDAR) that usually require high-cost equipment and longer learning curves.

SfM-MVS workflow differs from traditional photogrammetry mainly in three aspects: (i) features can be automatically identified and matched in images at differing scales, viewing angles and orientations, which is of particular benefit when small unstable platforms are considered; (ii) the equations used in the algorithm can be solved without information of camera positions or ground control points, although both can be added and used, and (iii) camera calibration can be automatically solved or refined during the process.

The product resulting from either traditional or digital photogrammetry is the same; the 3D coordinates of an object. However, this result can be visualized in many ways. From analogical photogrammetry, it is usually possible to obtain stereo-photogrammetry, restitutions, and ortho-corrections (2D). A brief description of each method is given in detail at Núñez Andrés et al. (2012) and Yilmaz et al. (2007). With the advent of digital photogrammetry, the visualisation of results has evolved. In addition to the aforementioned, it is common to work with 3D digital models. A 3D model is the process of producing a mathematical, coordinate-based representation of an object. One way to represent these models is by means of a point cloud (PC). A point cloud is a set of data points in space that represent an object in 3D and are defined by the 3 spatial coordinates. The result obtained by the SfM-MVS algorithms is a set of point clouds. However, other results can be obtained from SfM-MVS, such as 3D mesh, DEM's or orthomosaic, which are calculated from the point clouds (Agisoft, 2021).

2.1.2 Basic principles of SfM-MVS photogrammetric systems

As Iglhaut et al. (2019) state, the term SfM photogrammetry is commonly used to define the entire reconstruction workflow, from the image set to the dense point cloud. However, strictly speaking, SfM only refers to a specific step in the workflow that provides the camera parameters and a sparse point cloud (**Figure I.6**). To clarify for the reader, in this dissertation the term SfM refers only to the Structure from Motion algorithm and not to the whole photogrammetric process, which is referred to as SfM-MVS.

The basic principles of SfM-MVS photogrammetry are fully described in previous publications such as Eltner et al., 2016; Iglhaut et al., 2019; James & Robson, 2012; Westoby et al., 2012. The principal idea relies on estimating point positions in 3D (object space) from corresponding points on 2D surfaces (image space).

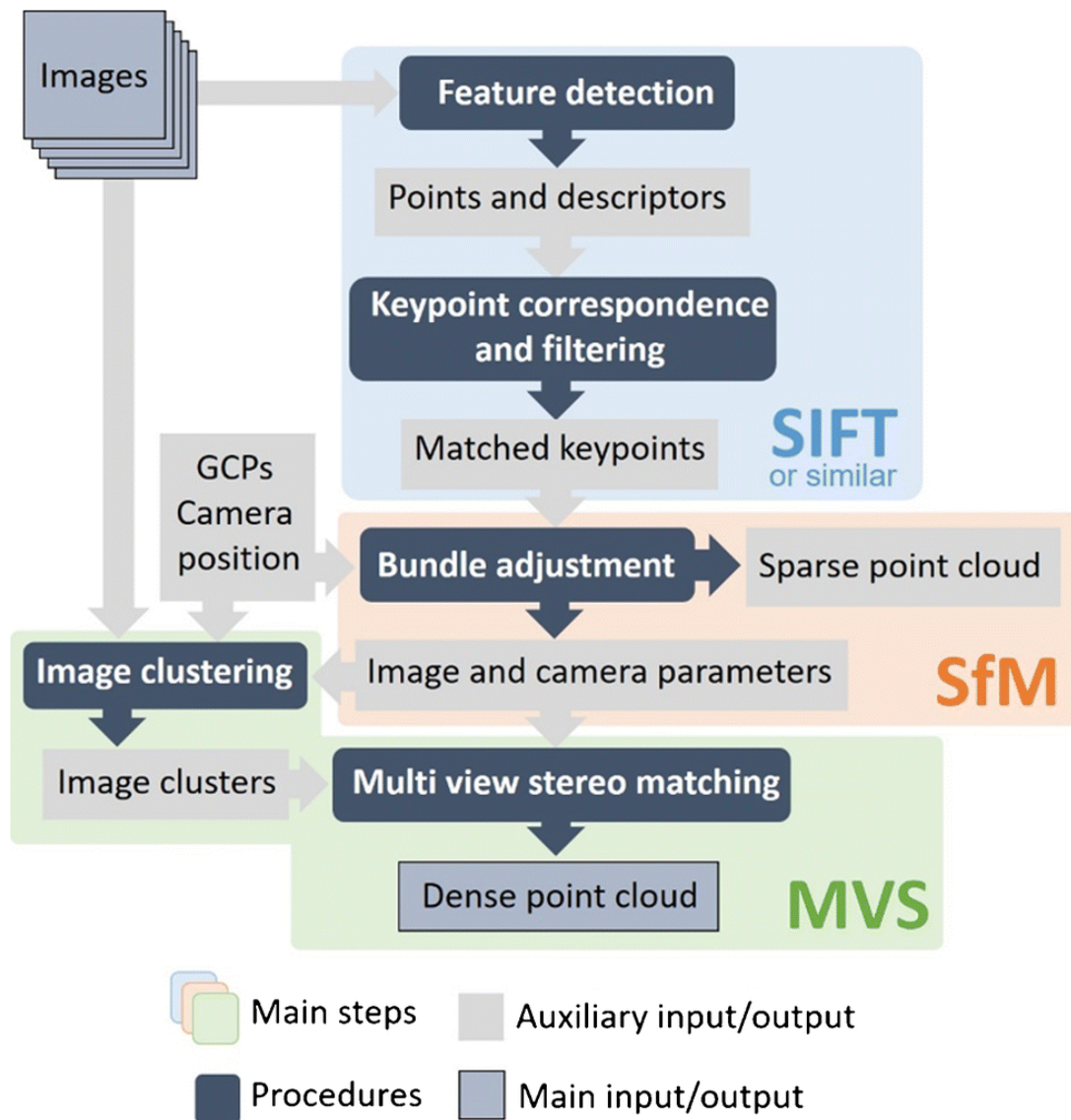


Figure I.6. Schematic workflow of the SfM-MVS process resulting in a dense point cloud from image sets. Reproduced from **Iglhaut et al. (2019)** and distributed under the terms of the Creative Commons Attribution 4.0 International License.

The first step in the SfM-MVS photogrammetric workflow for obtaining a photogrammetric model is based on two principles; the first is the application of algorithms based on computational vision. The aim of this step consists in finding a correspondence between images through the identification of key features (tie points) in two or more images, allowing the identification of homologous points in different photographs. The Scale-Invariant Feature Transform (SIFT) (Lowe, 2004, 1999) is an algorithm widely used for this purpose (blue section in **Figure I.6**). This process is scale, lighting, and orientation invariant for all

photographs, in order to account for different camera locations and zoom. The second principle is the application of the SfM algorithm (Triggs et al., 2000) that solves the problem of refining the 3D coordinates, considering both the motions between images and the technical characteristics and deformations of the lenses (orange section in **Figure I.6**). SfM is in charge of estimating the interior and exterior orientation parameters, including the position of each camera, as well as its orientation and their distortion parameters that satisfy the equations of the bundle adjustment (BA). This iterative process consists of minimizing the squared Euclidean distance between the coordinates of each point and its re-projection in each of the iterations, in order to progressively refine the value of each of these parameters. The SfM workflow results in a sparse point cloud (PC) containing the three-dimensional location of a series of key points in a local coordinate system, together with an estimate of the interior and exterior orientation parameters for each camera.

Although the sparse point cloud can already be considered as a result and is used in some studies (Iglhaut et al., 2019), in most cases, stereo multi-view matching algorithms such as PMVS2 (Patch-based MultiView Stereo) (Furukawa & Ponce, 2010), CMVS (Clustering Views for MultiView Stereo) (Furukawa et al., 2010) and other algorithms integrated in commercial software (e.g., Agisoft Metashape) are used to obtain a dense point cloud (green section in **Figure I.6**). These algorithms allow calculation of the depth maps of the model to reconstruct a dense PC. The result at the end of the SfM-MVS workflow is a dense cloud that can be used to obtain other subproducts. A more detailed description of the SfM-MVS procedure can be seen in Eltner & Sofia (2020), Iglhaut et al. (2019) or Westoby et al. (2012).

The SfM-MVS can be performed with different software, both commercial and open source (Eltner & Schneider, 2015). Some of these suites, such as Agisoft Metashape, allow for automation of the processing workflow using scripts via their Application Programming Interface (API). Hence, the usual pre-processing steps used to reconstruct 3D models such as image masking, marker detection or filtering of outlier points can be automated.

2.1.3 Fixed vs mobile photogrammetric systems

Photographs of an object/scene from different points of view are needed to implement an SfM-MVS workflow. The collection of these photographs can be done in a variety of ways. For example, historical images (Maiwald et al., 2017; Mölg & Bolch, 2017), drone captures

(Eltner & Schneider, 2015; Nex & Remondino, 2014), photogrammetric lab setups (Dias-Da-Costa et al., 2011; Verma & Bourke, 2019), mobile phone cameras (El-Din Fawzy, 2015; Tavani et al., 2020), a single commercial camera (Gómez-Gutiérrez et al., 2015), low-cost systems (Blanch et al., 2020; Giacomini et al., 2020), fixed installations (Blanch et al., 2021; Kromer et al., 2019) or video frames (Buill et al., 2016).

However, capturing the overlapping images to calculate 3D models can be reduced to two data acquisition perspectives, either using a set of stationary cameras pointing at the object of interest or using a single camera moving around the object of interest, i.e., fixed and mobile systems, respectively. Fixed systems create the 3D model with images always taken from the same position with a single camera for each. Therefore, the photogrammetric processing is based on limited camera perspectives. This has consequences for the reliability of the image-based 3D reconstruction. Micheletti et al., (2015) demonstrated that by providing an adequate spatial distribution of the image network geometry, acceptable accuracies can be achieved using even small image sets. However, they considered one camera for all images, which is not the case for stationary setups. In contrast to capturing the images with a single camera, where only one set of interior parameters have to be estimated (i.e., focal length, principal point, and distortion parameters), each new camera entails considering additional interior camera parameters because the physical properties are different for each lens (Eltner & Sofia, 2020). Considering these challenges of fixed systems, Kromer et al., (2019) were able to achieve detection limits between 2-3 cm in the ranges required for monitoring pre-failure deformation on slopes with only five stationary cameras.

Besides the geometric considerations of the imaging network, the use of fixed systems entails further difficulties regarding the operation of these systems in an autonomous manner. In this regard, a network infrastructure has to be provided to transmit the data or to check the system status. Furthermore, a sufficient energy supply is required. Despite these constraints, fixed camera solutions for SfM-MVS photogrammetry are growing in the field of geoscience monitoring and last year saw publications on a fixed rockfall monitoring system developed with very low-cost cameras published by Blanch et al. (2020) and presented in this PhD, an array of cameras used to study rock slope hazards on a road published by Kromer et al. (2019), an autonomous terrestrial stereo-pair photogrammetric monitoring system developed to observe rockfalls in mining environments published by Giacomini et al. (2020) or the

time-lapse camera setup presented by Blanch et al. (2021) and explained in more detail in the following chapters.

Mobile systems such as UAVs bring greater flexibility. Large sets of photographs can be acquired from a single camera, allowing for a larger number of observations from several perspectives for the bundle block adjustment (BA). This increase in input data allows for more reliable photogrammetric models. Verma and Bourke (2019), for example, used more than 50 photographs at close range ($< 2\text{m}$) to obtain sub-millimetre-resolution models of rock faces using a calibrated error evaluation chart. In addition, the ability to extend the mobile system by mounting a camera onto an Unmanned Aerial Vehicle (UAV) allows areas and perspectives to be reached that are difficult to access on foot (Gaffey & Bhardwaj, 2020). Commercial ready-to-fly solutions have led to an increase in the use of aerial photogrammetry in recent years (Eltner & Schneider, 2015; W. Liu et al., 2019; Nesbit & Hugenholtz, 2019; Nex & Remondino, 2014; Tannant, 2015; Wu et al., 2019). On the other hand, the inability to take pictures both from the same exact position (as in a fixed system) and at a high temporal frequency makes it difficult to use algorithms and workflows based on the redundant use of image bursts created to obtain higher quality models (Blanch et al., 2020). Although experience with multi-epoch imagery workflows such as Cook and Dietze (2019) or Feurer and Vinatier (2018) demonstrates a certain capacity for improvement with mobile systems.

In this research it has been decided to develop fixed photogrammetric systems. Although the rise of UAV monitoring makes any drone research very attractive, in this dissertation the decision was taken to study the potential of fixed photogrammetric systems. Since a priori, a monitoring with fixed systems would enable better control of the uncertainties and errors than a mobile system. For this reason, the research and the results presented in this volume are based on the development of fixed time-lapse photogrammetric systems.

For change-detection, the use of fixed systems enables images to be obtained always from the same position, so that the movement occurs only in the studied area and not in the position from where the images are captured. This strategy allows the use of advanced workflows that take advantage of the invariant position of the camera, as well as allowing the precise geo-referencing of the location of the images.

2.1.4 Low-cost high-resolution vs very low-cost low-resolution

Compared to other methods of terrain observation, digital photogrammetry is considered a low-cost monitoring system (Eltner et al., 2016; Javernick et al., 2014; Verma & Bourke, 2019; Westoby et al., 2012). However, the cost of photogrammetric systems varies widely depending on their configuration. Mid to high-cost systems (> 1.000 EUR) are composed of commercial solutions using cameras and devices with large sensors of high resolution. These cameras, usually DSLR or mirrorless full-frame cameras (43 mm sensor diagonal), can obtain images of more than 24 mega pixels. They have high sensitivity photoreceptors, produce very little digital noise, and hence possess exceptional image quality with a high capacity to extract information from dark and bright areas due to the high dynamic range of these images. Furthermore, these cameras can use high-quality fixed lenses that enable the capture of images with very little distortion and great sharpness, which is advantageous for obtaining high quality models (Eltner & Schneider, 2015). There have been several studies implementing photogrammetric systems with commercial, high-quality cameras (Giacomini et al., 2020; Kromer et al., 2019; Parente et al., 2019; Roncella et al., 2014). However, one limitation of these kinds of devices in fixed camera systems is their cost and the large amount of data that needs to be transferred remotely, as the size of each image can reach more than 30 MB.

Other than that, low-cost photogrammetric solutions involve the use of very simple photographic systems (less than a hundred euros). These systems are based on camera modules controlled by single-board computers, such as Raspberry Pi (Raspberry Pi Foundation, 2016), or microcontrollers, such as Arduino (open-source) systems. These cameras are associated with photographic sensor diagonals of less than 16 mm with resolutions that vary between 5 and 12 mega pixels. To reduce costs, they are equipped with low-quality plastic lenses that usually result in strong distortions. The quality of the images obtained with these cameras, revealing low sharpness and high digital noise, are the main constraint for their application in 3D measurement tasks (Blanch et al., 2020). However, low-cost solutions are easy to implement and simple to program. In addition, these systems are ideal for installation at sites exposed to destructive phenomena such as flash floods or mass movements. Various examples of low-cost photogrammetry implementations can be found in the field of geosciences (Eltner et al., 2018; Mallalieu et al., 2017; Santise et al., 2017).

Given the great potential of the two options, this dissertation addresses both types of photogrammetric systems. On the one hand, the creation of a low-cost, low-resolution photogrammetric system, and on the other hand a high-resolution photogrammetric system based on commercial cameras. The two systems are presented in the following sections.

2.2 Photogrammetric Monitoring

2.2.1 Photogrammetric monitoring approaches

The acquisition of point clouds (PCs) using photogrammetric techniques for three-dimensional (3D) modelling of natural surfaces has increased significantly in recent years (Dewez et al., 2016; Eltner et al., 2016). The ease of acquiring images, as well as the low cost of the whole system (devices to take images and processing software) have democratized access to photogrammetric data and ensure greater accessibility compared to LiDAR point clouds. Spurred on by this accessibility, more and more data are being acquired and consequently more natural surfaces are being reconstructed and investigated. The reviews published by Eltner et al., (2017); Iglhaut et al., (2019); Tannant, (2015); Westoby et al., (2012) show all the possibilities that this technique allows in the field of geosciences.

The use of digital photogrammetry for landslide monitoring has evolved considerably over the past few years. Photogrammetric monitoring methods can be divided into those using a single camera position plus Digital Image Correlation (DIC) techniques (Pan, 2018) to detect changes between two images captured at different times (Gabrieli et al., 2016; Travelletti et al., 2012), and those that use images taken from different positions (multi-view methods) (Stumpf et al., 2015). One advantage of these photogrammetric techniques is that, in addition to the analysis of current changes, they allow old deformations to be studied by scanning analogue photographs taken before the development of the methodology (Cardenal et al., 2008). Model comparisons and difference calculations can be obtained from: i) one-dimensional (1D) values resulting from topographic sections extracted from Digital Terrain Models (DTM) (Cardenal et al., 2008); ii) 2D displacements in the image plane obtained using DIC methods (Travelletti et al., 2012); iii) in 3D from the comparison of PCs obtained by SfM-MVS techniques (Stumpf et al., 2015); and iv) the 4D analysis based on multi-temporal PC comparisons (Kromer et al., 2019).

As mentioned by Gabrieli et al. (2016), it is possible to obtain 3D information of the displacement of a landslide with a single camera, using complex DIC methods and a reference DTM. Even so, several factors, such as the orientation of the deformation and the range and the magnitude of the movement, have a decisive effect on the accuracy of the results. In addition, classical DIC is strongly influenced by changes in illumination (Manconi et al., 2018) and normally assumes that the main deformation field is parallel to the internal camera coordinate system, which is not always the case. Thus, the deformation field should be subsequently ortho-rectified using a DTM (e.g., Travelletti et al., 2012).

Regarding the 3D and 4D comparisons mentioned above, these comparisons are usually performed by means of point cloud comparisons and are one of the most common monitoring methods. Inherited from LiDAR procedures, the same kind of comparisons can be made with photogrammetric data. From the use of different images of the same scene (multi-view strategy) it is possible to obtain 3D point clouds representing this scene (as mentioned in previous sections). The comparison of two-point clouds within a time-lapse enables the identification of the differences existing between them (change-detection). This strategy, which is widely used in the geosciences, is specifically addressed in a section included in this dissertation (**Section IV**). In **Chapter 9**, the reader will find a more detailed review of the state of the art and a proposal for improving and updating the process.

2.2.2 Landslide photogrammetric monitoring limitations

The use of methods based on multi-view techniques for the study of landslides also entails some limitations, as described extensively in Tannant (2015) and Stumpf et al. (2015). Both authors emphasise the importance of image acquisition, noting that SfM works best when images are taken with a distance between them proportional to the distance between the camera and the cliff. On the one hand, Tannant (2015) highlights that image matching algorithms may not work if images are taken at different times and dates resulting in a different appearance for the same features on the rock face. On the other hand, Stumpf et al. (2015) finds that the quality of the surface reconstruction degrades significantly when incidence angles exceed 30° , and an accuracy of only a few centimetres can be obtained at short distances of up to 200m.

The most recent studies in the field of geosciences emphasize the importance of two key elements of the SfM-MVS process to obtain good quality results (Eltner et al., 2017; Kromer et al., 2019). The first is the need to perform lens calibration to obtain the internal parameters of the camera. These parameters, some of which are highly sensitive, allow the elimination of radial and tangential distortion, correcting the deformations of the resulting models. The second element consists of positioning ground control points (GCP) in order to estimate the fit of the models to the real surface.

Although several authors have emphasized the importance of using GCP and lens calibration (Eltner et al., 2016; James, Robson, d'Oleire-Oltmanns, et al., 2017), in some contexts, such as landslide monitoring, this is impossible due to the unfeasibility of installing targets such as GCP on inaccessible slopes. In addition, obtaining calibration parameters in fixed systems is difficult due to lens variations caused by temperature changes (Elias et al., 2020). These limitations, combined with the reduced number of images obtained by fixed camera systems, imply a reduction in the quality of the resulting models compared to those obtained with a Terrestrial Laser Scanner (TLS).

This thesis addresses this limitation by presenting a processing algorithm (MEMI workflow, see **Chapter 5**) that enables better results to be obtained in 3D comparisons without the need to use control points or perform camera calibrations. As mentioned in the foregoing, the accuracy and resolution of photogrammetry-derived PCs are strongly controlled, not only by internal characteristics (instrument specifications) but also by external considerations (range, number and setup of stations, deformation magnitude, etc.). While TLS is believed to provide a more robust data set compared with SfM-MVS, no single technology is universally best suited to all situations because of the wide variety of fieldwork setup and instrumental considerations (Wilkinson et al., 2016). On the one hand, the limited number of stations and subsequent occlusions in TLS-derived PCs have been highlighted as one of the main TLS limitations (Sturzenegger et al., 2007) in landslide monitoring. On the other hand, loss of fine-scale details due to rounding off or over-smoothing of the SfM-MVS-derived surfaces on sharp outcrop corners has been observed by several authors (e.g., Nouwakpo et al., (2016); Wilkinson et al., (2016)).

Another important limitation of photogrammetric monitoring is the geometric error that occurs in the photogrammetric reconstruction. This error is presented and discussed in more detail in the introduction to the research in **Chapter 4**, since one of the algorithms developed (PCStacking) aims to minimize this error in very low-cost systems. The author has decided to omit the presentation of this limitation in this section as it is much more coherent to do so in **Chapter 4**.

2.3 Methodological Background (Point Clouds)

Given the methodological component of this thesis, a brief bibliographical review of the methods developed to obtain better results from point clouds has been carried out. In this short part, different algorithms, configurations, and workflows created prior to the development of this research are presented.

The first point (2.3.1) shows the improvements made to the point clouds, regardless of whether they were obtained by LiDAR or SfM-MVS. The second point (2.3.2) focuses on the improvements and algorithms that are directly applied to the SfM-MVS workflow and that enable better results to be obtained. Finally, the last point (2.3.3) explains in more detail two algorithms that will appear recurrently throughout the dissertation.

2.3.1 Improvements of PC

Different algorithms have been recently developed for the treatment of LiDAR PCs (Derron & Jaboyedoff, 2010; Jaboyedoff et al., 2012; Riquelme et al., 2014) and especially TLS (Terrestrial Laser Scanner) data (Abellán et al., 2011; Brodu & Lague, 2012; García-Sellés et al., 2011; Jaboyedoff et al., 2009; Kromer et al., 2015; Royán et al., 2014), entailing a wider use of PCs acquired by photogrammetric systems in several geoscience fields (Eltner et al., 2016; Smith et al., 2015; Westoby et al., 2012).

Examples include: a classification algorithm using a multi-scale dimensionality criterion called “CAracterisation de NUages de POints (CANUPO)” (Brodu & Lague, 2012); the geomorphological change detection algorithm “Multi-scale Model to Model Cloud Comparison (M3C2)” (Lague et al., 2013) or a four-dimensional (4D) workflow for detecting changes in PCs (Kromer et al., 2015; Williams et al., 2018). Notably, the work by Kromer et

al. (2015) proposed computing the median distances of a series of point clouds acquired at different time steps and with respect to a fixed reference, extending the M3C2 algorithm (Lague et al., 2013) to 4D. Kromer et al. (2015) and Lague et al. (2013) obtained a better level of detection on PC comparison by minimizing point scattering around a central value, but they do not improve the PC per se.

Although these algorithms were originally developed with the aim of improving results by considering the properties and errors of LiDAR datasets, they can be used with PCs captured using different strategies (e.g., SfM or sonar). Nevertheless, the characteristics of photogrammetric data such as non-linear and time-variant errors require the development of new methodologies specifically designed to overcome the constraints of this technique. Interestingly, improving PC quality by stacking multiple low-quality datasets as those generated using time-lapse cameras has yet to be explored.

2.3.2 Improvements of the SfM-MVS photogrammetric method

Strategies to obtain improved SfM-MVS photogrammetric models are required, especially in scenarios that entail the use of fixed and low-cost camera systems. These improvements can be implemented at different stages of the SfM-MVS photogrammetric workflow. Regarding the data collection stage, studies have been carried out to investigate the impact of using High Dynamic Range (HDR) images instead of conventional photographs to reconstruct 3D models in the fields of cultural heritage documentation (Ntregka et al., 2013) and geomorphic change detection (Gómez-Gutiérrez et al., 2015). Other studies have examined the use of high-resolution photographs (gigapixel) (Lato et al., 2012; Romeo et al., 2019).

Furthermore, attempts have been made to enhance SfM-MVS photogrammetric models by stacking images to reduce the noise from digital cameras (Santise et al., 2017), although with inconclusive results. Parente et al. (2019) demonstrated an improvement in monitoring quality when a fixed-camera approach was adopted, even with a poor camera calibration procedure. However, there are no algorithms or workflows available to improve the photogrammetric models via the modification of the calculated PCs based on error reduction strategies

Several studies have focused on improving the SfM-MVS photogrammetric results by pre-processing of the input data, such as enhancing the image quality (Guidi et al., 2014) as well as pre-defining calibration parameters and adjusting the imaging network configuration. For instance, James & Robson (2014) mitigated systematic errors common for UAV models by obtaining additional convergent images to enhance the strength of the image network geometry. Furthermore, it is important to retrieve suitable lens calibration parameters (Luhmann et al., 2016), which is especially the case for consumer grade cameras that usually exhibit stronger distortions. More recently, Elias et al. (2020) carried out a study to estimate the effect of temperature changes on low-cost camera sensors, highlighting the importance of also considering the temporal stability of cameras, especially during long-term observations.

Another focus has been on improvement of the SfM-MVS workflow itself to obtain 3D models with the highest possible quality, allowing for multi-epoch imagery change detection. The differences between these methods depend both on the characteristics of the object to be studied and on the possibility of automating processes and locating ground control points. Verma & Bourke (2019) presented a method that can obtain sub-millimetre accurate small-scale digital elevation models at close range. Another setup developed by Kromer et al. (2019) enabled the detection of rockfalls automatically from time-lapse imagery. Eltner et al. (2017) introduced a time-lapse SfM-MVS photogrammetry workflow that enabled the almost continuous detection of soil surface changes with millimetre accuracy.

The methodology proposed by Feurer & Vinatier (2018) improves SfM-MVS photogrammetry-derived 3D models by joining imagery from different points in time during image matching and 3D reconstruction. This has the advantage that systematic errors might be spatially consistent over time and therefore negligible during change detection. This methodology was put into practice by Cook & Dietze (2019). The workflow most recently presented by Blanch et al. (2021) represents a full integration of the research developed by Feurer & Vinatier (2018) and Blanch et al. (2020). It mixes the use of multi-temporal images with the redundancy of images obtained at the same moment. This workflow is also detailed in **Chapter 5** of this thesis.

Finally, methodological proposals have been made to improve the results, regardless of the pre-processing and workflow used. For instance, the PCStacking (i.e., point cloud stacking) algorithm developed by Blanch et al. (2020) and explained in the following chapters (see **Chapter 4**) improves the 3D models using subsequent photogrammetric reconstruction solutions for images shot over a short time interval. Another recently developed strategy to enable more reliable change detection involves the introduction of precision maps by James et al. (2017). Together with the M3C2 tool (Lague et al., 2013), the strategy allows change detection results to be obtained with information about the significance of the measured change.

2.3.3 Recurring algorithms

The aim of this point is to provide a brief overview of some of the algorithms developed by other authors that will be used recurrently in the following sections. The two algorithms introduced here are widely used by many authors and are well known in point cloud work.

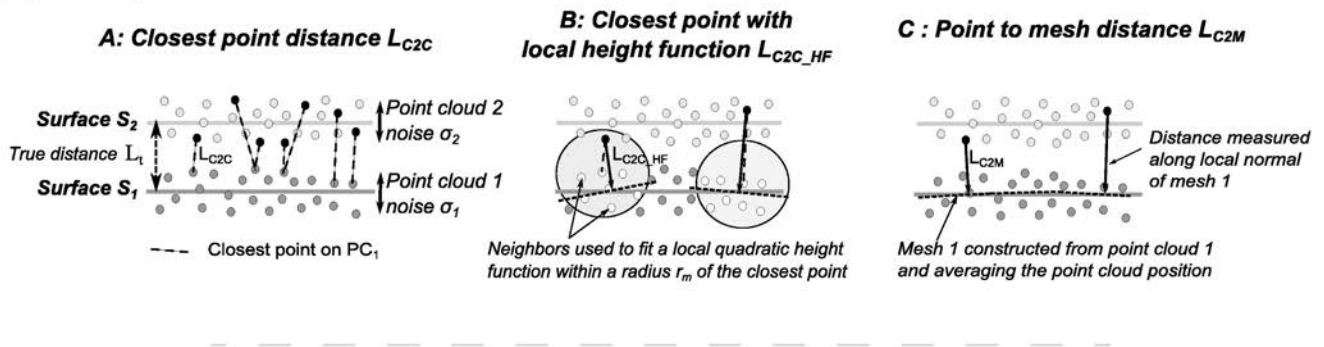
M3C2 (Lague et al., 2013)

The M3C2 algorithm is a point cloud comparison algorithm (Lague et al., 2013) included in the CloudCompare software (CloudCompare, 2021). This algorithm consists of an improved point cloud comparison algorithm, compared to the classical point-to-point or mesh-to-point comparison (**Figure I.7a**).

The algorithm yields better results as it uses a calculation method in which both the reference points (S1 at **Figure I.7b**) and the target points (S2 at **Figure I.7b**) are averaged taking into account their neighbouring points, while the direction of the normal of the average is used to "search" for the target point in order to measure the distance between the reference and the target points (**Figure I.7b**). The result of this algorithm is a point cloud with the difference value between points (Diff) as a new parameter.

This method enables the elimination of noise and anomalous measurements produced by the dispersion and variability obtained when considering a single point in each measurement (as in point-to-point), especially in complex topographies such as natural terrain. The paper written by Lague et al. (2013) provides a detailed description of the method and a discussion of the results.

a) Fig. 2 from Lague et al., (2013)



b) Fig. 3 from Lague et al., (2013)

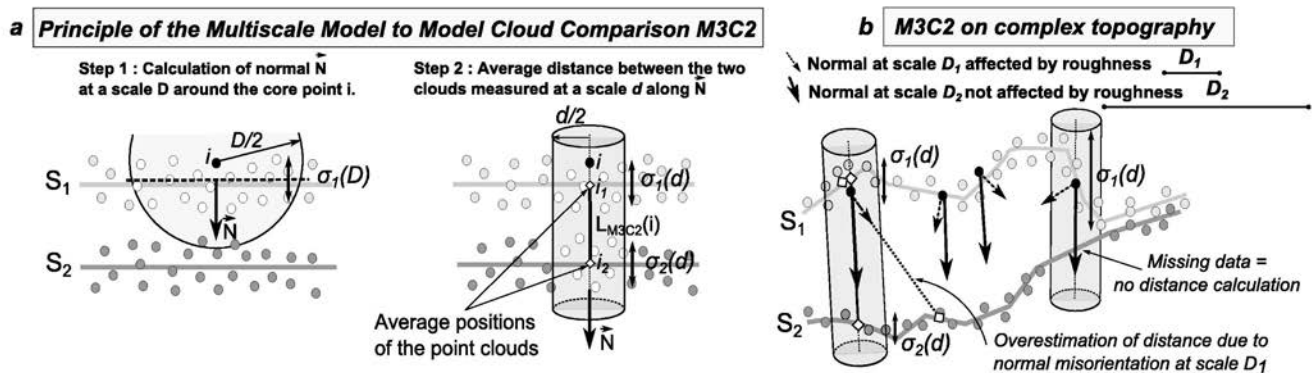


Figure I.7. a) Existing 3D comparison methods between two point clouds PC1 and PC2. **aA:** Simplest cloud-to-cloud distance L_{C2C} . **aB:** Closest point distance to local model distance L_{C2C_HF} . **aC:** Cloud-to-mesh (C2M) distance L_{C2M} and **b)** Description of the M3C2 algorithm and the two user-defined parameters D (normal scale) and d (projection scale). Reproduced with permission of the publisher (certificate available in the **Appendix A – Elsevier Authorisation** and in [this link](#)).

DBSCAN (Ester et al., 1996)

DBSCAN is a clustering algorithm developed by Ester et al. (1996) which is used to find clusters of points with significant difference value (Diff), that can be interpreted as relevant changes between two-point clouds. The DBSCAN algorithm works analysing all the neighbouring elements point by point. The parameters used for clustering by the DBSCAN algorithm are "number of points" and "search radius" (e.g., minPts=5, eps=3). With these two parameters, the algorithm analyses if for each point (in the case of the example) 5 points with Diff values higher than a given threshold are found within a search radius of 3 units with respect to the centre of the analysed point. If the result is positive, it means that the point is part of a cluster (red and green dots in **Figure I.8a**).

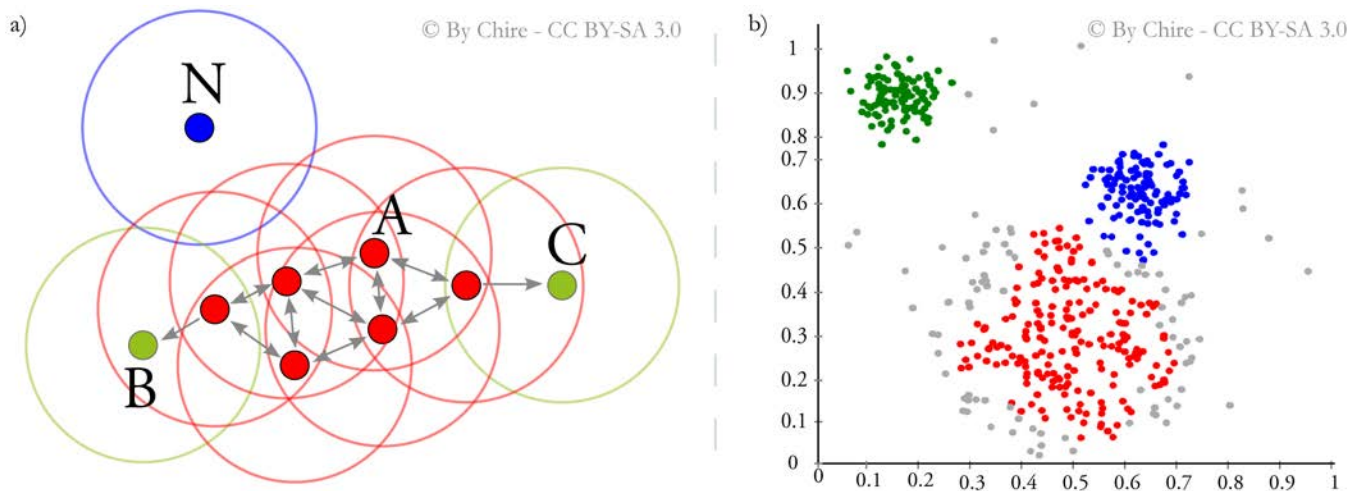


Figure I.8. DBSCAN Algorithm. **a)** The red and green dots are part of the cluster (they are within the search radius). The blue dot is not part of the cluster. **b)** Clustering result. The grey dots are not part of any cluster. The coloured dots are part of the respective clusters. **a,b)** CC BY-SA 3.0 licence

As soon as the necessary conditions are matched, the algorithm classifies the point as part of a cluster. Finally, the result is on the one hand the set of points that form different clusters, and on the other hand the set of points that do not form any cluster **Figure I.8b**. In addition, the algorithm can differentiate between the different clusters identified. For this reason, **Figure I.8b** shows the clusters in different colours. A more detailed explanation of the algorithm can be found in the author's publication (Ester et al., 1996).

2.4 Rockfalls

2.4.1 Rockfall phenomena

Rockfalls are an extremely rapid natural phenomenon occurring on near-vertical rock faces where one or more rock mass falls freely (source area) generally by the action of gravity. After the free fall, they can move by rolling or bouncing down the slope and are able to fragment into smaller pieces (transit area), finally ending their movement by forming rock accumulations (deposit area) (**Figure I.9a**). This type of event represents the most frequent and dangerous natural phenomenon in mountainous areas (Erismann & Abele, 2001; Whalley, 1984) as well as on coastal cliffs (Lim et al., 2010; Michoud et al., 2015; N. J. Rosser et al., 2005) (**Figure I.9b**).

In addition to their eminently natural character, these phenomena may also occur on anthropically modified slopes, particularly affecting the slopes of civil works (Kromer et al., 2015; Lato & Vöge, 2012; Michoud et al., 2012) (**Figure I.9c and Figure I.9d**).

Since they are eminently gravitational events (Hungr et al., 2014) that are triggered very quickly (more than 5 m/s) (Cruden & Varnes, 1996), the reaction capacity is null, and therefore rockfalls are highly dangerous and can cause destruction of property and the death of people (WP/WLI, 1995).

Another important factor in determining the danger of the phenomenon is the volume of material detached, because its energy is directly linked to the weight of the material mobilised and the height from which it falls. Given the increasing human exposure to this phenomenon, due to the growing occupation of high mountain areas as well as the increase and ageing of anthropogenic slopes, more and more people are exposed to high levels of rockfall risk (Copons et al., 2012).

The factors that influence the triggering of these processes are extremely varied and may depend on both single internal and external factors (Volkwein et al., 2011) or a combination of these. Internal factors are those that are specific to the geology and morphology of the slope, e.g., slope, fracture joints, water saturation or geomechanical characteristics of the rock. On the other hand, external factors are those that may affect different slopes indistinctly, such as gravity, climatic conditions, anthropic agents, or seismicity (Jaboyedoff & Derron, 2005).

Detachment of rock blocks from cliffs can be classified in various categories based on their pattern of movement, but the most characteristic, which constitute the phenomena studied in this thesis, are those classified as pure rockfalls on one hand and rock toppling on the other (Hungr et al., 2014; Varnes, 1978). Pure rockfalls are characterised as spontaneous movements that mobilise rock blocks, often bounded by discontinuities such as fractures or bedding, which detach from the wall and fall.

In contrast, rock toppling is characterised by the existence of a rotational component in the direction of the slope that eventually triggers the detachment of a column or slab of material

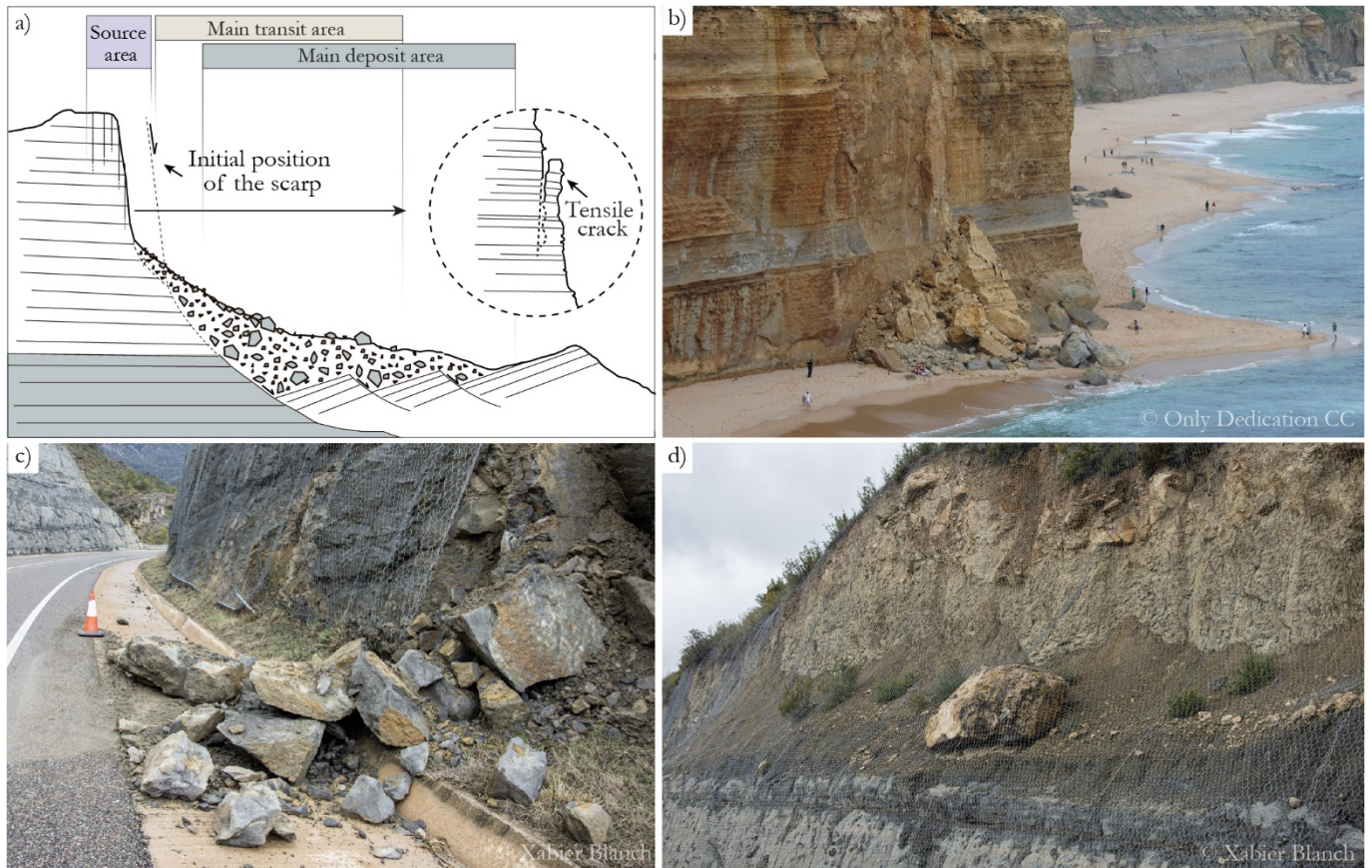


Figure I.9. **a)** Schematic representation of a generic rockfall mechanism and the different zones defined in the process. **b)** Rockfall on a coastal escarpment (the twelve apostles, Australia - Creative Commons license). **c)** Rockfall on an anthropic slope that has overcome the defences (Tremp, Catalonia). **d)** Rockfall retained by the installed defences (Tremp, Catalonia). Images **c, d)** have been acquired by the author.

separated by steeply dipping joints. (Hungri et al., 2014; Varnes, 1978). **QR 10** and **QR 11** link to complementary landslide and rockfall resources and classifications by the [British Geological Survey](#) and the [United States Geological Survey](#).

Over the years, different active defence strategies have been developed to contain and dissipate the energy of rockfalls (**Figure I.9d**). Due to the nature of the phenomenon, these strategies must be installed in a highly localised way in order to be effective. However, given the large areas that are susceptible to rockfalls, active defence strategies do not always prevent exposed elements from being impacted, thereby causing both material and human losses (**Figure I.9c**).



QR 10



QR 11

For this reason, it is becoming more and more common to deal with the problem of rockfall hazards from an approach based on rockfall monitoring, the aim of which is to detect zones with high activity and the pre-failure deformations to forewarn against future rockfalls.

2.4.2 Rockfall monitoring

Rockfall monitoring is based on two main strategies. The first is to identify rockfalls once they have occurred. This strategy is used to quantify the rockfall activity. From the analysis of the activity, it is possible to determine the behaviour of the escarpment and identify the most active areas. It is common to carry out rockfall inventories (Rabatel et al., 2008), determine magnitude-frequency curves (M-F) (Barlow et al., 2012), model events (Matas et al., 2017), study their fragmentation (Ruiz-Carulla et al., 2017) or delimit areas of activity concentration (Royán et al., 2015).

Mechanical knowledge of the rock mass and rockfall activity is very valuable for the definition of defence systems. The identification of rockfalls also makes it possible to identify the associated fractures, joints or discontinuities that delimit the rock blocks. In this way, from the structural study of the cliff (García-Sellés et al., 2011), it is also possible to delimit areas that are susceptible to fall (Riquelme et al., 2016). In addition, the identification of rockfalls also enables the detection of areas of accumulation of small detachments, which in some cases are identified as precursory evidence of a larger rockfall (Kromer et al., 2015; Royán et al., 2015; Sartori et al., 2010).

The second strategy is to identify the pre-failure deformation of a single block. This strategy is based on the fact that any instability can be represented using three phases of previous movement "[creep theory](#)" (Terzaghi, 1962). This approach makes it possible to anticipate the rockfall detachment (Atzeni et al., 2015; Royán et al., 2015). Anticipation enables the implementation of an active defence strategy, e.g., anchoring the moving blocks (Janeras et al., 2015), and facilitates the study of the evolution of the pre-failure deformation of the rockfalls (Royán et al., 2014). The monitoring of the previous deformation also can be correlated with external phenomena such as rainfall to determine which factors accelerate the detachment process and with the aim of making a spatial rockfall prediction (Abellán et al., 2010). In addition, the identification of pre-failure deformation makes it possible to be

alert to the real risk of rockfall and thus adapt safety measures more effectively as well as designing effective early warning systems (Crosta & Agliardi, 2003; Zvelebil & Moser, 2001).

There are many ways to monitor active slopes to identify rockfalls or pre-failure deformation, but in recent years new technologies such as GBInSAR (Atzeni et al., 2015; Teza et al., 2008), LiDAR (Oppikofer et al., 2008; Travelletti et al., 2008) or digital photogrammetry (Blanch et al., 2021; Kromer et al., 2019) have led to an increase in rockfall knowledge. Due to the relevance of the evolution of monitoring systems based on digital photogrammetry, a more detailed state of the art has been given in this chapter.

Highly technical aspects that do not form part of the publications of this thesis will not be addressed in the following chapters, so in this section the monitoring method developed by the RISKNAT research group is not explained. **Section IV** recovers part of this background and contains a more detailed analysis of the current RISKNAT monitoring system, as well as providing a solid basis for understanding the improvements described in **Chapter 8**.

2.5 Overview of the Publications

In accordance with the regulations, the two publications that enable the defence of this thesis to be conducted have been undertaken within the context of the main research explained in **Section 1.3**. Both articles are published in the journal [Remote Sensing](#) from MDPI. Currently (year 2021) the journal has a 2020 impact factor of 4.85. Updated magazine statistics can be accessed in **QR 12**.

This journal has been chosen for publication because of its high degree of specialisation in the field of remote sensing monitoring systems. In addition, more and more publications are emerging in the specific field of digital photogrammetry (**Figure I.10**). As an example of this specialisation, the two published articles are part of a special issue entitled: Advances in Photogrammetry and Remote Sensing: Data Processing and Innovative Applications.

Finally, in compliance with the author's desire to publish the research under an open-source licence, the chosen journal for the publications, Remote Sensing, is an open access journal.



QR 12



Figure I.10. Journals with the highest number of publications with the word "structure from motion". In addition, the total citations of the SfM articles are included. The size of the box and the colour reflect the ratio of publications (no citations).

2.5.1 Point Cloud Stacking: A Workflow to Enhance 3D Monitoring Capabilities Using Time-Lapse Cameras

This article was published on 13 April 2020 and includes the first methodological advances obtained in the thesis with regard to the partial **Objectives I** and **III** set out in **Section 1.3**. The main objective of this publication is to propose a new workflow called PCStacking, which enables improvement of the geometric quality of 3D point clouds obtained from very low-cost and low-resolution cameras.

This requirement is prompted by the availability of very low-cost photogrammetric systems based on Raspberry microplate systems. These devices, which are very cheap, have very poor image quality because they use very small photo sensors and plastic lenses. Although the use of the images obtained with these devices is valid for obtaining 3D models from SfM-MVS algorithms, the quality obtained is poor.

The approach addressed in the publication consists of stacking different point clouds obtained from consecutive images. The aim of this strategy is to eliminate the "geometric

error" generated when obtaining 3D models with conventional software. This workflow, which affects both image capture in the field and post-processing, is shown to significantly improve the quality of the point clouds obtained and allows change-detection to be carried out with higher quality and precision.

The article tests the PCStacking algorithm both with a synthetic model created ad-hoc to observe the behaviour of the algorithm and with real data from the Puigcercós study area. For both synthetic and real data, the difference errors (percentiles) are improved from 3.2 cm to 1.4 cm in synthetic tests and from 1.5 cm to 0.5 cm in real conditions.

A brief introduction to the research can be found in **Section 4.1**. The explanation of the methodological development is explained in **Section 4.2**, the results in **Section 7.1** and the discussion in **Section 7.2**. In addition, the results presented in the **Section 10.1** use the PCStacking algorithm developed in this publication. The developed codes (in MATLAB © language) can be found in **Appendix A – PCStacking algorithm**.

2.5.2 Multi-Epoch and Multi-Imagery (MEMI) Photogrammetric Workflow for Enhanced Change Detection Using Time-Lapse Cameras

This article was published on 9 April 2021 and reflects the most significant progress in the methodological area of the research. This article addresses the partial **Objectives II** and **IV** exposed in **Section 1.3**. The main objective of this article is to propose a new workflow called Multi-Epoch and Multi-Imagery (MEMI), which provides a significant improvement in the comparisons (change-detection) between two-point clouds.

This improvement is motivated by the critical need to improve workflows that yield better 3D comparisons between two-point clouds. These comparisons, which are crucial for rockfall monitoring, can be affected by the different geometric reconstructions performed by SfM-MVS algorithms.

For this reason, the approach adopted in this article consists of using images from different periods as if they were taken from the same moment in time. This is only possible with the installation of fixed time-lapse photogrammetry systems, which makes it possible to

reconstruct different photogrammetric models (before and after) from the same geometric reconstruction, so when the comparison is made, the results improve. Furthermore, following the idea published in the previous article, the time-lapse photographic acquisition capability is used to add more redundancy to the SfM-MVS software.

In the article, the entire workflow is tested using real images obtained from the Puigcercós study area. With the 3D models obtained, an exhaustive comparison is made with the classic workflow and with other advanced workflows. In addition, the results are subjected to an extensive comparison to quantify the performance of the proposed workflow.

The proposed workflow reduced the error up to a factor of 2 when compared to the classical approach, thus providing a standard deviation of 1.5 cm. In terms of absolute accuracy, the proposed method is 20% more accurate than models obtained with the classic workflow.

A brief introduction to the research and methodology are explained in **Sections 5.1** and **5.2**, respectively, while the results and partial discussion in **Sections 8.1** and **8.2**, respectively. In addition, the results presented in the **Section 10.2** and **10.3** use the MEMI workflow developed in this publication. The developed codes (in Python language) can be found in **Appendix A – MEMI workflow**.

Section II

MATERIALS AND

METHODS

CHAPTER 03 – MONITORING SYSTEMS

CHAPTER 04 – PCSTACKING ALGORITHM

CHAPTER 05 – MEMI WORKFLOW



Chapter 3

Photogrammetric Systems

03

3.1 Brief Disclaimer

The objective of **Chapter 3** is to document the **research, design and development** of the fixed time-lapse photogrammetric systems employed in this research. These systems were necessary to obtain the data used in the publications and constitute a key piece of the research carried out in this doctoral thesis.

The author is aware of the complexity of the chapter and the thematic distance between the following sections and the field of geoscience. All concepts are developed from a technical perspective, but only the key elements for the research are highlighted.

Therefore, the importance of including **Chapter 3** in this dissertation is based on:

- i. Showing all the work that has been conducted over the years, since the publications, based on the codes and algorithms, give no account of it.
- ii. Describing the entire development process to enable future researchers to understand, use and improve the systems. Enabling the continuity of research, as well as guaranteeing open access to knowledge.

3.2 General Outlines

Before starting the investigation in the study areas, several laboratory-scale tests were carried out to determine whether it is possible to detect both deformation and rockfalls by placing fixed cameras in front of an object and capturing time-lapse images. These experiments were performed using ice models with blocks of different sizes. Low-cost cameras were placed in front of the model, taking images every 30 seconds (**Figure II.1**).

In the QRs (animation may take a while to load) it is possible to see the setup that was performed (**QR 13**) as well as the animation plots of the results (**QR 14** and **15**, some mobile phone browsers may not play the animation). The positive results of the experiment allowed us to further explore the installation of fixed cameras in a real study area (**Figure II.1**).



QR 13



QR 14



QR 15

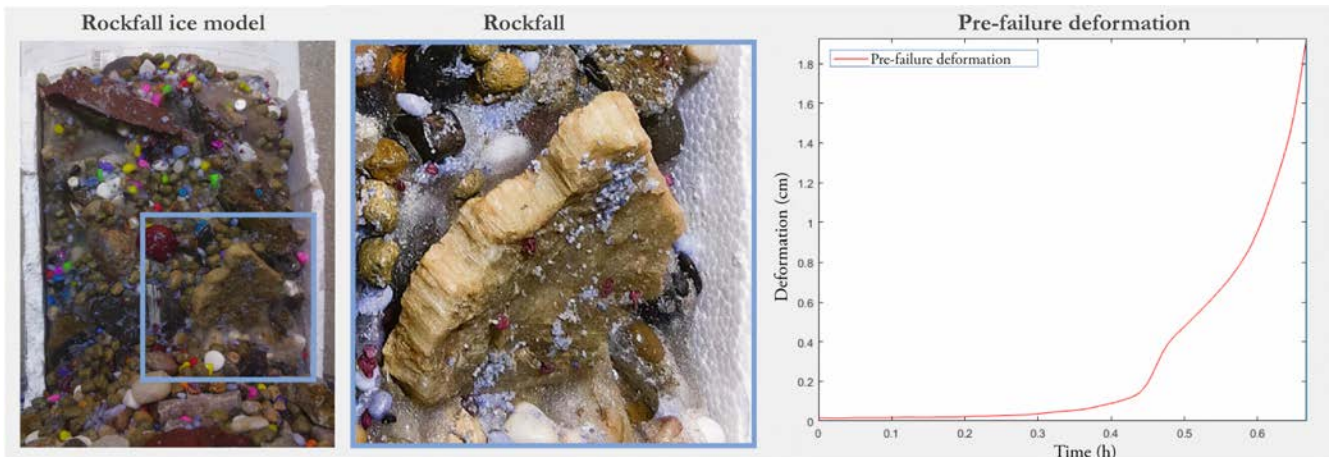


Figure II.1. Experiment carried out in the laboratory with ice models **QR 13**, using low-cost cameras. The plot shows the pre-failure deformation of the largest block. It is recommended to visualise the result in the **QR 14** and a similar example in **QR 15**.

The installation of fixed cameras in real studio areas is a much more complex matter than user-controlled lab tests. An easy way to install cameras in real studio areas capable of acquiring images every few minutes is by using an intervalometer. However, thanks to the introduction of camera control and management systems (control unit), any basic camera can be turned into a programmable photographic module.

The photogrammetric systems presented in this section should not be understood as a simple commercial camera installed with an intervalometer. These advanced systems should rather be understood as a set of cameras (lens and sensor), an advanced control unit, a connectivity system, data infrastructure and a self-sufficient energy system (**Figure II.2**) based on 3 very clear principles:

- i) **Programmable.** The programming of these control units provides us with complete control of the camera. In the field of photogrammetric monitoring, for example, we can obtain time-lapse photographs in burst mode of the study areas (for example, a burst of 15 photographs every 5 hours during the day).
- ii) **Remote access.** Due to the large amount of data that can be obtained, it is of great interest that these fixed systems installed in natural environments should be remotely accessed/downloaded. For this reason, photogrammetric systems for monitoring must be

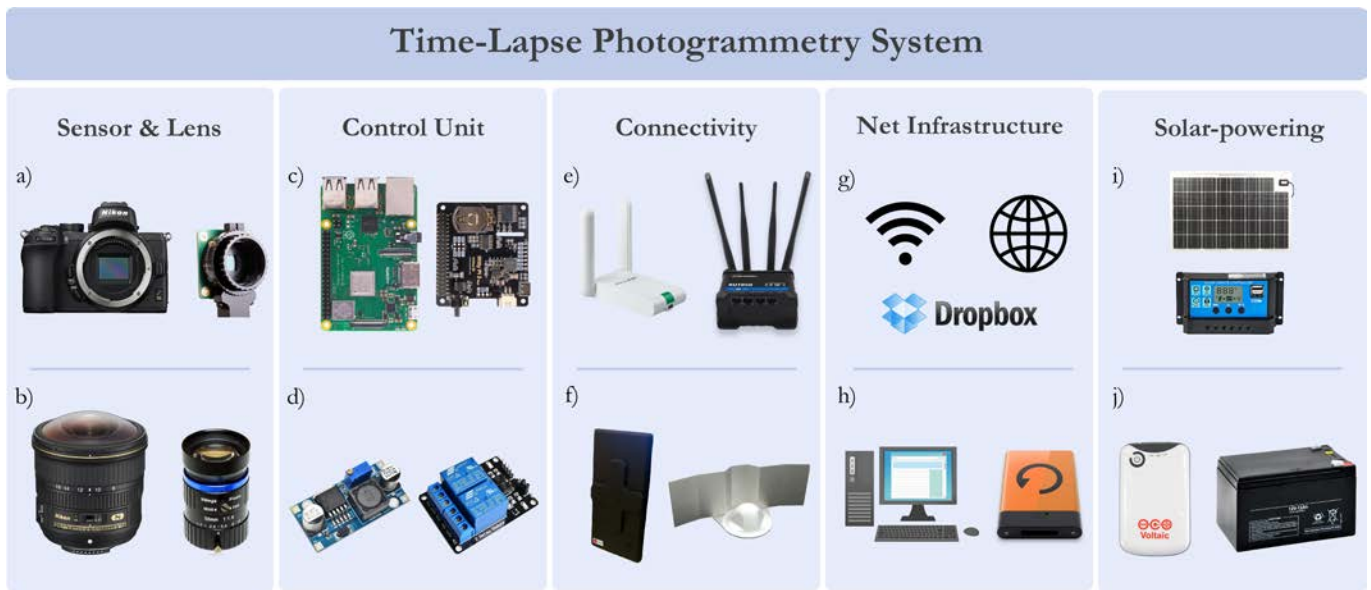


Figure II.2. Representation of the 5 modules that constitute a complete photogrammetric system. Each module shows the main components. The description of the sections **a-j)** is done in the main text and is developed in the following sections of the manuscript. All images/pictograms have been obtained under Creative Common licence or are product images directly obtained from the manufacturer.

capable of transmitting data as well as receiving basic programming instructions. This implies that the installation of the data transmission systems, as well as the entire construction of the network infrastructure to transmit, receive and store the collected photographs, must be understood as part of the fixed photogrammetric system (**Figure II.2**).

iii) **Solar-powered.** Fixed monitoring systems with remote data sending capability can also be supplemented with appropriate systems that allow not only a high degree of autonomy but also the ability to be self-sufficient. This feature makes it possible to install systems, based on batteries and solar panels, in natural environments in the middle of nowhere, far from fixed electrical installations (**Figure II.2**).

For this reason, throughout this thesis the term "photogrammetric system" refers not only to the installation of cameras, but also to the integration and coordination of the modules that enable the 3 principles established for the systems developed in this research to be fulfilled (**Figure II.2**).

As an example, **Figure II.2** shows a generic approach of the main components used in the development of the photogrammetric systems of this thesis. These can be summarized as follows.

- a) Photo sensor. This may be either high resolution (left) or low cost (right).
- b) Lenses. They must be appropriate to the characteristics of the sensor and the study area.
- c) Control and processing unit. Usually, embedded microprocessor boards such as Raspberry Pi or Arduino shield.
- d) Real Time Clock (RTC) and power management shield.
- e) Network receivers and transmitters. USB and 4G modems.
- f) Booster antennas, both for the 4G signal and for the wireless local network.
- g) Connection services and network servers
- h) Workstation for data downloading, processing and backup storage.
- i) Solar panel and solar controller.
- j) 5V power bank battery for very low-voltage systems and 12V AGM batteries for low-voltage systems. This part also includes all electronic components such as relays or step-downs to regulate the power supply of all systems (camera and control unit).

To obtain all the data necessary for the development of this thesis, it has been necessary to design, develop and install 3 different photogrammetric systems. Although the design of these systems has been carried out in different phases, the 3 systems have been designed with the aim of fulfilling the three basic premises defined above: to be programmable, to have remote downloading and to be solar-powered. Furthermore, the design of each system is based on the specifications of the research, as well as considering the limitations and characteristics of each study area, as shown in the following chapters.

3.2.1 Sensor and lens

The photographic sensor is the component responsible for transforming the photons that pass through the camera lens into an electrical signal. The smallest unit of information is called a pixel and, as a rule, each pixel stores the luminous intensity of each of the three primary colours: red, green, and blue. The number of pixels available on a sensor is a characteristic that determines the amount of information stored in the image. For the same

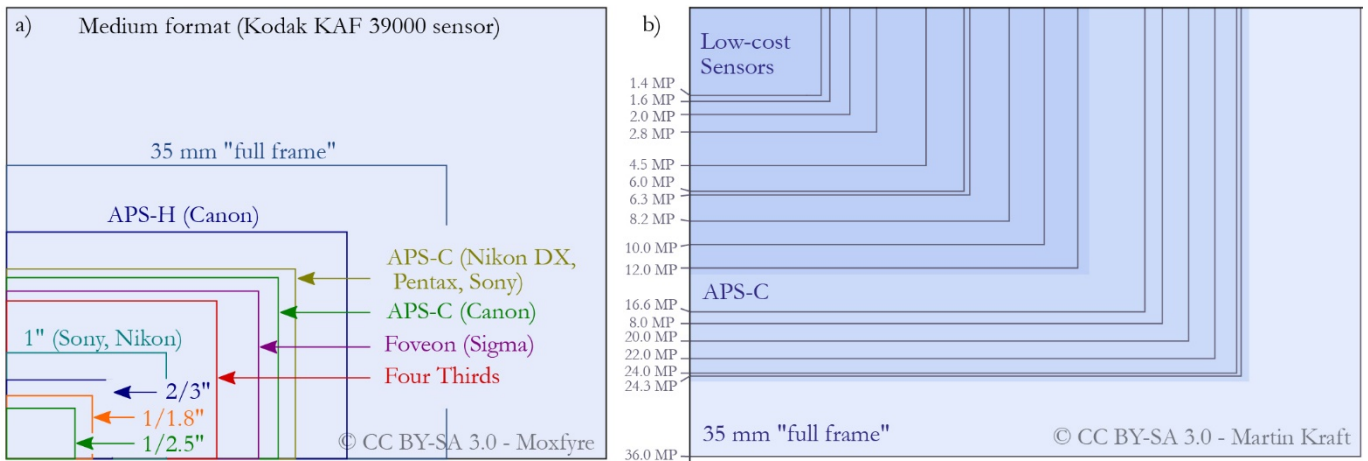


Figure II.3. a) Aspect ratio of the most common commercial sensors. CC BY-SA 3.0 Moxfyre. **b)** Evolution in megapixels of the sensors. The different shades of blue roughly divide the different sensor categories. CC BY-SA 3.0 Martin Kraft.

field of view, the more pixels there are, the more individualised the photons collected on the sensor, thus resulting in a higher spatial resolution, since the image is represented by a higher number of pixels.

However, the quality of the sensor depends not only on the number of pixels, but also on other parameters, such as the size of the pixels, the intensity levels it can store (colour depth), as well as the dynamic range it can transform into an electrical signal before saturating. The electrical transformation of the captured photons is performed in the sensor's own control unit and the result obtained is a RAW file in which the intensity of the three primary colours stored in each pixel is shown in a stacked way. The transformation of this RAW file to a standard image format (e.g., jpg, png, bmp) is known as digital photography.

Sensors are usually classified according to two basic parameters (**Figure II.3**). The first parameter is the size of the sensor. There is a wide range of sensor sizes on the market, from the 1/10" sensor (only 1.6 mm diagonal) to 8x10 large format sensors (300 mm diagonal). However, the most common sensor size for commercial cameras is the APS-C size (28 mm diagonal) and the full-frame size (43 mm), which corresponds to the dimensions of 35 mm analogue film. In the field of low-cost photography or cameras built into cell phones, the sensor size is smaller, with 1/4" (4.5 mm diagonal), 1/3" (6 mm diagonal) or 1/2" (8 mm diagonal) being the most common (**Figure II.3a**).

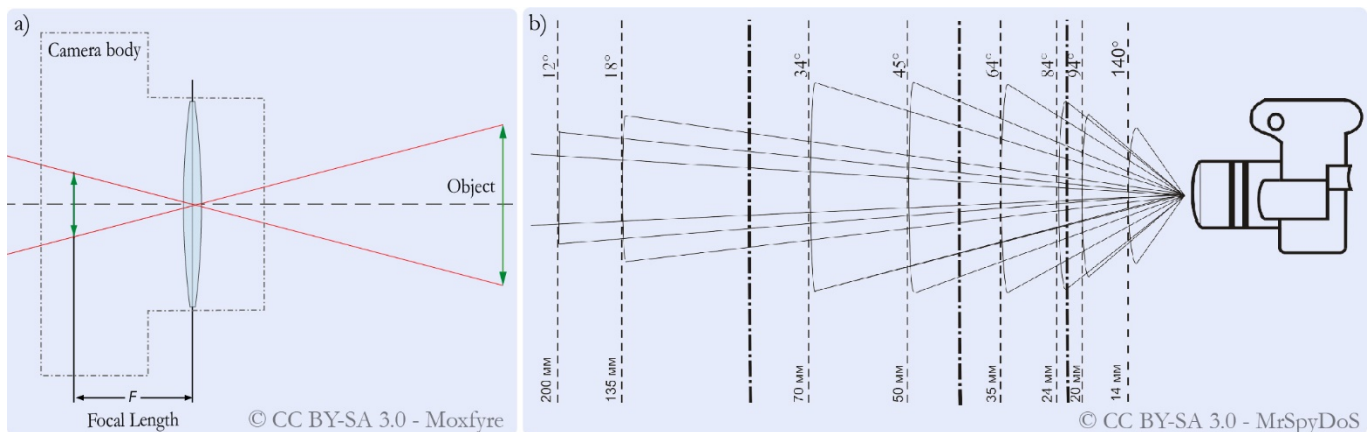


Figure II.4. a) Sketch showing the projection of a real object on the photographic sensor. The sketch helps to understand the basic concepts of optics inside a photographic camera. The focal length is represented. CC BY-SA 3.0 Moxfyre. b) Graphical representation of the different fields of view (represented in angles) obtained for different focal lengths. CC BY-SA 3.0 MrSpyDoS.

The second parameter for classifying photographic sensors is the number of pixels. Thanks to the miniaturization of technology, this parameter is constantly evolving, as demonstrated by the possibility of obtaining very small sensors capable of housing more than 100 million pixels (Samsung's ISOCELL Bright HMX ©). However, to guarantee very good image quality, it is not common to manufacture sensors with such a small pixel size. Thus, the most found on the market are commercial APS-C format cameras that have around 20-24MPx and full frame cameras around 36-46MPx. As for low-cost photography, the smallest sensors are usually between 5-10MPx (**Figure II.3b**).

Another key factor for ensuring good image quality is the photographic lens. This lens is responsible for delivering the photons from the outside of the camera to the surface of the sensor. This is done by means of a set of concave and convex lenses that allow the light rays to be transported and adapted to hit the sensor (**Figure II.4a**). The main characteristic of photographic lenses is the focal length. This is the distance between the optical centre (position of inversion of the light rays) and the photographic sensor (focal plane) (**Figure II.4a**). This distance has a direct impact on the number of light rays reaching the sensor. Thus, very small focal lengths (e.g., 10 mm) will allow a larger amount of light to enter, which in combination with the size of the sensor will define a large field of view (the photograph

shows a larger portion of the captured scenery). Conversely, larger focal lengths (e.g., 300 mm) allow less light to enter, which will be associated with a smaller field of view (**Figure II.4b**). In addition, other characteristics such as lens construction material (glass or plastic) or the number of internal lenses is also crucial in defining both the optical quality of the image (in terms of sharpness) and the distortions that may occur (and which significantly affect SfM-MVS processes).

3.2.2 Advanced Control Unit

The control unit is the system that manages the shooting process of the camera and its settings. The most basic control unit is the camera itself, which thanks to the internal intervalometer can take images without the need for an operator. Other simple systems make use of external intervalometers that are connected to the camera and automate the image capture per time interval (n seconds). An experience of that is reported on Royán (2015). However, in the framework of this research we will refer to the control unit as an advanced system to manage the communication with the camera, which is programmable and connected to the network.

These advanced control units are based on minicomputer boards (SBC) such as [Raspberry Pi](#), microcontrollers such as [Arduino](#) or electronic boards designed ad hoc for each system. However, as this last option is beyond the technical scope of this research, the advanced control units used to design the systems were based on commercial mini-computer boards. These electronic boards are highly programmable, and thanks to the existence of a large community and GNU General Public Licence libraries, an infinite number of projects (based on do-it-yourself experiences) can be realised.

The three systems designed and developed in this thesis are based on the Raspberry Pi, a mini-computer board of the [Raspberry Pi Foundation](#) (Cambridge, United Kingdom). The initial goal of this foundation was to democratize the power of computing and digital creation worldwide (Severance, 2013). Although the original objective was to promote the teaching of computing in schools, its low production cost and great versatility based on the use of the free [OS Raspbian](#) based on [Debian](#) (GNU/Linux) have made it a widely used tool in the scientific field (**Figure II.5a**).

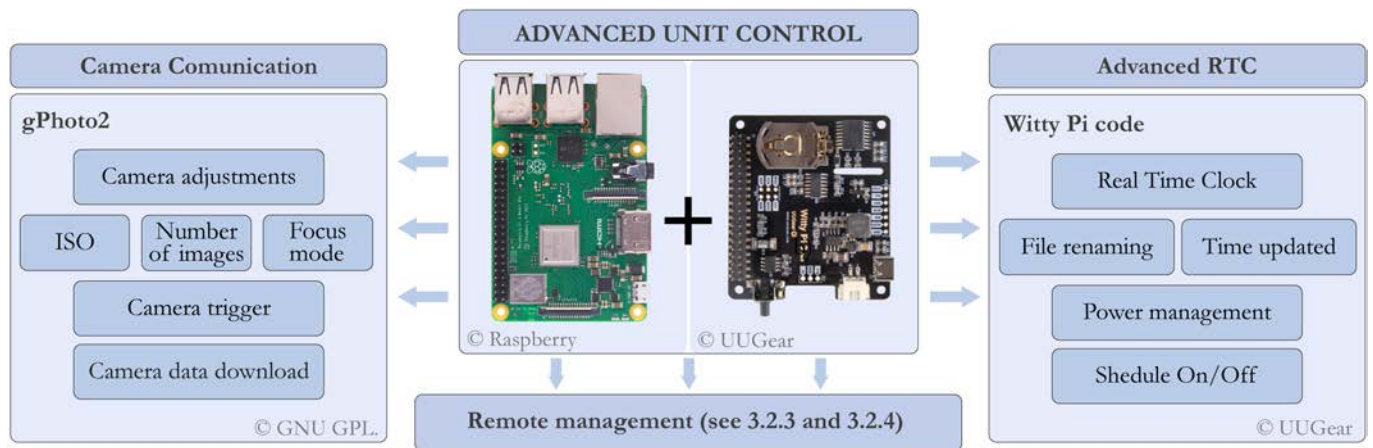


Figure II.5. Main functions of the advanced control unit. Each block contains its own programming environment and functions. Codes and scripts available in the digital repository of each photogrammetric system. (e.g., **Appendix A - HRCam System scripts**)

The [gPhoto2](#) software and its associated libgphoto2 library enable the Raspberry Pi to become an advanced control unit for photographic systems. gPhoto2 is a free, redistributable, ready-to-use set of digital camera software applications for Unix-like systems, written by a whole team of dedicated volunteers around the world (GPhoto2. Digital Camera Software, 2021) and is distributed under the GNU General Public Licence (GNU GPL). This library enables connection to more than 2,700 commercial cameras and controls their functions (**Figure II.5b**).

For example, the gPhoto2 library can be used to change camera parameters such as ISO, exposure speed, aperture, or another camera configuration. In addition, it is also possible to send commands, such as capturing an image or transferring it to the control unit. The programming of the advanced control unit can be found in the [GitHub digital repository](#) of each photogrammetric system. (e.g., **Appendix A - HRCam System scripts**).

Due to the absence of an internal battery, SBC boards are not capable of storing any active memory. Consequently, they are unable to memorize the current time and date. This means that at each start up the date will be incorrect. For this reason, one of the most common accessories of these systems is the inclusion of a Real Time Clock (RTC) that allows the system to store the time and maintain an active memory that counts the progress of time.

For this reason, another indispensable element in creating an advanced control unit is the use of a RTC.

The [UUGear WittyPi](#) © control board has been used as the RTC for all the projects that have been carried out in this thesis. This control board not only incorporates an advanced RTC, but also has the ability to manage power. The combination of these two properties allows the WittyPi to be fully programmable and to define complex ON/OFF sequences with a simple script (UUGear WittyPi3, 2021).

In addition, this advanced board can connect to servers in order to update the time whenever an internet connection is available, and can also override time changes that occur throughout the year (summer-winter). Thanks to the precise acquisition of time and date, the advanced control unit can assign this attribute to photographs, thereby facilitating their subsequent classification (**Figure II.5c**).

All these hardware and software (libraries and codes) has been ensembled and programmed to obtain images in an automatic way. The operating scheme that has been developed for the management of the images in the control unit is based on the following workflow:

- * Start the system (WittyPi).
- * Update time (WittyPi).
- * Activate the relays to switch the camera on (see **Section 3.2.5**) (Internal code).
- * Trigger order (gPhoto2).
- * Download images from the camera (gPhoto2).
- * Rename images to current date and time (Internal code).
- * Save images in the temporary output folder (Internal code).
- * Send the generated logs to the server (Internal code).
- * Send images to the server (see **Section 3.2.4**) (Internal code).
- * Move images from the temporary output folder to the temporary backup folder (Internal code).
- * Disconnect relays (Internal code).
- * Shutdown the system (WittyPi).

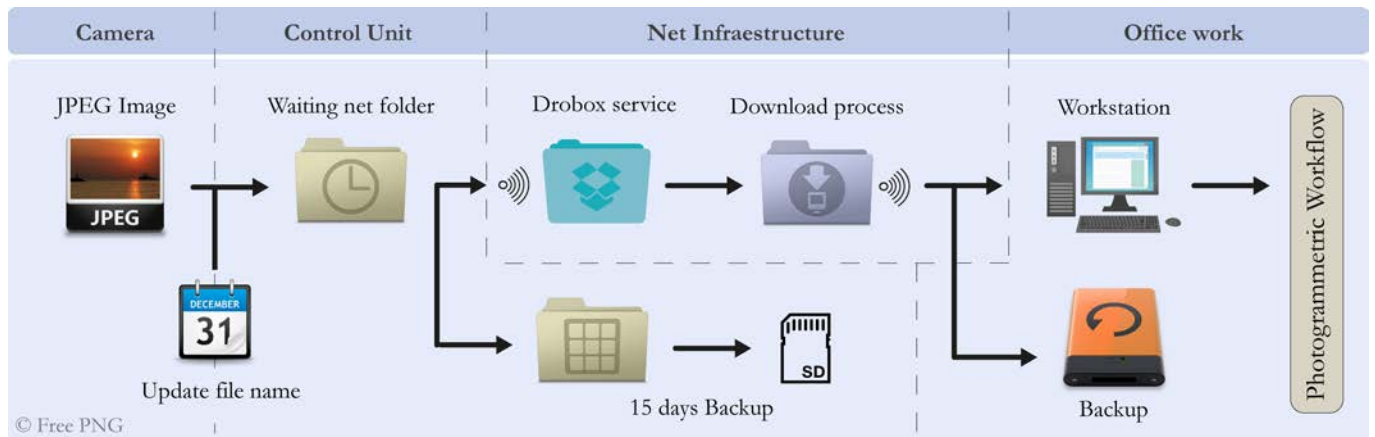


Figure II.6. Diagram of the time sequence of actions carried out by the control unit to transmit and securely store the acquired images to the workstation. There is one direct transmission line and two backups (one temporary and one permanent).

Should the connectivity fail, this sequence ensures that the images remain stored in the temporary output folder (**Figure II.6**). Whenever the control unit detects connectivity again, it will attempt to upload the entire contents of this folder to the server. Only when it is confirmed that the information has been successfully uploaded to the server, the images are moved from the temporary output folder to the temporary backup folder. The images are stored there for 15 days in case they need to be manually removed from the system. After 15 days the images are deleted, ensuring that the system always has some free memory (**Figure II.6**).

The entire system can be monitored from the generated log codes. Logs are small text files that store relevant system information and are sent directly to the server (**Figure II.7**). For this research, both automatic logs created by the RTC and logs generated manually are used. The codes that generate these registers and all the information they contain can be found in **Appendix A** (e.g., **HRCam System scripts**). Other file management and emergency backup functions are detailed directly with the presence of the codes presented in **Appendix A**.

Due to the need to integrate many different systems, libraries, and codes, all the programming undertaken in this doctoral thesis has been performed with [Python](#) (Python Core Team, 2015). This has been possible thanks to the great versatility of systems based on free code and licences. Python is a high-level, general-purpose interpreted programming language that


```

*****
Hora: 14:33 Data: 31/12/2020
Es realitzaran 4 captures fotogràfiques

** Inici seqüència fotogràfica **
Fitxer HRCam1_20201231_1413_4.JPG pendent d'enviar
Fitxer HRCam1_20201231_1411_2.JPG pendent d'enviar
Fitxer HRCam1_20201231_1413_2.JPG pendent d'enviar
Fitxer HRCam1_20201231_1411_3.JPG pendent d'enviar
Fitxer HRCam1_20201231_1413_3.JPG pendent d'enviar
Fitxer HRCam1_20201231_1411_4.JPG pendent d'enviar
Fitxer HRCam1_20201231_1411_1.JPG pendent d'enviar
Fitxer HRCam1_20201231_1413_1.JPG pendent d'enviar

Les carpetes HRCam1_Puigcercós i HRCam1_Puigcercós_filetransfer ja existeixen

** Identificació de la càmera **

Càmera Sony Alpha-A7r II identificada correctament

** Inici de la seqüència fotogràfica **

GPHOTO2 - Captura realitzada i descarregada
Nom del fitxer capt0000.jpg canviat correctament a HRCam1_20201231_1433_1.JPG
GPHOTO2 - Captura realitzada i descarregada
Nom del fitxer capt0000.jpg canviat correctament a HRCam1_20201231_1433_2.JPG
GPHOTO2 - Captura realitzada i descarregada
Nom del fitxer capt0000.jpg canviat correctament a HRCam1_20201231_1433_3.JPG
GPHOTO2 - Captura realitzada i descarregada
Nom del fitxer capt0000.jpg canviat correctament a HRCam1_20201231_1433_4.JPG

** Seqüència de captura fotogràfica finalitzada **

** Codi finalitzat correctament **

Temps d'execució: 50 segons
*****

```

Figure II.7. Log file fragment. It shows the status of the HRCam1 system in Puigcercós and the main script outputs. This log is automatically sent to the server after each boot.

is characterised by its great readability. The programming language is based on its own Python Software Foundation Licence (PSFL), which is comparable to the GNU General Public Licence (GNU-GPL) (Python Core Team, 2015). The use of this programming language has not only involved the generation of new codes, but also the transformation and adaptation to Python of part of the RISKNAT research group codes that are used in **Section IV** of this dissertation.

3.2.3 Connectivity System

To provide connectivity to the photogrammetric systems created in this thesis, part of the research has focused on the design, development, and installation of a connectivity system. This connectivity system has been designed to be robust, easy to install and capable of working in remote environments.

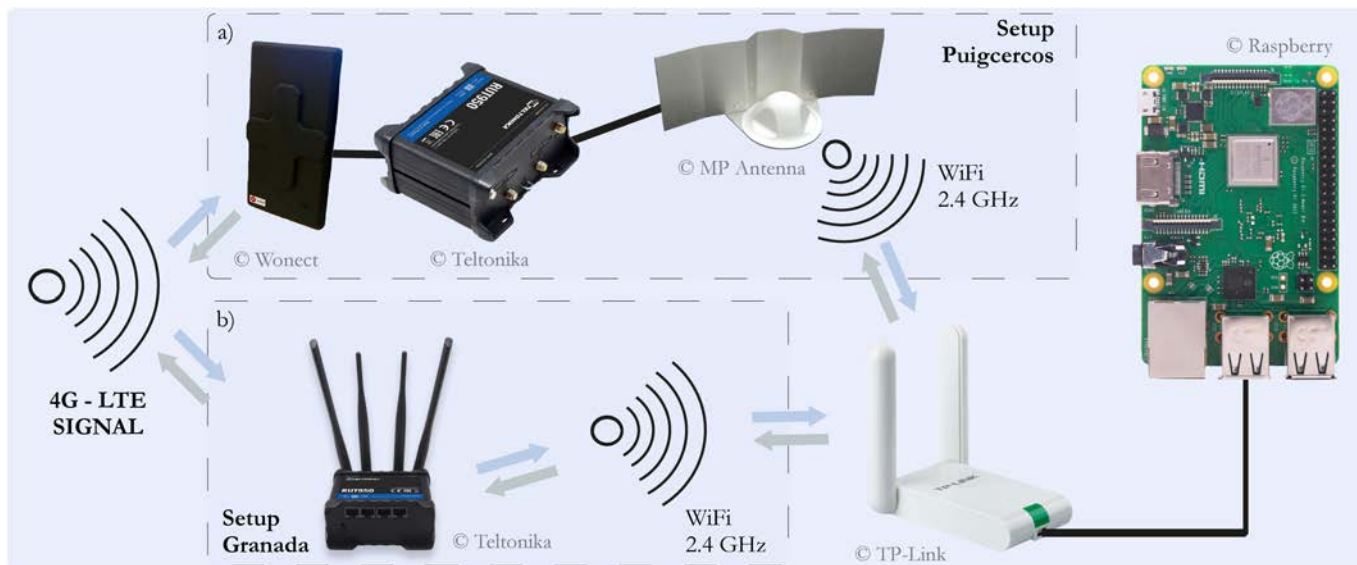


Figure II.8. Basic diagram of a general connectivity system. **a)** Connectivity system installed in Puigcercós. **b)** Connectivity system installed in Granada-Alhambra. In both systems, the source signal is 4G. Further details are provided in the respective sections

Two main systems are currently used to ensure the connectivity of a system at an isolated point. The first is satellite connectivity, which provides connectivity at almost any point on the earth's surface, but is also expensive and difficult to implement. The second and much more widespread method is to use the increasingly extensive mobile phone data network. This second method is the one used in this research, both for the systems installed in the Puigcercós study area and in the Granada-Alhambra area.

Mobile phone connectivity allows data to be sent over a distance. This transmission is done by packaging the information that is sent according to generic internet protocols and transforming it into waves. This transformation takes place in antennas and occurs at specific frequencies. These frequencies are decisive for the transmission speed as well as for the penetrability of the signal (coverage). For the systems used, and based on Spanish regulations, the frequencies used are 800, 1800 and 2600 MHz, which correspond to 4G and LTE data transmissions. These frequencies allow high coverage and transmission speeds of up to 30 Mbps.

To link the mobile 4G signal to the photogrammetric systems, a wireless network has been used in most systems (**Figure II.8**). This option is able to send and receive information using

waves. As in the case of mobile phone connectivity, the transmission/reception frequency and the antennas are decisive in defining the characteristics of the system. The systems developed in this thesis use the 2.4 GHz Wi-Fi frequency, which, although it does not provide as much speed as 5.0 GHz networks, enables greater distances to be reached (the higher the hertz, the greater the data transmission, but the lower the penetrability).

Modem is the device in charge of making the connections, establishing the transmission protocols, ensuring the orderly output of the packets, and sending them to the appropriate addresses. It is located between the income antenna of the mobile phone connection and the outcome antenna of the wireless network (**Figure II.8**). In the case of 4G modems (such as those used in this thesis), it is also responsible for housing the phone card and of connecting to the specific mobile data network.

The latest Raspberry Pi systems have an integrated network module that allows them to connect to the internet both via Ethernet and Wi-Fi. However, as will be seen in the next section, the systems designed in this thesis are built in small metal boxes with almost no openings to the outside (waterproof boxes), which produces a Faraday cage effect that blocks the wireless signal from reaching the control unit's integrated antenna. For this reason, an external Wi-Fi-USB receiver antenna capable of sending the internet signal to the system via a USB cable is used. All systems have been developed using the [TL-WN822N](#) antenna from [TP-LINK](#) © (**Figure II.8**).

Since the connectivity system is specific to a particular study area and not to every single system, the particularities of each network structure will be developed in the following sections: The Puigcercós connectivity system is developed in **Section 3.3.3** and the Granada-Alhambra connectivity system is explained in **Section 3.5.3**.

3.2.4 Net infrastructure

Providing connectivity to the photogrammetric systems is a key point because it provides greater autonomy to the systems, but although it is a necessary condition, it is not sufficient to obtain an advanced remote pipeline. The simple fact of providing connectivity does not imply a substantial change in the operation of the systems. To generate a remote system for sending and receiving information, a whole data infrastructure needs to be developed.

Nowadays, with the boom of the Internet of Things (IoT) there are many infrastructures, servers and cloud systems that can be easily transformed to suit any application. In our case, we have looked for maximum simplicity and have used robust cloud storage systems.

The system designed in this dissertation consists of transmitting the images directly from the advance control unit to a private [Dropbox](#) © (No GNU-GPL licence). Dropbox has been used for two main reasons; the first is the possibility of interacting with it by using Python scripting, and the second is its easy integration in Windows environments. This ability to be easily operable from two very different environments gives Dropbox very good operational adaptability. In addition, Dropbox allows free use of their service (limited space). For this reason, it has become a core part of our network infrastructure.

Python programming is performed by means of Dropbox's own library for Python. This library allows interaction with the Dropbox platform by scripting. With the appropriate scripting it is possible to automatically send the photographs obtained in each photogrammetric system in an ordered way to a specific folder (**Figure II.6**).

Having the images in a Dropbox folder implies that the images have already left the device and are on a server in the cloud. This could be a very basic network infrastructure, but as the storage capacity of Drobox is limited for free accounts, and the full subscription only allows 2 TB of storage (it would be insufficient), it is necessary to develop further steps in the infrastructure.

Thanks to the good integration of the Dropbox service in Windows environments, we can easily and instantly obtain the images that have emerged from the photogrammetric system in any Dropbox application installed in a Windows environment. For this thesis, the Workstation of the RISKNAT research group is used as a server. The Dropbox application of this Workstation automatically downloads the images from the photogrammetric systems (**Figure II.6**). This solution allows us to obtain the images on any computer, but does not solve the storage problem, since the Dropbox application receives images every day and its capacity is limited. For this reason, a code has also been programmed to empty the Dropbox folder every day and send the images to a hard drive. This clears the Dropbox folder of consumed space and stores all the images of the day on a secure hard drive on the

workstation. In addition, the last step in this infrastructure is to make a daily backup of this hard drive to another one. Thus, all remotely retrieved images are automatically stored daily on two different hard drives (**Figure II.6**).

This system has enabled us to transfer an enormous amount of data between the photogrammetric systems and our workstation. However, the system has its limitations and dependencies. The main limitation is that it always requires a connected computer. If Dropbox folder is not released, all the available storage quickly fills up. In this case, the control units stop sending photographs and the connection between the workstation and the photogrammetric system is interrupted.

For these cases, the control unit operation workflow stores these unsent images in the temporary back up folder (waiting folder net folder in **Figure II.6**). When connectivity is re-established, the code tries to send again all files stored in this temporary folder. System failure would occur when the control unit's memory also becomes full. In this case, the system is unable to store any more images and therefore the photogrammetric system would not be operative.

Furthermore, part of the research project was based on the idea of generating a network structure capable not only of downloading images in one direction from the photogrammetric system to the workstation, but also of interacting with the system and modifying its parameters from the workstation. This infrastructure is supposed to generate a bidirectional communication with the photogrammetric systems. This infrastructure was successfully designed and developed, but as it was never used and its implementation implied extra complexity both in the field of programming and electronics, it has been discontinued in the last updates of the system.

Communication between the workstation and the photogrammetric systems was designed on the basis of remote desktop software that allowed connection to the control unit. The [TeamViewer](#) © software (No GNU-GPL Licence) was used for this function. This software allows installation in Windows and Linux environments as well as the creation of free accounts. Once the control unit was power on and a network connection was established, the control unit could be accessed from any computer with the TeamViewer software

installed. The access is done from the private credentials that are associated with a user account. To avoid the automatic shutdown of the control unit at the end of the operating image acquisition, a system was developed using relays (see next section) that allowed the control unit to be opened indefinitely. Once the remote operations are ended, an extra relay could be activated, causing the automatic control unit to shut down.

As mentioned above, this system was designed and implemented, but never used, as the main drawbacks of this system outweighed the benefits. The main drawbacks are:

- * It is only possible to connect to it at scheduled times. If the system does power on, it is impossible to connect. Therefore, it is not valid for "fixing" systems that do not start properly.
- * Quick action must be taken to remotely activate the relays before the system starts the shutdown cycle. If not, the control unit orders shutdown, and the connection is lost.
- * Transmission through the virtual desktop consumes a significant amount of data and requires a good internet connection. And neither element has enough strength in Puigcerçós.
- * There is a real risk that the system remains open and does not shut down automatically, which would lead to total battery consumption and consequently to system failure.
- * It requires more electronic installation (cables and relays) and these elements are particularly sensitive in adverse climatic environments, as discussed in the following sections.

3.2.5 Solar-powering system

Both the camera and the control unit need electricity. For systems installed in urban environments with access to electricity, it has not been necessary to develop a power supply system. With the transformers included in the Raspberry Pi and the accessory enabling the camera to be plugged into the mains, a permanently powered system can be installed. However, for systems that are installed in natural environments without access to electricity, an ad hoc power supply system has been developed for each system (**Figure II.9**).

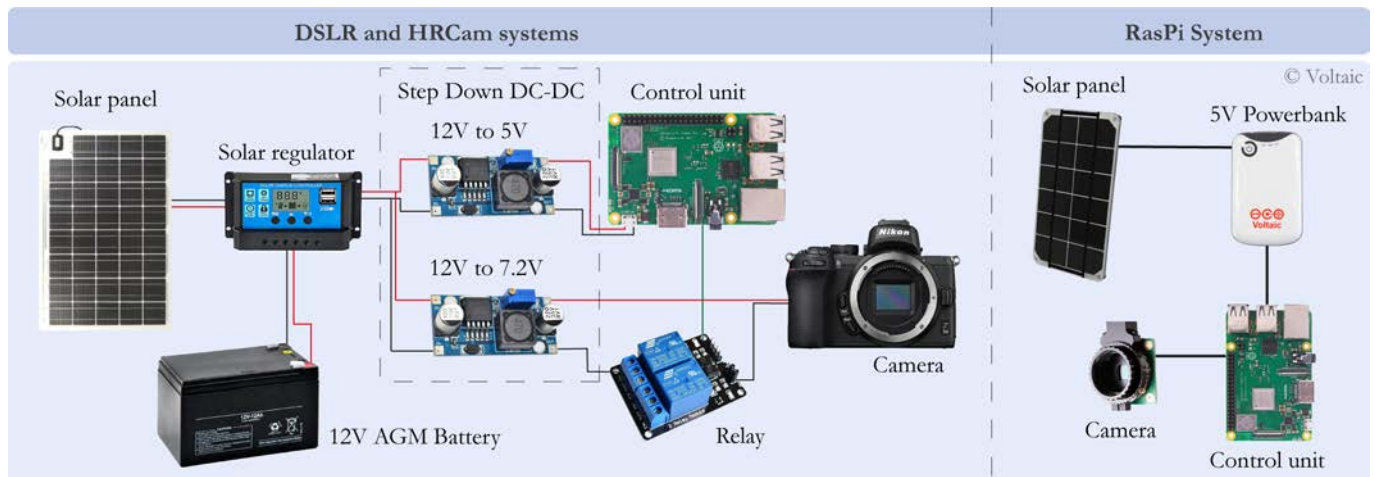


Figure II.9. Diagram showing the two power systems designed to supply solar energy to designed systems. **Left:** DSLR and HRCAM systems. **Right:** RasPi System.

For the more complex systems (**DSLR** and **HRCam** systems) a solar power supply system has been developed. This system consists of:

- * A photovoltaic panel that transforms sunlight into electrical energy. For the systems installed in Puigcerçós (**HRCam**), 10 W solar panels are used, and some installations in Granada-Alhambra (**DSLR**) use 20 W panels.
- * A charge regulator that controls the charging of the battery. This regulator is responsible for protecting the battery, bypassing the current and allowing the battery to be charged or discharged once certain voltage, current and temperature conditions have been achieved.
- * A battery. For the systems we have developed we use AGM batteries. In these batteries the electrolyte is located in plates instead of in liquid form, so they are suitable for installation in remote areas, since they do not require maintenance and there are no problems with evaporation, corrosion, etc. For the systems developed, 12 V and 7 Ah batteries are used.
- * Because the battery voltage is 12 V and the systems work at a different voltage, step downs have been installed. A step down is a DC-DC converter which by an adjustable regulator can reduce the voltage at the output. From the battery, two power lines have been installed, one at 5 V for the control systems and one at 7.2 V for the camera power supply.

- * Finally, relays are also part of the power supply system. We have installed relays that can be controlled by the electronics of the control unit. These relays act as switches for the power supply to the camera. In this way, the camera is only switched on when the control unit requires it, preventing it from being powered on 24/7.

The electrical system was designed to optimise every watt generated. Therefore, a relay system was designed, a 12 V infrastructure was used, and voltage regulators were implemented (**Figure II.9**). This design, together with the optimisation of the code to consume as little power as possible, have resulted in a cost-effective, robust, and maintenance-free power system. It is highly reliable and also provides an extended autonomy. In different tests that have been carried out, it is estimated that in the case of a power failure, the battery is capable of providing enough energy to continue capturing and sending images for 20 days (capturing 4 images 3 times per day).

However, this system also has its limitations, the main one being that without sunlight there is no energy. Although this may sound like a minor issue, we have encountered problems with certain installations in Granada-Alhambra. The location of some cameras does not allow the photovoltaic panels to be installed at the desired orientation. This limitation, together with the few hours of solar radiation that occur at our locations in winter, has led us to oversize the electrical system by installing more powerful solar panels (initially 10W to 20W) and bigger batteries (from 7 Ah to 12 Ah). However, this point will be discussed in future sections.

The **RasPi** system installed at Puigcerçós has a much lower power requirement. As the photo sensor is directly powered by the control unit, the whole system runs at 5 V (**Figure II.9**). This voltage is becoming increasingly standardised because it is the voltage that allows most electronic systems to operate and is, for example, the standard voltage output of USB. For this reason, we used a power bank to power this system directly as a battery. At the same time, this power bank is provided directly by a 3.5 W solar panel. However, not all power banks are useful. It is necessary to choose a power bank that is capable of being charged by a solar panel (with an integrated charge regulator) and that allows power distribution when charging. This factor is very limiting, as most power bank systems do not allow charging at their outputs if they are receiving power through their input terminal.

For this system we used a [Voltaic](#) © system already created for this purpose, which in addition to providing compatibility between the solar panel and the power bank has other extra capabilities. The Always On Mode keeps the battery in a very low power mode while the connected device is off. This permanent low consumption ensures that devices can detect that the power bank is on and are able to start up again. A further extra capability is the aforementioned pass-through charging mode, which means that the Voltaic battery can charge from solar and charge your device at the same time (Voltaic Systems, 2021).

Based on the measurements, the Voltaic V15 power bank pack is used to power the RasPi system, which includes a 3.5 W solar panel and a 4,000mAh power bank (**Figure II.9**). This configuration provides more than 15 days of autonomy for the RasPi system in a highly compact and resistant system.

3.3 RasPi - Photogrammetric System (Puigcercós)

3.3.1 Design and location

Automated photographic systems including an intervalometer, a waterproof box and a remote connection system are available on the market, but at a very high price. For that reason, the main purpose of the RasPi system has been to generate a very low-cost photogrammetric system, assuming that lower cost means lower quality. When the first prototype was created, no papers with similar systems were published, so the development and installation of these cameras was done without any guidance or help. Consequently, the result has achieved thanks to experimentation and self-learning. The main idea was to create photogrammetric systems of very small size, with a very simple control unit and powered by a small battery (**Figure II.10**).

The initial design did not include any remote transmission system because it was still under development. The whole system was encased in a metal box with a waterproof seal. Due to the small size and light weight of the system, its fixing would be by means of pillars. In the first phase of design, we used the simplest components available for this purpose. For this reason, the control units were based on Raspberry Pi Zero W and the WittyPi2 management shield. For the camera, the solution offered by the Raspberry Foundation is used. More details are given in the following **Section 3.3.2**.



Figure II.10. Rendering of the RasPi system. Includes the basic elements such as the solar panel, the powerbank, the control unit and the Raspberry Pi Camera.

Stage 1	Stage 2	Stage 3	Stage 4
First functional 3 systems - Initial main script - WittyPi 2 - Raspberry Pi Zero W - No connectivity 	Add 2 new systems All system/scripts updated <i>add</i> - Connectivity system 	System upgrade <i>add</i> - Raspberry Pi 3 B + - External WiFi antenna <i>remove</i> - Raspberry Pi Zero W Main script update	Main script update <i>remove</i> - sending images

Figure II.11. Main stages of the development of the RasPi photogrammetric system. **Stage 1)** Main initial components and scripts. **Stage 2)** Field intervention to install 2 new systems and introduce connectivity to the systems. **Stage 3)** Raspberry Pi version upgraded and installation of external Wi-Fi antennas. **Stage 4)** Current status of the system. (Codes available in the repository: **Appendix A – RasPi System scripts**)

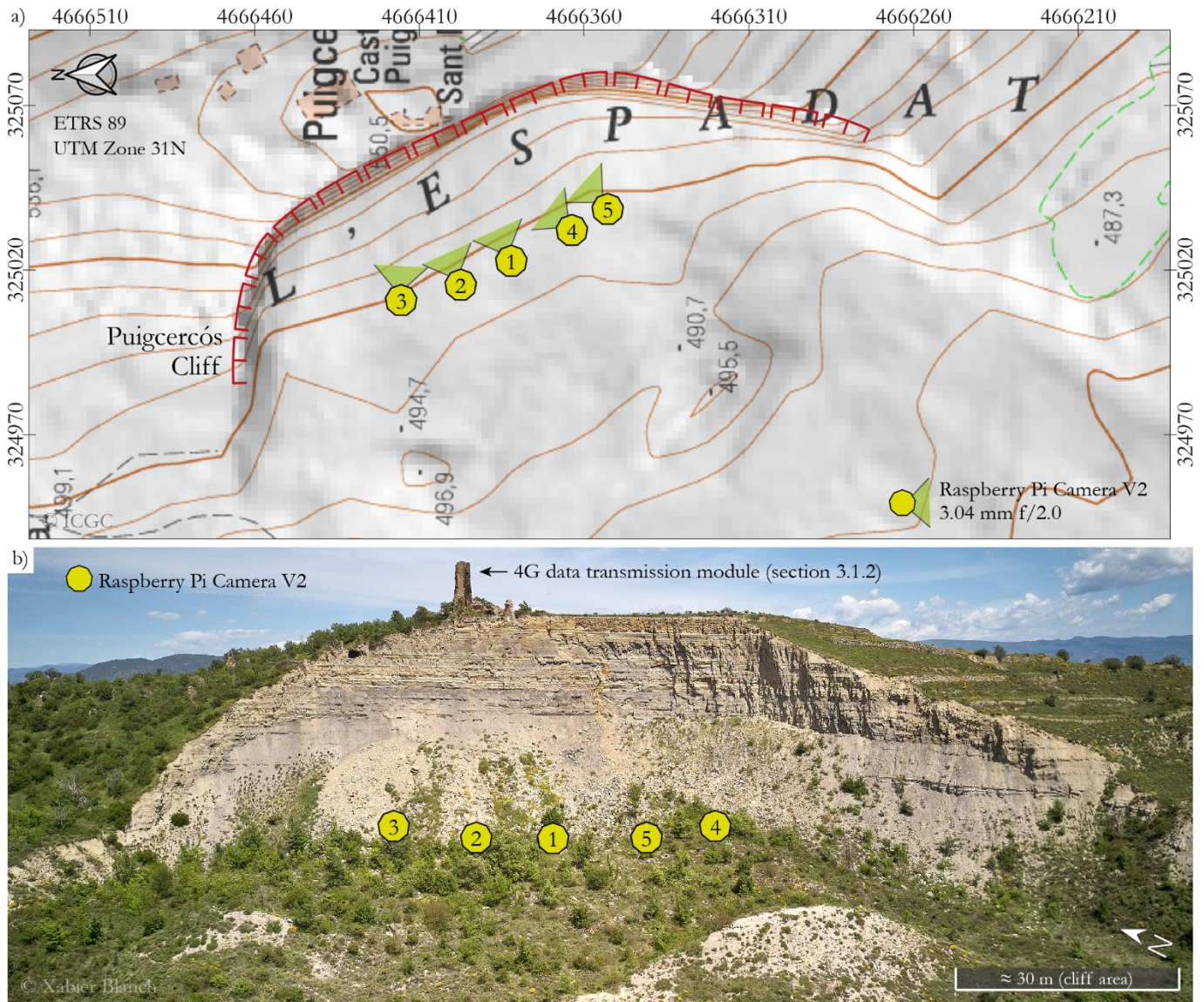


Figure II.12. a) Locations of the RasPi cameras in Puigercós. All systems have the same camera and shooting configuration. [ICGC](#) base map, no north oriented. b) Frontal image of the Puigercós cliff with the locations of the RasPi systems.

The system has been improved over the course of the research. From the initial design to the current system there have been 4 main evolutions. **Figure II.11** shows the different stages. In stages 1, 2 and 3, the system's hardware and configuration were changed. The programming of the code was modified at each stage according to the research. These modifications were made when faults were detected, or new improvements were implemented. The internal RasPi system codes and scripts are published in **Appendix A – RasPi System scripts**.

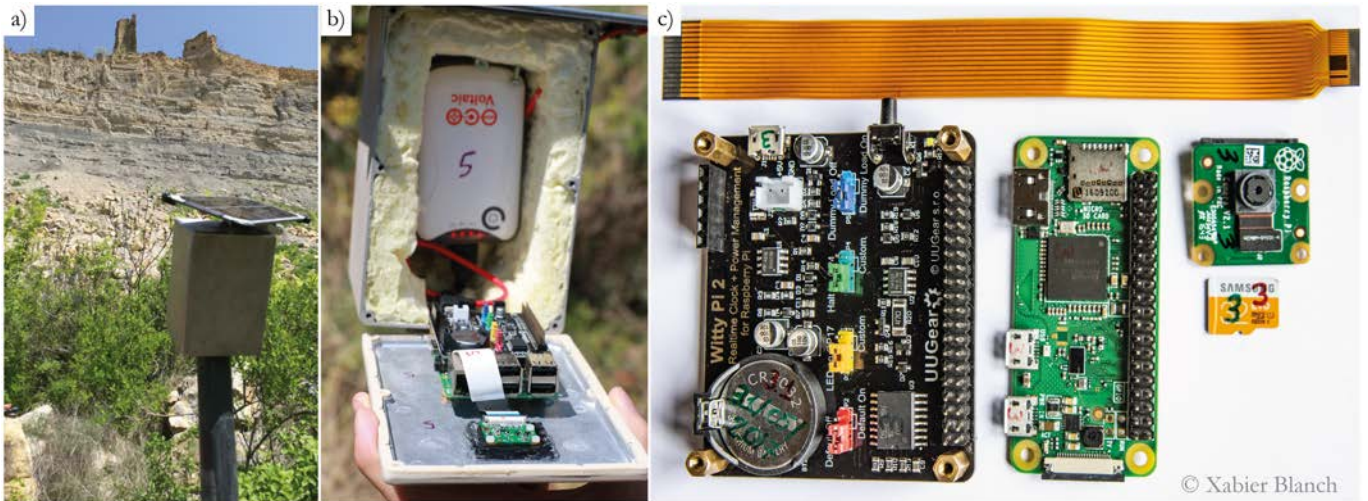


Figure II.13. Low-cost photogrammetric systems developed ad-hoc for rockfall monitoring on the Puigcercós cliff. **a,b)** Images of the installation on the Puigcercós cliff. **c)** Main electronic components (left to right): WittyPi2, Raspberry Pi ZeroW, Raspberry Camera Module v2 and MicroSD card.

These systems are installed in Puigcercós. In order to identify the best locations, extensive field work was carried out by performing different tests. Since the initial idea was to install only 3 systems, systems 1, 2 and 3 are located in the best central positions of the escarpment. Finally, the extension of the system with the installation of cameras 4 and 5 (stage 2) provided greater coverage of the central and right part of the scene (**Figure II.12**). The cameras are located about 60 meters from the vertical of the cliff and are distributed equispatially with approximately 20 meters between them. Given the proximity to the escarpment, the cameras are installed at an angle, which means that the photographs obtained show the escarpment in a low-angle shot. Image overlap is around 90%. Because Raspberry Cameras are licenced and can be manufactured by different suppliers, cameras 4 and 5 have a slightly different colour calibration. This is a drawback when working with very low-cost cameras.

3.3.2 Main components

The system consists of five photographic modules and a data transmission module. Each photographic module is composed of a Sony IMX219PQ © photographic sensor of 8 megapixels and 1/4" format assembled on a commercial Raspberry Pi Foundation Camera Module V2 board that is characterized by a 3.04mm focal length plastic lens (29 mm equivalent in 35 mm format) and a maximum aperture of f/2.0. These sensors are controlled

by a Raspberry Pi, a small microcomputer produced by Raspberry Pi Foundation. This computer takes the images and stores and transmits the data to the servers. A solar panel (3.5 W) and a battery (4500 mAh) are used to power each module. In order to manage the energy source, as well as to carry out the functions of the timer, the commercial board Witty Pi 2 by UUGear is used as a real-time clock and for power management (**Figure II.13**). All these components can be assembled for less than 150€. Thanks to the remote transmission, system based on a 4G Wi-Fi data network, and to the solar charging system, the system has very low maintenance costs. The systems have been installed in waterproof metal enclosures. As previously mentioned, this material interferes with the reception of the Wi-Fi signal of the Puigcercós connectivity system (Faraday cage effect). For this reason (stage 3 in **Figure II.11**) the systems had to be significantly modified by introducing an external Wi-Fi antenna connected via USB.

3.3.3 Puigcercós connectivity system

The system developed at Puigcercós provides connectivity to the two different photogrammetric systems installed in Puigcercós (RasPi and HRCam systems). As presented before, the Puigcercós cliff is located far from any populated area, so it has no access to wired internet or fixed electricity power supply. The system has been designed based on a central 4G modem that distributes connectivity between all the connected photogrammetric systems. Because we are in an area with little signal coverage, it was decided to mount the system far from the cameras in order to prioritise the obtention of a good 4G signal. For this reason, the Puigcercós system was installed on the tower remaining from the old village, which is located at the top of the cliff (**Figure II.14**). This set-up implies that the core of the connectivity system is placed more than 100 m away from the photogrammetric systems.

This location was chosen after studying the area, analysing the nearest phone antennas and mapping the existing signal coverage at different points in the study area. Thanks to the height of the tower and its privileged surveillance position, we have a direct view of the town of Tremp located 4km away where the nearest mobile phone antenna is situated.

As we have already mentioned, a fundamental element of the connectivity system is the antennas used, since very different characteristics are obtained depending on their setup and technology. In the design of the system, we have removed the antennas included with the

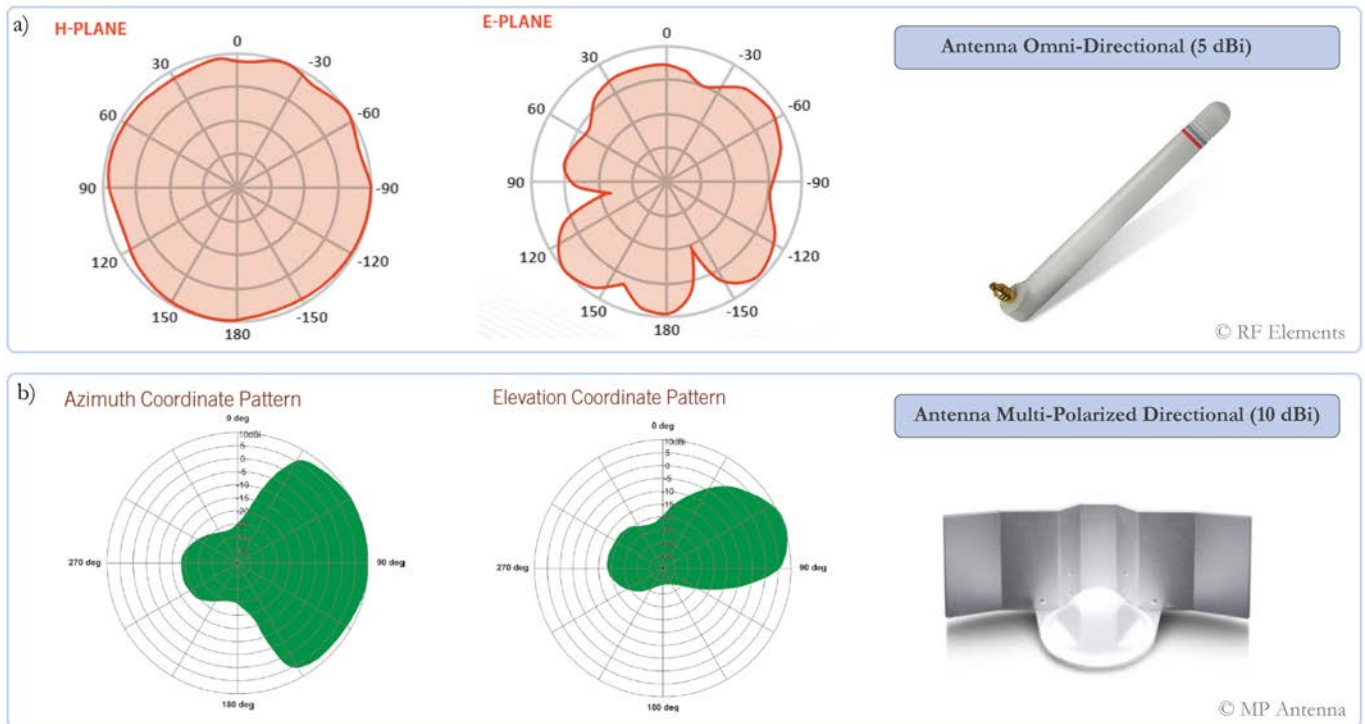


Figure II.14. a) Radiation pattern of an omnidirectional antenna similar to those included in Teltonika modems. Used in Granada-Alhambra system. b) Radiation pattern of the sectorial antennas used for the Puigcerçós system (MP Antenna, 2019).

modem, because they are omnidirectional antennas. These antennas are characterised by emitting waves in a doughnut shape around the central axis of the antenna, with a 360° coverage. In addition, in the vertical plane the antennas also have a fairly general radiation pattern. On the other hand, these antennas have very little capacity to reach long distances and the gain of these antennas is usually limited, because this broad radiation pattern implies that much of the energy is being used to carry the waves to areas that are of no interest for our proposal (**Figure II.14a**). In the case of the antennas that come with the [RUT950](#) modem from [Teltonika](#) ©, the Wi-Fi antenna has a gain of 5 dBi and the 4G-LTE antenna has a gain of 3 dBi (Teltonika Networks, 2021). These characteristics are not optimal for the Puigcerçós system, as the nearest phone coverage antenna is 4 km away, and the devices that have to connect via Wi-Fi are more than 100 m away.

For this reason, the Puigcerçós connectivity system uses different antennas to cover these distances. For the mobile phone signal, a panel antenna with [MiMo technology](#) has been used; this antenna integrates two panels with 25 dBi gains. These panels are characterised by

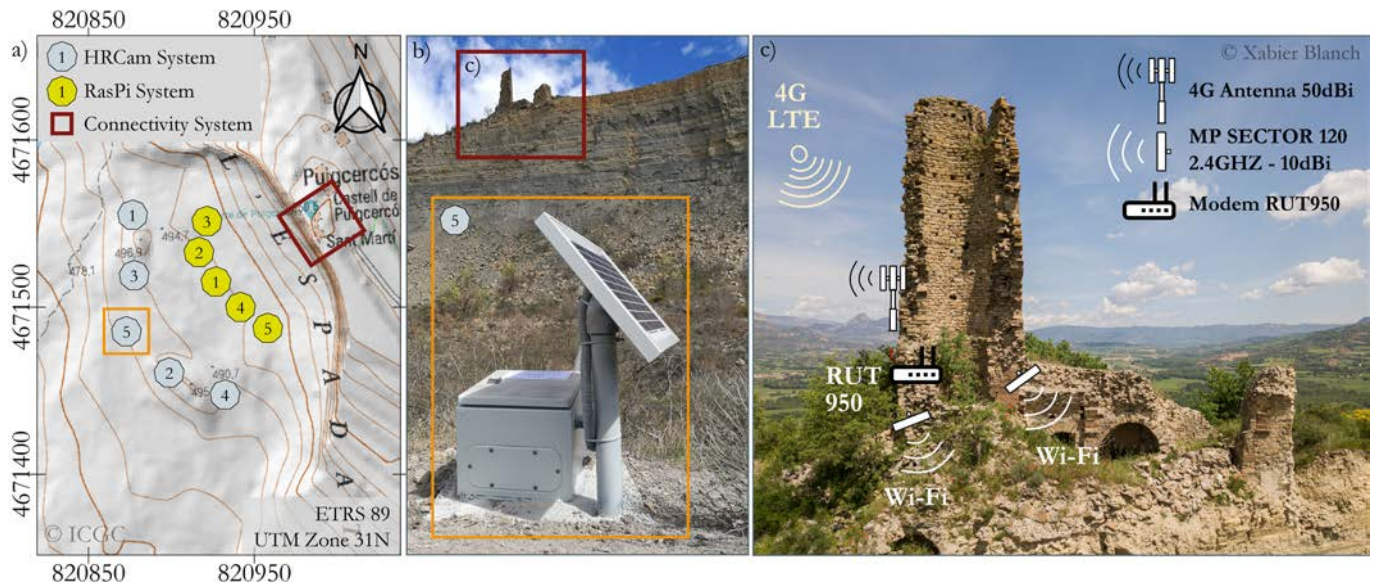


Figure II.15. a) Schematic map of the location of the Puigcercós connectivity system. [ICGC](#) base map, coordinates in UTM Zone 31N and ETRS89. b) Location of the connectivity system. c) Location of the 4G antenna, modem and Wi-Fi antennas in the ruined Puigcercós tower. **QR16** shows images of the Puigcercós connectivity device.

a radiation pattern that is concentrated in a single direction (**Figure II.15b**). Therefore, a very precise installation based on the azimuth of the transmitting antenna is needed to obtain a good signal strength. This antenna is installed on the outer face of the Puigcercós tower (**Figure II.14**). **QR 16** shows real images of the modem and the installed antennas.



The Wi-Fi antenna has also been modified. Due to the location of the modem and the photogrammetric systems, a sectorial antenna from [MP Antennas](#) © was used. The sectorial antennas allow radiation in a specific sector defined on the basis of the construction of the antenna. In the case of Puigcercós, two antennas were used with a radiation pattern of 120° in the horizontal plane and 60° in the vertical plane (MP Antenna, 2019) (**Figure II.15b**). This focalisation allows all the energy received by the antenna to be used to send the signal in a specific sector of space, thus preventing dispersal of the signal (and the energy) in areas where it is not necessary. These antennas are carefully positioned inside the ruined tower, with the precise azimuth and vertical angle in order to provide the maximum energy, enabling the devices to receive the signal with the maximum possible strength.

Finally, as mentioned in the general section, all photogrammetric systems have a TL-WN822N Wi-Fi access point installed. This access point, which uses omnidirectional

antennas, is responsible for receiving the wireless signal and routing it to the photogrammetric system via the USB cable. With all this connectivity system, it has been possible to obtain upload and download speeds in the photogrammetric systems of around 5 Mbps. In addition, in order to prevent interference with the available bandwidth, the upload configuration of the photogrammetric systems is spread over time, so that each photogrammetric system can use all the bandwidth to send images to the server.

3.4 HRCam - Photogrammetric System (Puigcercós)

3.4.1 Design and location

Due to the results obtained with the low-resolution photogrammetric system (RasPi), and analysing the possibilities of scaling up the system with higher quality components, a high-resolution photogrammetric system has been designed in this research. This system, called HRCam (from High Resolution Cameras), consists of five commercial cameras with their corresponding control units, batteries, and lenses. The system design is based on that designed for the low-cost system, but scaled up. However, this upgrade of components requires a total change in the electronic design and scripting of the control unit because the low-cost system uses Raspberry embedded systems, but the commercial camera systems do not (**Figure II.16**).

The initial system had 3 commercial cameras. However, during the system testing stage it was possible to expand the system from 3 to 5 cameras. Over the course of the research, the system has been modified and improved. The evolution of the system can be divided into 4 clear stages (**Figure II.17**).

Stage 1, where the 3 initial photogrammetric systems were designed, ensembled and tested in the faculty under controlled environmental conditions. After observing the good results of these devices in the faculty, it was decided to extend them to 5 cameras, and the systems were installed in the Puigcercós study area (**Stage 2**). In this same development stage, after the first real experiences in the study area, it was decided to modify the connectivity system by installing external antennas (the metal boxes greatly penalised connectivity in open spaces, as mentioned above) and external aspects such as the installation of sunshades over the scope glass to prevent it from getting too dirty.



Figure II.16. Rendering of the HRCam system. Includes the basic elements such as the camera, lense, solar panel, solar charge regulator, AGM battery, relays, DC-DC converters and the control unit.

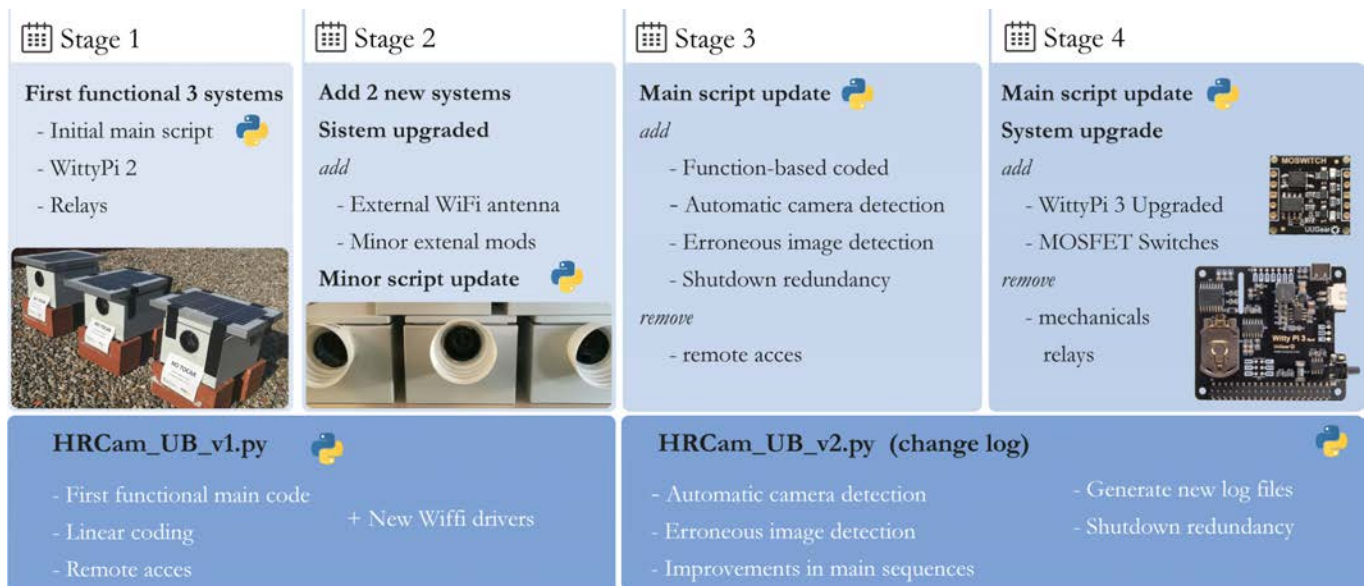


Figure II.17. Main stages of the development of the HRCam photogrammetric system. **Stage 1)** First 3 systems. **Stage 2)** Installation of the lens hood to prevent soiling of glass. **Stage 3)** New script HRCam_UB_v2 with advanced functions **Stage 4)** Harward upgraded. Upper image: MOSFET Switches. Lower image: WittyPi 3 (Both from UUGear). (Codes available in the repository: **Appendix A - HRCam System scripts**)

The main objective of **Stage 3** was to improve the programming of the device from the initial code HRCam_UB_v1 to HRCam_UB_v2 (**Figure II.17**). In Stage 3, this script was considerably improved, making the whole system much more robust and less susceptible to bugs or crash. Finally, **Stage 4** consisted of a new improvement of the components. Due to the different failures that were observed over time, it was decided to change both the relays and the WittyPi board for more robust solutions, as described later. The codes and scripts that support the HRCam system are published in **Appendix A - HRCam System scripts**.

For the installation at the Puigcercós location (**Figure II.18**), concrete bases had to be built ad hoc in the study area (an area of difficult access, with no electricity or water). The purpose of these bases is to provide a stable, fixed, and rigid area where the waterproof metal boxes containing all the systems can be fixed (**Figure II.19**). In addition, the tubular structure that supports the solar panel emerges from the interior of this concrete base. After studying the possible locations, it was decided to install the 5 photogrammetric systems in the elevated areas of the landslide deposit (**Figure II.18**). These elevated areas caused by the rotational component of the landslide allow a better perspective of the cliff to be obtained as well as avoiding vegetation obstruction.

The average distance between the camera modules is 30 m and the distance to the main rock face of the cliff is around 100 m. The theoretical depth error for this camera setup, assuming a stereo-classic case and error-free camera parameter estimations, amounts to 2.3 cm (Eltner et al., 2016). However, higher accuracies can be expected because five instead of two cameras capture the same area of interest with slightly convergent perspectives.

3.4.2 Main components

The initial 3 systems use a full-frame (35.9×24 mm) mirrorless Sony Alpha 7R III © with a resolution of 42.4 MPx (pixel pitch of $4.51 \mu\text{m}$). These cameras are equipped with a 35 mm f/2.8 lens. The other two systems use a DSLR camera Canon 77D © with a cropped sensor APS-C (22.3×14.9 mm) and with a resolution of 24.2 MPx (pixel pitch of $3.72 \mu\text{m}$). The Canon cameras are equipped with a pancake 24 mm f/2.8 lens. The use of a 24 mm lens on an APS-C cropped sensor generates the same field of view as using a 35 mm full-frame lens. Sony and Canon modules are alternatively positioned in the study area (**Figure II.18**).

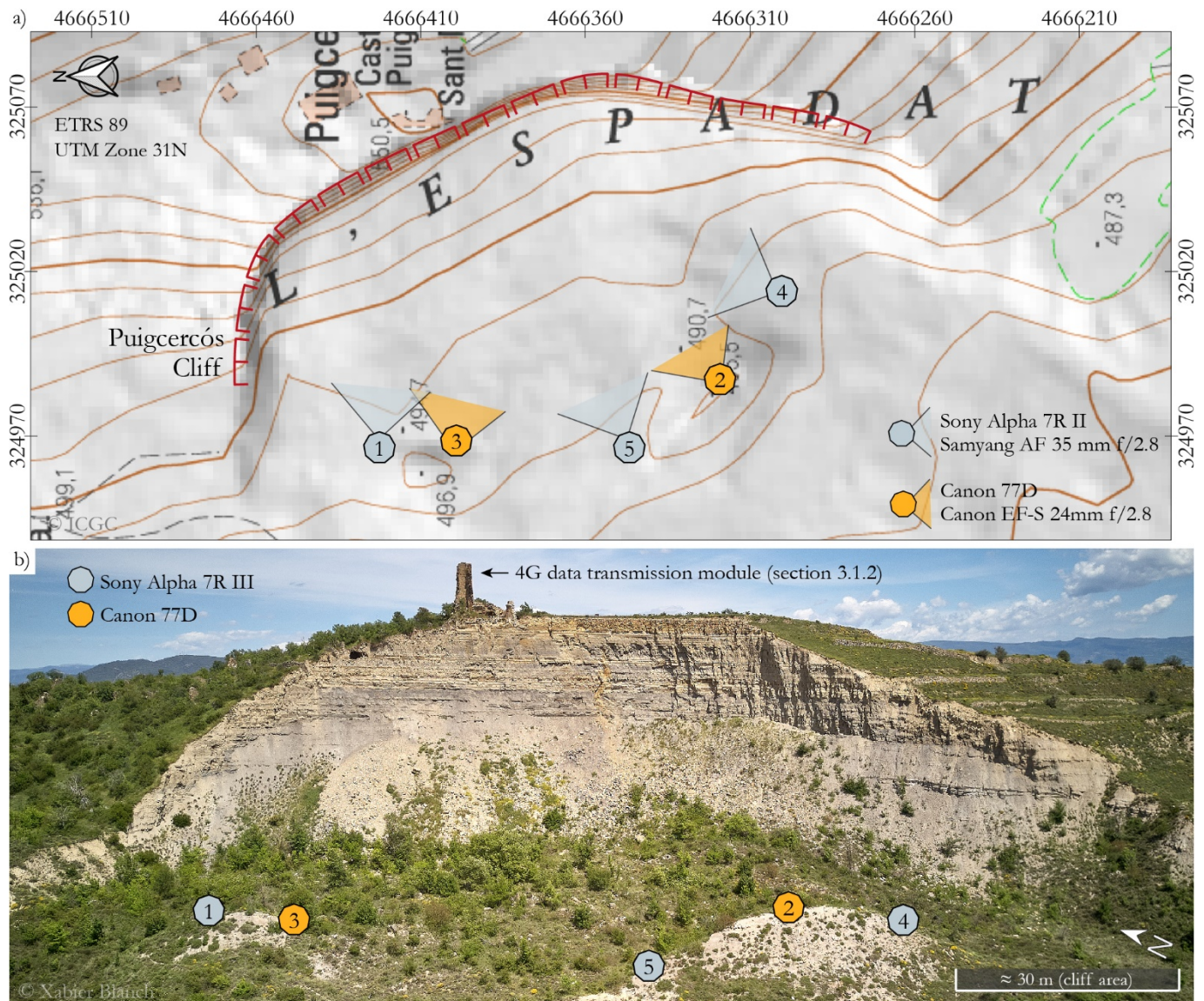


Figure II.18. a) Map with the locations of the HRCam cameras in Puigercós. Orange markers show the localization of the Canon cameras and grey markers represent the Sony cameras location. [ICGC](#) base map, no north oriented. **b)** Frontal image of the Puigercós cliff with the locations of the HRCam systems.

The microcomputer used for the unit control is a Raspberry Pi 3 Model B+ (Raspberry Pi Foundation, 2016). It is in charge of scheduling data acquisition, capturing the images, transmitting the data, and managing the battery of the devices. A commercial Witty Pi 2 board from UUGear is used as a real-time clock and power management system for the Raspberry Pi 3, and to manage voltage differences and schedule the system. Finally, a solar panel (20W) and a battery make each module autonomous in terms of power (**Figure II.19**).



Figure II.19. Photogrammetric system mounted at Puigcercós. **a)** Internal view of the camera module composed of a camera and the auxiliary control system. **b,c)** Exterior views of a module: **b)** Installation works and **c)** final integration with the environment.

As the HRCam system is located in the Puigcercós study area, the external connectivity system is the same as the one explained in the previous section for the RasPi systems (see **Section 3.3.3**).

The electrical installation can be seen in more detail in **Figure II.11a**. However, as mentioned above in stage 4, it was decided to replace the mechanical relays (electromagnets) with a static relay SSR (solid state relay). The mechanical relays have caused problems in the different installations, due either to the quality of the devices or to climatic incidents. For this reason, in stage 4 they have been replaced by [MOSWITCH-SPDT](#) relays of the UUGear brand. These new relays no longer depend on a mechanical component that is activated by the passage of current (electromagnet) that activates the switch, as in mechanical relays.

The MOSWITCH-SPDT relay is activated by the state of activation of the MOSFET transistors (metal-oxide-semiconductor field-effect transistor) incorporated in the device. This means that from a certain external current, the transistor is activated by allowing the current to pass through.

In addition, stage 4 was also used to change the UUGear WittyPi control board, upgrading it from version 2 to version 3. The changes that were incorporated in this update and more

information about the new shield can be seen in this [link](#) (UUGear website). These modifications simply produce a change in the electrical performance of the system while at the same time requiring an important modification of the device scripting.

3.5 DSLR - Photogrammetric System (Granada-Alhambra)

3.5.1 Design and location

The last system designed in the context of the thesis is the system installed in Granada, called the DSLR system due to the use of DSLR (Digital Single Lens Reflex) cameras. Thanks to the encouraging results obtained with the HRCam photogrammetric system, the Patronato de la Alhambra y el Generalife, together with the University of Granada, requested us to design a monitoring system for the escarpment of the Tajo de San Pedro located at the bottom of the Alhambra historical complex.

The initial system design is based on the experimental HRCam system. However, due to the installation of the systems in an urban area, it has not been possible to fully copy the designs. Thus, although the renderings in **Figure II.16** serve as the initial design idea, the final installed systems have undergone modifications, especially in the power supply section.

Another difference compared to the HRCam system is that the location of the cameras could not be freely chosen. One of the most difficult factors in the design and implementation of this system was to find 5 accessible locations with good visibility of the escarpment and obtaining the respective authorisations.

These locations, which are distributed throughout the Albaicín quarter of Granada (**Figure II.20**), entailed the adaptation of the design of each individual system for every space, both in the system development and installation phases.

For example, in the design phase the focal lengths of the lenses had to be adapted for each location, since it was our intention to install fixed lenses with the aim of maximising the optical quality of the images. It was necessary to conduct a prior analysis for each location in order to determine the focal length needed to obtain the desired field of view (**Figure II.21**).

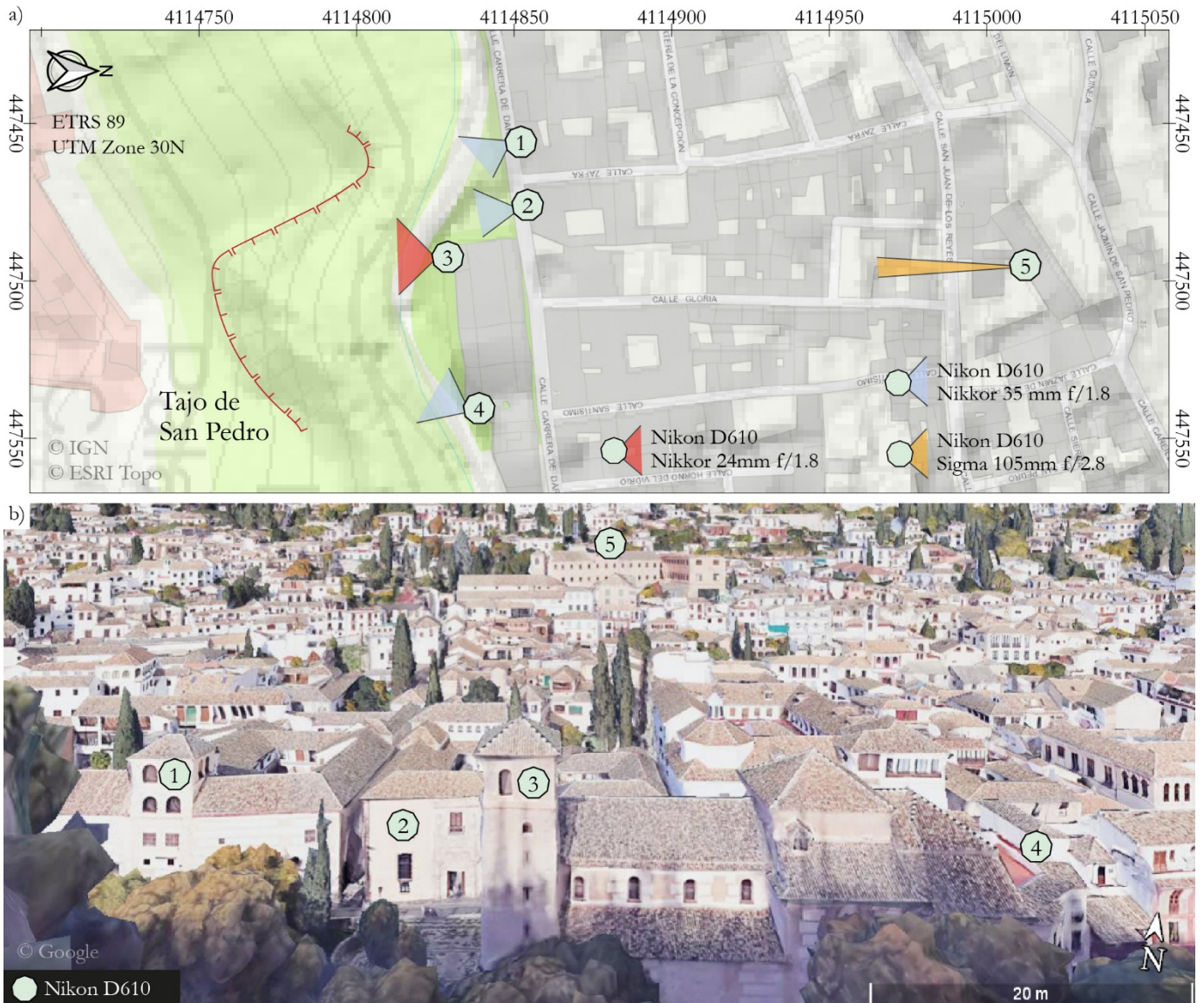


Figure II.20. a) Map with the locations of the DSLR cameras in Granada-Alhambra. All systems have the same camera model, but different lenses. [IGN](#) and [ESRI Topo](#) base map. **b)** 3D simulation of the view from the Tajo de San Pedro with the DSLR systems location. [Google Earth](#) model.

Part of the complexity of working in an urban environment can be appreciated with the development of the connectivity system explained in next **Section 3.5.3**. It is much more complex than the one developed in the Puigcerçós study area. Working on windows, arches, balconies and terraces made it difficult to install the systems because no ad hoc work can be carried out to adapt them (**Figure II.22**). The main objective of the project was to have the least possible impact on the buildings (most of them historic) and to try to achieve the best possible integration with the landscape.

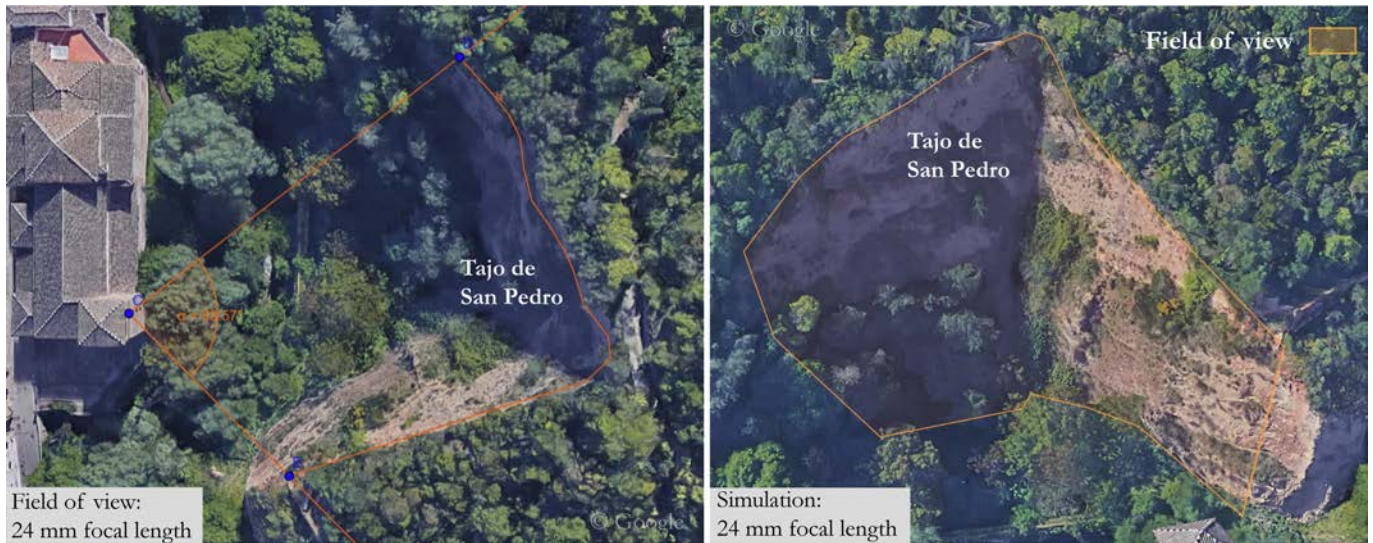


Figure II.21. Simulation carried out to obtain the best focal length for each DSLR system. In this case, the figure shows the simulation performed for the DSLR3 located in the bell tower of the church of San Pedro (The location closest to the escarpment). [Google Earth](#) model.

The different locations where the cameras have been installed are shown in **Figure II.20**. Two systems are installed in the church of Tajo de San Pedro. This church is the closest building to the Tajo de San Pedro (70 m) and provides a direct view of the escarpment. One system has been installed under the arch of the bell tower (**Figure II.22a**) and another on the terrace of the church.

A further system has been installed in the bell tower of the Convento de Zafra (**Figure II.22b**). Although this location does not provide a complete view of the escarpment, it makes the geometry of the network more robust.

Another system has been installed on a balcony of the Museo Arqueológico y Etnológico de Granada (**Figure II.22c**). Like the convent, this building is located in the second line of houses in front the cliff (100 m) and does not provide a complete view of it. However, its position in front of the Tajo gives good quality images in photogrammetric terms.

Finally, the last camera is located in the Escuela Hogar Madre Teresa, which is located at a great distance from the escarpment (260 m). However, as it is a building that juts out from the skyline of Granada, it provides a valuable view of the Tajo de San Pedro.



Figure II.22. External images of 3 different DSLR systems. **a)** System in the bell tower of the Church of San Pedro (DSLR3). **b)** DSLR2 system installed on the balcony of the Archaeological Museum. **c)** Camera installed in the Zafra Convent (DSLR1).

In the installation stage, we found that some systems could not use solar panels because it is forbidden to install them visibly on the outside of the building's façade. For this reason, various systems are connected directly to the conventional electricity supply, instead of being powered according to the classic systems explained in the previous chapters. This modification implied a change in the design of the systems during the installation process.

As with the previous systems, during this research the DSLR system has been improved. When significant advances were achieved in the experimental HRCam system in Puigcerçós, these were transferred to the DSLR system. For this reason, **Figure II.23** shows similar stages to those defined previously in HRCam, where the hardware and the software were upgraded. The codes and scripts that operate the DSLR system are published in **Appendix A - DSLR System Scripts**.

3.5.2 Main components

The five modules installed in the DSLR system use a Nikon D610 © full-frame (35.9×24 mm) camera with a resolution of 24.3 MPx ($5.95 \mu\text{m}$ pixel pitch). Due to the simulations carried out (**Figure II.21**), it was decided to equip the cameras with the following lenses: i) the closest camera located in the bell tower of the church of San Pedro uses a Nikkor © lens with a focal length of 24 mm and an aperture of $f/1.8$.

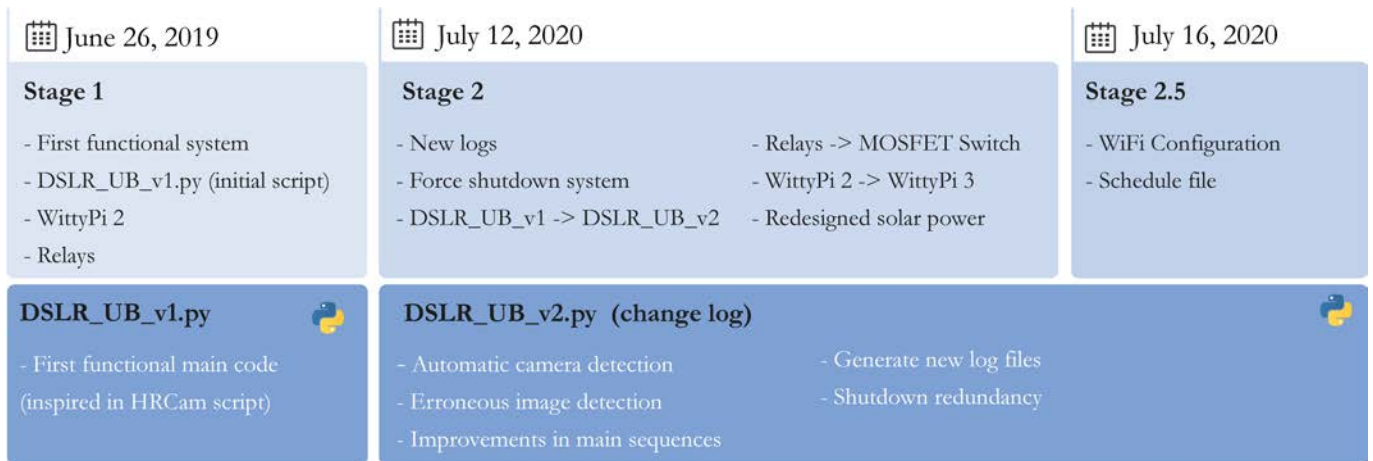


Figure II.23. Main stages of the development of the DSLR photogrammetric system and its scripts (codes available in the repository: **Appendix A - DSLR System Scripts**).

The development is similar to that of the HRCam system.

ii) the cameras located in the museum, the convent and the church terrace use a Nikkor 35mm f/1.8 lens, and iii) the camera located furthest away, in the school, uses a SIGMA © 105mm f/2.8 fixed lens.

Analogous to the HRCam system, the microcomputer used to control the unit is a Raspberry Pi 3 Model B+ (Raspberry Pi Foundation, 2016) from the Raspberry Pi Foundation. In addition, a commercial Witty Pi 2 board from UUGear is used as a real-time clock and power management system, which in later phases was upgraded to the Witty Pi 3 from UUGear.

The electrical system is divided into two parts; the solar-powered systems use 7,000 mAh batteries and solar panels, as previously described, while the plug-in systems use AC-DC current transformers to power both the camera and the electronic devices. In this case, scheduling is managed by means of electrical plug-in timers. All the systems are embedded in waterproof metal enclosures and the connectivity of each device has been solved according to its needs, as explained in the following section.

3.5.3 Alhambra connectivity system

The Granada connectivity system uses the antennas integrated in the modem. This solution means that the whole connectivity system is contained in a small device. Given the technical characteristics of the systems and the complex locations in the middle of the city, the



Figure II.24. Location of the 3 connectivity systems installed in Granada-Alhambra. Numbers represent the photogrammetric system. [IGN](#) and [ESRI Topo](#) base map and [Google Maps](#) images. **a)** Global location map. **b)** System located in the Escuela-Hogar. **c)** Systems installed in the Church of San Pedro, Zafra Convent and Archaeological Museum. **QR17** (next page) show images of the devices installed in Granada.

connectivity of the Granada-Alhambra systems could not be solved with a single centralised system, as is the case in Puigcerçós. Therefore, the Granada-Alhambra connectivity system has 3 modems (**Figure II.24**); 1 Teltonika [RUT950](#) modem and 2 Teltonika [RUT240](#) modems distributed according to connectivity needs.

The three modems use the system's own antennas to obtain the signal from the city of Granada 4G-LTE network (3 dBi Omnidirectional) and transform it into a hidden Wi-Fi network that connects the devices. In addition to this Wi-Fi network, and because many of the systems are located in buildings where it is possible to use cable, the systems closest to the modems are connected via ethernet cable.

The use of the original antennas is not the most efficient for large open spaces, because their radiation pattern is extremely wide (360°) and consequently has a short-range distance. However, being immersed in the middle of the city with good signal coverage, and having the devices relatively close (20 m), the original antennas fulfil their function.

The 3 modems contain SIM cards associated with a 20 GB monthly mobile phone contract. They are installed in sealed plastic boxes of which only the antennas are outside the boxes. As in Puigcerçós, the antennas of the modems are oriented in the direction of the mobile phone antennas of the city.

The modem responsible for providing connectivity to photogrammetric systems 1, 2 and 3 is the most powerful model from the Teltonika company (Teltonika's RUT950). This modem has 4 antennas, 2 of them in the mobile frequency and the other 2 in the 2.4 GHz Wi-Fi frequency. This system is placed under an arch of the bell tower at the church of San Pedro (**Figure II.24**) and its location allows both good reception of 4G signal and good Wi-Fi signal radiation towards systems 1 and 2. Because it is located inside the tower, the system 3 is connected to the modem via an Ethernet connection.

Systems 4 and 5 are too isolated from the location of the first modem. For this reason, it was decided to install modems with lower characteristics (RUT240) in each device. Thus, each device has a modem integrated in the photogrammetric system. As the modem is installed next to the unit control, the connection is made via an Ethernet cable (**Figure II.24**).

This difference can be clearly seen in **QR17**, which shows, on the one hand, an image of the main connectivity system providing Ethernet connectivity to system 1 and Wi-Fi signal to systems 2 and 3 (**Figure II.24**), and, on the other hand, an image of the isolated system 4 where the small RUT240 modem can be identified right next to the photogrammetric system.



QR 17

4.1 Introduction to the research

Once the different photogrammetric systems have been presented, **Chapter 4** focuses on explaining the methodology of the PCStacking algorithm. This chapter contains the essential methodological parts of **Publication I** presented in **Section 2.5** and that can be found in **Appendix B**.

The methodology explained below has been developed in order to be able to work with the images obtained with the **RasPi system**. As we have already mentioned, this system makes it possible to obtain models from low-cost and low-resolution cameras. One consequence of the use of this system is the obtention of geometric errors, as detailed in the following section.

The following section presents the research conducted in this specific field, the development of the methodology and the various tests carried out to test the algorithm. As will be seen below, the algorithm uses the 3D model stacking strategy to obtain an average value. All these concepts are introduced and developed below. In order to facilitate the reading of the dissertation, the author has decided to retain only those elements of the publication that are specific to the understanding of the methodology developed.

4.1.1 Point Cloud Errors (Photogrammetry vs. LiDAR 3D)

Since the SfM-MVS technique is based on iterations of various processes during the bundle adjustment, the obtained point cloud (PC) is a possible solution among many possible results. The quality of the generated PC depends both on the number of homologous points identified and on the quality of the bundle adjustment (Parente et al., 2019). For this reason, any repeatability analysis carried out using different images of the same site implies the generation of photogrammetric models with significantly different geometries due to the different random solutions in both camera position estimation and internal calibration parameters. These geometric differences, which can be called **geometric errors**, will be more or less significant depending on the quality of the homologous points and the bundle adjustment, which depends on the quality of the photographs.

This type of error contrasts strongly with the errors that are obtained in the LiDAR PCs. LiDAR, whose operation is extensively described in Petrie and Toth (2008) and Jaboyedoff et al. (2012), generates geometrically consistent models; however, due to its operation, the PCs obtained have a random Gaussian noise distributed along all points (Kromer et al., 2015). This dispersion, called **random error**, was easily solved and was the theoretical basis of the development of many algorithms for the processing of LiDAR data (Abellán et al., 2009; Lague et al., 2013).

4.1.2 Techniques for Image Stacking (2D)

Using 2D stacking algorithms to enhance digital imagery is a common strategy in several disciplines such as astronomy, computer-vision, and microscopy; recent examples of astronomical image processing include successful attempts to increase the signal-to-noise ratio (SNR) (Bin et al., 2018) and the combination of different wavelengths to de-noise imagery of celestial bodies (Kurczynski & Gawiser, 2010). Image stacking strategies using photographs taken at different f-stops or with the focus point on different parts of the subject (aka “f-stop stacking” or “focus stacking”, respectively) have also been used to extend the depth of field of the composite images in order to overcome blurriness (Zhang et al., 2013). In addition, various 2D stacking strategies have been tested to derive high quality imagery from a series of 2D photographs, leading to considerable improvements in photogrammetric models, e.g., when using super-resolution images (Lato et al., 2012). However, stacking 2D images under specific conditions might not always entail noteworthy increases in SNR, as reported by Santise et al. (2017).

Similarly, diverse image stacking techniques are commonly employed when using satellite Interferometric Synthetic-Aperture Radar (InSAR) techniques to monitor ground deformation, as recently reported by Selvakumaran et al. (2018). Indeed, atmospheric noise is filtered when using these strategies, leading to a higher SNR and a more accurate DinSAR time series, as pointed out by Manconi (2018). In the same way, 2D stacking plays an important role in other fields such as Seismic Data Processing, improving the overall SNR and overall quality of seismic data (G. Liu et al., 2009). Although several publications describing stacking techniques on 2D matrices were found in the literature, no other publications dealing with the improvement of 3D objects (e.g., PCs) were identified during our literature review.

4.1.3 Aim and Objectives

The aim of this section is to present and validate a workflow to enhance the monitoring capabilities of time-lapse camera systems by stacking individual 3D point clouds generated from Multi View Stereo photogrammetry (SfM-MVS).

The proposed workflow allows the accuracy of the individual PC to be improved by getting the most out of the iterative solutions obtained during the bundle adjustment process, a key step in the SfM-MVS photogrammetry workflow. More specifically, bundle adjustment resolves an indeterminate system with a larger number of unknowns than equations (intrinsic and extrinsic camera parameters vs. number of cameras/perspectives, respectively), thus, multiple solutions in the form of PCs satisfying these equations are possible. Since the average value in a local coordinate system of the “range” coordinate converges for a large enough size sample (i.e., total number of PCs), a gain in precision can be obtained by stacking and averaging this value on the individual PC, allowing the correction of individual geometric aberrations, as shown below.

The proposed workflow was tested using a synthetic point cloud, created using mathematical functions that attempted to emulate the photogrammetric models, and data collected from a rock cliff located in Puigcerçós (Catalonia, NE Spain), using very low-cost photogrammetric systems specially developed for this experiment. This work demonstrates that the proposed workflow is especially well-suited for improving precision when a high temporal sampling procedure can be set up or when low-cost time-lapse camera systems are being used, or both.

4.2 Materials and Methods

4.2.1 PCStacking Workflow

The proposed workflow makes the most of the different solutions generated iteratively during the bundle adjustment and is based, on the one hand, on optimal data collection using time-lapse camera systems and, on the other hand, on an algorithm that generates an enhanced PC from a series of stacked PCs. The proposed method of data collection differs from classic photogrammetry in that, for each of the camera positions, multiple and successive images are captured, in synchrony with the other cameras.

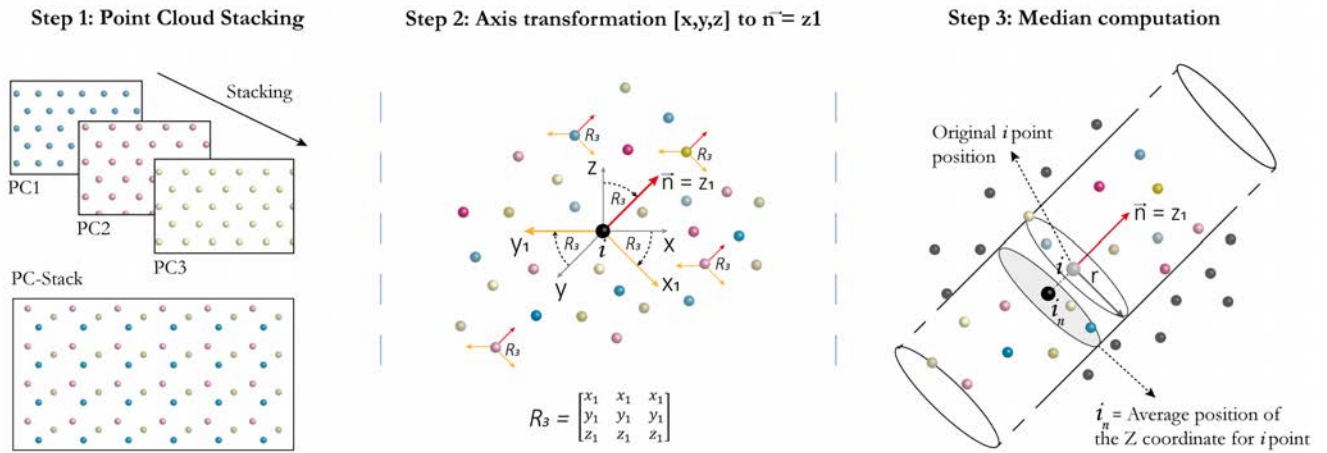


Figure II.25. The three steps developed by the Point Cloud Stacking algorithm. **Step 1:** All points are stored in the PC-Stack cloud. **Step 2:** Coordinates system change. **Step 3:** Point averaging on the normal axis.

This allows the generation of different approximate solutions (Point Clouds) that serve as input data in the PCStacking algorithm. Each individual PC is then stacked and processed in order to generate an enhanced 3D model as the output (**Figure II.25**).

The main steps of the algorithm are (**Figure II.25**): **Step 1**) point cloud stacking, **Step 2**) local axis transformation and **Step 3**) median computation along the normal vector. More specifically, all the individual PCs are stored in a single point cloud (“PC-Stack”) in the first step. Then, a Principal Component Analysis (PCA) is used to transform the global coordinate system to a local coordinate system, so that the third principal component on this orthogonal transformation (rotation and translation) would be defined as the local normal vector. Finally, the algorithm averages the third eigenvalue along the third eigenvector on each point of PC-Stack using the median operator. For practical purposes, this local vector can also be computed with a cylinder of radius r and infinite length in the local normal direction.

An extra-dense PC is obtained as a result, where all points have the averaged (median) coordinate for a local subset of points. The overall principle of the proposed algorithm is quite straightforward: point cloud precision can be enhanced by increasing the sample size in order to compensate for systematic errors in a large enough number of datasets, although this does not improve accuracy.

The main steps in the algorithm can be found in the pseudo-code below (The code developed in MATLAB can be found at **Appendix A – PCStacking algorithm**):

```

1   algorithm PCStacking is
2   Start
3       get the number of Point Clouds ( $m$ ) from a designated folder
4       load  $m$  Point Clouds into the workspace
5       merge all Point Clouds into a single matrix (PC-Stack)           [step 1]
6       input search radius value ( $r_1$ )
7       for each Point in PC-Stack
8           create a subset1 of PC-Stack inside  $r_1$ , with coordinates  $(x,y,z)$ 
9           apply axes transformation (PCA), being normal vector  $\rightarrow Z_1$  axes       [step 2]
10          compute median value of the subset1 along eigen vectors  $(X, Y, Z)$        [step 3]
11          end
12          output the mean coordinates of the stacked Point Cloud
13  End

```

4.2.2 Experimental Design (I): Synthetic Test

Synthetic Point Clouds Creation

A synthetic test space formed by PCs that emulate the errors observed in **Photogrammetric Point Clouds** (Phot-PC) was performed in order to assess the PCStacking algorithm. In the first instance, a regular perfect surface (without any geometric error) was created using Equation (1). This surface is considered the **Reference Point Cloud** (Ref-PC) (**Figure II.26**):

$$z_{\text{Ref-PC}} = 2e^{-x^2-y^6} \quad (1)$$

Then, two different errors are added into the synthetic function, modifying the position of their points in order to simulate the typical errors in photogrammetric data. The first error added is based on a function that keeps the X and Y coordinates but adds a deviation in Z (Equation (2)). This Z deviation is generated using sinusoidal functions because the differences in each point must be related to the previous one. The goal of this process is to

generate a geometric error with a solution of continuity avoiding random errors. The values $\{x, y, z\}$ in Equation (2) correspond to the coordinates of the points in the Ref-PC and the parameters $\{A, f, d_1, d_2\}$ are calculated randomly using predefined ranges. This means the synthetic test suite generates a different error (z_{sin}) in each iteration (**Figure II.26**):

$$z_{sin} = A * \sin((x \cdot f) + d_1) \cdot \sin((y \cdot f) + d_2) \quad (2)$$

The result of Equation (2) is added directly to the Z coordinate in Ref-PC, obtaining a PC with deformations along the Z axis, which can be considered as the **geometric error** inherent to the photogrammetric models. The second error added to the Ref-PC is a random Gaussian distribution error. This error, similar to the one inherent to LiDAR PCs, has little presence in photogrammetric models.

However, it is introduced in order to avoid totally regular surfaces. This error is entered into the three coordinates and is defined as x_{disp} , y_{disp} and z_{disp} . Finally, the **Synthetic Point Cloud** (Synt-PC) is obtained from the sum of the Ref-PC coordinates, the geometric deformation obtained by the sinusoidal function Equation (2) and the Gaussian scattering errors (Equations (3)–(5)):

$$x_{Synt-PC} = x_{Ref-PC} + x_{disp} \quad (3)$$

$$y_{Synt-PC} = y_{Ref-PC} + y_{disp} \quad (4)$$

$$z_{Synt-PC} = z_{Ref-PC} + z_{sin} + z_{disp} \quad (5)$$

The first row in **Figure II.26** shows the original Ref-PC created with Equation (1) without errors. The first column shows the random functions generated by the sinusoidal function Equation (2) and the second column shows the sum of this function with the Ref-PC. The third and fourth columns display cross-sections showing the geometric differences of the resulting PCs with respect to the Ref-PC. This Synt-PC generator code can be found in **Appendix A – PCStacking algorithm** (NP_Sintetic_funciont.m).

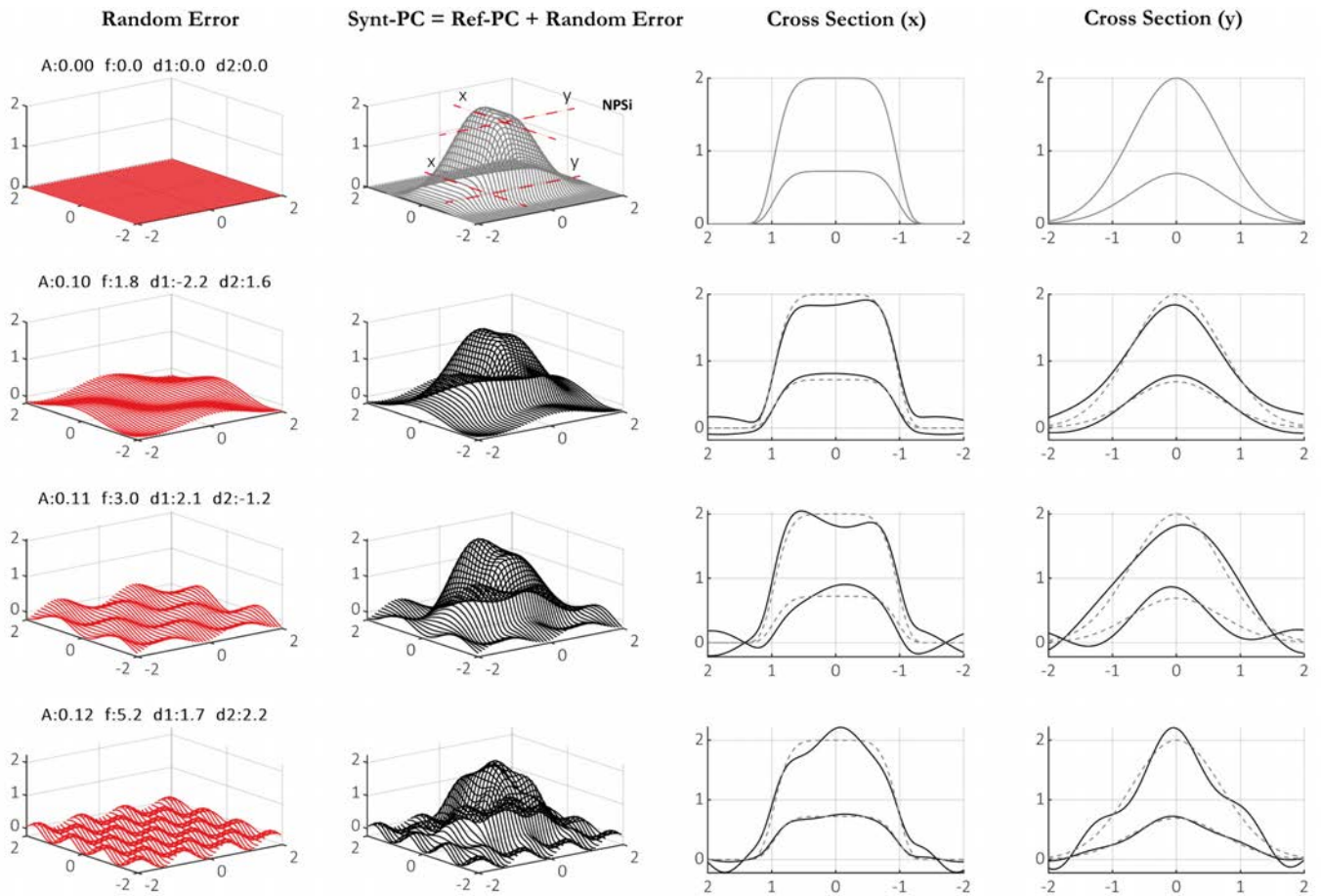


Figure II.26. Synthetic Point Clouds (Synt-PC). **First row:** Function without error, representing the reference PC (Ref-PC) (Equation (1)). **Rows (2 to 4):** Functions created with errors based on random parameters (Equation (2)). **Columns (left to right):** Error function; sum of Ref-PC + Error function, X cross-section, Y cross-section. Dotted lines correspond to the Ref-PC and continuous lines to the Synt-PC.

As the PCStacking algorithm needs different simultaneous photogrammetric models to obtain an **Enhanced Point Cloud** (Enh-PC), 20 random functions were generated, and 20 different Gaussian scattering errors were calculated in order to obtain 20 Synt-PC. This allowed analysis of the performance of the PCStacking algorithm, as well as the sensitivity of the method. These 20 Synt-PCs emulate the different simultaneous photogrammetric models that would later be generated using real photographs. **Figure II.27** shows the X and Y cross-sections of five of these Synt-PCs as well as a comparison between two of them using the M3C2 algorithm (Lague et al., 2013) in CloudCompare software (CloudCompare, 2021). This comparison was carried out to verify whether or not the differences between different Synt-PCs resembled the differences between two real photogrammetric models (**Section 2.3.3**).

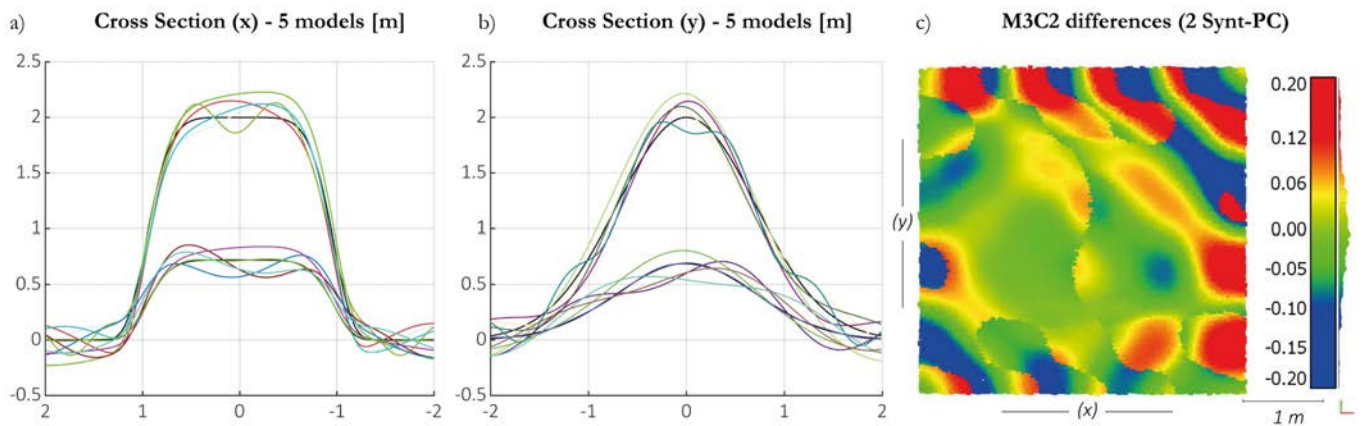


Figure II.27. **a)** X cross-sections of 5 Synt-PC (each colour corresponds to a different Synt-PC), the black line corresponds to the sections of the Ref-PC. **b)** Y cross-sections of 5 Synt-PC (each colour corresponds to a different Synt-PC), the black line corresponds to the sections of the Ref-PC. **c)** Distribution of differences between two Synt-PC computed by M3C2.

PCStacking Application

After obtaining the 20 Synt-PCs, the following workflow was designed to test the PCStacking method. This involved applying the PCStacking algorithm to the 20 Synt-PCs to obtain the Enh-PC_n (n being the number of Synt-PCs considered). The resulting Enh-PC_n was then compared with the Ref-PC. The Synt-PCs were introduced into the algorithm in an incremental way, from two to 20 Synt-PCs. Then, each Enh-PC_n was compared with the Ref-PC in order to assess the performance of the designed method, as well as its sensitivity to the number of Synt-PCs introduced.

PCStacking synthetic test summary:

- * Design a Reference PC (Ref-PC)
- * Create 20 Synthetic PCs (Synt-PC)
- * Application of the PCStacking algorithm: (n = 2 : 20)
- * Input: n Synthetic PCs (Synt-PC)
- * Output: Enhanced PC (Enh-PC_n)
- * Comparison between the Enhanced PCs (Enh-PC_n) and the Reference PC (Ref-PC)
- * Analysis of computed differences

The Enh-PC_n vs. Ref-PC comparison was carried out using the Point to Mesh algorithm to avoid the influence of statistical averaging of the results using other comparison methods such as the M3C2 algorithm (Lague et al., 2013). In this case, the conversion of the Ref-PC into a mesh does not introduce errors because the Ref-PC is a regular surface. For this reason, the distances obtained in the comparison correspond to the real distance between each point of the Enh-PC_n and the synthetic surface computed from the Ref-PC. The performance of the developed method was evaluated through the statistical values of the differences between Enh-PC_n and Ref-PC, assuming that an improvement means achieving an Enh-PC_n more and more similar to the Ref-PC. Thus, the differences obtained in the comparison must tend to zero.

Redundancy Test

Due to the use of random parameters to produce the Synt-PCs, the workflow explained in the previous section was repeated 20 times. Therefore, 400 (20 × 20) different Synt-PCs were calculated to test the PCStacking method, covering a large number of possibilities and providing more consistent results. In each iteration, the standard deviation corresponding to each Enh-PC_n vs. Ref-PC comparison was calculated. As this process was repeated 20 times in an iterative way, 20 standard deviation values were obtained for each Enh-PC_n vs. Ref-PC comparison.

This procedure allowed us to evaluate whether the described method works independently of the random parameters introduced to produce the Synt-PC. This redundancy test was carried out because in some tests the random values of the Synt-PC were too low, which resulted in a Synt-PCs with little error that generated a much improved Enh-PCs. With the generation of 400 Synt-PCs and the computation of the standard deviation of the 400 comparisons (Ref-PC vs. Enh-PC1, 20x20 times) the median values showed the real range of the PCStacking algorithm.

4.2.3 Experimental Design (II): 3D Reconstruction of a Rocky Cliff

To observe the performance of the PCStacking algorithm using real data, a test was performed with images obtained by using a photogrammetric system of very low-cost fixed time-lapse cameras on a rock cliff situated in Puigcercós (Catalonia, NE Spain).

Pilot Study Area

The images used for the test were captured from the Puigcercós cliff (Catalonia, NE Spain). This rock face (123 m long and 27 m high) is the result of a large rototranslational landslide (Hungre et al., 2014) that occurred at the end of the 19th century (Corominas & Alonso, 1984; Vidal, 1881) and is extensively described in **Section 1.4.1** of this thesis.

Field Setup and Data Acquisition

The acquisition of data was carried out using the RasPi low-cost photogrammetric system developed ad-hoc for this study. The system is fully described in **Section 3.3**. The distribution of five photogrammetric modules in five different positions enables the acquisition of daily photogrammetric models of the cliff, inferring a very high temporal frequency of monitoring of rockfalls and deformations. This system is thus ideal as a case study to monitor the performance of the PCStacking method and to evaluate its ability to generate higher quality photogrammetric models.

Since there is no ideal surface of the terrain that corresponds to the Ref-PC in the synthetic test, the algorithm was tested by comparing the two models acquired on consecutive days (February 25 and 26, 2019) from an area without any activity. Due to the non-activity and therefore the non-existence of movement, we assume that the difference between the models must be zero.

Point Cloud Reconstruction

The system developed at Puigcercós was configured to capture 15 images in the same photo burst synchronized in the five installed cameras. From these 15 photographs captured by each camera, 15 different photogrammetric models of the same moment in time were reconstructed using Agisoft Metashape (2019 Agisoft). To improve the software calculation process, different tools such as zone masking, cutting out working areas and optimizing camera positions were used. The results were always obtained at the highest quality, both in the calculation of homologous points and the dense point cloud.

Due to the large size of the rockface and the requirement to work in an area without deformation, we carried out the test in a specific zone. This truncated rectangle has a size of 12.5 m × 10 m and an area of approximately 100 m². The computational cost to perform the

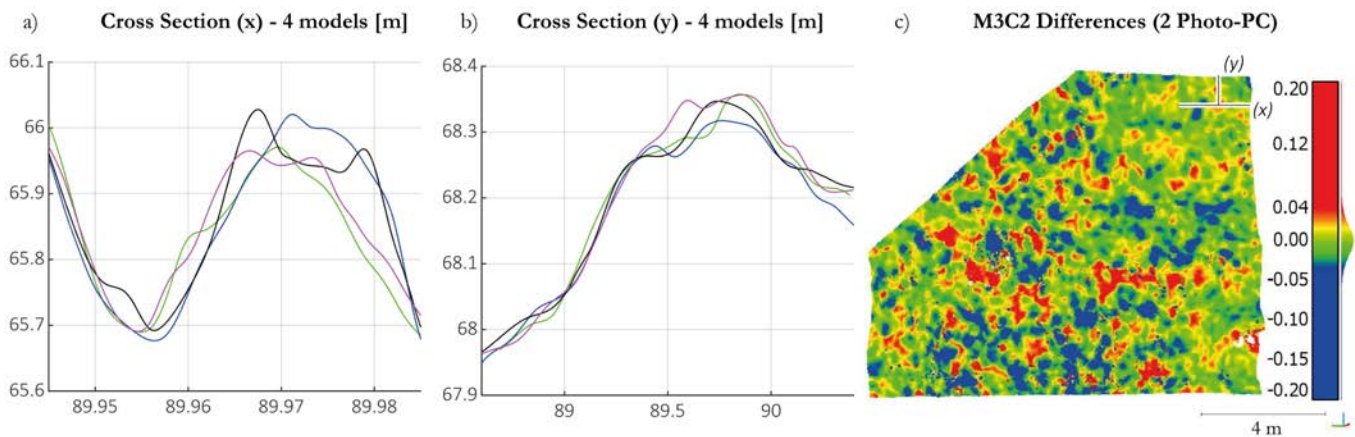


Figure II.28. a) X cross-sections of four Photo-PCs generated using five images (each colour corresponds to a different Photo-PC). **b)** Y cross-sections of four Photo-PCs generated using five images (each colour corresponds to a different Photo-PC). **c)** Distribution of differences of two Photo-PCs computed by M3C2. (x) and (y) shows the cross section represented in **a)** and **b)**.

entire process for a given radius in this small area is around 60 minutes to generate the 3D models with Agisoft Metashape and 70 minutes to apply the PCStacking algorithm. These times have been achieved with medium-high performance commercial equipment (Intel © Core (TM) i9—7900X up to 4.30 GHz, 64GB RAM and NVIDIA © GeForce GTX 1080 Ti). The raw point clouds obtained by the Metashape software are composed of approximately 150,000 points.

As the test was carried out on two consecutive days, a total of 30 **Photogrammetric Point Clouds** (Photo-PC) were generated. The calculated models were aligned and scaled with a reference LiDAR to produce metric values for comparison. **Figure II.28a** shows the X and Y cross-sections of four Photo-PCs. It demonstrates the correct alignment of the models but shows clearly different surfaces due to the poor quality of the acquisition system.

The differences between two PCs, computed using the M3C2 algorithm (Lague et al., 2013) (**Figure II.28b**), are randomly distributed due to the different geometries generated in the photogrammetric reconstruction process. Analogous to the synthetic test, full statistical analyses were performed with the real data to determine the extent of the improvement provided by the method. All the results obtained are shown in **Section III**.

5.1 Introduction of the research

The research presented in this chapter consists of the second workflow developed in this research. This workflow is a new automatic pipeline to obtain improved 3D models using fixed time-lapse cameras. **Chapter 5** contains the essential methodological parts of the **Publication II** presented in **Section 2.5.2** and can be found in **Appendix C**.

This study proposes a new method that allows the calculation of photogrammetric models with high spatial resolution, high temporal frequency and high accuracy. The MEMI algorithm presented in the following sections corresponds to the algorithm developed for the improvement of photogrammetric models obtained with commercial cameras (HRCam and DSLR systems). It is an essential part of the workflow used for rockfall detection at Puigcercós and Granada presented in **Section IV** of this dissertation.

As in the previous chapter, the following sections present the specific methodology of the method proposed in **Publication II**. The introductory and general backgrounds have been removed to facilitate the readability of the text and to avoid repetition of concepts.

5.2 Materials and Methods

5.2.1 Data Acquisition

Images for the image-based reconstruction of high-resolution point clouds were taken by the HRCam photogrammetric system developed ad hoc for the Puigcercós pilot study area. The system is fully described in **Section 3.2**.

Images were obtained at a sub-daily frequency for 4D analysis of the rockfalls. The camera modules captured four images in a burst mode three times per day. Thus, three times four images were taken from five camera modules, resulting in 60 images of the Puigcercós cliff every 24 hours. The images were taken at 9 a.m., 1 p.m. and 6 p.m., although the most-used images were taken at 6 p.m. to avoid shadows on the escarpment. All images are obtained in JPG format using the highest quality. The focus point is set manually, and the exposure time

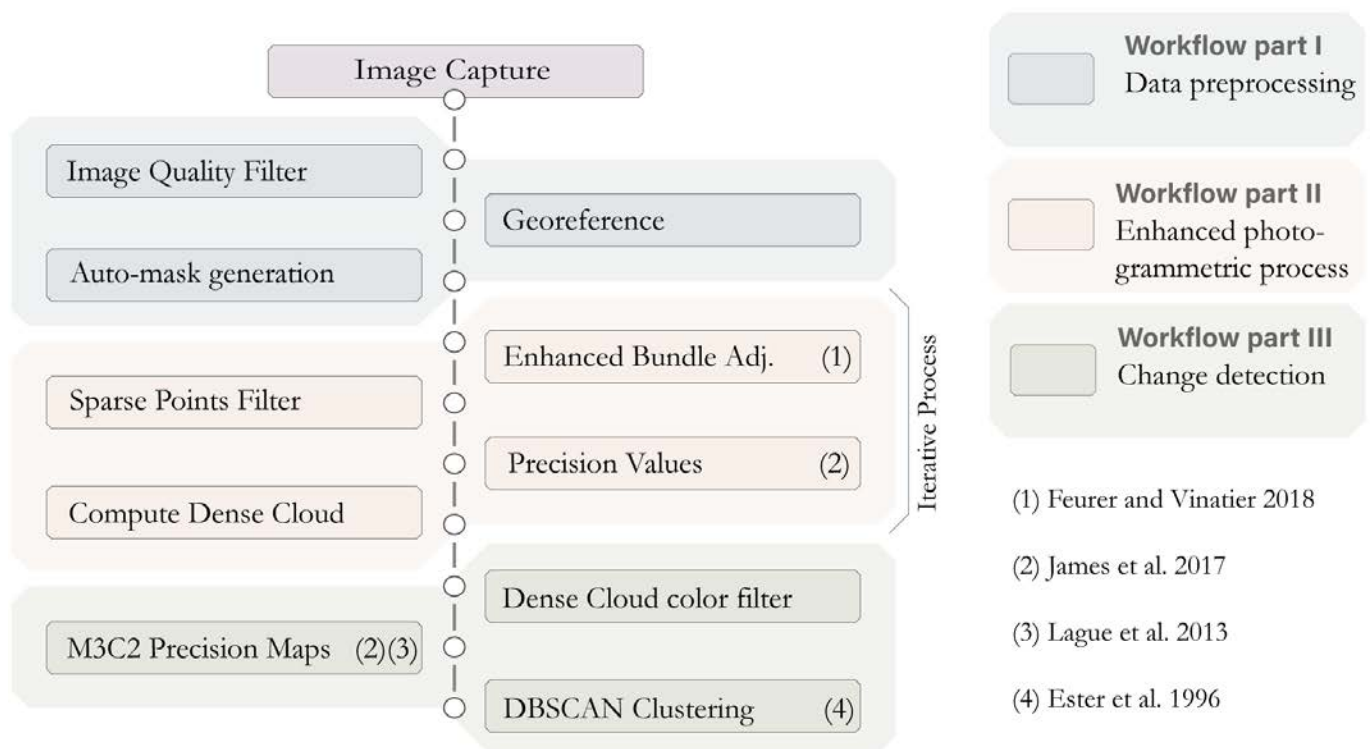


Figure II.29. 4D pipeline designed for the automatic analysis of rockfalls in Puigcerçós.

The colours represent different parts of the process grouped according to their description in the manuscript.

is automatically calculated according to the aperture, set at $f/11$ to obtain an acceptable depth of field. The configuration of the photogrammetric system can be easily modified to increase the acquisition of images on a more exhaustive daily basis. The scripts of the photogrammetric system that allow for scheduling, capturing, and sending the images remotely to the server were developed using the open-source Python programming language (version 3.7) (Python Core Team, 2015). The images were transmitted daily to the workstation where, after server storage, the automatic photogrammetric processing of the images was activated to obtain the 3D models to carry out change detection, also automatically.

LiDAR data was acquired as the reference dataset. The data was obtained with the ILRIS-3D-Optech © TLS (Terrestrial Laser Scanner). This high precision device allows the generation of a point cloud (2.500 points/s) with the 3-D coordinates (X, Y, Z) of each point with an accuracy of 7 mm when scanning at a distance of 100 m, according to the manufacturer's specifications. The standard deviation of the instrumental and

methodological error was defined as 1.68 cm at an average distance of 150 m by Abellán et al. (2010) and derived from this parameter, the change detection threshold for the scanning distance of the Puigcercós cliff was defined as 3.0 cm by Royán et al. (2014) The TLS data was captured in October 2019.

5.2.2 From 2D to 4D – Workflow for Automatic Change Detection with Time-Lapse Imagery

To highlight the improvements made in this study, the methodology is divided into three sections: i) Workflow part I, which refers to the tools developed for automatic pre-processing of data; ii) Workflow part II, which focuses on the improved photogrammetric workflow to acquire time-lapse 3D data, called multi-epoch multi-imagery (MEMI); and iii) Workflow part III, which introduces an automated change detection approach demonstrated at Puigcercós (**Figure II.29**). These three steps are part of a whole working pipeline that allows change detection models to be obtained automatically from the different images, as described below.

Data Pre-Processing (Workflow Part I)

Data pre-processing is essential because images were not captured under controlled environmental conditions. Image quality and data acquisition geometry change due to lack of maintenance, excess humidity, presence of fog, changing lighting conditions, vegetation growth, temperature changes and small variations in camera positions because of impacts, animals or metal dilations during the long-term observation period. Data pre-processing is particularly important because the success of the following stages strongly depends on the quality of the input data. Several tools have been developed to perform data editing steps that users usually need to do when preparing data for photogrammetric processing. These steps utilize techniques from computer vision and image analysis to enable geometric georeferenced models of maximum quality. The developed tools comprise:

Image Quality Filter. The cliff is located in a mountainous area where fog, snow and heavy rainfall are frequent, making the use of quality filters mandatory. Images are filtered based on an image quality estimation made with the OpenCV library (Bradski, 2000). The applied function is a Laplacian variation (Pech-Pacheco et al., 2000; Pertuz et al., 2013). If images are

not sharp enough due to unfavourable environmental conditions, the time-lapse photogrammetry processing workflow is stopped at this step.

Georeference. This tool enables us to determine if the cameras have changed their position, based on a reference image (A. Yilmaz et al., 2006). Although the camera systems are fixed to the ground, camera movements are possible, e.g., due to temperature changes, wind or animals. Also, changes in the interior camera geometry are likely due to heating and cooling of the housing (Elias et al., 2020; Schwalbe & Maas, 2017). In this study we used the Lucas–Kanade method (Baker & Matthews, 2004; Lucas & Kanade, 1981), also implemented in OpenCV, which has been shown to be suitable for tracking targets in geoscience applications (Lin et al., 2019). It is used to track control points, assigned in a reference image, in the target image. To ensure good georeferencing, Ground Control Points (GCPs) are located in the images, thus providing their 2D coordinates, and their corresponding 3D coordinates are assigned in object space. In this study, the real-world coordinates of GCPs were extracted from a TLS point cloud of the escarpment and were assigned manually by correlating TLS points with image pixels. The precision of this approach of GCP retrieval is discussed in **Section 8.2.3**.

Auto-mask generation. During the image-based 3D reconstruction steps a mask was applied to calculate a dense, high-resolution, large data volume point cloud only for the area of interest. Thus, the images are masked to the area of interest in their field of view. Due to changes in the camera geometry these masks need to be updated. The tracked GCPs allow calculation of the parameters of a perspective transformation to warp the binary masks from the reference images to the targeted images according to their movements.

Enhanced photogrammetric process (Workflow part II)

The second part of the presented workflow is an advancement of the photogrammetric workflow described in Feurer and Vinatier (2018) and Cook and Dietze (2019). In these studies, it was referred to as the time-SIFT or multi-epoch imagery workflow. We will use the acronym MESI (Multi-Epoch Single-Imagery) to refer to this workflow. Furthermore, an enhanced workflow was introduced that exploits the redundancy of images due to bursts of captured images from the fixed time-lapse camera setup for the multi-temporal analysis, and this is referred to as Multi-Epoch Multi-Imagery (MEMI).

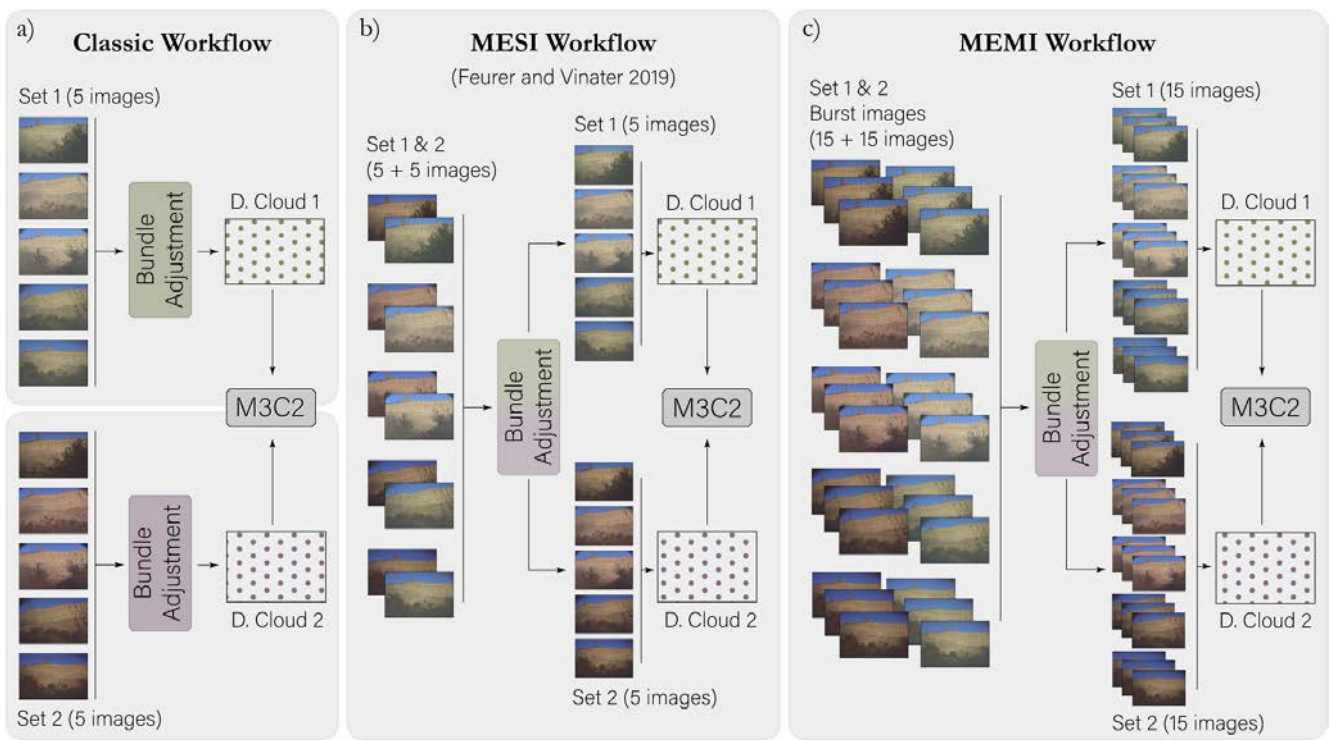


Figure II.30. Three different SfM-MVS photogrammetry workflows to calculate multi-temporal point clouds for change detection. The colour shading denotes images obtained at different time epochs. **a)** The classic workflow corresponds to the standard SfM-MVS photogrammetric approach. **b)** The multi-epoch imagery workflow (MESI) adopts the method defined by Feurer and Vinatier (2018), i.e., joining images from multi-epochs during image matching and bundle adjustment. **c)** The Multi-Epoch Multi-Imagery (MEMI) workflow considers (additionally to b) redundant image bursts from each epoch.

In the classic time-lapse SfM-MVS photogrammetry workflow, two separate bundle adjustments are performed to reconstruct the image geometry and the sparse point cloud, which refers to the 3D coordinates of the tie points (Eltner et al., 2017). Each bundle adjustment is done with the individual photos of the single epochs, i.e., individually for set 1 and set 2 (**Figure II.30a**).

In each set there is only one image from each camera. Eventually, the dense point clouds are obtained after each bundle adjustment. These point clouds are geo-referenced in a local, scaled coordinate system via GCPs extracted from the LiDAR scan. However, due to errors, e.g., during their tracking in the images, alignment errors between the point clouds are possible, which is partly compensated for by ICP-type (Iterative Closest Point) algorithms

(Chen & Medioni, 1992). For the MESI workflow the method described in Feurer and Vinatier (2018) and Cook and Dietze (2019) is implemented, performing image matching using data from different time epochs. The time-SIFT approach is described as “joining multi-epoch images in a single block” (Feurer & Vinatier, 2018). The result of the bundle adjustment using MESI is a sparse point cloud that contains tie points matched across overlapping frames from different points in time (**Figure II.32b**).

Only one bundle adjustment is performed to calculate sparse 3D point clouds, merging image Set 1 and Set 2. Consequently, spatially correlated systematic errors typical for SfM-MVS photogrammetry (James et al., 2017) are assumed to display similar magnitudes across the epochs, and therefore are mitigated during change detection after differencing of point clouds. The bundle adjustment with merged multi-epoch single images also has the advantage that the observation number increases strongly (several thousand more image points) while only a few additional unknowns (14 for each camera, i.e., exterior and interior camera orientation parameters) are introduced, increasing the reliability of the estimated parameters. After estimating the camera parameters, the images are separated again into the original sets to calculate the two dense point clouds using only images from the same epoch. The computed dense models do not require further alignment because they were already aligned in the same coordinate system during the bundle adjustment, considering the across-epoch tie points.

Besides the multi-epoch merging of images during 3D reconstruction, the improvements due to capturing bursts of photographs during one point in time shown in Blanch et al. (2020) were also implemented in this study. Thus, image bursts from each epoch and multi epoch imagery were combined. The dense point clouds were computed in the automatic multi-epoch multi-imagery (MEMI) workflow using more than one image per camera location (**Figure II.30c**). Therefore, each dense point cloud was created using 15 images (per epoch) instead of five as in the classic and MESI workflow. This resulted in two dense point clouds, but for the MEMI approach each one was calculated with the burst of images taken during different epochs. Again, the clouds share the geo-reference and spatially correlated errors (calculated from all 30 images in the bundle adjustment). This enables good alignment to enhance the detection of changes between models. However, this approach only works if stable areas are large enough within the field of view of the cameras. This workflow was

implemented using Agisoft Metashape Pro (version 1.6.6) (Agisoft, 2020) software and was automated using the available Python API (version 1.6.4) (Agisoft LLC, 2018). In line with previous work (Kromer et al., 2019), a further processing step was integrated into the automatic workflow. To improve the accuracy of the 3D reconstruction a filter, based on a reprojection error and reconstruction uncertainty, was applied to the sparse point cloud after the bundle adjustment (**Figure II.29**) to reduce outliers.

The last step of the automatic photogrammetric process involved a workflow introduced by James et al. (2017) (**Figure II.29**) to export sparse point coordinate precision estimates from Metashape (James et al., 2017). Given the sensitivity of the precision parameters, an iterative bundle adjustment was performed until the precision values of the control points and the tie points stabilized. The sparse point precision was used to calculate 3-D precision maps (James et al., 2017). These precision maps improve the level of detection (LoD) estimation, because instead of considering a uniform value for the entire point cloud, a LoD is calculated considering the spatially correlated errors from the 3D reconstruction (James et al., 2017).

Change detection (Workflow part III)

The final step of the introduced 4D pipeline, after reconstructing multi-temporal 3D models of high quality, is automatic change detection. First, a colour filter was applied to the dense point cloud to remove shadowed areas, because in this study the shaded areas were not correctly calculated and therefore led to errors in the detection of changes.

Afterwards, the M3C2 algorithm (Lague et al., 2013), integrated into the software CloudCompare (version 2.11) (CloudCompare, 2021), was used to calculate the model differences between different epochs considering the precision maps option (James et al., 2017). The point cloud difference calculation resulted in a new point cloud with an additional scalar containing the metric distances between the compared dense clouds.

Thereby, the DBSCAN algorithm (Ester et al., 1996) was used to automatically extract clusters of points that had difference values above a threshold and a minimum number of neighbours within a certain distance. The use of this methodology for LiDAR point clouds is explained in detail in Tonini and Abellán (2014).

As a result of the application of the clustering algorithm, a new point cloud was generated that only contained points that match the characteristics required for be part of a change cluster. The introduced automated enhanced workflow for change detection from photogrammetric models ends at this point.

The provision of the source-code enables the workflow to be implemented and adapted according to the individual applications and their specific analytical requirements. Due to automation, the 4D pipeline presented in this study obtains multi-temporal 3D point clouds from the automatically captured input data with all the changes identified ready for further analysis.

5.2.3 Performance Assessment

To assess the performance of the three different approaches, the classic approach, MESI and MEMI were compared for a period when no changes occurred. Three tests were designed to assess the relative accuracy of change detection, to evaluate the interior point cloud precision and to determine the absolute point cloud accuracies by comparing the point clouds to each other and to an independent LiDAR reference.

Relative Accuracy of Detected Changes

The three workflows described in **Figure II.30** were performed with the same input data to observe potential differences between the resulting change detection models, and to assess the accuracy of change detection, without considering absolute errors of change. To enable the evaluation of absolute accuracies of change detection, independent TLS measurements from the same time period would be needed (Cook & Dietze, 2019).

In order to analyse the relative accuracy, two different tests were performed. The input data for each test consists of a burst of images captured by each of the five camera modules on two consecutive days. Due to the use of images from contiguous dates, with no obvious changes in the area of interest, it is possible to assess the performance of the multi-temporal change detection because no changes should be visible in the final change map. For the first test, the images considered were taken on November 8th and 13th, 2019.

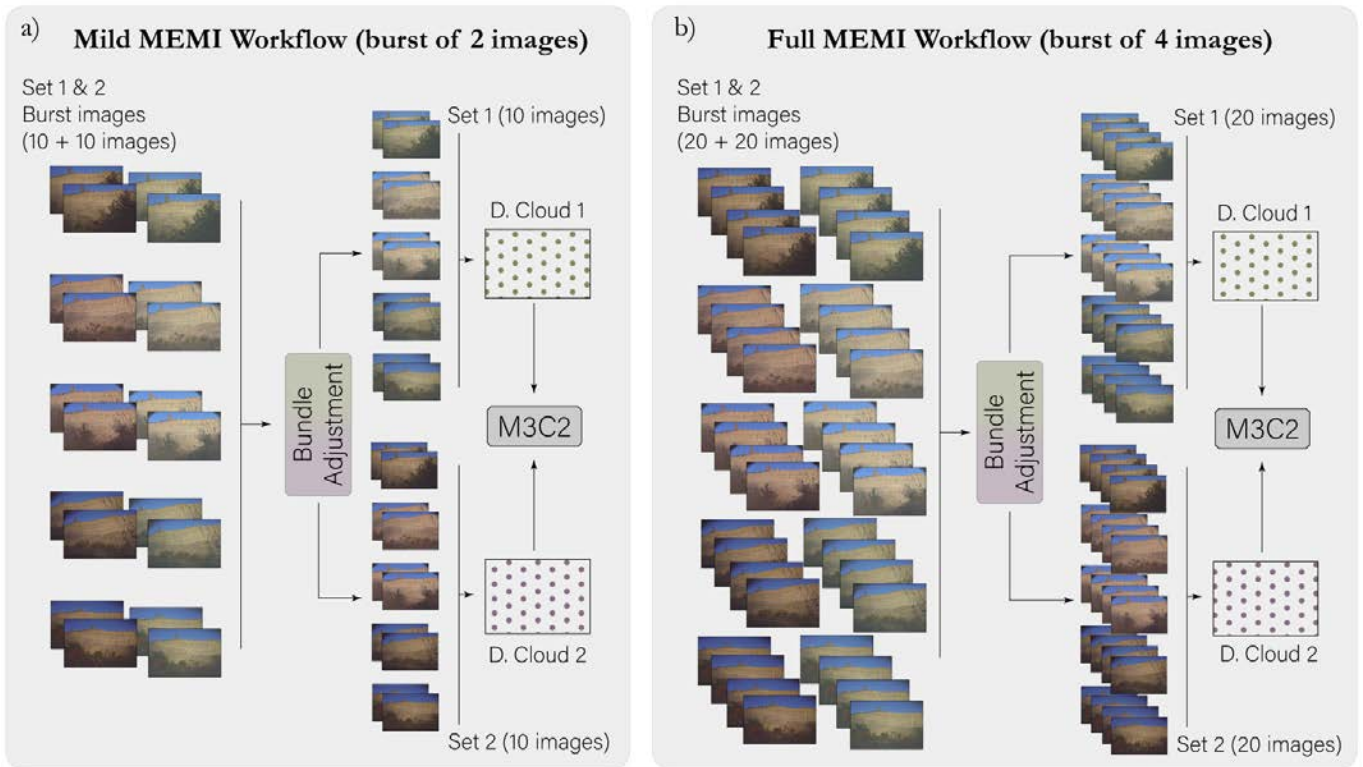


Figure II.31. a) Mild MEMI workflow created for the change detection evaluation. **b)** Full MEMI workflow created using all images available.

Due to the setup configuration at that time, bursts of three images were captured by each of the five camera modules. The second test was performed using images captured on the 23rd and 24th of May 2020. As a result of a system improvement, the second test benefitted from a higher burst, with four images captured by each of the five camera modules.

To assess in more detail the improvement in change detection due to the increased number of images from each burst, an additional evaluation was performed, using the MEMI workflow, but with a burst of two images instead of a burst of four. The MEMI workflow using only two images is referred to as the mild MEMI workflow (**Figure II.31a**), whereas the enhanced workflow that implements all (i.e., four) images is referred to as the full MEMI workflow (**Figure II.31b**).

Comparison of the resulting 3D point cloud differences from the three workflows was carried out using the M3C2 from Lague et al. (2013), implemented in the CloudCompare software. All comparisons (classic, MESI, mild MEMI, and full MEMI) were performed

using the same software configurations and images taken from the same modules at the same time, but introducing more images from each burst the more complex the workflow. No filter was applied nor were any of the sparse point clouds considered differently. Although we used the same GCPs to geo-reference the images in all workflows, the point clouds obtained in the classic workflow needed to be aligned using the ICP algorithm (Chen & Medioni, 1992) because Set 1 and Set 2 did not share exactly the same camera orientation due to the separate bundle adjustments.

Interior Precision of the Point Clouds

As well as considering the relative accuracy of change detection, we also assessed the interior precision of the retrieved 3D point clouds (Cook & Dietze, 2019) with a test using the precision estimation algorithms described in James et al. (2017). The approach (**Figure II.32**) allowed us to quantify the performance of the time-lapse SfM-MVS methods in a different way than the change detection test, presenting the spatial distribution of errors in terms of precision in centimetres and using a LiDAR TLS to retrieve ground control.

For this test we used the images corresponding to November 8 and 13, because they were the most similar to the LiDAR TLS scan performed in October 2019. In 2019, the photogrammetric systems were not optimized to obtain bursts of four images, so the results presented were obtained using only bursts of three images, and with no separation into mild and full MEMI.

Following the approach proposed by James et al. (2017), the precision estimation values (σ_x σ_y σ_z) were estimated for each point of the sparse cloud. With a simple interpolation process, the precision estimation values (σ_x σ_y σ_z) were transferred from the sparse cloud points to the dense (James et al., 2017).

Absolute Accuracy of a Single Point Cloud

In order to determine the performance of the time-lapse SfM-MVS algorithms in terms of absolute accuracy, the final performance assessment consisted of comparing the photogrammetric models to LiDAR data. It was assumed that the LiDAR data represent a reference geometry, so the smaller the differences between the LiDAR and the photogrammetric models, the higher the absolute accuracy of them.

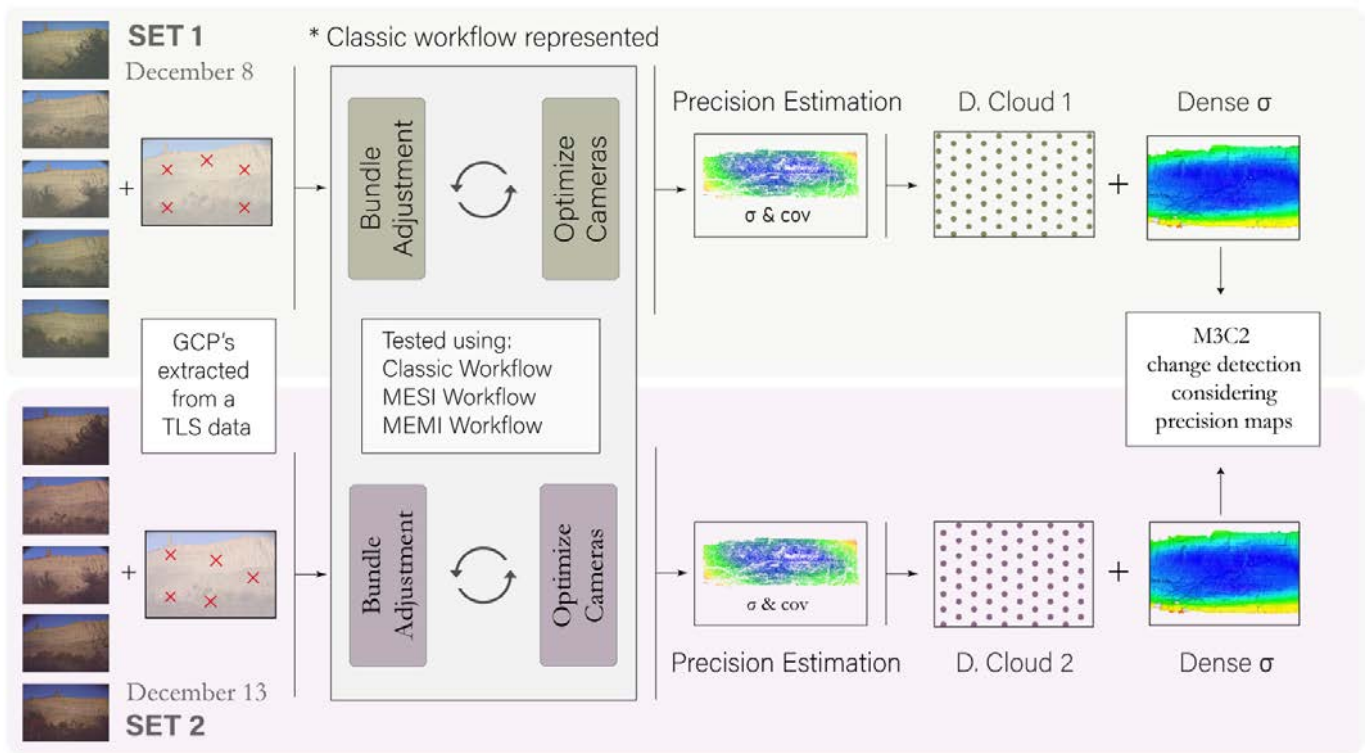


Figure II.32. Pipeline performed to obtain the precision estimation in order to only detect significant changes (consecutive dates analysed). The 4D process illustrated in this figure comprises the classical workflow but the MESI and MEMI workflow has also been evaluated.

Due to the interval between the captured LiDAR data (October 2019) and the first captured photogrammetric data (November 2019), and the high number of rockfalls affecting the cliff, the period between datasets included several changes. In order to avoid eliminating the errors and smoothing of the results, the detected changes were not eliminated for the absolute accuracy test. Therefore, this assessment does not represent a non-deformation scenario between the LiDAR data and the photogrammetric models.

The results and partial discussions obtained in all comparisons are presented in **Section 8.1** and **8.2** respectively. The script with the MEMI workflow for Agisoft Metashape (programmed in Python) can be found in **Appendix A – MEMI workflow**. The repository contains the different scripts for each phase of the workflow.

Section III

RESULTS AND

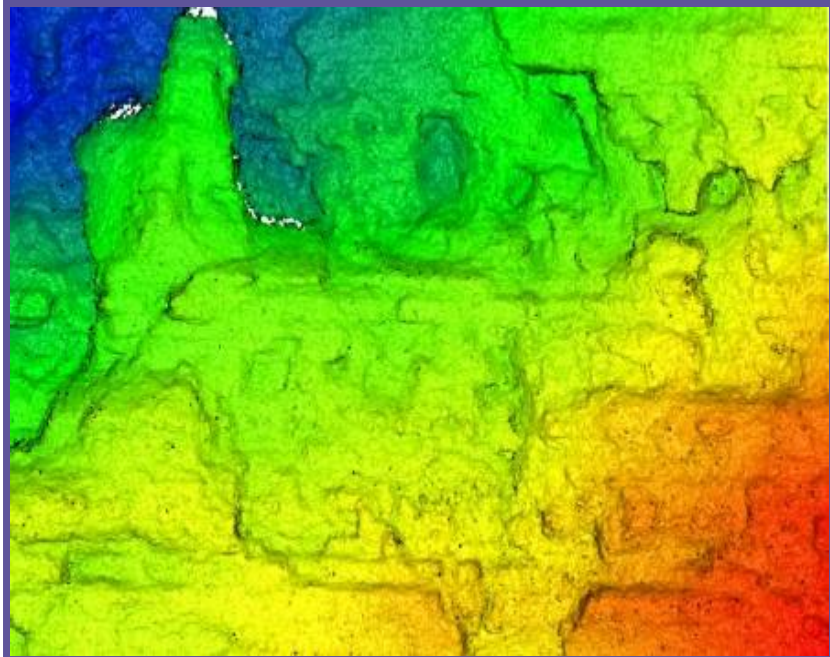
PARTIAL

DISCUSSIONS

CHAPTER 6 – PHOTOGRAMMETRIC SYSTEMS

CHAPTER 7 – PCSTACKING ALGORITHM

CHAPTER 8 – MEMI WORKFLOW



6.1 Results

6.1.2 RasPi System

The photogrammetric system was installed at the beginning of May 2018 with only 3 cameras. Throughout this time, as shown in **Figure II.11**, the system has evolved considerably with 4 main update stages. From the beginning, this system has been functional. Its simplicity, solid construction, and easy integration (camera and control unit are the same brand concept) make it a very robust system. In addition, the use of metal boxes gives it a very good resistance and durability. However, over time it has also experienced failures and some components have had to be replaced.

Figure III.1 shows the System's operability. The boxes highlighted in green and light green are days in which at least 3 systems have been working (minimum to be able to make a photogrammetric model). However, having three systems working does not mean that photogrammetric models can be made, as we sometimes have photographs that are not usable (internal humidity, fog, dirt, etc.). The quality of the images produced by this low-cost system is lower than the obtained using commercial cameras, due to the size of the sensor, the low resolution, and the quality of the lens.

Figure III.2 shows a real image of each camera obtained automatically by the photogrammetric system. Even though they are images of the same time, cameras 4 and 5 show a different tonality. As can be seen, the sharpness of the images is not very high, and consequently the resulting photogrammetric models are not of high quality. **Figure III.2a** and **Figure III.2b** shows current images of the RasPi systems at Puigcerçós. **QR 18** links to a photo gallery where it is possible to view the images obtained by the photogrammetric system at maximum resolution. The same images shown in **Figure III.2** are displayed.



QR 18

As mentioned above, the photogrammetric models obtained are not of very high quality. **Figure III.3a** shows a photogrammetric model obtained with the standard setup. Visualising a 3D digital model on paper is a difficult task, for this reason a detailed inset of the model is attached for better visualization **Figure III.3b**. In addition, to help visualise the depth of the

RasPi System - Calendar heatmap

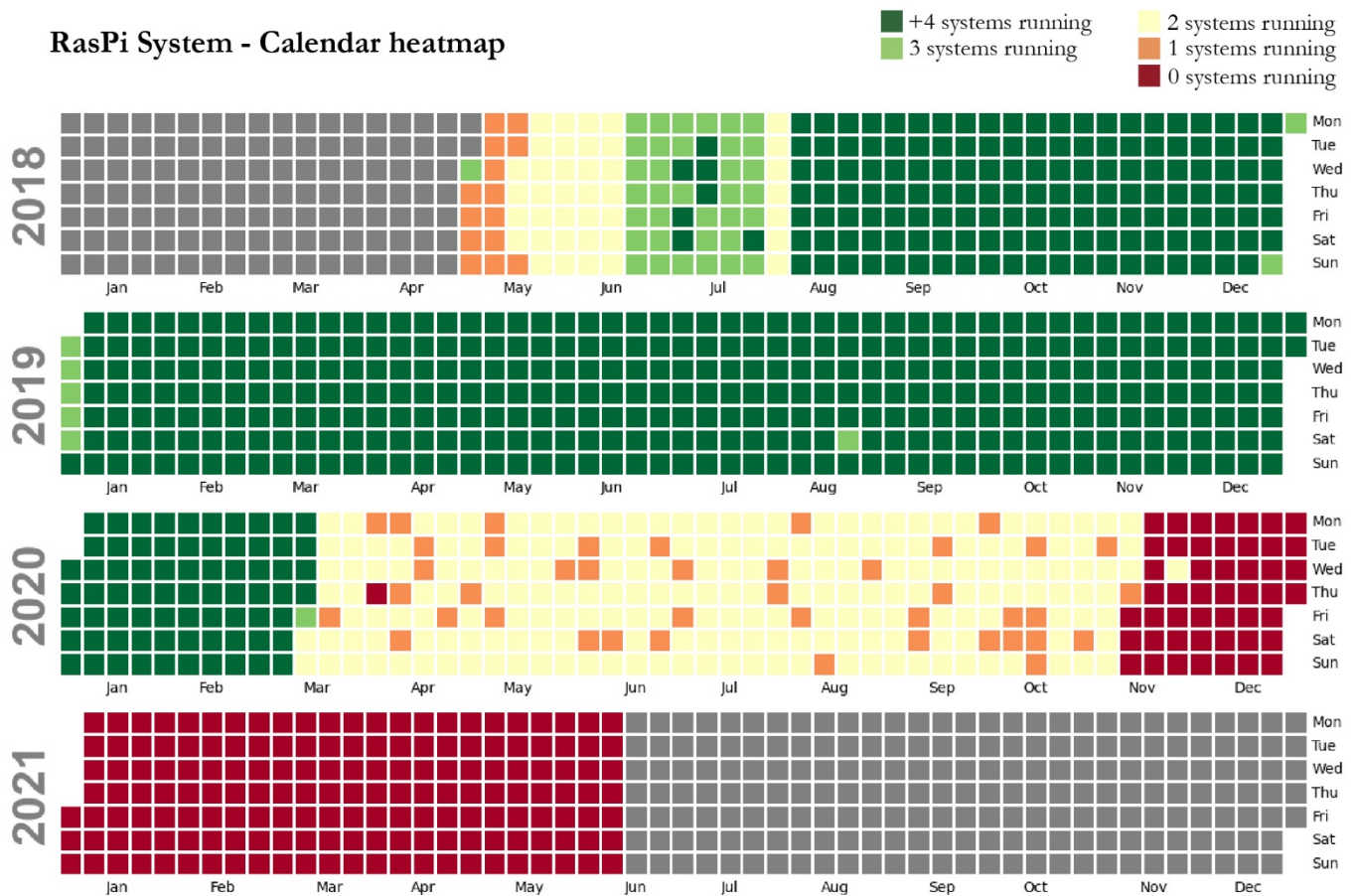


Figure III.1. Heat map of the RasPi system operating calendar. The different shades of green indicate the possibility of obtaining photogrammetric models (at least 3 or more images are acquired).

model (the most important parameter for detecting rockfalls), the same inset has been coloured with a depth map. This colouring makes it possible to see how well the depth has been reconstructed. In the case of **Figure III.3c** (and particularly in comparison with the following systems), it is easy to identify that they are black points where the depth is not well resolved.

However, the author strongly recommends consulting the 3D model by using a digital support and "navigating" through it to understand the differences in quality. The digital model of the RasPi system can be accessed at the following **QR 19**. To facilitate the reader's understanding of the 3D models obtained by the different systems, the model resulting of each system will be shown in the following sections in the same way as described above.



QR 19



Figure III.2. Images obtained with each photogrammetric system on 29 November 2019 at 15:45h. **a,b)** Recent images of the RasPi system. The difference between image **a)** and **b)** is the installation of the external Wi-Fi antenna to improve signal reception.

a) Puigcerçós - Raspi
3D Dense Cloud
2018.12.19 - 15:45h

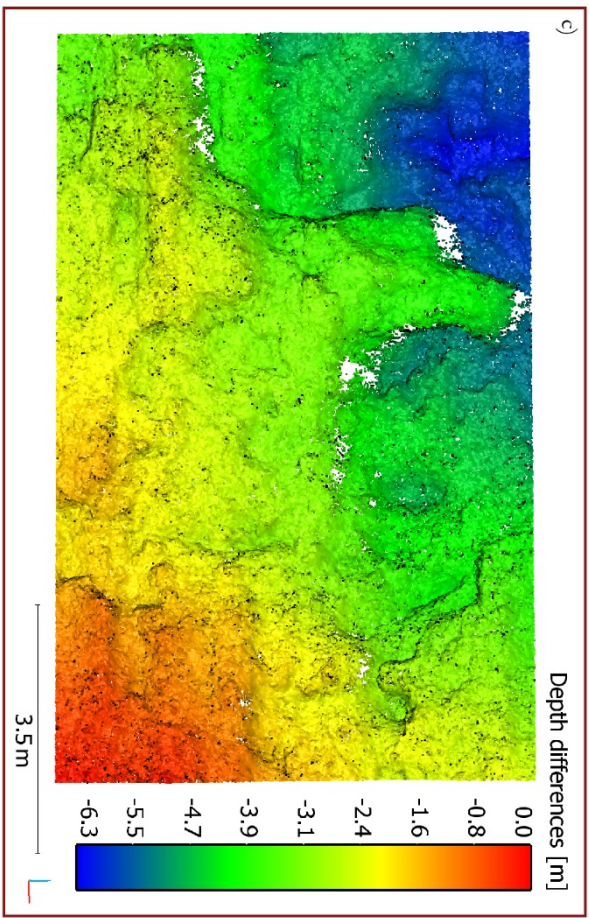


Figure III.3. a) Point cloud of the photogrammetric model. b) Detail of the central area of the escarpment. c) Depth differences map.

6.1.2 HRCam System

The HRCam system was installed in the middle of March 2019, with 5 cameras. As can be seen in **Figure III.4**, the overall performance of this system has been continuous, but with quite a few factors that have affected the systems. These failures, which will be discussed later, have been caused mostly by the climatic severity of the study area as well as by the complexity of the systems. As in the previous system, we noted that the waterproof metal case gave a good resistance and durability to the system. But in the case of the HRCam cases, they had to be drilled to put the view glass in. For this reason, they have not guaranteed the same protection against water, fog, and humidity.

In contrast to the previous RasPi system, the quality of the images produced by this system is much higher. The use of commercial cameras together with fixed lenses allows very sharp photographs to be obtained, with higher resolution and lower geometric distortions. **Figure III.5** shows an image obtained with each system installed and **QR 20** links to the photo gallery of these images obtained by the HRCam system. Because of the images obtained, the



QR 20

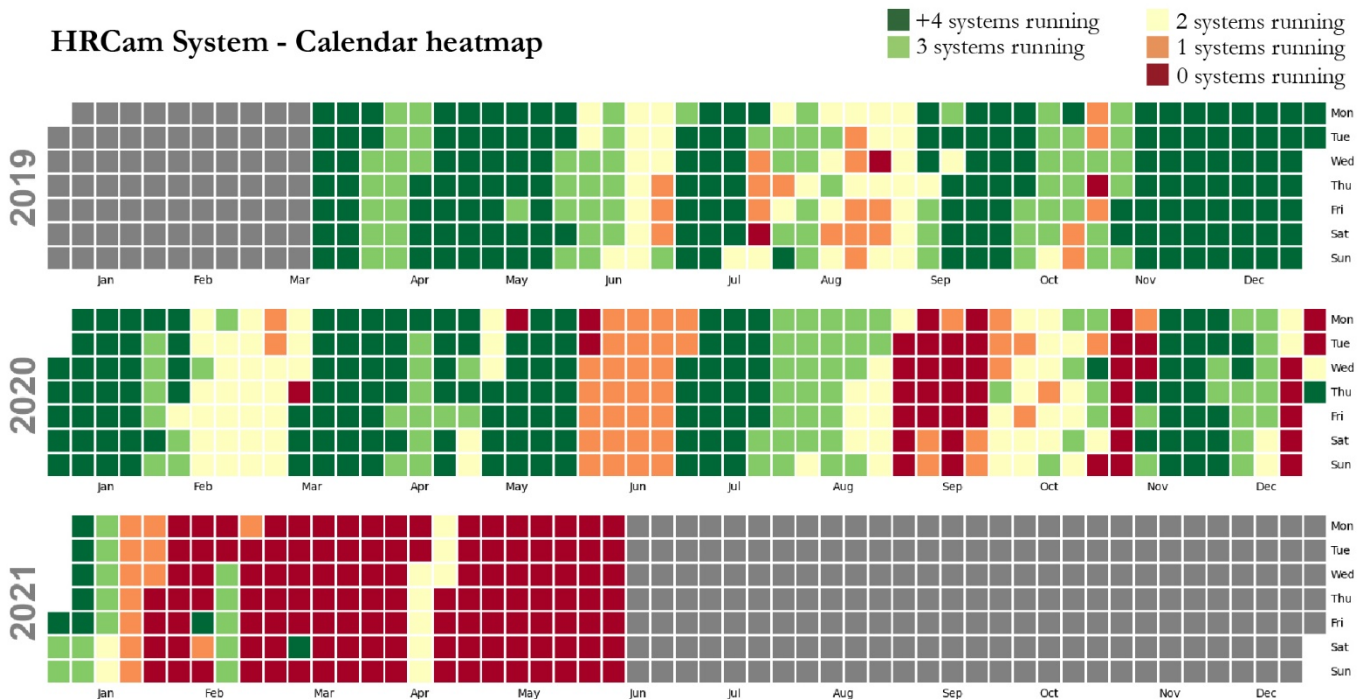


Figure III.4. Heat map of the HRCam system's operating calendar. The different shades of green indicate the possibility of obtaining photogrammetric models (at least 3 or more images are acquired).



Figure III.5. Images obtained with each HRCam photogrammetric system on 22 April 2019 at 17:47h. **a,b)** Recent image of two HRCam systems.

resulting photogrammetric models can be regarded as of high quality. **Figure III.6a** shows a photogrammetric model obtained with the standard configuration. **Figure III.6b** shows the definition of the photogrammetric model that can also be identified in the depth differences map in **Figure III.6c**. The **QR 21** code allows a digital visualisation of the photogrammetric model obtained by the HRCam system.



QR 21

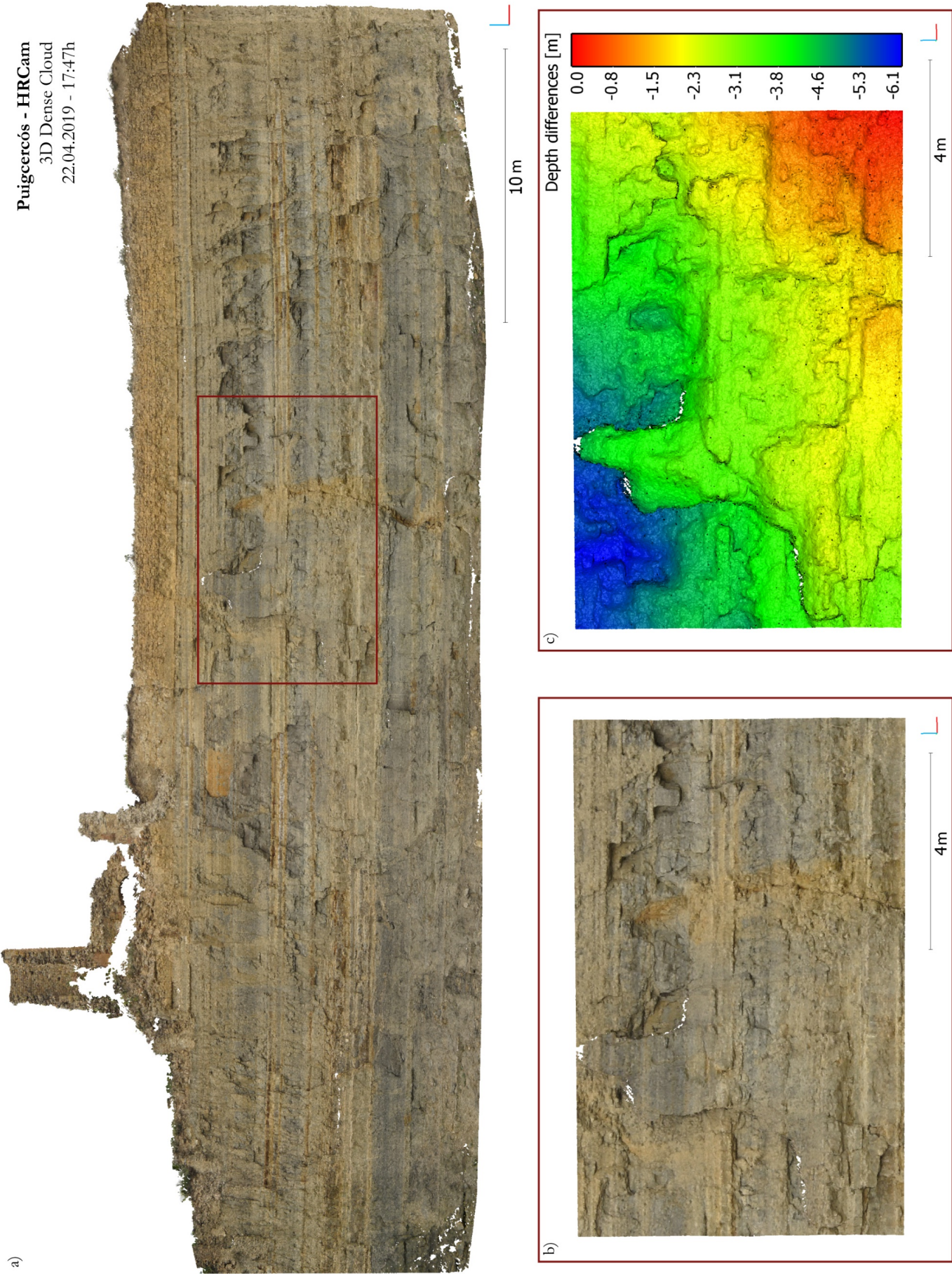


Figure III.6. a) Point cloud of the photogrammetric model. b) Detail of the central area of the escarpment. c) Depth differences map.

6.1.3 DSLR System

The DSLR system became operational on 26 June 2019. As can be seen in **Figure III.7**, the overall performance of this system has been continuous, with one episode of non-operation in the middle of 2020. **Figure III.7** also shows how the systems have not operated beyond January 2021. This is because due to the Coronavirus pandemic it has not been possible to perform adequate maintenance as quickly as necessary, particularly after the winter, when the system suffers from the low solar radiation that falls on the solar panels. For this reason, the solar energy system was oversized in **Stage 2** of the system (**Figure II.23**). Nevertheless, thanks to the maintenance work carried out, it has been possible to provide all the reports required by the Patronato de la Alhambra y del Generalife.

The quality of the images acquired by this system is comparable to those obtained in the HRCam system. The following **QR 22** is linked to the image gallery of the DSLR system. Here you can see in detail the images acquired by each of the 5 installed systems. Although



QR 22

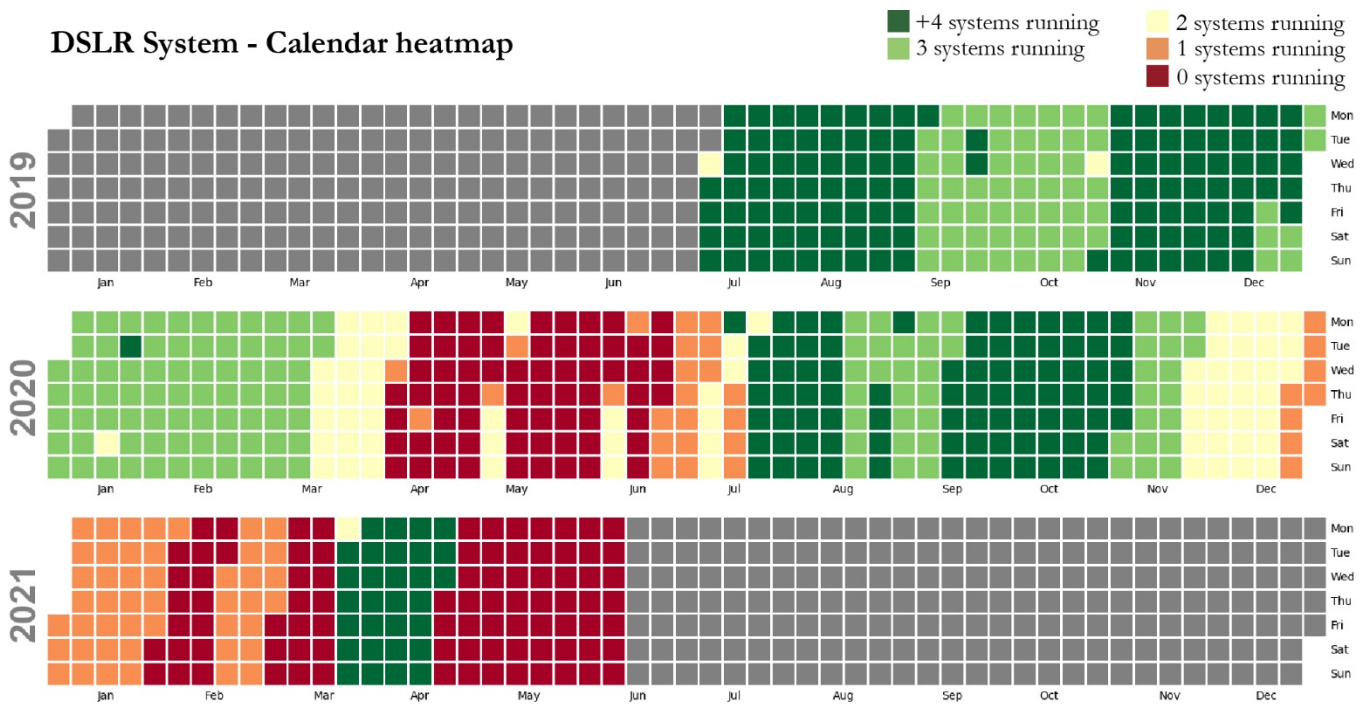


Figure III.7. Heat map of the DSLR system's operating calendar. The different shades of green indicate the possibility of obtaining photogrammetric models (at least 3 or more images are acquired).

lower resolution cameras are used, very good quality photographs are obtained. **Figure III.8** shows an image obtained with each system installed. As a consequence of the images obtained, the resulting photogrammetric models can be considered of high quality. **Figure III.9a** show a photogrammetric model obtained with the standard configuration.

However, it should be noted that the difficulty of locating the cameras in the urban grid of the Albaicín meant that it was not possible to obtain a 3D model of the entire cliff. The lack of locations on the left flank of the Tajo de San Pedro means that the right side of the cliff cannot be adequately reconstructed (**Figure III.9a**). For this reason, although the results obtained are very good because they focus on the most active area of the escarpment, it should be noted that a complete model of it is not obtained.

In a similar way to the results shown in the previous sections, the following results have been presented. **Figure III.9b** and **Figure III.9c** show in detail a central area of the escarpment.

Although the quality of the model obtained does not achieve the same quality as that observed with the previous system HRCam, the results obtained are sufficiently valid to be applied in rockfall detection processes. The blank areas are zones where the reconstruction could not be carried out correctly due to the presence of vegetation.

In the following **QR 23** code, the reader has access to the digital visualisation of the 3D model generated by the photogrammetric system installed in the Tajo de San Pedro.



QR 23



Figure III.8. Images obtained with each photogrammetric system installed in Granada. Images were taken on 12 July 2019 at 09:17h. **a)** Image of the system installed on the terrace of the Church of San Pedro (DSLR4). The difficulty in installing the system can be seen, as it had to be installed on raised supports. **b)** System installed in the bell tower of the church (DSLR1), where greater camouflage with the surroundings was required.

a) **Granada - Alhambra**
3D Dense Cloud
07.12.2019 - 09:17h

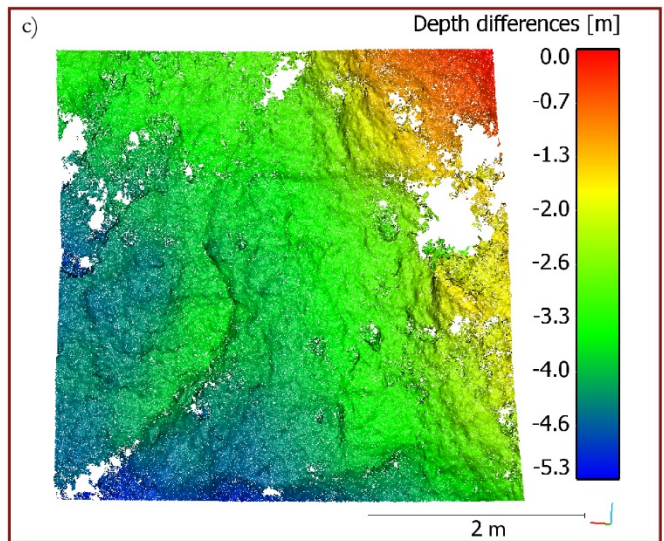
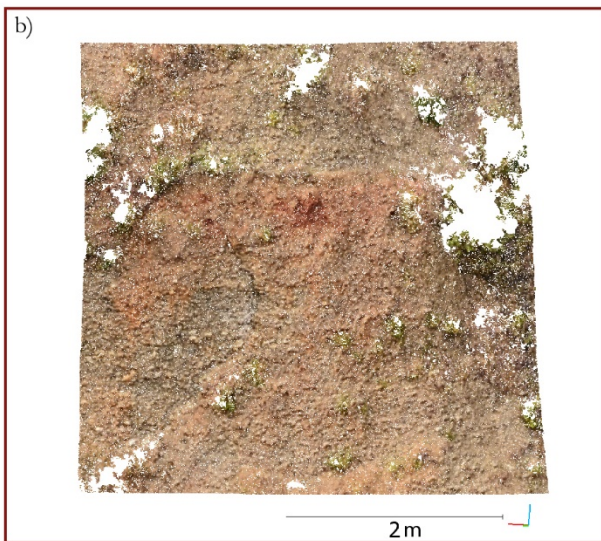
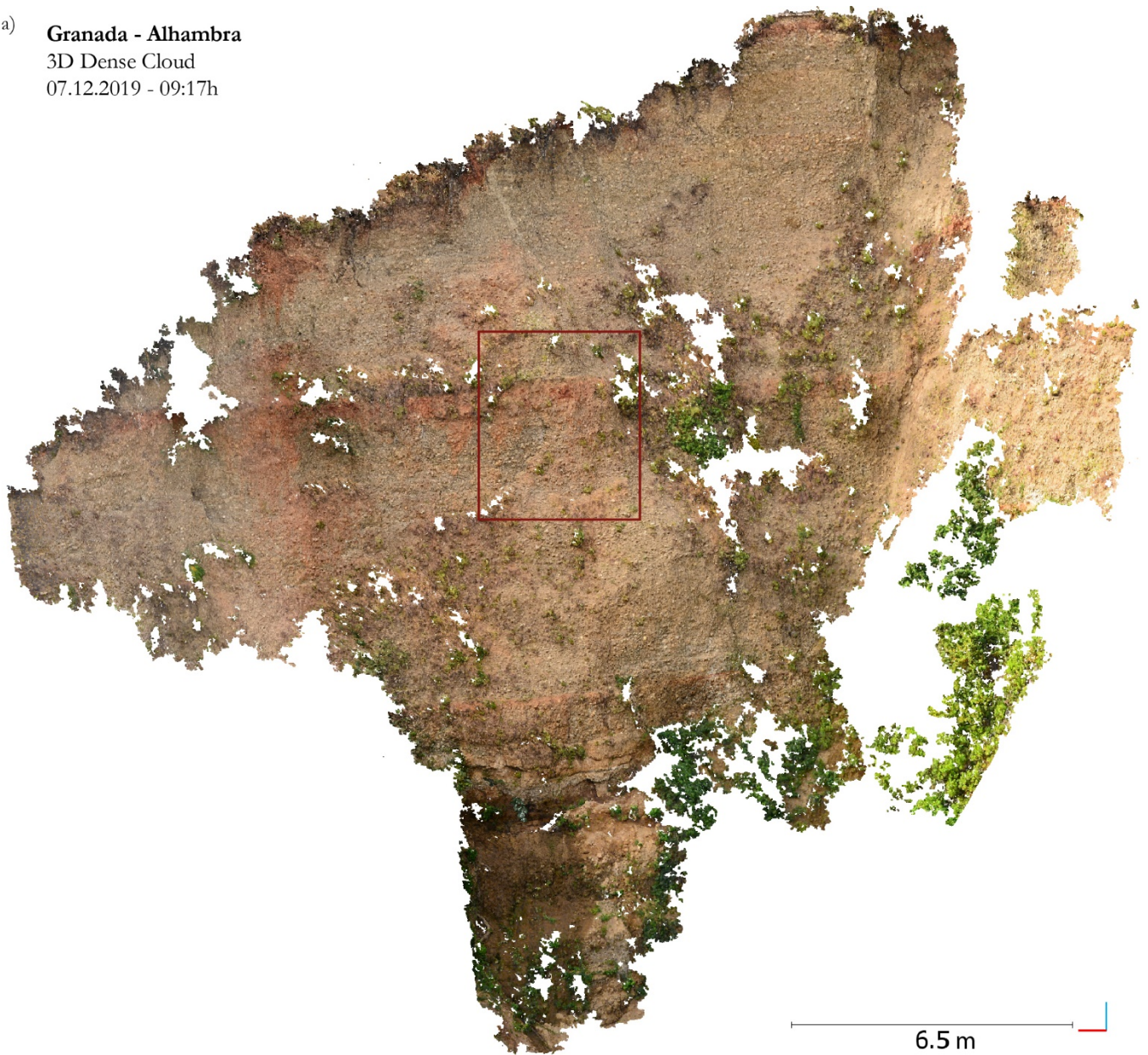


Figure III.9. a) Point cloud of the photogrammetric model. b) Detail of the central area of the escarpment (red inset). c) Depth differences map (red inset).

6.2 Partial discussion

The design, installation and maintenance of the photogrammetric systems have been carried out without any previous experience. Moreover, the lack of publications with similar installations at the beginning of this research accounts for the absence of reliable references about the state of the art. For this reason, obtaining the data and images necessary to be able to develop the algorithms of this thesis is, by itself, a very positive result.

All the design and research has been conducted through self-learning and with the information obtained thanks to the immense community that shares its knowledge freely on the internet. The sum of different knowledge capsules, ranging from configuring a solar charging system to learning how to use the library to connect the control unit with the camera, has facilitated the development of the photogrammetric systems.

However, this great capability of synthesising dispersed knowledge in order to generate "new products" has also proved to be the greatest weakness. This is because there has been no in-depth study and no specific expertise for resolving the design in the best possible way. Consequently, although cameras have generally worked well, there have often been periods of time in which systems have failed. **Figure III.1**, **Figure III.4**, and **Figure III.7** show that the operation of the photogrammetric systems has been neither regular nor as good as desired.

Even so, valuable data was obtained from all the systems installed. All 3 systems have been able to acquire and send the images autonomously to the server. The correct positioning (good photogrammetric geometry) of the cameras has made it possible to generate photogrammetric models of the desired area, and although the systems require maintenance, no system has completely broken down or become unusable.

In general terms, most failures can be associated with adverse weather conditions. This conclusion is based on three observations: i) the cameras that suffered the fewest errors were those located under a cover; ii) several times, we have encountered devices that malfunctioned with excessive internal humidity and iii) the RasPi system, a much more hermetic system, has provided larger windows of use with a good performance.

Thus, the author considers that the design of the HRCam and DSLR systems has not been optimal. The metal enclosures used were not completely watertight. This problem is due to the way the front lens was installed, which creates micro-gaps where humidity can enter.

In addition, the weather conditions in the study areas are particularly severe. At both Puigcercós and Granada, very high temperatures can be reached in summer and very low temperatures in winter. These temperature contrasts affect the metallic systems such as the box or the front filter ring. This is especially noticeable in HRCam and DSLR systems because the viewing window of the box was created by drilling and embedding a photographic filter. Since the expansion of glass and metal are noticeably different, the filter glass, which was originally fixed to the metal ring, nowadays can easily be dislodged.

Furthermore, in the case of Puigcercós, dense fogs can linger for several days, thereby saturating the air inside the metal box with humidity, which can condense on the metal walls at night, forming water droplets that affect the electronics.

6.2.1 RasPi System

This system has performed well and has not required much supervision. Although the image quality is not particularly good, acceptable photogrammetric models can be obtained for rockfall identification. The failures or disconnections of the systems during 2020 and 2021 are due to the prioritisation of the installation and use of the HRCam system. For this reason, the supervision and maintenance of this system has been slightly discontinued.

The raw results obtained are useful for the production of a 3D model. But many errors occur in the reconstruction of the model. For this reason, **Figure III.3c** shows white spaces and some black dots representing points where the reconstruction is not correct, in addition to geometrical errors that can only be detected when comparing models with each other (as done in **Chapter 4**). Besides, the reconstruction at the edges of the model is frankly bad, so should a complete monitoring of the Puigcercós cliff be required, it would be necessary to install more cameras. With the current distribution, only the central area of the cliff can be analysed.

Over time, the design has proved to be correct. We have detected no design errors and the selected case has withstood the weather very well. The concrete pipework has successfully supported the systems and has not shifted or moved significantly.

The connectivity system developed for the Puigcercós study area, which provides connectivity to this system and to the HRCam system, has worked correctly. During the course of this thesis, it has only been necessary to change the solar panel, since the original panel was broken (probably by an animal). The Wi-Fi antennas that were installed provide a good internet connection over a very large and remote area. In the same way, the 4G antenna is able to provide a good data connection even in an isolated area. The ability to provide internet in a remote study area without being permanently connected to either a wired power supply or a telephone cable is also an unexpected success of this research.

6.2.2 HRCam System

The HRCam system constitutes the main evolution after the RasPi system. This system is based on the same principles as the RasPi system, but scaling the components. This scaling of components, however, entails changing the whole concept of the system. This system is the one that has involved the most learning process, while at the same time giving rise to the most problems. It has always worked properly after each revision, but failure after a few months was a common occurrence. These failures have been associated with weather conditions, as the systems operated continuously during long months of testing in the faculty (controlled environment).

In addition, the use of numerous electronic components (e.g., relays, or dc-dc converters), third-party boards (e.g., WittyPi, and Raspberry) and different cameras brands (e.g., Sony, and Canon) made it very difficult to standardise the system. Each system at Puigcercós works in its own way based on its camera brand, the Raspberry version, and the arrangements undertaken in the field.

However, given the various improvements in codes and the installation of better components made throughout this thesis, it has been possible to obtain longer periods of data acquisition. As the learning curve increases, the systems become more robust.

The metal enclosures of the systems are currently their weak points because they allow humidity to enter, which seriously damages the electronic systems. Although the author has made many efforts to waterproof the electronics, it has not been possible to completely isolate the systems. Furthermore, the temperatures reached inside the metal boxes in Puigcerçós are extremely high, so solutions such as silicone sealant, power tape or thermal adhesive are not valid as they soften and lose their firmness and properties. Other methods such as encapsulation in epoxy resin or insulation with high resistance polymer have been tried, but the operation is very difficult to perform as the electronic components have elements that cannot be submerged or covered by resins (e.g., microSD card or USB connectors).

The resulting models are of very good quality. The HRCam system is the one that enables the highest quality models to be obtained, and consequently the one that should allow a more accurate identification of changes. Given that the images captured have 100% coverage between them, the model obtained is robust and shows coherence even at the edges of the model. Moreover, this is achieved by the use of cameras with very different characteristics (sensor size and number of different pixels), so it is reasonable to assume that if all systems use cameras with the best characteristics, the quality of the model obtained would be much higher.

The sizing of the battery and the solar panel is correct and in no case have we encountered any problems with power supply. In the same way, the concrete support made ad hoc for the installation of the metal boxes has functioned perfectly throughout the development of this thesis.

6.2.3 DSLR System

The photogrammetric system installed in the Tajo de San Pedro was the last to be designed. Thus, this system makes the most of all the learning obtained in the RasPi and HRCam systems installed in Puigcerçós. It is also the system that demands the most responsibility from us since it has been installed in a high-risk location. It was consequently designed as an upgrade of the HRCam system by installing the best components, simplifying the process, and eliminating all those accessories or experimental improvements that were not strictly necessary (in order to minimize the risk of failure).

The DSLR system has also worked well over substantial periods of time. However, as can be seen in **Figure III.7**, it has undergone two periods of inactivity as a consequence of the Covid pandemic. While it was possible to return to the site in order to reactivate the systems when the Covid restrictions were relaxed, more recently it has not been possible to carry out the maintenance work required. The systems have the same deficiencies as the Puigcercós designs. Nevertheless, we are able to identify the effects of climate on the devices in these systems better, since those that are under cover are subject to far fewer errors than those that are exposed to the elements.

The greatest difficulties we have encountered with the systems installed in the Tajo de San Pedro have been related to solar energy and the Wi-Fi network. The neighbourhood where the cameras are installed consists of very narrow, winding streets and old houses with thick stone walls. Furthermore, since it is strictly prohibited to place the solar panels where they are visible, we were obliged to install them in inconvenient locations in order to capture any solar radiation. For this reason, some of the solar panels received no solar radiation at all during the winter, and the batteries that power the devices ran out of energy. Likewise, the connectivity system had to be divided into 3 different systems, tripling the complexity of the system with 3 different routers that are exposed to the weather. In addition, this neighbourhood does not enjoy good mobile phone coverage.

Curiously, working in the middle of an urban grid has been more difficult than working in the middle of nowhere. Part of this difficulty is also reflected in the fact that we have not been able to choose the locations of the cameras freely. Thus, the model in **Figure III.9** does not represent the entire escarpment of Tajo de San Pedro, but only the left flank (the main flank of the escarpment).

This situation is far from ideal, but given these conditions it is the only model that can be obtained. In addition, the limitations of the camera locations mean that each system has a set of lenses with different focal lengths, which is not an optimal configuration for SfM-MVS processing. Therefore, although the model obtained has a high photogrammetric quality, it does not have the same resolution as the one obtained with the HRCam systems in Puigcercós.

7.1 Results

This chapter contains the results and partial discussions obtained with the PCStacking algorithm. The methodology corresponding to the different tests carried out can be found in **Chapter 4**. These results are part of the **Publication I**.

7.1.1 Synthetic Test

The histograms of the differences between the Enh-PC_n and the Ref-PC (**Figure III.10a**) provide a quantitative assessment of the improvement achieved with the PCStacking algorithm. The increase in the number of input models (Synt-PCs) resulted in a better fit between Enh-PC_n and Ref-PC.

The boxplot in **Figure III.10b** illustrates the distribution of the differences calculated from the comparisons between Enh-PC_n vs. Ref-PC. The boxplot depicts a decrease in the errors when more inputs were used. The 25th and 75th percentiles progressively reduced to 50%

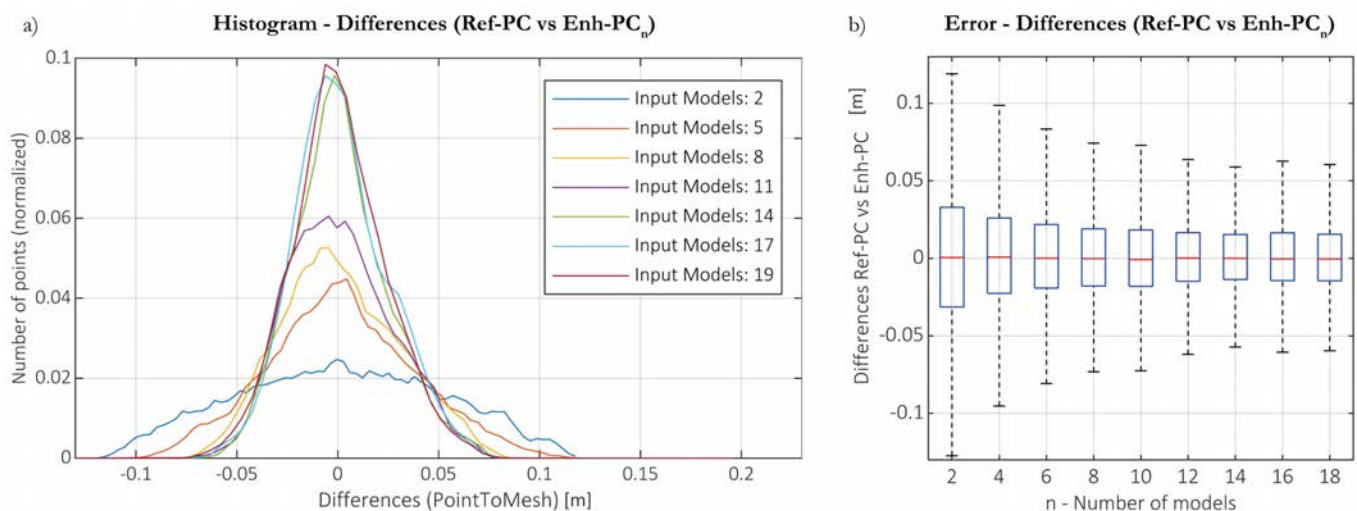


Figure III.10. Results from the application of the PCStacking algorithm with synthetic data. **a)** Histogram of the differences between the Enh-PC_n and the Ref-PC. Each coloured line represents a different number of Synt-PCs introduced into the PCStacking algorithm. **b)** Boxplot with the errors of the differences obtained in the different comparisons (Enh-PC_n vs. Ref-PC).

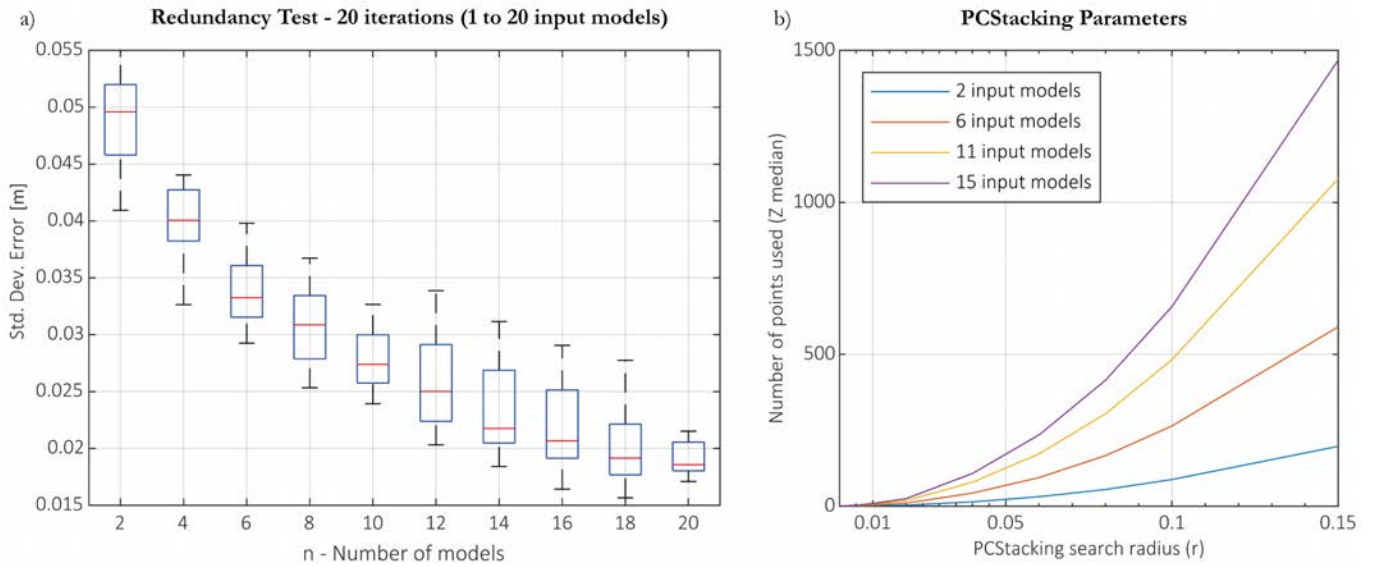


Figure.III.11. a) Evolution of the standard deviation of the comparison Enh-PC_n vs. Ref-PC in the redundancy test. The standard deviation decreased from 4.9 cm to 1.8 cm. A total of 400 Synt-PCs were used to compute this plot. **b)** Number of averaged points according to the search radius (r). Each coloured line represents a different number of Synt-PCs introduced into the PCStacking algorithm.

after using 18 models. Specifically, the percentiles were progressively reduced from ± 3.2 cm to ± 1.4 cm after using the PCStacking algorithm with 18 models. Likewise, the minimums and maximums in the boxplot also show a reduction close to 50%. The comparisons between Enh-PC_n vs. Ref-PC in the redundancy test (**Figure.III.11a**) reveal a considerable reduction of the standard deviation when increasing the number of models introduced. The average standard deviations of the comparisons of all iterations decreased from 4.9 cm to 1.8 cm when 20 PC were used.

The quartile bars (**Figure III.10b** and **Figure.III.11a**) demonstrate non-constant values because in some iterations the Synt-PCs may have much greater error than in others. As an example, in **Figure III.10b**, the 75th percentile bar belonging to the input of 16 Synt-PCs is larger (1.4 cm) than the one belonging to the input of 14 Synt-PCs (1.3 cm). This random distribution of error is the main reason for carrying out the iterative test.

One effect of using the PCStacking method is that the result obtained (Enh-PC_n) accumulates all the points of the different Synt-PCs used, producing both a more accurate

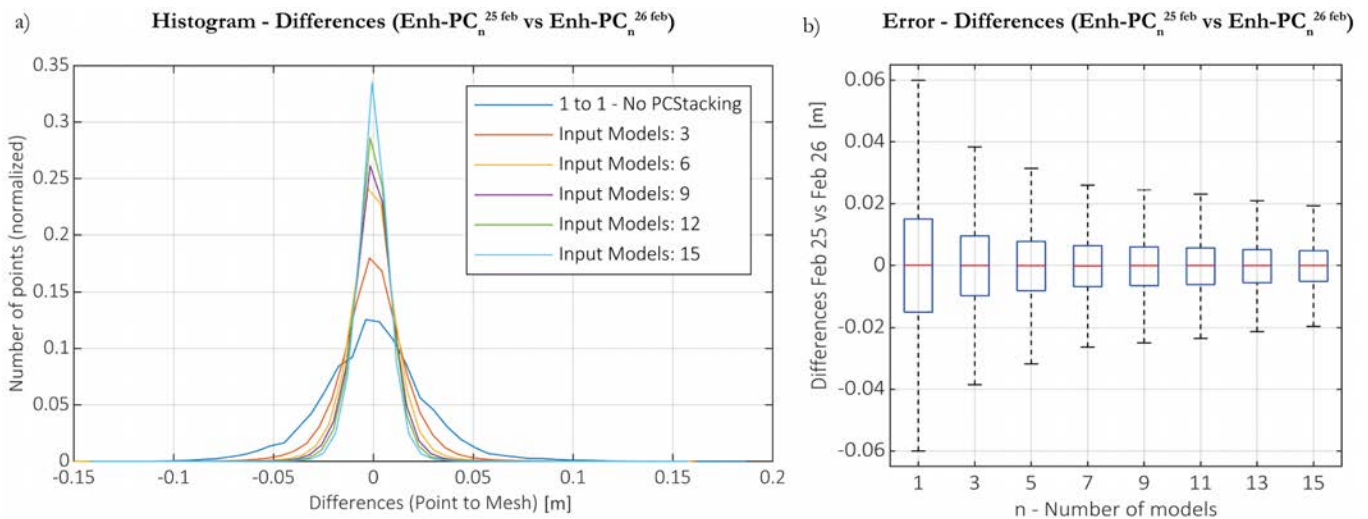


Figure III.12. Results from the application of the PCStacking algorithm to real images.

a) Histogram of the differences between the Enh-PC_n^{25 feb} and Enh-PC_n^{26 feb}. Each coloured line represents a different number of PCs introduced into the PCStacking algorithm. **b)** Error of the differences obtained in the different comparisons (Enh-PC_n^{25 feb} vs. Enh-PC_n^{26 feb}).

and denser Enh-PC. The plot in **Figure.III.11b** depicts the number of points available to average the Z coordinate, which depends on the number of Synt-PCs used as input data and on the search radius defined. This value is a very good indicator of when the algorithm has enough input points to compute the new Z coordinate.

Using this parameter as a filter, those points that were averaged using a smaller number of points were removed from the Enh-PC. For this research, all the points in the Enh-PC that were averaged using less than as many points as Synt-PCs introduced were removed. In this way, this filter easily allows the removal of points in some Enh-PC that are not generally in all Synt-PCs, such that unrepresentative points produced during the reconstruction of the model are removed.

7.1.2 3D Reconstruction on a Rocky Cliff

The process for evaluating the algorithm using real images taken on 25th and 26th February 2019 involved: i) Calculation of the Enh-PC_{n=2:15} from the February 25th PCs; ii) Calculation of the Enh-PC_{n=2:15} from the February 26th PCs; iii) Point to mesh comparison (in CloudCompare) between a February 25th Photo-PC and a February 26th Photo-PC without

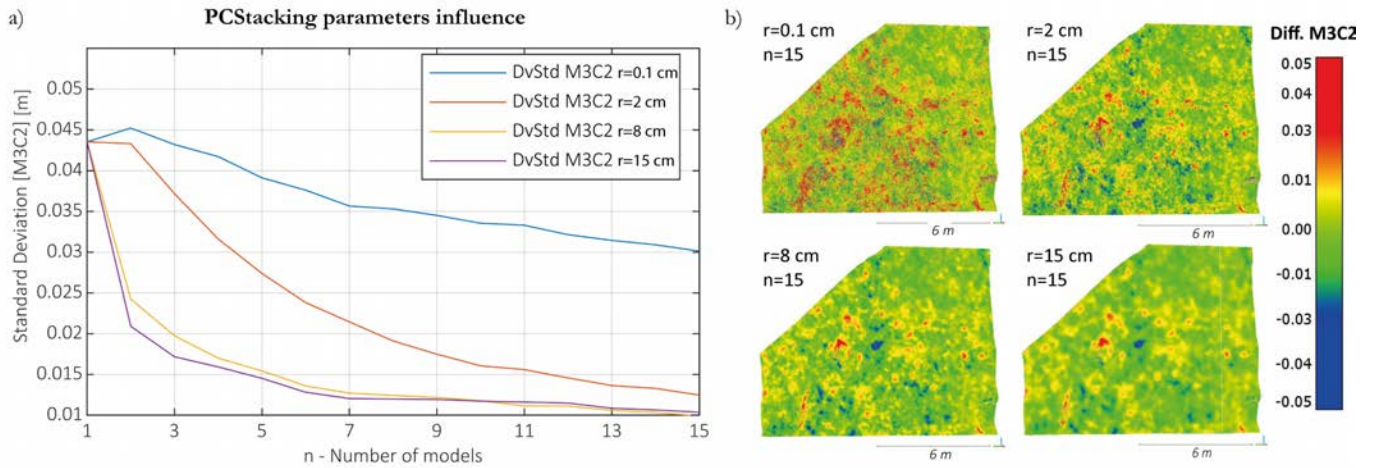


Figure III.13. Influence of the search radius (r) on the PCStacking results. **a)** Standard deviation of the $\text{Enh-PC}_n^{25 \text{ feb}}$ vs. $\text{Enh-PC}_n^{26 \text{ feb}}$ comparison. **b)** Comparisons between $\text{Enh-PC}_{15}^{25 \text{ feb}}$ and $\text{Enh-PC}_{15}^{26 \text{ feb}}$ for different search radii (r).

applying any enhancement algorithm; and iv) Point to mesh comparison (in CloudCompare) between all $\text{Enh-PC}_{(2;15)}^{25 \text{ feb}}$ vs. $\text{Enh-PC}_{(2;15)}^{26 \text{ feb}}$. The outputs from these comparisons are the distances in metric values existing between the two models studied. Given that between 25th and 26th February 2019 there was no change in the analysed cliff, the expected difference in an ideal case must be zero.

The results obtained are shown in **Figure III.12**, which is analogous to **Figure III.10**. The histogram of the values obtained in the comparison (25th February vs. 26th February) (**Figure III.12a**) demonstrates that the precision of the values increases when more models are added to the algorithm (the differences tend to zero). Moreover, **Figure III.12b** shows a decrease in the 25th and 75th percentiles of almost 70%. Values decreased from ± 1.5 cm for a simple comparison to ± 0.5 cm when comparing the $\text{Enh-PC}_{15}^{25 \text{ feb}}$ vs. $\text{Enh-PC}_{15}^{26 \text{ feb}}$.

Figure III.13 depicts the sensitivity of the algorithm from the input parameters of the code. The plot in **Figure III.13a** shows the standard deviation obtained in the comparisons made by M3C2 (Lague et al., 2013) between $\text{Enh-PC}_n^{25 \text{ feb}}$ and $\text{Enh-PC}_n^{26 \text{ feb}}$. Each plotted line represents different parameters in the search radius (r) of the PCStacking algorithm (**Figure II.26**). Note that for the smaller radius ($r=0.1$ cm) the algorithm does not lead any improvement, because as in the synthetic test (**Figure.III.11**), the small search radius does not provide enough points to average the Z coordinate in the direction of the normal.

When the search radius is larger the algorithm has more points to average, resulting in a decrease in the standard deviation of the comparisons. The images in **Figure III.12b** show the comparisons using the M3C2 algorithm between $\text{Enh-PC}_{15}^{25 \text{ feb}}$ and $\text{Enh-PC}_{15}^{26 \text{ feb}}$ for the different search radii described.

Since the proposed algorithm involves averaging the Z coordinate along the normal axis at each point, obtaining the normals at each point in the correct way is critical. As discussed in Lague et al. (2013), the roughness of the surface makes the calculation of normals dependent on the scale at which it is performed. Thus, calculating normals using inappropriate scales means that the averaging is not done in the right direction. Consequently, the efficiency of the algorithm decreases considerably.

In the case of the Synth-PC, the normals were calculated using the CloudCompare software. However, for the real case of the Puigcercós Cliff, the normals were computed automatically using Agisoft Metashape software (2019 Agisoft).

7.2 Partial discussion

7.2.1 Synthetic Test vs. Real Data

The cross-sections obtained from the synthetic point clouds (Synt-PCs) (**Figure II.28a**) and real photogrammetric models (Photo-PC) (**Figure III.10a**) are very similar. Likewise, the random distribution of the error obtained in a comparison of two Synt-PCs (**Figure II.28b**) is similar to that obtained from real data (Photo-PC) (**Figure II.29**). The use of random parameters in the sinusoidal function allows the generation of different PCs with errors that are geometrically consistent in each iteration. This is important because in the reconstruction of models obtained using low-cost photogrammetric systems, surfaces with different geometries are always generated even though the input photographs are captured at the same time. The result of using the described functions (Equations (1) and (2)) together with the random parameters (Equation (3)–(5)) generated synthetic PCs with a similar pattern to that of photogrammetric models.

Despite the above mentioned observations, the comparison between two Synth-PCs using the M3C2 algorithm (Lague et al., 2013) (**Figure II.28b**) depicts some repeatability in the

distribution of the differences, while the pattern of the comparison between two Photo-PCs (**Figure II.29b**) is absolutely random. This is because Synth-PCs were created by the sinusoidal function (Equation (2)), which is periodic. Even so, we believe that this conceptual dissimilarity in the distribution of the differences does not affect the PCStacking method trials proposed in this thesis.

To sum up, the synthetic study suite designed to test the PCStacking algorithm worked well, and the generated PCs are comparable to PCs obtained from low-cost photogrammetric models. Thus, this methodology based on the generation of synthetic functions can be extrapolated to the synthetic study of different PC improvement algorithms.

7.2.2 The PCStacking Method

The results of the assessment of the PCStacking workflow reveal a significant improvement in the precision of the enhanced point clouds. This advance was observed with both synthetic and photogrammetric PCs. In the synthetic case, the initial error of the comparison was larger (± 3.2 cm), and the reduction occurred more progressively while introducing a greater number of Synth-PCs to the algorithm, reaching ± 1.4 cm in the Enh-PC₁₈ comparison (**Figure III.10**). In contrast, real photogrammetric models had a smaller comparison error that ranged from ± 1.5 cm to ± 0.5 cm when 15 PCs were used. In this case, 50% reduction in error was achieved when using only five PCs (**Figure III.12**). This is because: i) the synthetic PCs were designed with a higher geometric error with a distribution dependent on random parameters (see Equation (2)); and ii) the errors in the real photogrammetric PCs are not homogeneous and tend to be concentrated in areas where the software has more difficulty identifying homologous points. Consequently, synthetic data has larger and more distributed errors, so the algorithm needs more input point clouds to reduce the error. Even so, the algorithm succeeded in reducing the errors in both the synthetic test and the real case, and the number of PCs used was sufficient to stabilize the error reduction.

Concerning data acquisition, the application of the algorithm using only one image per camera position (classic capture scheme), instead of a set of images as in this study, would reduce its efficiency considerably. The use of different simultaneous images captured in the same burst means that each model is built on the basis of a totally different point identification process and bundle adjustment. This is because the intrinsic errors of the

photographic sensors will always generate differences between the images, despite the short time between shots. Consequently, SfM-MVS algorithms produce different geometries generating slightly different models. The averaging of these differences through the PCStacking algorithm improves the precision of the PCs obtained from images captured using low-cost systems.

The results of the redundancy test applied to Synt-PCs reveal that the developed code is robust. The goal of this test is to eliminate any possibility of associating the improvement with the use of low random values for the generation of the Synt-PCs. As shown in **Figure.III.11a**, the standard deviation of the 20 iterations performed progressively decreased as the number of input models increased. The differences in the error bars are related to the randomness of the parameters contemplated in Equation (2) to introduce the random error to the Synt-PCs. Thus, some iterations produce Synt-PC with errors greater than others. This results in point averaging between point clouds with greater dispersion, thus augmenting the error in the Enh-PC_n vs. Ref-PC comparison.

The considerable increase in the number of averaged points shown in **Figure.III.11b** is due to two key parameters: 1) the number of input PCs and 2) the PCStacking search radius. Therefore, these two parameters control the quality of the result (**Figure III.13**). For this reason, in a real situation, a sensitivity study to determine the parameters that would improve the results is required.

7.2.3 Current Limits and Margins for Improvement

As shown in **Figure III.10**, **Figure.III.11** and **Figure III.12**, the improvement obtained by the application of the PCStacking method was not linear. In addition, **Figure III.13a** reveals that a sensitivity study of the parameters used is required because, depending on the point density of the input data, the algorithm will start working optimally from a certain search radius. The use of a very large search radius may end up involving excessive smoothing of the Z coordinate. However, the use of a very small search radius will not provide enough information for the PCStacking algorithm to perform point averaging.

The reduction in error (**Figure III.13a**) observed when using a 0.1 cm radius (extremely small) was due to the effect of the densification of the PCStacking algorithm and the

averaging of the M3C2 algorithm. In our work, the PCStacking algorithm, with a radius of 0.1 cm, did not average any value because the density of points was too low to include more than one point. Thus, the Enh-PC obtained can be considered the same as if all the input Photo-PCs had been merged without any processing. Since the search radius of the M3C2 for the comparison was the same for all analyses (1 cm), the use of the M3C2 resulted in a reduction in the error as more input Photo-PC were introduced. If the PCStacking algorithm had not had the property of densifying the PC for the 0.1 cm search radius, there would have been no improvement.

In order to identify the improvements produced by the PCStacking algorithm, the comparisons between Enh-PCs and Ref-PC in the synthetic test, and between Enh-PC_n^{25 feb} and Enh-PC_n^{26 feb} in the real case test, were calculated using the Point to Mesh comparison algorithm. Since the application of this algorithm does not produce any improvement by itself, the error reduction shown in **Figure III.10** and **Figure III.12** can be associated with the PCStacking algorithm. On the other hand, when a real representation of the distribution of differences between two PCs was needed (**Figure II.27**, **Figure.III.11** and **Figure III.13**), the M3C2 algorithm was used, since this allows better visualization of the results as well as discrimination between positive and negative values of the differences obtained.

Another important consideration before applying the method is the correct determination of the normals for each point. As cited in Lague et al. (2013), miscalculation of normals will result in poor adjustment of the method. Since the normals must be calculated based on a search radius, taking into account the roughness of each surface, it is necessary to find the best fit between both the method and the radius to obtain an optimal result with the PCStacking algorithm. However, the normals calculated directly by the digital photogrammetry software are sufficiently well-computed to allow the PCStacking algorithm to work properly.

Although the results presented show an interesting improvement in the field of point clouds, due to the differences in the errors of the photogrammetric models with respect to the LiDAR data explained in the introduction, the efficiency of the PCStacking algorithm will not be equivalent with the LiDAR data. Even so, the algorithm has not been tested with other acquisition systems. Thus, the performance of the algorithm in point clouds obtained

with other technologies has yet to be verified. If the proper computation of the normals cannot be guaranteed, the PCStacking method can be applied by modifying part of the algorithm. Instead of averaging only the Z coordinate in the direction of the normal, it will be necessary to average all the coordinates $\{x,y,z\}$ in the direction of the respective normals. In this case, exploratory tests showed that the method also produced better PCs but with greater surface smoothness.

Another discussion point is the computational cost of applying the algorithm. At its highest quality, digital photogrammetry software generates very dense PCs that easily exceed millions of points. Because the PCStacking algorithm is based on the introduction (and accumulation) of different PCs, the workspaces can easily exceed tens of millions of points. Since Z-coordinate averaging is done point-to-point, the computational cost is high.

Nevertheless, the PCStacking algorithm can also be used in low performance computers by simply subsampling the original PCs. Therefore, a necessary improvement of the method will involve optimizing the calculation. This optimization could be achieved using dedicated PC library methods that significantly speed up the process, as well as the use of PC fractionation methods.

8.1 Results

This chapter presents the results and partial discussions obtained with the MEMI workflow. The methodology corresponding to the different tests carried out can be found in **Chapter 5**. These results are part of **Publication II**.

8.1.1 Relative Accuracy of Detected Changes

The differences between the two models on two consecutive days resulting from the MEMI workflow tended mostly to zero (**Figure III.14** and **Figure III.15**), whereas the classic and MESI workflow revealed higher deviations, with the largest values measured with the former approach.

This can be observed in the maps of differences (**Figure III.14a,b,c**) and in the histograms (**Figure III.14d**) obtained using the 23rd and 24th of May 2020 images. The smallest differences between the two compared days were achieved with the MEMI workflow using four images (full MEMI workflow). The standard deviation of the M3C2 differences decreased by 50%, from 3.37 cm in the classic workflow to 1.68 cm in the full MEMI workflow. The boxplots (**Figure III.14e**) also highlight the increase in performance from classic to full MEMI, showing that both the average difference and the range of differences decreased. The computational cost of each workflow as well as the main characteristics of the models obtained are described in **Table III.1**.

Figure III.15 also shows the M3C2 distance maps for the three different workflows (classic, MESI, MEMI), using the images captured on 8th and 13th of November 2019 to assess the relative accuracy of the point clouds (**Figure III.15a**). The measured change detection with the MEMI workflow showed the lowest range of differences with respect to the other methods (**Figure III.15a**). In addition, the histograms (**Figure III.15b**) show a considerable reduction in the standard deviation of the differences (nearly 50%) when using MEMI, decreasing from 2.83 cm with the classic workflow to 1.54 cm with the MEMI workflow (**Table III.2**).

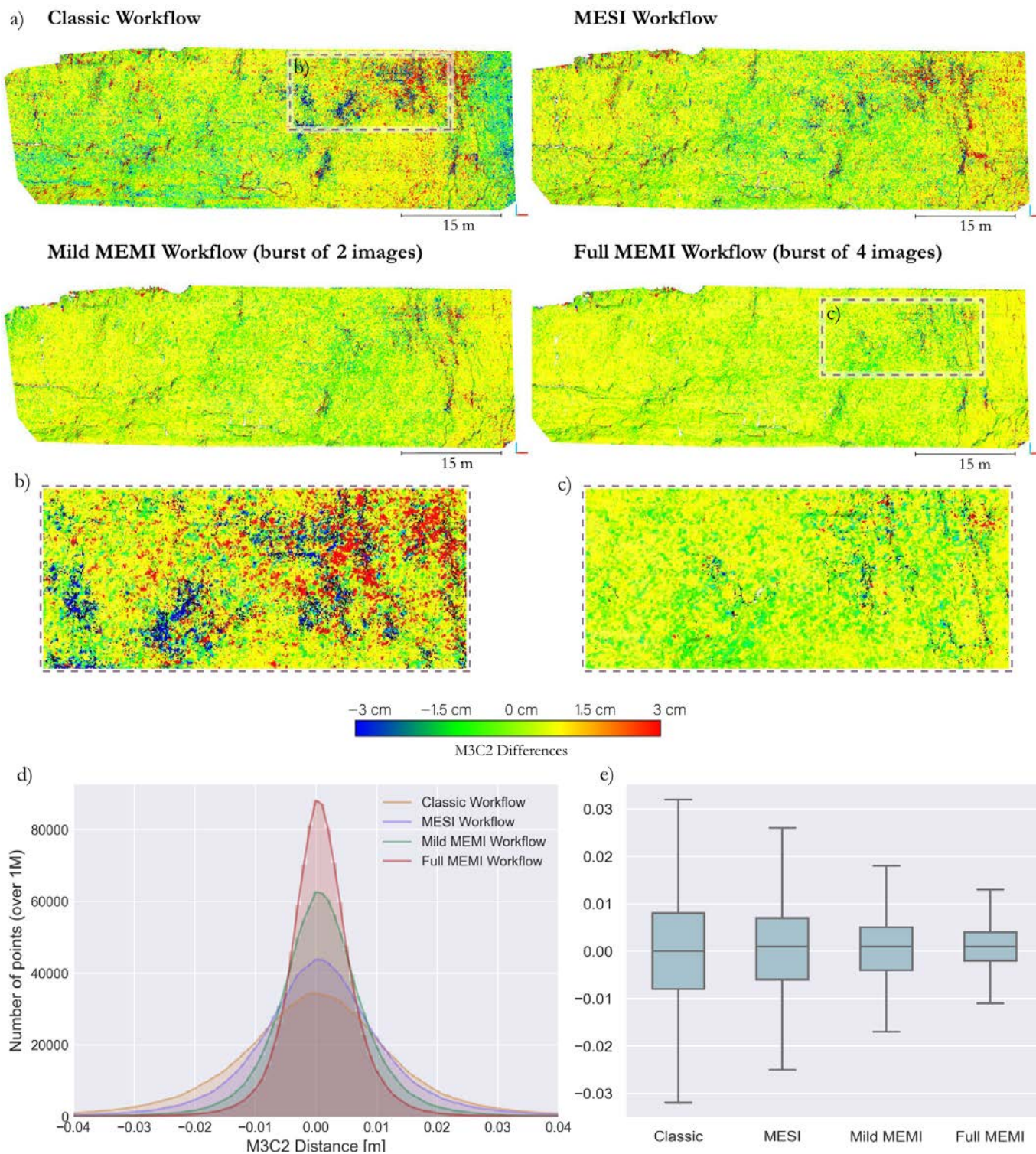


Figure III.14. a) Graphic representation of the differences between the models of May 23 and 24, according to the workflow used. The four models are represented using the same colour scale. Zoom detail (inset) of the **b)** classic workflow and the **c)** full MEMI workflow. **d)** Histogram with the M3C2 results. **e)** Error bar plot with the dispersion of the values obtained in each comparison.

Table III.1. Main parameters of the results obtained in the May 2020 test.

	Classic Workflow	MESI Workflow	Mild MEMI Workflow	Full MEMI Workflow
Tie points	55.106	67.950	177.451	217.619
Matching time	20 s	1 min 6 s	3 min 30 s	8 min 53 s
Matching memory	4.85 GB	4.90 GB	5.18 GB	5.07 GB
Alignment time	4 s	27 s	2 min 41 s	6 min 2 s
Dense Point Cloud (points)	11.432.934	11.336.012	10.453.432	11.101.038
Depth map time	23 s	31 s	1 min 30 s	4 min 32 s
Dense Cloud time	35 s	36 s	59 s	1 min 51 s
Mean M3C2 distance (mm)	-0.55	1.01	1.03	0.78
St. Dev M3C2 (cm)	3.37	3.00	2.22	1.68

8.1.2 Interior Precision of the Point Clouds

Figure III.16 shows the results obtained from the precision estimation test using the November 2019 images. **Figure III.16a** shows the distribution of σ_y , which is the most important parameter for change detection in this study as it is the direction of highest deformation (depth direction). The results of the MEMI workflow show that precisions between 0 and 3 cm were concentrated in the central zone of the area of interest. Thus, this zone demonstrated the best photogrammetric reconstruction performance.

With increasing distance from the central region (of highest image overlap) the precisions decreased in a spatial, radial-symmetric pattern. Similar patterns, but with higher magnitudes of precision, were identified in the MESI workflow. Such high values of σ_y were not obtained in the classic workflow, as shown in the error boxplots (**Figure III.16b**). In general, the estimated precision of change detection was considerably higher with the MEMI workflow when compared to the classic and MESI approaches. The use of MEMI reduced both the error values as well as the range of these values along the escarpment, reaching σ_x and σ_z values below 2 cm (**Table III.3**).

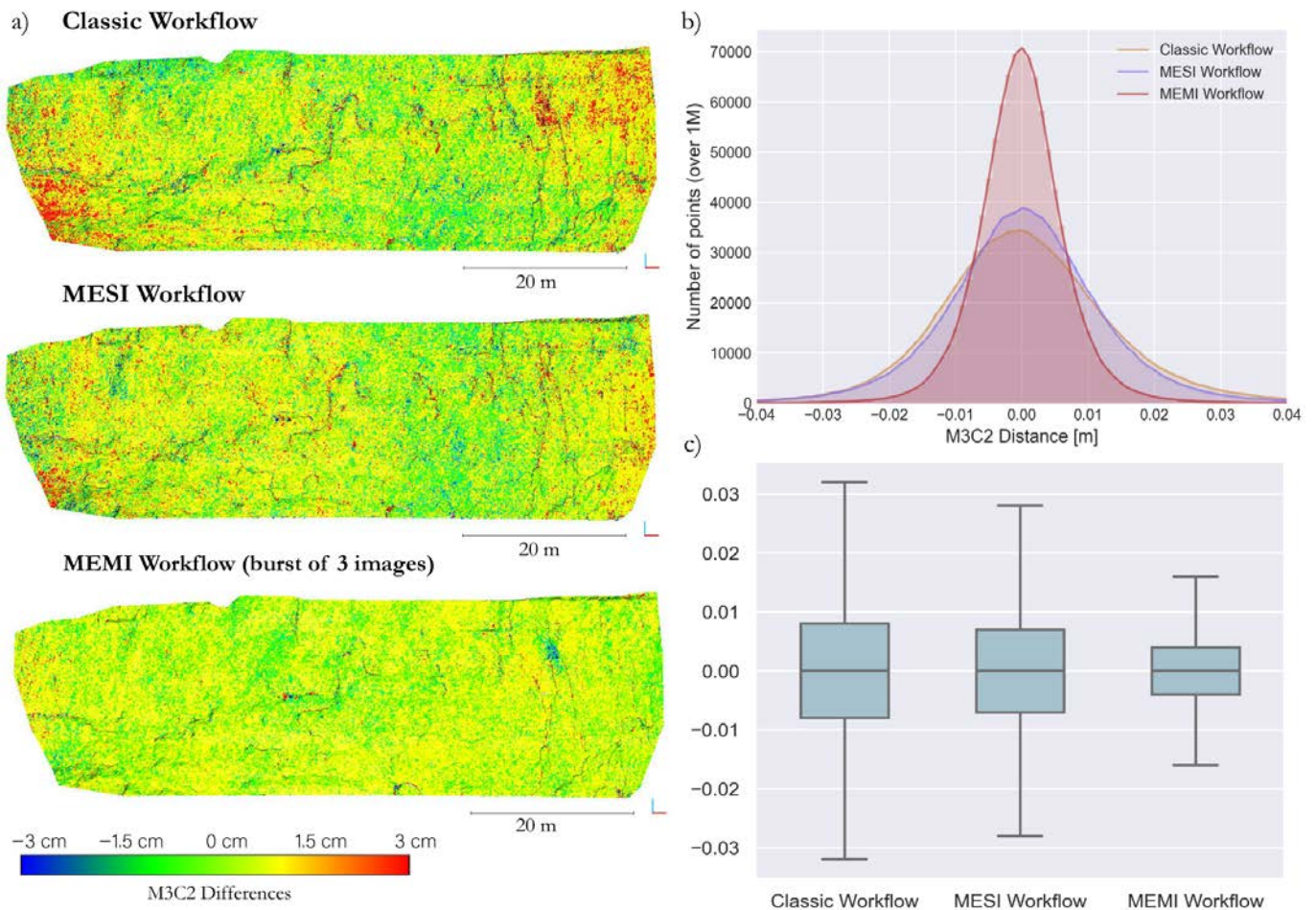


Figure III.15. a) Graphic representation of the differences between the models of November 8 and 13, according to the workflow used. The three models are represented with the same colour scale. b) Histogram with the M3C2 results. c) Error bar plot with the dispersion of the values obtained in each comparison.

8.1.3 Absolute Accuracy of a Single Point Cloud

Figure III.17 shows the M3C2 results obtained in the comparison of the three approaches described in **Figure II.30** in comparison to a reference LiDAR dataset. **Figure III.17a** illustrates a small part of the cliff with the results of the M3C2 comparisons. Three images are represented using the same colour map.

We observed that the MEMI vs. LiDAR data results showed lower random errors and that the detected rockfalls were better represented than in the classic or MESI results. In general, non-deformation zones (yellow and green) predominated in the MEMI comparison with

respect to the other approaches. However, it should be noted that the best comparison was not error-free either, as very small clusters with false deformation were identified.

Due to the presence of rockfalls, the absolute standard deviation parameter does not represent a correct accuracy parameter. For this reason, **Figure III.17b** shows the relative variation of the standard deviation with respect to the best comparison (MEMI vs. LiDAR data).

Table III.2. Main parameters of the point clouds and M3C2 results obtained in the November 2019 test.

	Classic Workflow	MESI Workflow	MEMI Workflow
Tie points	39.953	89.681	204.939
Matching time	18 s	1 min 3 s	8 min 36 s
Matching memory	4.86 GB	4.87 GB	5.13 GB
Alignment time	4 s	31 s	5 min 56 s
Dense Point Cloud (points)	11.263.507	11.242.875	10.961.212
Depth map time	36 s	431 s	5 min 52 s
Dense Cloud time	39 s	39 s	1 min 55 s
Mean M3C2 distance (mm)	0.87	0.47	0.09
St. Dev M3C2 (cm)	2.83	2.45	1.54

Table III.3. Main results obtained in the precision estimation test.

	Classic Workflow	MESI Workflow	MEMI Workflow
σ_x (mean)	37.5 cm	3.0 cm	1.7 cm
σ_y (mean)	44.8 cm	5.4 cm	3.0 cm
σ_z (mean)	15.5 cm	1.9 cm	1.1 cm

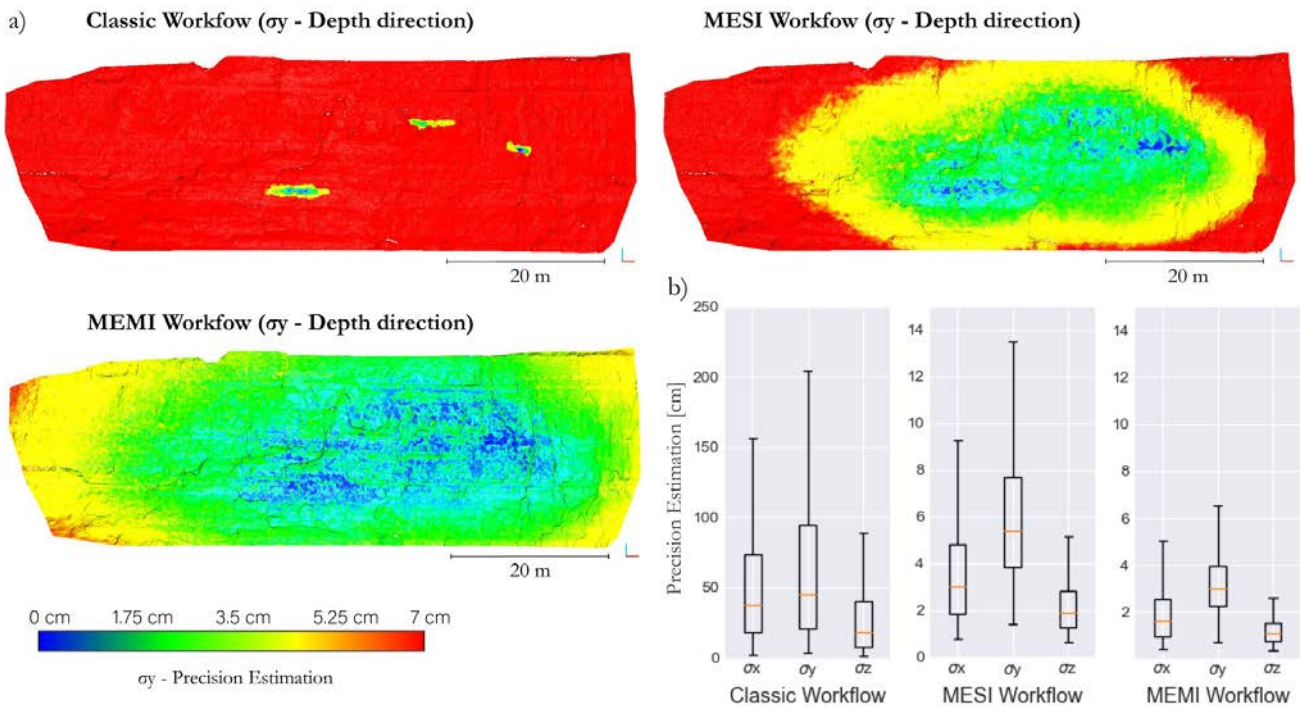


Figure III.16. a) Results obtained from the precision estimation test, considering the distribution of σ_y (depth direction). b) Error boxplots of the range of the precision estimations (note the different scale on the y axis).

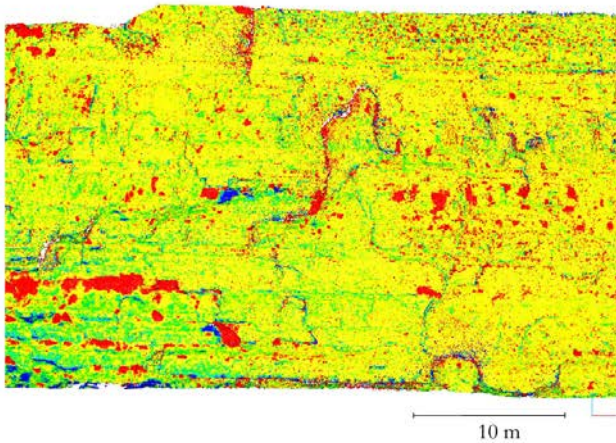
The standard deviation of the M3C2 comparison increased by 19% when using the MESI algorithm and by 24% when using the classic workflow. Also, the graph in **Figure III.16b** shows how the comparison with the highest points (97% of the points) within the range of ± 10 cm was the one made using the MEMI approach. The other workflows had lower values (close to 96%), which means that more points were in the range above ± 10 cm.

8.2 Partial discussion

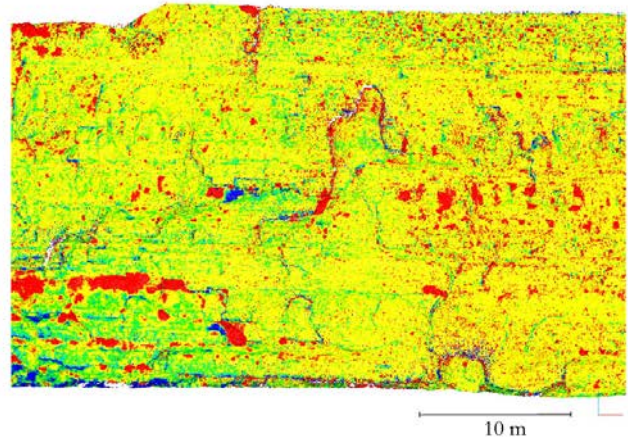
8.2.1 Automated and Multi-Epoch Multi-Imagery (MEMI) Workflow

The results presented in this chapter demonstrate a significant improvement in the methodology employed to obtain automatic photogrammetric models using time-lapse cameras. The use of new methodologies such as the multi-epoch imagery (MESI) workflow already represents a considerable improvement in photogrammetric models as described in Feurer and Vinatier (2018) and Cook and Dietze (2019). However, the multi-epoch multi-

a) Classic Workflow vs LiDAR Data



MESI Workflow vs LiDAR Data



MEMI Workflow vs LiDAR Data

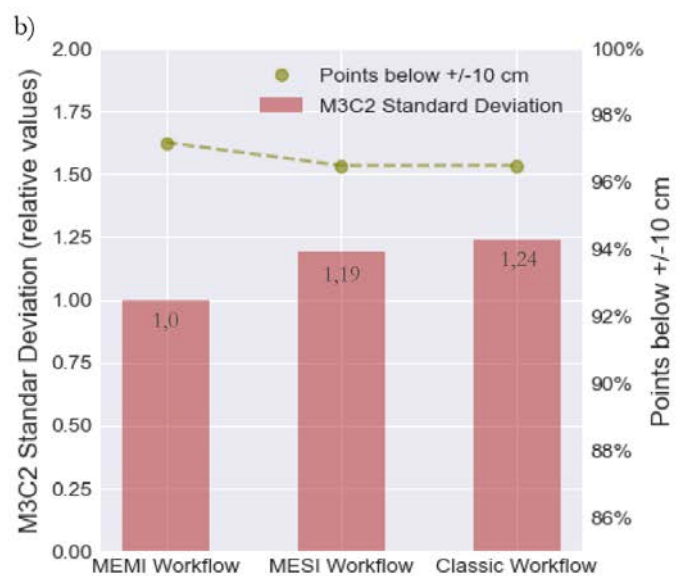
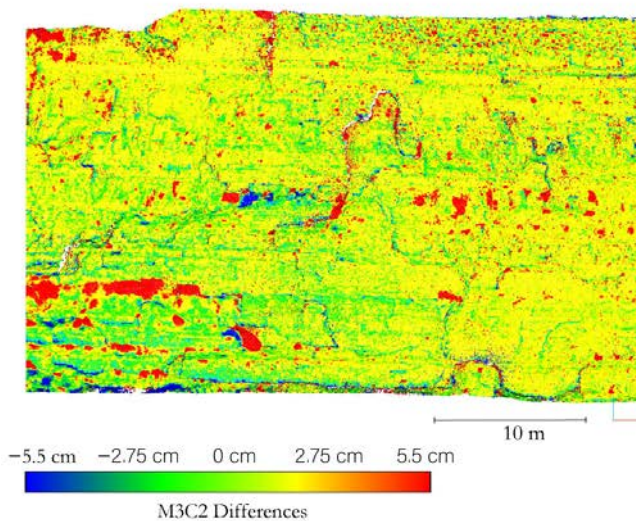


Figure III.17. a) Graphic representation of the differences between the LiDAR data (October 2019) and photogrammetry models (November 2019), according to the workflow used. The three models are represented with the same colour map. The larger red clusters indicate rockfalls that occurred during the comparison period. **b)** Bar plot showing the relative M3C2 standard deviation of the comparisons.

imagery (MEMI) workflow proposed in this thesis allowed us to obtain photogrammetric models with greater geometric consistency and less error in the change detection comparison.

The main limitation of the pipeline presented in this chapter is that it requires simultaneous photographs from the same locations during two different periods, so it cannot be applied to images obtained by UAV, manual systems or historical pictures. A system of fixed cameras

is required for the proper performance of the system. Although the cameras are installed in fixed systems of concrete, the acquired images are not identical because there are variations in sensor position due to vibration, wind or temperature change, which is why it is necessary to apply automatic algorithms that allow one to track and obtain automatic GCP.

It should be noted that the results obtained in all performance assessments were obtained automatically using the entire pipeline proposed herein. The automation of the process increases the capacity for analysis and allows the data to be constantly processed in a server without the attention of an operator. Furthermore, it overcomes one of the main limitations that exist when working with a great deal of data, which is the effort and man-hours required to work with the data manually. Overcoming this limitation is critical to 4D change detection work.

Focusing on the photogrammetric workflow presented in this thesis, we can define the enhanced workflow as a method for fixed cameras in which no lens calibration is required. Many articles have previously described the need for correct lens calibration. The results obtained using the classic method and MESI workflow reveal how some of the errors obtained have a dome effect classically associated with poor characterization of the intrinsic parameters of the camera.

The MEMI workflow eliminates these errors thanks to the better characterization of the intrinsic parameters in the automatic lens calibration process performed by the photogrammetric software. All results have been obtained without any initial parameters developed based on a camera pre-calibration.

This improvement may be due to the redundancy of input data when solving the automatic calibration. However, the working method does not succeed in eliminating the classic limitations that are characteristic of all photogrammetric processes. The quality of the model obtained decreases as we approach the extremes of the model, because the photographic coverage of these points is more precarious. Also, in the shaded or poorly resolved areas of the images we find problems when making the photogrammetric reconstruction. The use of advanced methods does not end with the classic limitations of photogrammetry, such as the loss of quality at the ends of the model, but helps to mitigate its effects.

Despite the above limitations, the workflow presented allows the comparison of photogrammetric models with a better quality than when using the classic method, and allows work without lens calibration and without control points. These improvements simplify and facilitate the use of photogrammetric systems, especially in dangerous areas where it is impossible to reach the study area. A clear example of the application of this method is rockfall monitoring where it is impossible to access the cliff to install control points due to the danger of rockfall.

The results obtained in this study enable us to show both the improvements obtained using the multi-epoch single-imagery (MESI) workflow and the more advanced workflow multi-epoch multi-imagery (MEMI) developed in this work. The use of MESI workflows leads to an increase in accuracy and precision due to the fact that the spatial error behaviour is mitigated during change detection (i.e., by subtracting models and thus errors).

Multi-imaging (at the same point in time) leads to increased accuracy and precision, since the photons hit the sensor with a normal distribution and therefore slightly different image features are subsequently detected (leading to slightly different models). Therefore, the more images the greater the consistency obtained in the bundle adjustment, and consequently the higher the accuracy and precision. The synthesis of these two enhancement concepts is what produces the improvements we obtained for photogrammetric tracking systems from fixed time-lapse camera systems.

However, it should be noted that further work is needed to correctly identify which mechanism provides the best results. The use of proprietary software that works as a black box precludes us observing exactly which part of the processing is affected by the use of multi-imagery. Although the improvement in the results obtained is evident, the reason why the use of multi-imaging has an impact on the results cannot be fully explained using our research.

8.2.2 Relative Accuracy of Detected Changes

One of the methods used in this chapter to present the workflow improvements is a change detection analysis between photogrammetric models obtained on consecutive days. Working with photographs obtained on consecutive (or almost consecutive) days allows us to assume

that there are no significant differences between the models, and consequently that the change detection comparison should be close to 0. Moreover, this type of comparison allows us to quickly determine the errors that occur in the reconstruction process.

For this publication, two change detection tests were performed. The first test used the best possible data, using a burst of images of four photographs from two consecutive days in May 2020. The second test used the earliest available images (and closest to TLS data) captured on two close dates in November 2019. In this configuration only bursts of three photos were available. The M3C2 method, widely used in the quantification of differences in photogrammetric models, was used to eliminate non-representative deformation errors in comparisons of two point clouds.

In both tests (**Figure III.14** and **Figure III.15**) we can see graphically how the differences obtained tended to zero when we used a MEMI workflow. These graphic observations were corroborated by the analysis of histograms. Both histograms showed that the classic workflow accumulated fewer points near zero with a greater dispersion of differences. On the other hand, the MEMI workflow accumulated many more points near the zero-deformation value and produced histograms with a lower dispersion of values.

The evolution of these values can also be observed in the error bar plot of **Figure III.14e** and **Figure III.15c**. **Figure III.14e** shows that when using the MEMI workflow with a burst of two images per position (mild MEMI workflow), the results obtained contained smaller geometric errors than when using the classic method or the multi-epoch single-imagery described by Feurer and Vinatier (2018).

The results shown in **Figure III.14** and **Figure III.15** were obtained from different input data. Both figures show how the comparison accuracy improved with the pipeline presented in this article, reaching M3C2 standard deviations of around 1.5 cm. The improvement in the comparison accuracy is a relevant factor, since it enables the threshold in the detection of changes to be reduced, thereby increasing the ability to identify changes in the photogrammetric models studied. However, both figures also show how in the areas farthest from the centre there is a tendency to accumulate errors. These errors were mitigated in the more complex workflows, but they did not disappear. This suggests that these are areas

where the identification of homologous points is poor, and the reconstruction of the model does not achieve the same quality. In future works, it would be of great interest to test the performance of the MEMI algorithm in scenarios with larger differences between captures in order to determine whether the accuracies obtained in non-deformation scenarios are valid in scenarios where there are significant changes.

8.2.3 Interior Precision of the Point Clouds

In order to determine the interior precision of the point clouds, GCP was used to quantify precision at the real scale. However, the working method presented in this thesis does not necessarily require control points, since the resulting models for comparison share the same location of cameras and are perfectly positioned between them. It is interesting to note that the use of this workflow eliminates the tedious alignment process between point clouds. Because we work with fixed cameras, we can use GPS to obtain the location of each sensor, allowing the photogrammetric software to provide a georeferenced model without the need to use GCP control points, or we can align the locations with georeferenced data. However, the use of GCP allows better georeferencing as well as the possibility of implementing control points.

To calculate the precision, we took advantage of the methodology developed by James et al. (2017), which allowed us to obtain precision parameters from the control points that were used in the model. In the graphic visualization (**Figure III.16a**) we can see the evolution of σ_y (parameters that indicate the precision in the direction of the deformation). Obtaining these values is subject to the precision of the GCPs introduced in the bundle adjustment phase. It should be remembered that for this work the GCPs were extracted from the local coordinates of a LiDAR TLS 3D model, so the precision obtained in the GCP extraction was not particularly high.

However, we are publishing these results with the intention of showing the progression of the estimation precision within the different workflows, as the same GCPs were used for all cases. We do not wish to focus on the absolute results, but rather on the fact that the comparison is relevant in relative terms. For this reason, **Figure III.16b** shows how values were reduced considerably as more complex workflows were used.

Although obtaining the coordinates of the control points must be done in a more robust way, achieving precision values of less than 2 centimetres on the x and z axes and close to 3 centimetres on the y axis is remarkable. This precision estimation test represents a good way of expressing the improvement in real precision obtained using the MEMI workflow shown in this study.

8.2.4 Absolute Accuracy of a Single Point Cloud

The results obtained in the comparison of the different photogrammetric workflows with a LiDAR point cloud confirm the improvement that the MEMI workflow represents. It should be noted that the results do not show a perfect non-deformation comparison because there was a one-month difference between the LiDAR acquisition and the photogrammetric models.

This temporal gap is the reason why, in the comparison, in addition to obvious erroneous clusters, obvious rockfalls were identified, as shown in **Figure III.17a**. It should also be noted that the identification of rockfalls was much more reliable in the MEMI comparison than in the other workflows tested.

Due to the presence of rockfalls, the absolute values obtained are not representative of the absolute accuracy of the method. For this reason, the results are expressed in relative terms (**Figure III.17b**). Both the graphical comparison and the relative quantification of the M3C2 standard deviation demonstrate that the use of the MEMI workflow substantially improves the absolute accuracy.

The use of multi-temporal multi-imaging algorithms minimizes the geometric error, yielding a 3D model much more similar to the one obtained by LiDAR (perfect in geometric terms). Furthermore, the improvement in absolute accuracy was due to the use of multi-images, as the differences between the classic workflow and the MEMI were not as clear. However, future work in which LiDAR data and photographs can be obtained simultaneously (non-deformation between LiDAR model and photogrammetric model) will allow the absolute accuracy of the different working methods proposed in this research to be achieved in a much more robust way.

Section IV

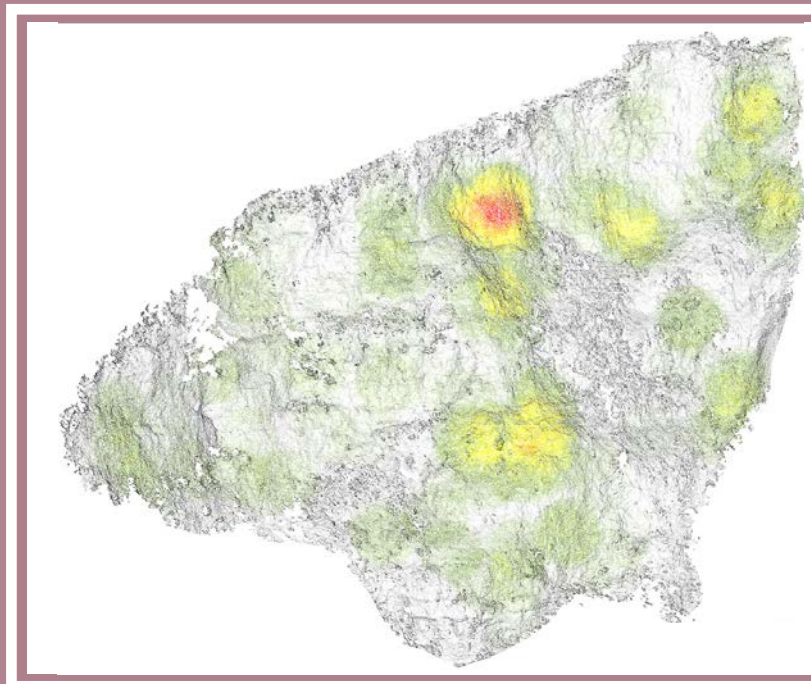
ROCKFALL

MONITORING

CHAPTER 9 – ROCKFALL MONITORING WORKFLOW

CHAPTER 10 – APPLICATION CASES

CHAPTER 11 – BRIEF DISCUSSION



Chapter 9

Rockfall Monitoring Workflow

09

At this point of the thesis, the development and improvement of photogrammetric systems, algorithms and workflows that allow better 3D comparison has been presented and discussed. Everything developed before this section has multiple uses in many different fields of remote sensing and monitoring.

Although the publications in this thesis focus on the development and improvement of the photogrammetric method for obtaining point clouds, throughout this research, significant contributions have also been made to the workflow used to identify rockfalls from point cloud comparison (regardless of the type of point cloud used) evolving the research into the field of geology and geohazards.

The simple acquisition of point clouds does not by itself enable the characterisation and identification of rockfalls. Different algorithms and workflows are needed to identify the rockfall, to calculate its volume or to recognise the deformation prior to the rockfall (pre-failure deformation). The point clouds used in these processes are typically acquired from LiDAR or digital photogrammetry.

The methodology and application cases shown below have not been published. Although they are currently used for the production of scientific reports, they have not yet been analysed as deeply as the author would desire.

For these reasons, the author decided to organize all the content relating to rockfall monitoring in a single section that is separate from the results published. **Section IV** describes and exemplifies the contribution that this thesis makes to the field of geosciences, and specifically to geohazards, and should be understood as an example of the application of all the methodology developed (hardware and software).

9.1 Brief background

The classical workflow used with LiDAR datasets for rockfall identification is extensively described in the previous theses of the RISKNAT research group members Abellán (2009) and Royán (2015). They give an extensive description of the methods and workflows used not only to identify rockfalls and calculate its volume, but also to identify pre-failure deformations. Over time, these workflows have been evolving as new methods have been proposed and new processing software has been developed. The origins of the 3D temporal comparison methodology can be found in Rosser et al. (2005) and Lim et al. (2005), where they present the basic framework of:

- * Point Cloud acquisition
- * Alignment of these datasets
- * Comparison between the aligned point clouds
- * Calculation of the differences between datasets

Several examples of the application of this general structure can be found in Abellán et al. (2009); Barlow et al. (2012); Lim et al. (2010) or Oppikofer et al. (2008).

Focusing this brief background on the methodological advances developed by the RISKNAT research group, the doctoral thesis of Abellán (2009) improves the method proposed by Rosser et al. (2005) and Lim et al. (2005), but concentrating on the detection of pre-failure deformation. For this purpose, Abellán developed an extended workflow capable of identifying rockfalls and pre-failure deformation.

Furthermore, Abellán describes the use of Nearest Neighbour (NN) averaging filters. This contribution, made especially for LiDAR datasets, makes it possible to identify the pre-failure deformation that cannot be done in the raw data. Subsequently, Tonini & Abellán (2014) introduced the use of clustering algorithms.

These algorithms enable rockfalls to be extracted from the 3D change detection result. This extraction can be performed in several ways, the most common in the literature is the use of the DBSCAN algorithm (Ester et al., 1996), briefly explained in the introduction to this

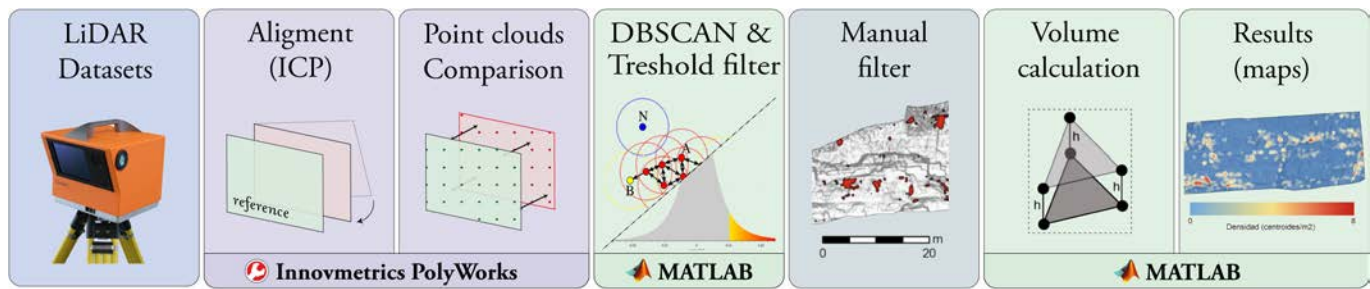


Figure IV.1. Workflow developed by researchers Abellan (2009) and Royán (2015) from the RISKNAT research group. The colour of the box represents a different process or software.

dissertation (see 2.3.3, page 63). Finally, the thesis by Royán (2015) sets out all the methodology described in these lines and develops the workflows and codes for the detection of rockfalls that form part of the beginning of this research.

The workflow developed in RISKNAT, which is the precursor to my specific research in the field of rockfall monitoring, can be summarised by the following elements shown in **Figure IV.1**, which are defined as follows (each point corresponds to each box in **Figure IV.1**):

- a) Data acquisition from terrestrial LiDAR.
- b) Alignment of two-point clouds using the Iterative Closest Point (ICP) algorithm of Chen & Medioni (1992) in the proprietary software InnovMetric Polyworks ©.
- c) Point-to-point or mesh-to-point comparison between the two aligned point clouds, also in the InnovMetric Polyworks © software with black box algorithms.
- d) Rockfall classification using the DBSCAN clustering algorithm (Ester et al., 1996) in MATLAB © proprietary programming code and threshold filter to remove points with irrelevant deformation (explained in detail on page 190).
- e) Manual filtering by visual inspection to remove those elements that have been classified as rockfalls but are not rock detachments (False Positives). Usually, Royán (2015) refers to edge errors or vegetation.
- f) Volume calculation using a script developed in MATLAB ©, adding the volumes of all the triangular prisms that constitute the rockfall (Royán, 2015).
- g) Output. These may be rockfall inventories, location maps, centroid calculations, density maps or magnitude-frequency curves

The aim of this specific part of the research is threefold: i) First, to adapt the previous knowledge acquired by the RISKNAT research group for rockfall identification from LiDAR datasets to the new photogrammetric datasets arising from the new workflows (specifically MEMI Workflow); ii) to transform old workflows that use privative software to free programming languages and open-source software; and iii) to try to automate all stages of the processing flow as far as possible to avoid the bottleneck stemming from the need of a user to process the data.

As we have seen previously, the use of photogrammetric processing algorithms such as MEMI workflow does not require further alignment, because the two resulting point clouds share exactly the same external camera orientations. For this reason, the workflow developed in this part of the thesis does not require the point clouds alignment. Thus, the adaptation of the workflow according to the origin of the dataset is necessary. Moreover, part of the workflow has been adapted to new algorithms (such as the M3C2 comparison method (Lague et al., 2013)) that have emerged in recent years.

The desire to use free programming languages and open-source software has already been mentioned at the beginning of this thesis. The author strongly believes that the best way to advance science is to share knowledge, and the first requirement is to be able to share, reuse and distribute it without being subject to any proprietary licence. This conceptually feasible task requires a change of all old scripts (from MATLAB language to Python) and the creation of new scripts and workflows for the new software used.

The last objective is the most ambitious. Given the high degree of automation of the entire photogrammetric process described in the previous chapters, the idea is also to automate the entire rockfall identification process. Success in this section would mean that, automatically and without user intervention, the whole system (photogrammetric devices + photogrammetric workflows + rockfall processing) would enable the obtention of images in the field and after a few minutes extract the list of identified rockfalls as a result. Achieving this goal or getting close to it would constitute an unprecedented improvement in the field of low-cost automatic monitoring systems.

Finally, the large amount of data generated from the photogrammetric systems designed in this thesis requires that their management and processing be automated as much as possible in order to optimize the use of these systems and take advantage of their full potential. Otherwise, it would be very difficult and time-consuming to process all the acquired data.

9.2 Rockfall detection workflow update

As explained in the previous chapters of the thesis, the final goal of the entire photogrammetric flow described in this project is to automatically obtain the best possible point clouds that represent as accurately as possible the reality of the terrain captured from the installed cameras (upper part **Figure IV.2**). Once this result has been achieved, the automatic rockfall detection process can be carried out.

Since the point clouds obtained using the MEMI workflow do not require alignment, the first step to update the rockfall detection workflow is to remove the ICP alignment. This initial step enables the rockfall detection workflow to be performed with the certainty that the point clouds are completely aligned. Although it may seem trivial, part of the failure in identifying rockfalls with LiDAR data stems from the lack of a correct alignment between the point clouds, and this made it necessary to repeat the whole process from beginning to end.

Consequently, the first step in our workflow is to directly compare the two-point clouds obtained as a result of the MEMI workflow. In this case, a methodological novelty is also adopted. This is based on using the M3C2 comparison algorithm (Lague et al., 2013) instead of the classical point-to-point or mesh-to-point comparison processes. These improvements have been addressed in the introduction to the thesis (see **2.3.3**, page 62).

This comparison is applied directly on the raw point clouds (**Figure IV.3a**). The result is a new point cloud where a difference attribute (diff) is added (**Figure IV.3b**). This attribute contains the distance between the two point clouds at each point. This parameter is of vital importance in our rockfall identification workflow, as it is responsible for indicating if an area has suffered a change or not.

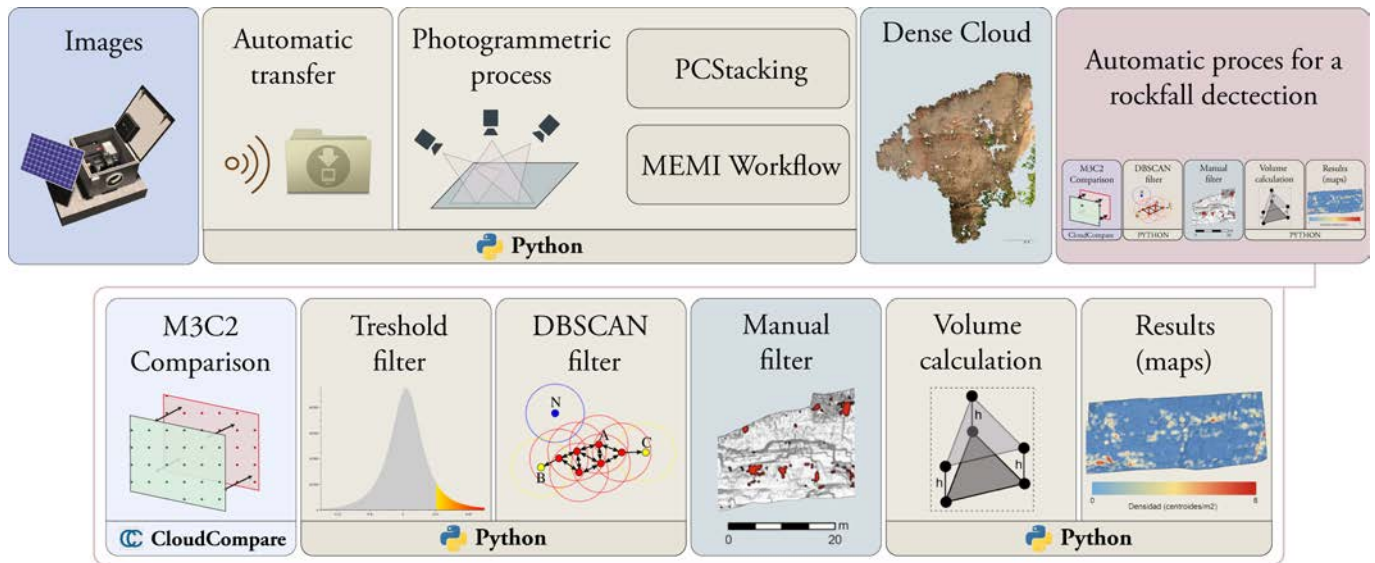


Figure IV.2. Update of the rockfall detection workflow. The top row shows how the rockfall detection workflow fits into the general photogrammetric flow developed in this thesis. The bottom row shows the implemented update, with new stages and new programming languages. The colour of the box represents a different process or software.

To summarize, we can say that:

- * $\text{Diff} \approx 0 \Rightarrow$ No changes between the two-point clouds.
- * $\text{Diff} > 0 \Rightarrow$ Positives changes (e.g., loss of material, erosion).
- * $\text{Diff} < 0 \Rightarrow$ Negative changes (e.g., gain of material, sedimentation).

The sign of the differences does not strictly express the direction of the deformation as it depends on which point cloud is considered the reference point cloud in the comparison algorithm.

The next step is to perform a filtering using a threshold value of the difference attribute to eliminate all the points that have a smaller difference between the two-point clouds (**Figure IV.3c**). When applying this filter, we remove all the points that have a smaller difference between the two-point clouds. If we apply a threshold filter of 0.03 m, we eliminate: i) All the points that have not suffered any change ($\text{Diff} \approx 0$); ii) Points that have a change of opposite sign to the one we are interested in ($\text{Diff} < 0$), and iii) Points that have suffered a change, in the desired direction, but the value is too small to be considered a real positive change (it can be caused by the dispersion of the point cloud) ($0 > \text{Diff} > 0.03$).

The establishment of this threshold is subjective and can be achieved in different ways. The values used in this thesis (between 0.03 m and 0.05 m) are defined in accordance with those previously described by Abellán 2009 and Royán 2015. The points that pass this filter are points that can potentially be identified as rockfalls.

Since the rockfalls that we have identified are represented by more than one point (usually hundreds or thousands), it is crucial to determine whether a point is isolated or forms part of a small group of points, which are produced by noise, or whether it is part of a considerable concentration of points, which may potentially be a rockfall (**Figure IV.4a**). To perform this task, the DBSCAN clustering algorithm (Ester et al., 1996) is used. This algorithm introduced by Abellán (2009) in the workflow is briefly described in the introduction to this thesis (page 67) and extensively described in Ester et al. (1996).

However, experience with both LiDAR and photogrammetric datasets indicates that not all clusters obtained after DBSCAN process can be associated with rockfalls. The presence of vegetation, edge errors (typical of LiDAR), shaded areas or errors in the photogrammetric reconstruction can lead to wrong clusters (not representing a rockfall) that overcome both the initial threshold filter and the DBSCAN algorithm. For this reason, it is necessary to introduce a manual filtering. In this filtering stage, an expert operator analyses the results cluster by cluster and, on the basis of their shape, density, situation, and viability, determines whether or not they are a rockfall (**Figure IV.4b**).

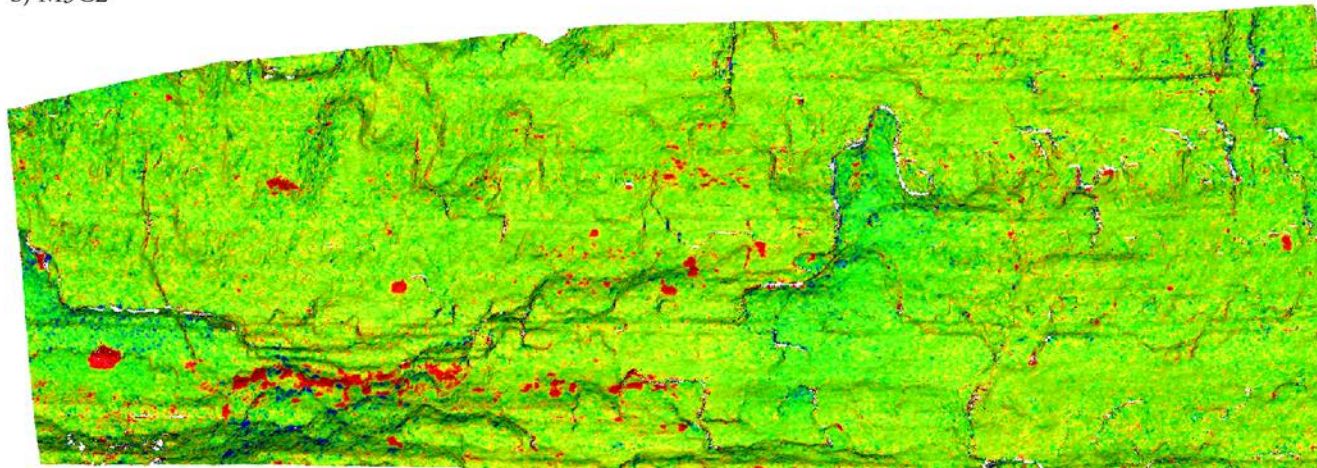
With the rockfalls identified, the last step is the calculation of their volume. The calculation method is extensively described in Royán (2015) and is based on: i) triangulating all the points that make up the rockfall; ii) transforming these triangles into triangular prisms using the average difference value as the height; iii) calculating the volume of the triangular prism, and iv) summing all the volumes obtained. In addition, based on the location of each rockfall and its volume, different representations of the results can be obtained, such as a density map shown in **Figure IV.4c**, which represents the density of rockfalls in a certain radius.

The entire workflow described above has been implemented using the Python programming language, both the new procedures and those inherited from the initial RISK NAT workflow. The different scripts can be found in the digital repository of this thesis (**Appendix A**).

a) Point cloud (6,800,000 points)



b) M3C2



c) Treshold (0.03 m - 94,150 points)

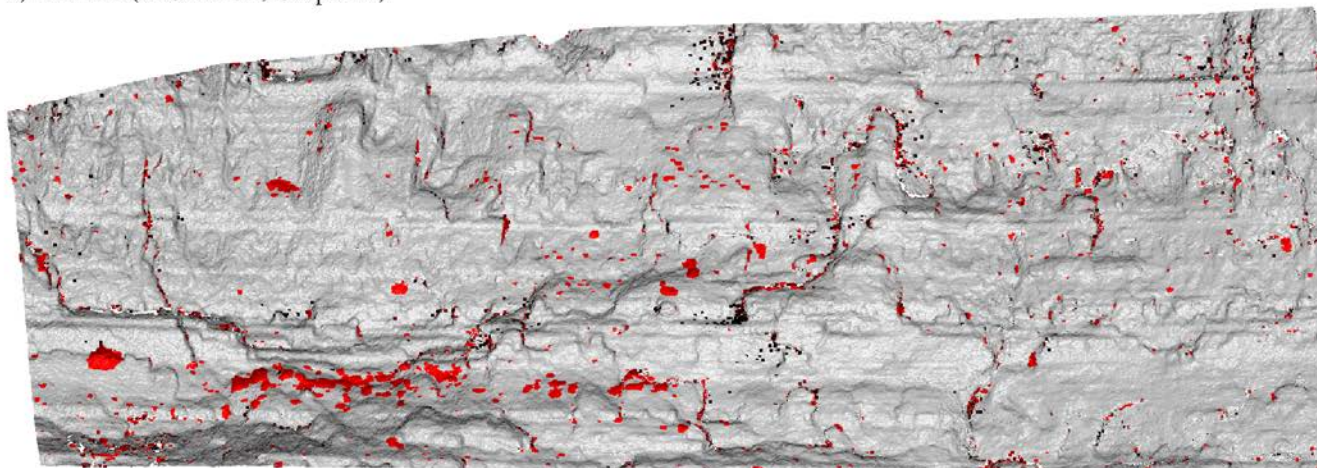
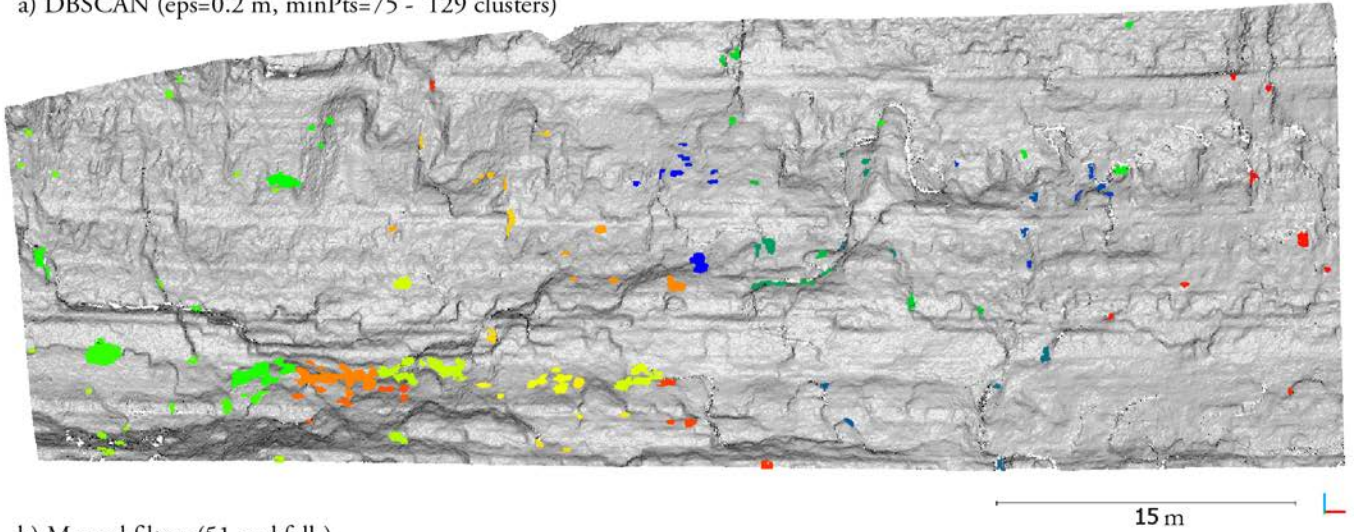
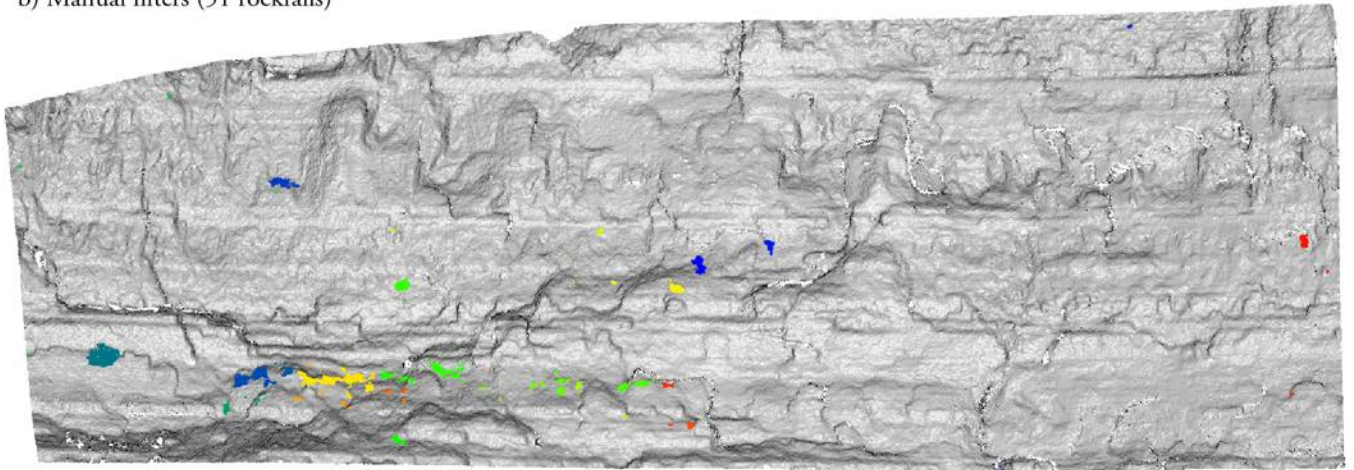


Figure IV.3. Snapshots of the different stages in the rockfall detection process:
a) Original point cloud. **b)** Result of the M3C2 comparison. Green colours indicate $\text{Diff} \approx 0$, red colours indicate $\text{Diff} > 0$. **c)** In red, points over the treshold ($\text{Diff} > 0.03$).

a) DBSCAN (eps=0.2 m, minPts=75 - 129 clusters)



b) Manual filters (51 rockfalls)



c) Density map 3D sphere (r = 5 m)

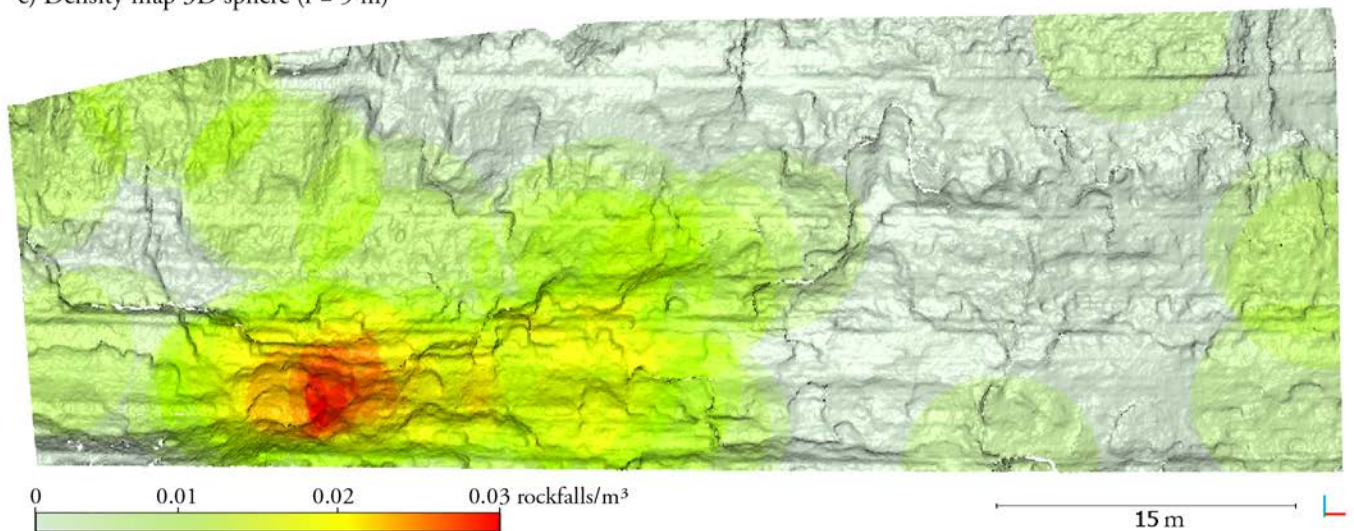


Figure IV.4. Snapshots of the different stages in the rockfall detection process: **a)** Clustering results. Each colour corresponds to one cluster. **b)** Result of manual filtering removing wrong clusters (noise). **c)** One possible outcome: density map.

9.3 Rockfall detection workflow automation

The updating of the methodology and the scripts shown in previous subsection provide a series of improvements that will be discussed in the following section, but it does not represent a full automation of the process. As with the old workflows the new Python codes have to be applied one by one. This is reasonable for the management of LiDAR datasets that are acquired periodically, but compromises the ability to process daily photogrammetric data and does not allow for near real time monitoring.

9.3.1 Global Overview

The automation process proposed for obtaining rockfalls ranges from the photographic acquisition in the field to obtaining the rockfall results in the server. Automation in photogrammetric devices has already been explained in previous chapters and published. However, in this section it is necessary to review and develop aspects related to the automation of the method which, because they were not the objective of the research, were omitted in the publications. All the automation has been designed around the use of the high-resolution systems (HRCam in Puigcercós and DSLR in Granada-Alhambra). Therefore, the photogrammetric process included in the automation is the MEMI workflow developed in this thesis.

In order to see the integration of the whole process, it is convenient to recall **Figure II.30** (page 128), which shows 3 processing phases according to colour. Part I) pre-processing of the data; Part II) application of the MEMI workflow; and Part III) workflow for rockfall detection.

The main idea of the developed workflow is summarized in **Figure IV.5**. With the following 4 elements i) the images acquired in the field, ii) the main code, which is the core of the system, iii) the libraries, functions, and scripts, and iv) the reference system. With these elements (grouped under the name **XBGRockfall**) it is possible to obtain automatically and in near real time the rockfalls that occur in a specific period (**Figure IV.5**). The digital repository **Appendix A - XBGRockfall** contains all the scripts developed to perform the rockfall identification. Codes are programmed in Python and have been generated for use with Agisoft Metashape and CloudCompare.

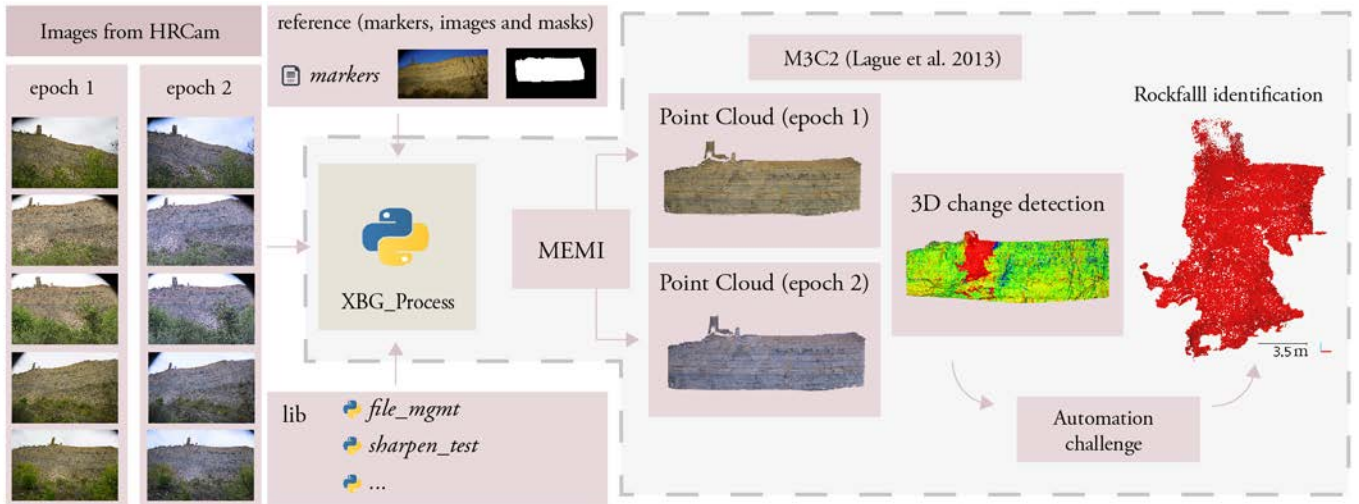


Figure IV.5. Diagram of the developed **XBGRockfall** automation software. The central element "core" is fed by the i) input data, ii) reference system and iii) processing libraries. The core is in charge of applying the MEMI algorithm, performance of the M3C2 comparisons and, from the strategies described in the automation challenge, identifying the rockfalls. Code available in the repository: **Appendix A - XBGRockfall**.

To this end, the design of the automation is based on the classic structure of a main code that makes calls to the different libraries expressly created for that purpose. The main code executes the different libraries sequentially. Thus, the result of one process (a function) is the new entry of the next process. In this way, an entire series of necessary actions are executed in a chain. Accordingly, a system of folders and files has been designed where the input data, the data obtained during processing and the results obtained are stored. The mix of codes/scripts and working structure (files and folders) may be referred to as the developed software **XBGRockfall**.

To facilitate the reader's understanding, in addition to the scheme in **Figure IV.5** two figures illustrating the real tree of files and folders of the software are shown. The designed software comprises all the codes and structures shown in **Figure IV.6** and **Figure IV.7**. The legend includes the different icons for each type of file.

In the same way, in the text, the names of **the codes** are expressed in bold and blue, **the folders** are written in red, and *the files and outputs* in green and italics.

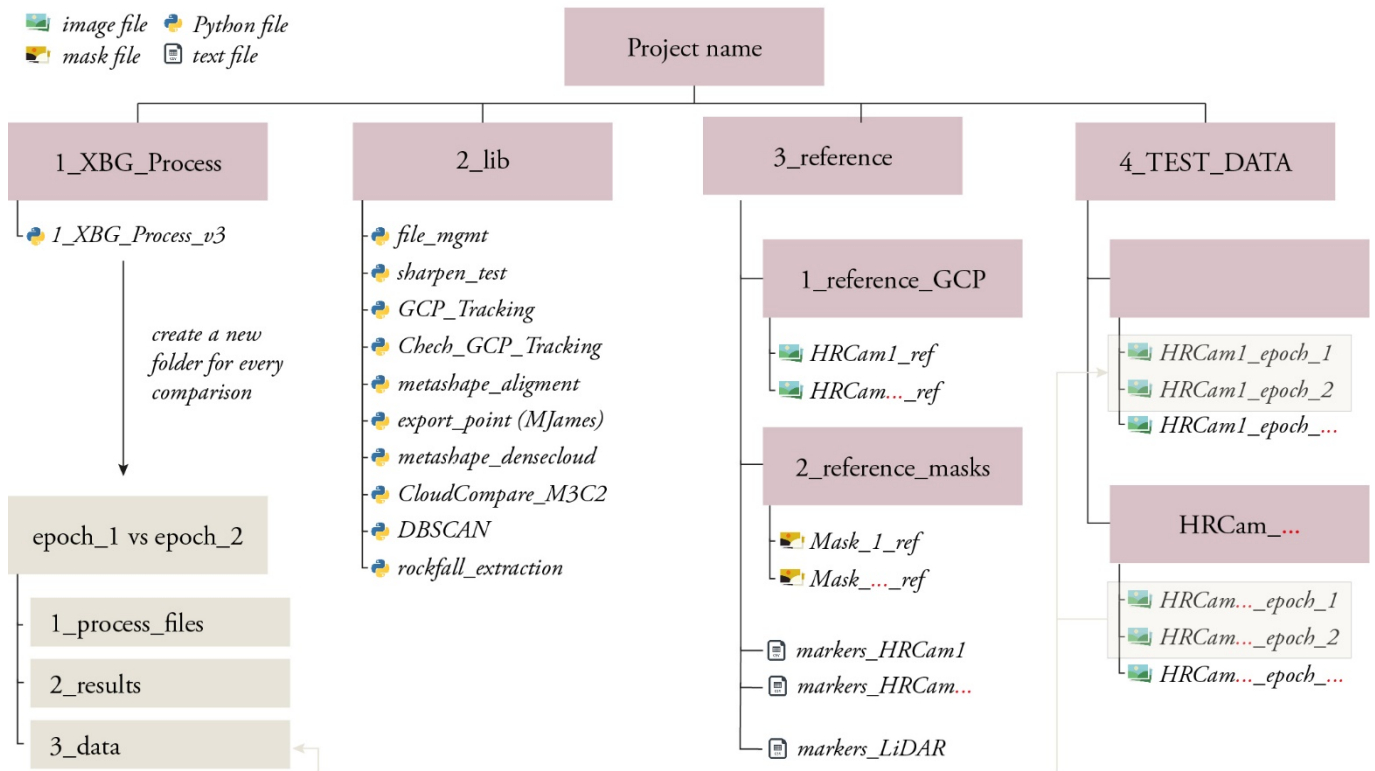


Figure IV.6. Tree diagram with the basic structure of the software. Grante boxes are folders containing the codes and files required for the photogrammetric processing. The light grey folders are the folders generated by the main code for each comparison and contain the files related to the rockfall identification process. (developed in detail **Figure IV.7**).

Figure IV.6 shows a first folder (**1_XBG_Process**) with the main script called **1_XBG_Process_v3**. The second folder (**2_lib**) contains all the codes, scripts and functions that are called by the main code **1_XBG_Process_v3**. In addition to the functions of the workflow, it also contains most of the codes that enable automation. Folder **3_references**, contains all the elements required for the subsequent referencing of the photogrammetric models. Finally, folder **4_Test_Data** is where all the raw data (images) for processing are stored.

The software starts running when the main code **1_XBG_Process_v3**, which can be run scheduled on any computer, is executed. The first step in the main code is to call the **file_mgmt** function (in folder **2_lib**). This function is in charge of creating all the new folder structure generated for each comparison where the processed files and results are stored (e.g.,

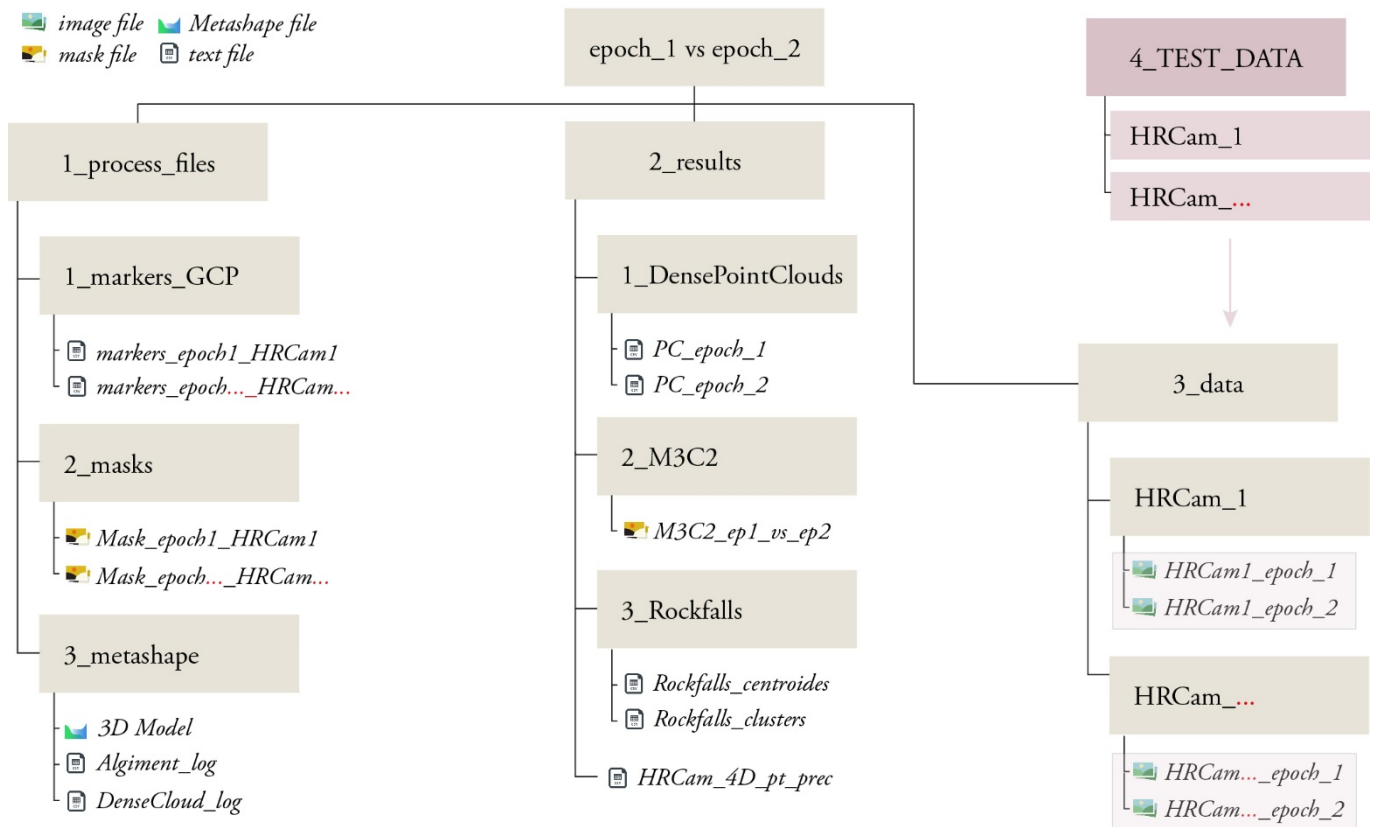


Figure IV.7. Tree diagram with the basic structure of the folder that is generated to store each comparison. The whole structure is generated when the software starts up and is unique for each comparison.

epoch_1 vs epoch_2 in **Figure IV.6** and **Figure IV.7**). It is also in charge of moving the images from the storage folder (*4_Test_Data*) to the new working folder created ad hoc (*epoch_1 vs epoch_2/3_data*).

The next step is to apply the image quality filter shown in **Figure II.30** (page 128) and presented in the MEMI publication, which is developed into the *sharpen_test* code (in folder *2_lib*). This code applies a Laplacian filter to the image in order to analyse the sharpness of the edges, and returns a value that is used as a threshold to eliminate those input images that do not meet the minimum quality requirements.

Following the workflow, to reference the models, we use images from epoch 0 (reference images), which we have referenced using 3D coordinates from LiDAR data (*HRCam_1_ref*, *HRCam..._ref*, one image for each photogrammetric module, in folder

3_reference/1_reference_GCP, Figure IV.6). To do the reference process it is necessary to have, on one hand, the files with the 2D coordinates of the different ground control points (GCP) in the reference images, which are stored in folder **3_reference** as *markers_HRCam1_ref, markers_HRCam..._ref* (**Figure IV.6**) and on the other hand, the file with the 3D coordinates of the GCP in the LiDAR point cloud (*markers_LIDAR* in folder **3_reference, Figure IV.6**).

A computer vision method has been used to obtain the coordinates of the GCP's on the new images (different from epoch 0), that will be used to reference these images. The code developed from the Python OpenCV library is designed to find the differences in pixel position between the reference time (epoch 0) and the new epoch. The calculation of this differences has been carried out using the Lucas-Kanade algorithm (Lucas & Kanade, 1981). From the calculation of these differences, the code is able to find the rototranslation matrix representing the movement that the camera may have experienced. In this way, to obtain the 2D coordinates of the new images, it is only necessary to apply the obtained matrix to the coordinates of the GCP in reference images. The new 2D coordinates for the GCP in subsequent images (*markers_epoch1_HRCam1, markers_epoch..._HRCam...*) are stored in folders **epoch1 vs epoch_2/1_process_files/1_markers_GCP** in **Figure IV.6** and **Figure IV.7**.

Furthermore, the working masks for each reference image (epoch 0) have also been made manually and stored in folder **3_reference/2_reference_masks** (*Mask_1_ref, Mask..._ref*, **Figure IV.6**). By applying the rototranslation matrix to these masks, new masks that perfectly match with the new epoch images are obtained. These generated masks (*Mask_epoch1_HRCam1, Mask_epoch..._HRCam...*) are stored in **epoch1 vs epoch_2/1_process_files/2_masks** in **Figure IV.6** and **Figure IV.7**.

Part of this referencing strategy has already been explained in the methodological section of the MEMI workflow (subsection 5.2). The result of the whole process is the new epoch images with a perfectly adjusted mask and well-placed ground control points on the images. The photogrammetric software is in charge of associating the 2D coordinates of the images with the 3D coordinates of the LiDAR. The use of LiDAR coordinates allows us to scale the models in order to obtain real measurements (**Figure IV.6**).

All the referencing and automatic masking process is programmed in the **GCP_Tracking** function (folder **2_lib**, **Figure IV.5**). The **Check_GCP_Tracking** function, also in folder **2_lib**, analyses whether the offsets between the reference and the current epoch are consistent between the GCPs. If not, it will be necessary to stop the processing because the coordinates and masks obtained will be wrong and the results would not be geometrically consistent.

When the images to be analysed are referenced and the masks have been transferred over these images, the photogrammetric reconstruction workflow starts. (Part II in **Figure II.30**, page 128). The photogrammetric reconstruction workflow that has been programmed automatically is the MEMI workflow developed in the previous chapters. This is divided into two parts, the first one, conducted by the **metashape_align** code, is in charge of initialising the project inside the Agisoft Metashape software (Agisoft LLC, 2020) and of performing the SfM process and Bundle Adjustment of the cameras, with the aim of obtaining the sparse point cloud. In addition, at this point in the process, an automatic filter is applied to eliminate the points in the sparse cloud that have produced the worst reprojection error. The file obtained with the sparse point cloud (**3D Model**) is stored in the folder: **epoch1 vs epoch_2/1_process_files/3_metashape**.

Once this result is obtained, the **export_point (MJames)** code is activated. This code applies the script developed by James et al. (2017), which performs the estimation of the accuracies. At the end of this process, the first result of the software is saved: the **HRCam_4D_pt_prec** located in **epoch1 vs epoch_2/2_results** store the estimation of the accuracy of the sparse point cloud. This result can be used to assess the accuracy of the 3D models obtained.

The second part of the photogrammetric reconstruction starts with the **metashape_densecloud** code, which loads the **3D Model** file again in the Metashape software. This script is in charge of computing the dense point cloud. In this case, filters have also been developed to remove those points that have nearly black colours, as they usually represent shadow areas (no information in the image). At the end of this process some files are saved. First of all, the **3D Model** file is overwritten with the complete Agisoft Metashape process, and as a result, in **epoch1 vs epoch_2/2_results/1_DensePointClouds** the dense point clouds obtained for each epoch are stored (**PC_epoch_1** and **PC_epoch_2**).

With the acquisition of the dense point clouds, the MEMI processing comes to an end. The next part of the automatic chain corresponds to the rockfall acquisition workflow (Part III in **Figure II.30**, page 128). The first script used is **CloudCompare_M3C2**, which performs the M3C2 comparison (Lague et al., 2013) between the two obtained dense clouds. The CloudCompare software only allows interaction via windows command prompt and does not support Python programming. For this reason, the code developed in Python does not interact directly with this software, although it has instructions to automatically launch commands from the windows terminal. The result of the comparison (**M3C2_ep1_vs_ep2**) is stored in **epoch1 vs epoch_2/2_results/2_M3C2**.

Once the comparison is done, the **DBSCAN** code is run. This script performs the two automatic filtering actions. On the one hand, filtering based on the difference value threshold (threshold filter) and, on the other hand, the clustering of the DBSCAN algorithm (Ester, et al., 1996). The result is a list of clusters (**Rockfall_clusters**) that needs to be reviewed manually to identify the rockfalls.

After the operator has selected the rockfalls, the **rockfall_extraction** code is applied. This is responsible for calculating the volumes of each rockfall and stored in the **Rockfall_centroides** file in the **epoch1 vs epoch_2/2_results/3_rockfalls**. With the acquisition of the volume, the processing of rockfalls is completed. By calculating the volumes and centroids, maps, plots, and analysis can be made.

As previously explained, all the results and intermediate files generated during this quasi-automatic process are stored in the file structure created at the start of the process (**Figure IV.6**). This structure, which is generated for each comparison, contains 3 folders. The first one, **1_process_files**, contains the files generated during the processing. In addition to the files mentioned above, two log files (**Alignment_log** and **DenseCloud_log**) containing the operations performed and the results obtained in the Metashape software are also stored in **epoch1 vs epoch_2/1_process_files/3_metashape**.

The second main folder, **epoch1 vs epoch_2/2_results**, contains the files or results obtained that have been described in the respective steps. Finally, the third folder, **epoch1 vs epoch_2/3_data**, contains the original images that have to be analysed (**HRCam1_epoch1**,

HRCam1_epoch2, and so on). This folder is fed directly from folder **4_TEST_DATA** of the initial structure of the software (**Figure IV.6**). Since the software is designed as an iterative process that computes different epochs each time, the **4_TEST_DATA** folder in the main root contains all the images to be processed, while the **epoch1 vs epoch_2/3_data** folder located within a specific project (comparison between 2 epochs) only contains the images of the two epochs to be processed.

9.3.2 Automation challenge

As we have seen, all these codes used sequentially enable an almost complete automation of the process. The photogrammetric models tend to generate a significant dispersion of points in the areas perpendicular to the sensor, as well as erroneously reconstructing areas with surface vegetation. In addition, some shots may have areas with fog, water drops on the glass or birds flying. For all these reasons, models may show lower quality reconstruction in these areas. As a consequence, clusters that do not correspond to rockfalls (wrong clusters) can be identified and must be filtered using manual strategies.

Consequently, manual filtering and user intervention, is still required. This challenge, which does not allow for a complete automation of the entire workflow, may be addressed in several ways, which are described below. The ultimate goal of all the strategies detailed below is to minimize the number of false positives that are identified as rockfalls.

Restrictive parameters

One way to automate the whole process is to use more restrictive values for some parameters used in the rockfall monitoring workflow. The first one corresponds to the difference threshold filter selected to distinguish the points presenting a deformation higher than the fixed threshold from those that do not. This parameter, inherited from the use of LiDAR, is used to remove the gaussian distribution error of the points in the point cloud. In the real application cases provided in the following chapter, values between 3 and 5 cm are used. If higher values such as 15 cm were used, the points selected as possible clusters would be reduced, essentially eliminating scattered errors and not affecting the most significant rockfalls. However, an increase in this parameter would affect both the detection of small rockfalls (with a depth of less than 15 cm), and the calculation of the volume of the identified

rockfalls. In this case, the computed volume would correspond to those points with a depth larger than 15 cm, excluding the part of the volume of the triangular prisms formed by points with a shallow deep.

Other parameters that can be modified are those belonging to the DBSCAN clustering algorithm. In this case, modifying both the search radius (eps) and the minimum number of points (n_points) will allow the elimination of smaller and therefore less significant clusters of points. The problem with oversizing these parameters is twofold: i) only isolated errors can be eliminated, because when erroneous points are concentrated in a specific area with sufficient density, they will still be associated as a cluster; and ii) a set of small individual rockfalls can be considered as a bigger one, oversizing the real volumes. In the same way, but in the opposite direction, since very large rockfalls (more than 1m^3) have the point density and distribution very different from the small ones, having areas without points, undersizing the parameters can result on large rock blocks classified as a set of smaller rockfalls.

Statistical filters

In order to avoid having to modify the parameters, and to avoid having to deal with their consequences, the statistical solution has also been considered during the development of this thesis. This method consists of analysing all clusters and trying to discern what differentiates rockfalls from wrong clusters. For this reason, several parameters are automatically calculated for all detected clusters. These parameters are shown in **Table IV.1**.

Table IV.1. Parameters computed for statistical analysis.

Volume	Volume of each cluster
Area	Area of the cluster on the XZ-axis (perpendicular to the sensor)
Num. Points	Number of points inside a cluster
Ratio	Division between cluster height and width
Density Vol.	Number of points divided by volume
Density Area	Number of points divided by area.
Median Ny	Median of Ny (normal vector in the direction of the sensor)

Once the parameters have been obtained, clusters are classified into those that are rockfalls and those that are not (expert criteria). From this classification, the ranges of values that distinguish the rockfalls are determined. In this way, the clusters are classified as true rockfalls only if its parameters are within the ranges of the parameters that characterize the rockfalls. Thus, any cluster that fails to match in any of the parameters is automatically discarded and is considered a wrong cluster.

While it allows the automation of the rockfall monitoring workflow, this method also has its weaknesses. As can be seen from the methodology explained above, the choice of parameters and their ranges is crucial for the determination of rockfalls. For this reason, a very precise adjustment of these parameters for a specific observation period is insufficient for a global study, and will probably lead to future rockfalls remaining unidentified because they exceed the ranges established for some of the parameters.

Moreover, in certain study areas such as the Tajo de San Pedro in Granada, which has a lot of vegetation and slopes with different orientations, the clusters have very different parameters, and it is very difficult to find a correlation between the parameters manually. Therefore, although it can be efficient in study areas such as Puigcercós, the application of this method cannot be generalised for real study areas presenting a greater dispersion and randomness of the errors in the photogrammetric reconstruction.

Recurrence algorithm

This algorithm was designed to filter out errors that exceed the statistical filters. The basic concept of this algorithm is that if in the comparison of the captures t_n vs t_{n+1} a rockfall is detected, the same rockfall must be identified using two different point clouds with a greater time window that contains t_n and t_{n+1} , for example t_{n-1} vs t_{n+2} . In this case the cluster identified can be assigned as a true positive (rockfall). The main problem with this algorithm is the double computational cost, because it is necessary to apply the entire workflow to two different datasets (t_n vs t_{n+1} and t_{n-1} vs t_{n+2}). Moreover, this implies that the confirmation of the rockfall is not obtained just a few minutes after obtaining the images. It is necessary to wait for the next cycle of data collection (which may be 24 hours later) to confirm the rockfalls of the previous cycle. This idea of validation is promising and may help to make the

results more robust. However, a complete development is not presented in this thesis, since during the testing phases some issues emerged which, due to lack of time, remain unsolved. The limitations that have arisen are as follows:

- * Errors in certain areas occur in all captures due to the wall configuration and camera distribution, leading to persistent errors in subsequent models.
- * The volumes and centroids of the rockfalls differ from one comparison to another because of the differences on the photogrammetric reconstructions. Thus, it is difficult to design a method that determines with certainty that a rockfall detected at t_n vs t_{n+1} corresponds to the same at de t_{n-1} vs t_{n+2} comparison.
- * Due to the high activity of the cliffs analysed, the areas affected by rockfalls may change rapidly. Consequently, rockfalls detected in each comparison may be hidden or altered by larger rockfalls in subsequent comparisons.

Machine Learning algorithms

The natural evolution of the statistical filter is Machine Learning (ML). Technically, the use of statistical filters is a learning process where the user performs the "learning" from the observation of the rockfall parameters. The aim of Machine Learning algorithms is to transfer this "learning process" from the user to the machine using artificial intelligence (AI).

There are currently many Machine Learning models and endless possibilities to explore in this field. Many articles describe in detail how ML algorithms work (Aha et al., 1991; Choi et al., 2020; Pedregosa et al., 2011). They are becoming increasingly widespread in the field of geosciences (Akiyama et al., 2020; Eltner et al., 2021; Karpatne et al., 2019), and similar approaches are even being used in the field of landslide or rockfall identification (Fanos et al., 2020; Ghorbanzadeh et al., 2019; Zoumpekis et al., 2021).

For the application of Machine Learning algorithms, it is necessary to calculate all possible parameters available. For this reason, the parameters in **Table IV.1** have been extended for this test. These new parameters can be visualised in the following **Table IV.2**. For the ML analysis, the coordinates of the cluster centroids have been added to help the algorithm to eliminate as quickly as possible those clusters that are recurrently found in the same locations

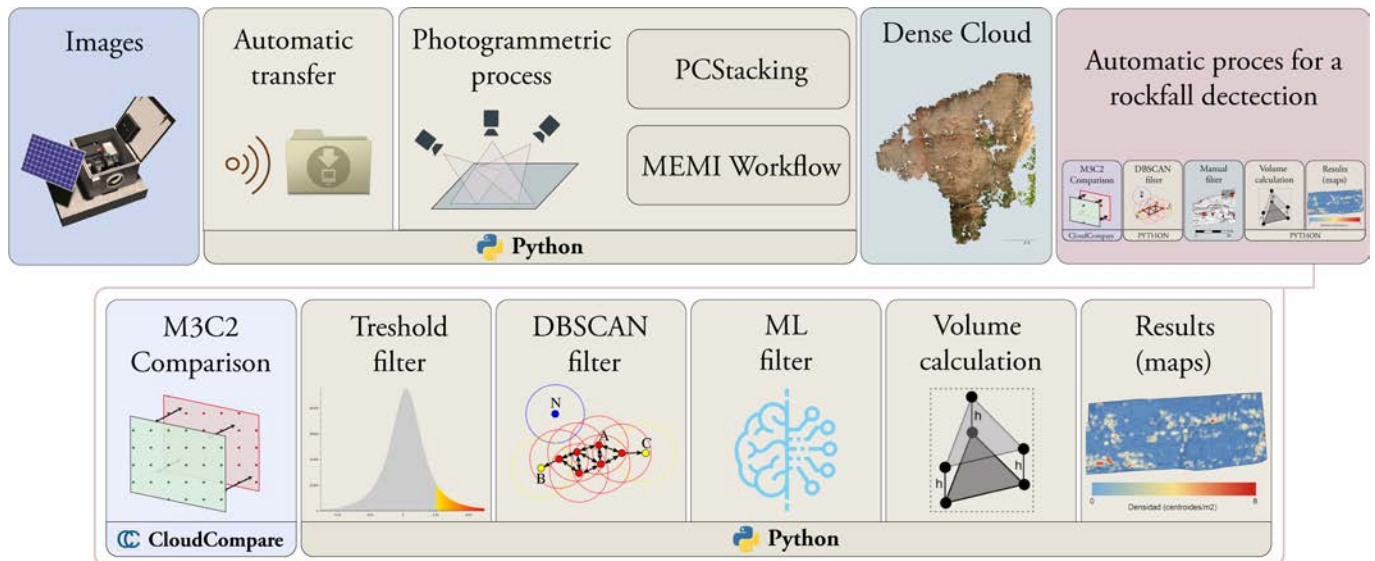


Figure IV.8. Final proposal of the automatic workflow for the detection of rockfalls. This approach allows an automatic processing from the image acquisition to the calculation of the volume of the rockfall. The colour of the box represents a different process or software.

(usually persistent errors or due to the presence of vegetation). All parameters have been calculated for all points forming the cluster.

However, in order to add more parameters, all these calculations have also been performed on the cluster core. This cluster core is defined as a new cluster containing only the points that make up the central part of the cluster. With this strategy, possible peripheral points are eliminated and parameters such as density, or medians of normals are more consistent.

Thanks to the previous cluster classification performed by the user, the algorithm is able to automatically identify the classifiers, intervals and parameters that allow classifying whether a cluster is a rockfall or a wrong cluster. This procedure is carried out through many iterations that randomly test the weight (or influence) that each parameter should have for the identification of rockfalls.

By seeking to minimise the error in each iteration from the defined cost function, the algorithm finally determines which parameters and ranges allow the classification of a cluster as a valid rockfall.

Table IV.2. Parameters computed for ML analysis. All these parameters have been calculated twice. Once for the whole set of points forming the cluster and once for the central core of the cluster.

Median X	Median of X coordinates (Centroid)
Median Y	Median of Y coordinates (Centroid)
Median Z	Median of Z coordinates (Centroid)
Area	Area on the XZ-axis (perpendicular to the sensor) of the cluster
PC1 (Num & Stdv)	Number and Standard Deviation of points inside each cluster for point cloud 1
PC2 (Num & Stdv)	Number and Standard Deviation of points inside each cluster for point cloud 2
Ratio	Division of the total height of the cluster and its width
Density	Number of points divided by area.
Nx (Med & Stdv)	Median and Standard deviation of Nx (normal vector in the X direction)
Ny (Med & Stdv)	Median and Standard deviation of Ny (normal vector in the direction of the sensor)
Nz (Med & Stdv)	Median and Standard deviation of Nz (normal vector in the Z direction)
Diff (Med & Stdv)	Median and Standard deviation of difference value
M3C2 (Med & Stdv)	Median and Standard deviation of M3C2 results. Significant change and Interquartile Range (IQR) for each cluster in PC1 and PC2
Outliers (Numbers & Density & Z_score)	Number and density of outliers for each cluster. Computed using Z_score function

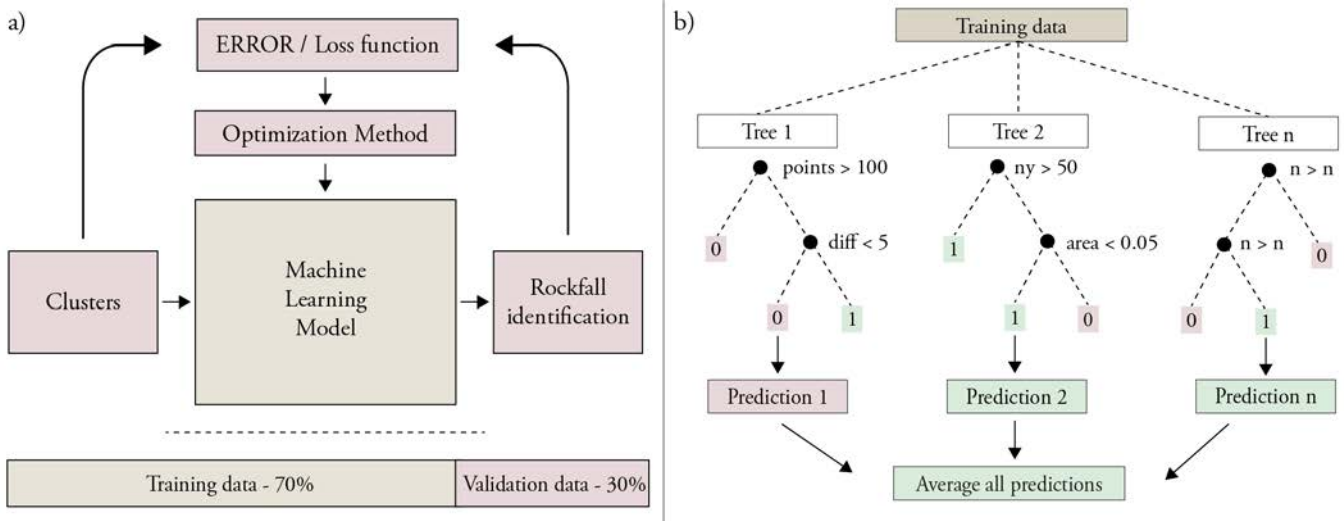


Figure IV.9. a) Basic diagram of the iterative operation of a machine learning model.
b) Schematic of a machine learning model based on Random Forest Classifier algorithm using 3 decision trees.

This iterative process is simplified in the following steps (**Figure IV.9a**): i) the ML model is initialized with random parameters; ii) some known data (training data) is fed into the model to obtain predictions; iii) compare the model's labels (predictions) with the known labels using the loss function; iv) the ML model is optimized to reduce the loss by adjusting the parameters; v) repeat steps i to iv until the predictions from the model are good enough.

The iterative execution of this process enables storage in the ML model the parameters that allow a prediction as close as possible to the real labels to be obtained. Furthermore, this set of weights and parameters is stored directly in a “model” adjusted to the study area. Future 3D comparisons can be automatically filtered using this pre-trained model, resulting in a list of rockfalls.

This type of processing requires a large amount of input data. For this reason, this algorithm has been tested with data obtained over 2 years in the study area of Tajo de San Pedro – Granada. This is a challenging area because the quality of the models is not as good as those acquired using the HRCam photogrammetric system. Different orientations on the escarpment, the presence of vegetation and poor camera distribution generate models with numerous false positives in the rockfall monitoring workflow.

These data contain a total of 2,028 clusters, of which 135 have been classified on the basis of expert criteria as rockfalls, and the remaining 1893 are considered as vegetation or erroneous clusters (henceforth: wrong clusters). The larger the input data, the more examples the algorithm can analyse and the more features it can learn, improving the future classification of rockfalls. The application of this algorithm produces a model that stores all the classification criteria (values and weights). For future data, it is only necessary to apply the generated model to the new data to obtain the identification of each cluster.

In order to evaluate the performance of the algorithm, three types of training data have been used:

- * One with all clusters obtained and classified (93.3% wrong clusters, 6.7% rockfalls)
- * A smaller dataset, without vegetation, because these clusters can be filtered automatically beforehand. It contains 962 wrong clusters and 135 rockfalls. (86% false clusters, 14% rockfalls)
- * Another dataset containing 135 rockfalls and 135 wrong clusters, in order not to provide highly imbalanced training data (50% false clusters, 50% rockfalls)

All these datasets have been split into two groups, 70% of random data have been used as training inputs, while the remaining 30% have been kept to evaluate the performance of the generated model on “new” data (**Figure IV.9a**).

There are many Machine Learning methods, but for the test conducted in this thesis we used a binary classification algorithm, as we are only interested in obtaining a 0 or a 1 for each input cluster, according to whether the algorithm considers it to be a rockfall or not.

The structure used for this test was the Random Forest Classifier (Breiman, 2001) (**Figure IV.9b**). This structure is based on the use of numerous decision trees. A decision tree (Quinlan, 1986) is a Machine Learning structure based on selecting a sequence of parameters and ranges to identify the correct label. This structure is similar to the statistical analysis discussed before and is based on hierarchical series of binary decisions. However, the use of

a)

		ML Predictions	
		Wrong cluster	Rockfall
True labels	Wrong cluster	True Negative (Wrong cluster)	False Positive
	Rockfall	False Negative	True Positive (Rockfall)

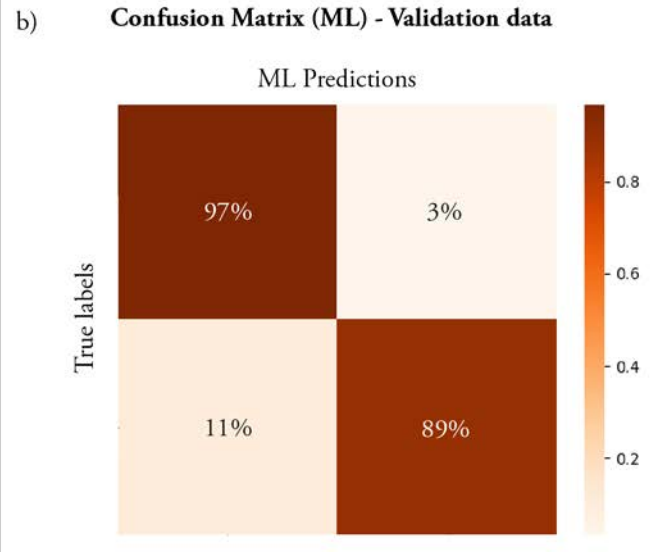


Figure IV.10. a) Explanation of the confusion matrix obtained in a binary classification. The green boxes show the matching between real classification and prediction, the red boxes show the discrepancy between real classification and prediction. b) Best confusion matrix obtained in different tests. The confusion matrix shows an overall classification above 92.6%, which is distributed as shown in the figure.

a single decision tree to perform the classification is not optimal, since the result will be highly conditioned by the selected parameters as well as their order and ranks. For this reason, the random forest structure recreates a multitude of decision trees. To obtain the final label, it simply analyses all the results obtained and assign the majority label (**Figure IV.9b**).

The results obtained have been very positive, although some limitations have emerged, such as the small amount of data or the quality of the rockfall identifications. Due to this lack of data, models are sometimes obtained with low accuracy. After some tests, the best result has been obtained with the balanced dataset, achieving an overall accuracy of 92.6%.

Figure IV.10a and **Figure IV.10b** shows the confusion matrix of the validation carried out with 30% of the data not used for training. This confusion matrix shows the percentage of true negatives (97%) and true positives (89%) obtained for the best attempt. A graphical representation of the identified rockfalls and wrong clusters is presented in the following chapter.

It should be noted that in all the tests performed, a very good stability in the accuracy of the predictions of the wrong clusters (non-rockfall) has always been obtained. This means that the model always correctly identifies what is not a rockfall, and the number of false positives is very low.

In contrast, for the rockfall predictions, the values obtained are not as good due to the presence of some false negatives. In addition, no stability in the result has been identified, so the accuracy of the identification varies greatly in each test (from 50% to 90% depending on the attempt).

Figure IV.10b illustrates one of the best attempts obtained using the developed ML algorithm and, also shows that the value of the true positives is lower than that of the true negatives (89% vs. 97%). This result suggests that we may be identifying real rockfalls as wrong clusters. This is a possible scenario, as the manual labelling of “rockfall” may have been partially erroneous.

Obtaining a very good Machine Learning model for rockfall identification requires more effort in data preparation, by both increasing the amount of data acquired and improving the quality of the labelling. For example, avoiding the use of manually mislabelled rockfalls.

Although not fully developed due to the time constraints, the result obtained provides the basis for an automatic photogrammetric system for rockfall monitoring. Thus, the endeavour to minimise the false positives and false negatives that are identified constitutes a challenge for the future. A task that will undoubtedly benefit from using more and better labelled data.

In order to share the experience developed in this field and in line with the trends of sharing training data and Machine Learning models, the main code with the programming of the Machine Learning model, as well as the data used for training and the final model computed (weights and parameters) shown in Figure IV.10 is available in the GitHub digital repository of this thesis. (**Appendix A - Machine Learning**)

Chapter 10

Application Cases

10

The aim of this chapter is to give some brief examples of the application of the research work set out in this thesis. The results obtained with all the installed photogrammetric systems (RasPi, HRCam and DSLR), all the published processing algorithms (PCStacking and MEMI), and with different options of automatic rockfall monitoring workflows, have been chosen to illustrate the developments of this thesis. To simplify the understanding of the results, only one example of application is shown for each system, algorithm or process.

The intention of this section is not to conduct a detailed analysis of the results obtained, since this is not the aim of the dissertation, but to show the different possibilities that can be obtained by applying the described methodologies in the field of rockfall monitoring. As previously mentioned, an in-depth analysis of these results in a geological context would have

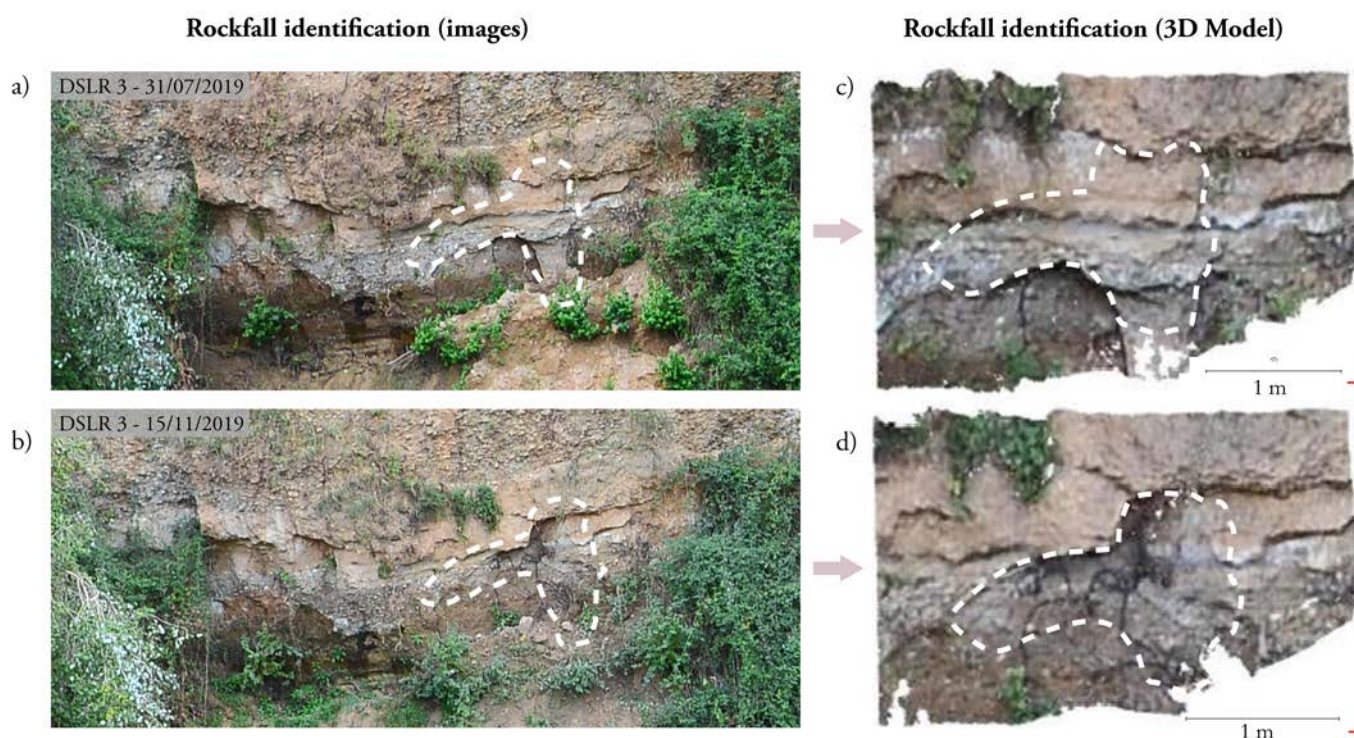


Figure IV.11. Rockfall identification. DSLR system image showing a capture **a)** before and **b)** after a rockfall, and the corresponding photogrammetric models **c)** before and **d)** after the rockfall. The **QR 24** shows the animated sequence of the 3D models.

been desirable, but the temporal conditions of this research have made it impossible to do so. Nevertheless, the author considers it particularly relevant to show these results in order to conclude the research carried out during these years.

As an initial approximation, the first result presented is the identification of a single rockfall. The identification of each individual rockfall forms the basis for the more complex results shown in the following figures. **Figure IV.11** shows how the identification of a rockfall is visualised in the images acquired by the systems and in the corresponding photogrammetric point cloud. The **QR24** shows a visual alternation between the 3D models. The result in **Figure IV.11** has been obtained using the DSLR systems installed in the Tajo de San Pedro, applying the MEMI workflow and carrying out manual filtering of the rockfall.

10.1 Puigcercós I – RasPi System

The results that can be obtained with the very low-cost system are well illustrated by the following examples, which help to demonstrate the great possibilities that these very low-cost systems provide.

10.1.1 Rockfall detection

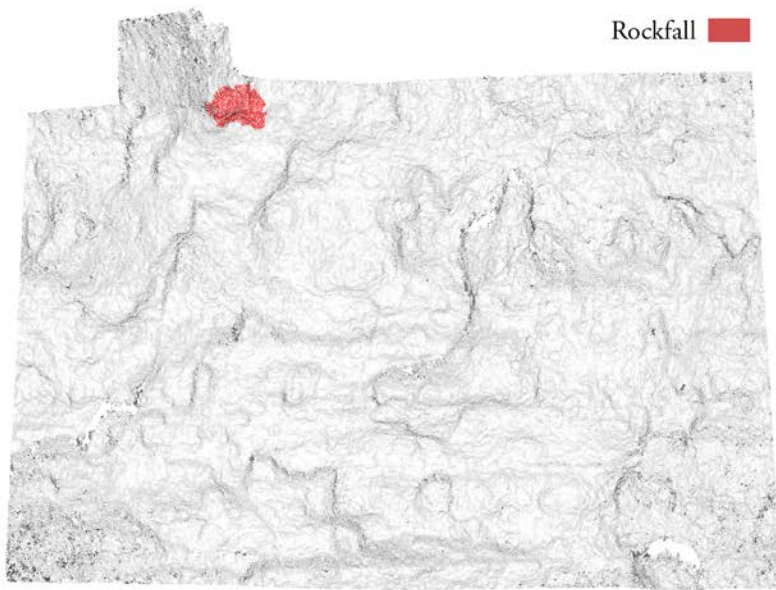
The first example was published at the EGU Conference (Blanch et al., 2019). Thanks to the high temporal frequency monitoring provided by the photogrammetric systems designed, it was possible to obtain a comparison of the cliff (**Figure IV.12a**) between the day before and the day after an earthquake affected the Puigcercós study area (45km from the epicentre) (**Figure IV.12b**). This analysis allowed us to determine that during a 48-hour window when the earthquake occurred there was also a medium magnitude rockfall (approx. 1m^3) (**Figure IV.12c**).

Although the aim of this thesis is not to correlate the rockfall with the earthquake, thanks to the high temporal frequency and the possibility of receiving the images the day before and after the earthquake, we were able to obtain this valuable result. This prospective analysis of the possible earthquake-rockfall relationship could not have been carried out with classical monitoring methods, because earthquakes are not predictable and therefore it is very difficult to obtain the before and after images in a very small space of time.

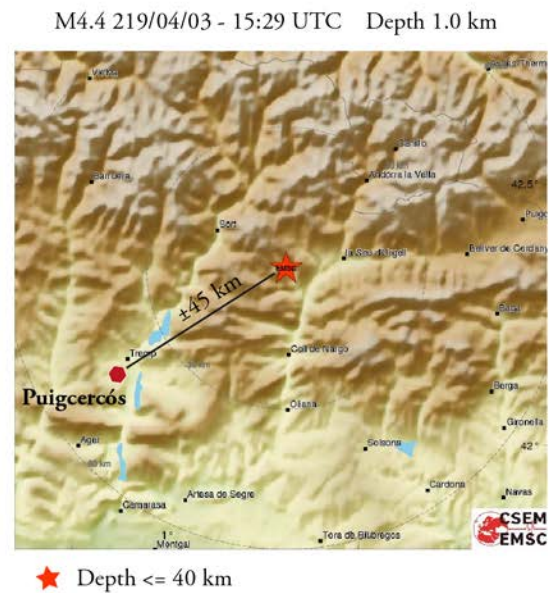


QR 24

a) RasPi System - 02/04/2019 vs 04/04/2019



b) Earthquake 03/04/2019 (Map from EMSC)



c) RasPi Camera 02 - 02/04/2019



RasPi Camera 02 - 04/04/2019



Figure IV.12. a) Rockfall identified on 04/04/2019 comparing two photogrammetric models. b) The day before (03/04/2019) there was an [earthquake M4.4 45km from the Puigcercós cliff](#). Map modified from European-Mediterranean Seismological Centre (EMSC). c) Images obtained automatically by the RasPi system. The rockfall has been delimited in white.

The selected way of showing the results obtained in the detection of rockfalls is based on the M3C2 comparison (**Figure IV.12a**). This comparison shows the areas that remain stable in grey (unchanged between the two periods) and the rockfall remarked in red (other minor rockfalls or pre-failure deformation have been leaked).

The result in **Figure IV.12** has been obtained using the RasPi systems installed in the Puigcercós cliff, applying the PCStacking workflow and carrying out manual filtering of the rockfall (semiautomatic process).

10.1.2 Pre-failure detection

Moreover, thanks to the availability of a large time-series of data and the fact that in the Puigcercós cliff there was mobilisation and subsequent rockfall of a large area (more than 100 m³), one result obtained with the very low-resolution systems is the pre-failure deformation of this rockfall (**Figure IV.13**).

This result shows the deformation evolution of the rockfall under study. It was obtained by comparing each new 3D model with an initial reference, as shown in **Figure IV.13b**. In the deformation plot, it is possible to see different stages of acceleration corresponding to the expected deformation creeps. Similar results on other rockfalls, obtained with LiDAR, can be found in the thesis developed by Royán (2015). This result obtained with photogrammetric systems is in accordance with the result obtained in the laboratory in the test stage and presented at the beginning of this thesis (**Figure II.1**, page 80).

The result shown in **Figure IV.13** was obtained using the RasPi systems installed in the Puigcercós cliff, applying the PCStacking workflow and carrying out manual filtering of the selected rockfall. No algorithm for the automatic detection of pre-failure deformation has been developed. This type of result is frequently used to monitor rockfalls that have already started to mobilise and is often used to estimate a fall date. Although obtained with very low-resolution systems, this result allows considering photogrammetric systems for early warning applications whenever the mobilised block is of large magnitude (>100 m³).

10.2 Puigcercós II – HRCam System

Different results have been obtained with the HRCam system. The following are the 3 most relevant types of results that have been acquired with this system installed in the Puigcercós cliff during this research. In addition, a comparison of 3D models is presented to evaluate the improvement that the MEMI workflow produces in the long-term (71 days) model comparison.

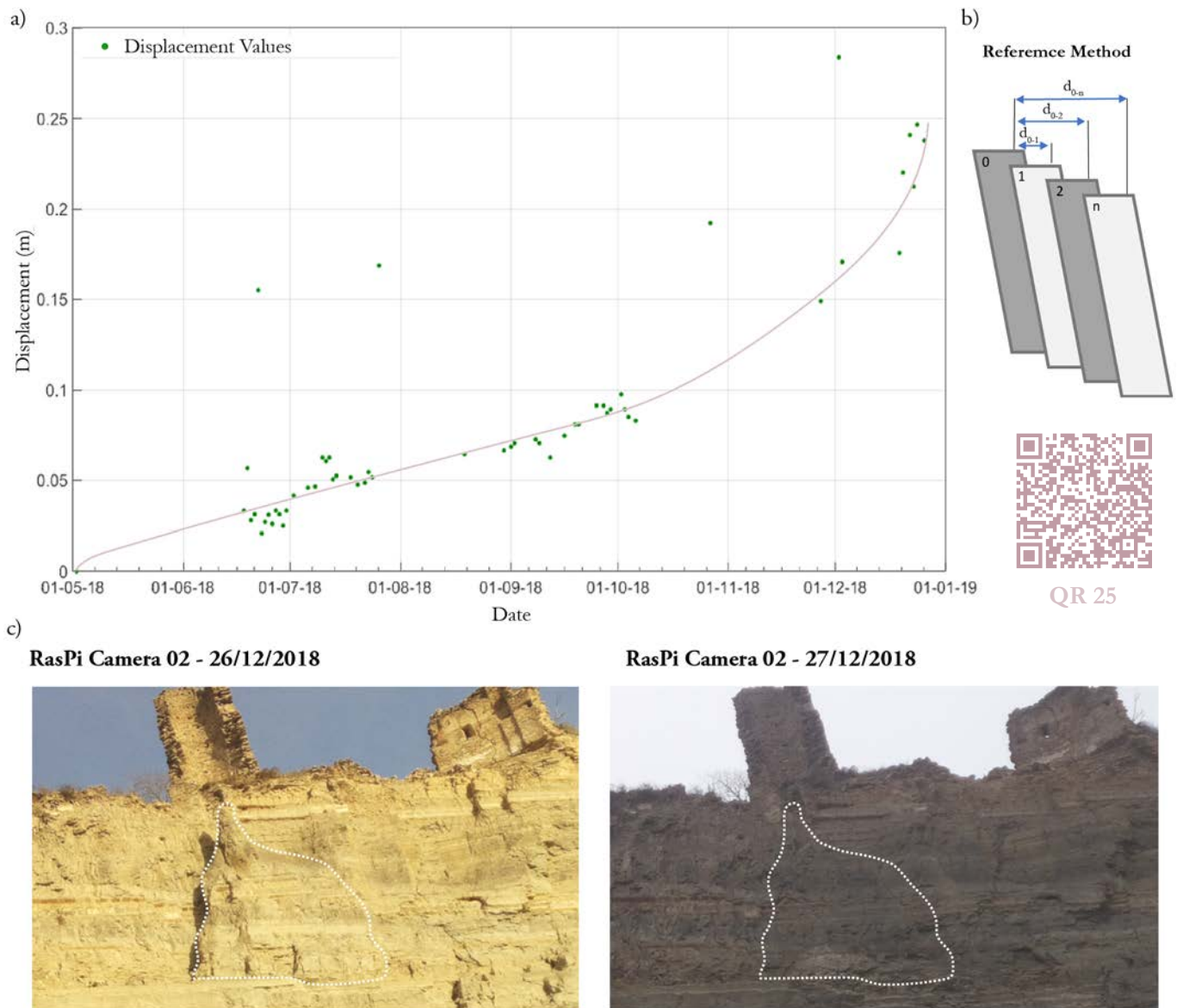



Figure IV.13. a) Pre-failure deformation of a large-scale rockfall computed thanks to the daily images obtained with the RasPi system during 6 months. A clear final acceleration phase is identified. b) Schematic illustration of the reference method. c) Images obtained automatically by the RasPi system. The rockfall has been delimited in white. The **QR 25** code shows a video of the detached block.

10.2.1 Major events

The first result refers to the possibility of detecting large rockfalls. In this case, **Figure IV.14a** and **Figure IV.14b** shows two rockfalls of large magnitude (over 100m^3). The purpose of showing these episodes of great magnitude serves, on the one hand, to demonstrate the great

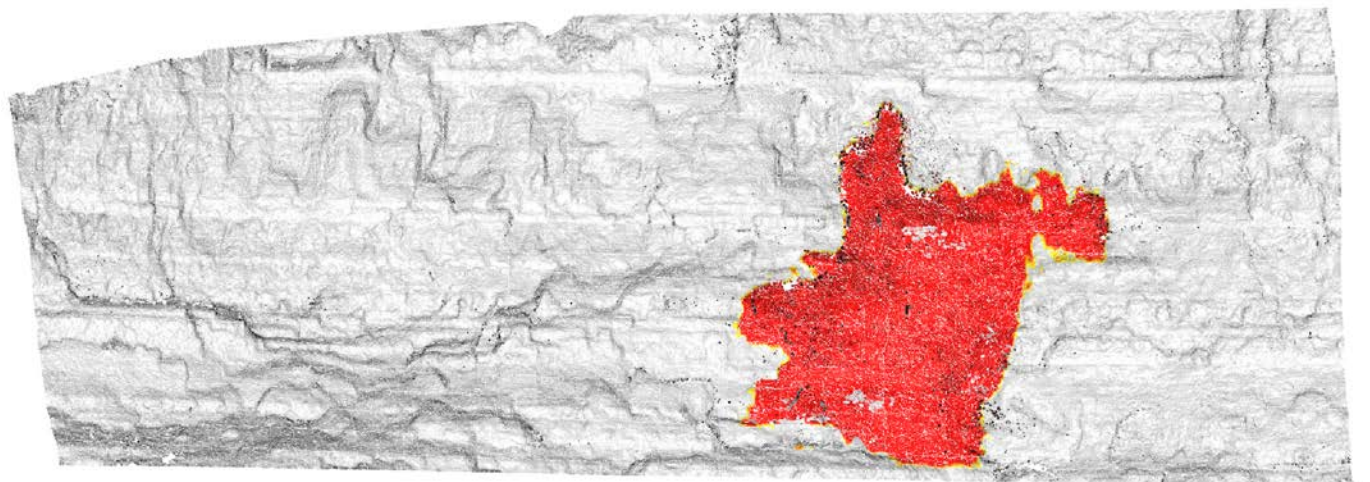
a) Puigcercós - 25/04/2019

Rockfall 



20 m

b) Puigcercós - 26/01/2020



15 m

Figure IV.14. Large rockfalls identified using the HRCam system and the application of the MEMI algorithm in Puigcercós. The red areas denote the large rockfalls identified. **a)** The rockfall of 25/04/2019 has an approximate volume of 115 m³ **b)** and the rockfall of 26/01/2020 has a volume of approximately 135 m³.

activity that takes place on the Puigcercós cliff and, on the other hand, to show that the MEMI workflow presented in this thesis is working well, even when there is a great difference between the images of each epoch. The difference in the images is due to the detachment of a large portion of the rockface between the initial and the final epochs. The result shown in **Figure IV.14** shows two large rockfalls, obtained using the HRCam systems

installed on the Puigcercós cliff. The result was processed by applying the MEMI workflow and manual filtering of the rockfalls (updated RISK NAT workflow).

10.2.2 Automatic monitoring

The second output obtained with the HRCam system serves to display an automatic monitoring (updated and automated RISK NAT workflow) during a specific observation period (from 29.12.2019 – 21.01.2020). **Figure IV.15** shows the results obtained over 32 days of monitoring.

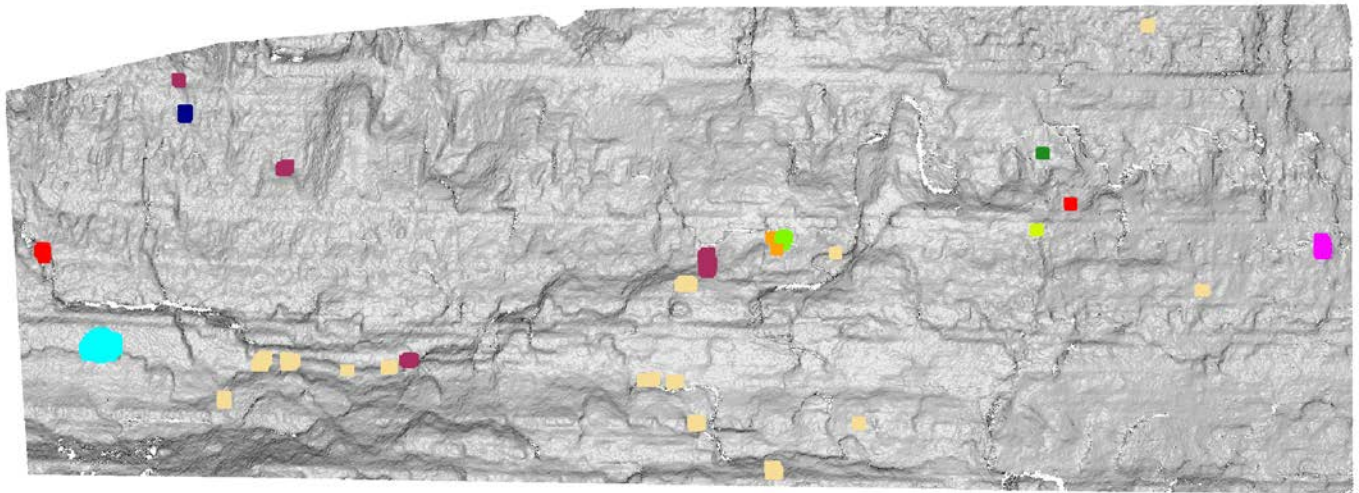
Using the statistical and recurrence algorithms developed in the previous section, the designed automatic workflow identifies 29 rockfalls. Only one comparison was made per day, so the rockfall monitoring interval is 24 hours. The manual identification of the rockfalls has been extracted from Garcia-Besora (2021) under my supervision, in the context of a master's thesis.

The result shown in **Figure IV.15a** was obtained using the HRCam systems installed in the Puigcercós cliff, applying the MEMI workflow and carrying out an automatic filtering of the rockfalls. Given the simplicity of the Puigcercós wall, this strategy based on the statistical filter together with the recurrence algorithm may be sufficient to detect most of the rockfalls automatically. However, it has not yet been possible to analyse its performance when larger rockfalls occur.

Thanks to the possibility of automatically processing large amounts of data (several days), it is possible to perform analyses such as the one shown in **Figure IV.15b**. In it, the number of daily rockfalls is shown together with the daily precipitation in the area. Although no correlation is intended in this work, these comparisons are presented to demonstrate the possibilities of the installed systems.

Furthermore, although this result has been obtained by back-processing, the same workflow can be applied to the daily real-time models. Obtaining the identification of rockfalls minutes after the acquisition of images.

a) Puigcercós - 20/12/2019 to 21/01/2020 (32 days) - 29 Rockfalls



b) Number of Rockfalls/day (overlapping daily rainfall)

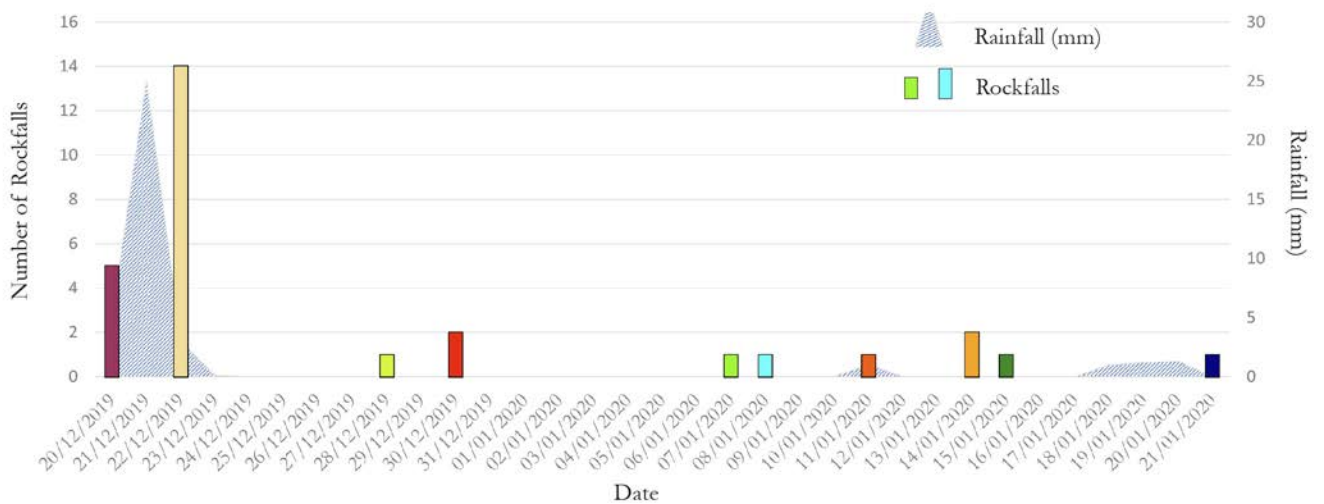


Figure IV.15. Rockfalls identified automatically over a period of 32 days. **a)** 29 rockfalls have been identified, the colour code relates the rockfalls on the 3D model to the day of detection in the plot. The size of the rockfalls has been increased in order to display them correctly. **b)** The plot shows the number of daily rockfalls together with the daily rainfall (obtained from [Meteoblue](#) ©).

10.2.3 Pre-failure deformation

The last example of application of the HRCam system is the pre-failure deformation identification. **Figure IV.16** shows an area where pre-failure deformation is clearly identified. The results have been obtained after a direct comparison between 2 models with a difference of 50 days. The identified values vary between 6 mm at the base and 2.5 cm at the top of the

Puigcercós - 02/12/2019 vs 21/01/2020 (50 Days)

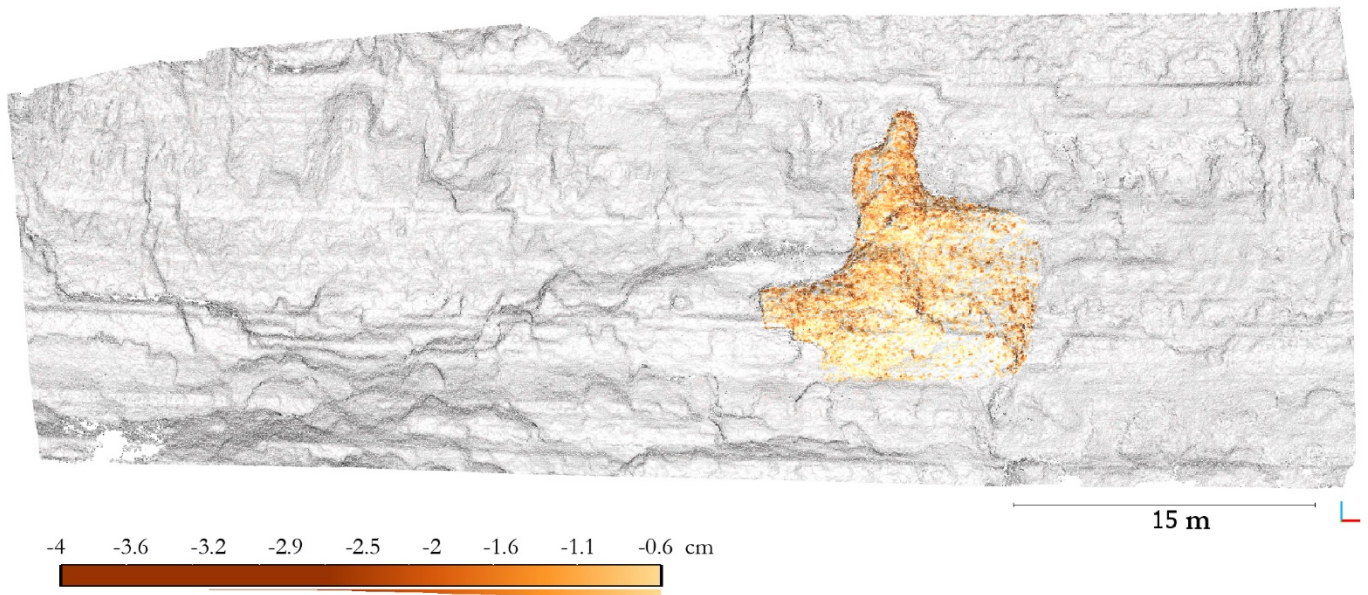


Figure IV.16. Pre-failure deformation of a rock block at Puigcercós cliff. The comparison was made between 3D models 50 days apart. It can be seen how the deformation increases with the height of the block, so that a rock toppling movement can be identified. Finally, this block fell on 26/01/2020 (**Figure IV.14**).

block. A small histogram of the deformation distribution is shown below the colour bar in **Figure IV.16**. While **Figure IV.13** showed a continuous pre-failure deformation analysis, in this case the result shows a single comparison (similar to classical LiDAR work, where there is no 4D tracking).

The deformation results shown in **Figure IV.16** are the raw value obtained with M3C2 algorithm (Lague et al., 2013), experiences like Abellán (2009) or Royán (2015) show that the results can be improved with the application of specific filters and algorithms. However, in the context of this thesis due to temporary limitations, these improvements could not be applied.

The result shown in **Figure IV.16** was obtained using the HRCam systems installed in the Puigcercós cliff, applying the MEMI workflow and carrying out manual filtering of the selected block.

10.2.4 MEMI workflow performance

Figure III.14 and **III.15** show the results obtained by applying the MEMI workflow to the Puigcerçós point clouds. These results are focused on quantifying the maximum threshold (performance) that can be achieved in the 3D comparisons, and to see how the error changes according to the different workflows applied. For this purpose, comparisons have been carried out on two consecutive days during a period of low activity, as this allows us to evaluate when the comparison starts to show instrumental noise (avoiding rockfalls and deformations).

However, this situation does not always correspond to reality, as in these figures, the classical workflow benefits from the use of images from consecutive days. This means that the differences between the images are reduced as much as possible. Consequently, the geometries obtained by the SfM-MVS process are extremely similar.

For this reason, **Figure IV.17** presents the result of an M3C2 comparison between two 3D models separated by a longer period of time. Thus, changes occur in both the positions of the cameras and the surface of the cliff. These differences affect the geometries of the 3D models obtained using the classical SfM-MVS workflow (more different geometries are generated). And, consequently, the difference threshold for identifying rockfalls is higher. **Figure IV.17** shows the comparison between the 3D models generated on 9 November 2019 and 19 January 2021 using the classical workflow and the MEMI workflow. **Figure II.30** (page 129) shows the differences between these two workflows.

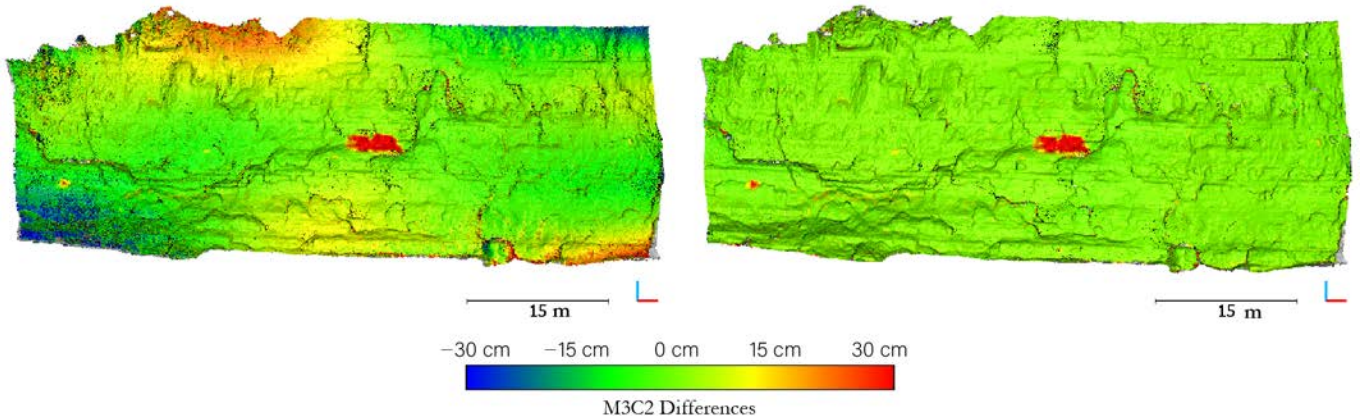
Figure IV.17a and **IV.17c** shows the comparison made with the classical method (the difference is in the colour bar). To obtain this M3C2 comparison, 2 completely different 3D models have been generated, each corresponding to each date of the comparison. The models have been made with a single image from each HRCam photogrammetric system (5 images per model). Once the two dense point clouds were obtained, an ICP alignment and an M3C2 comparison were performed.

Figure IV.17b and **IV.17d** shows the comparison applying the MEMI workflow. In this way the camera positions are computed jointly for the two chosen dates. In addition, 3 images from each photogrammetric system have been used (30 images in total).

Puigcercós - 09/11/2019 vs 19/01/2020 (71 days)

a) Classic Workflow (Display threshold -> 30 cm)

b) MEMI Workflow (Display threshold -> 30 cm)



c) Classic Workflow (Display threshold -> 3 cm)

d) MEMI Workflow (Display threshold -> 3 cm)

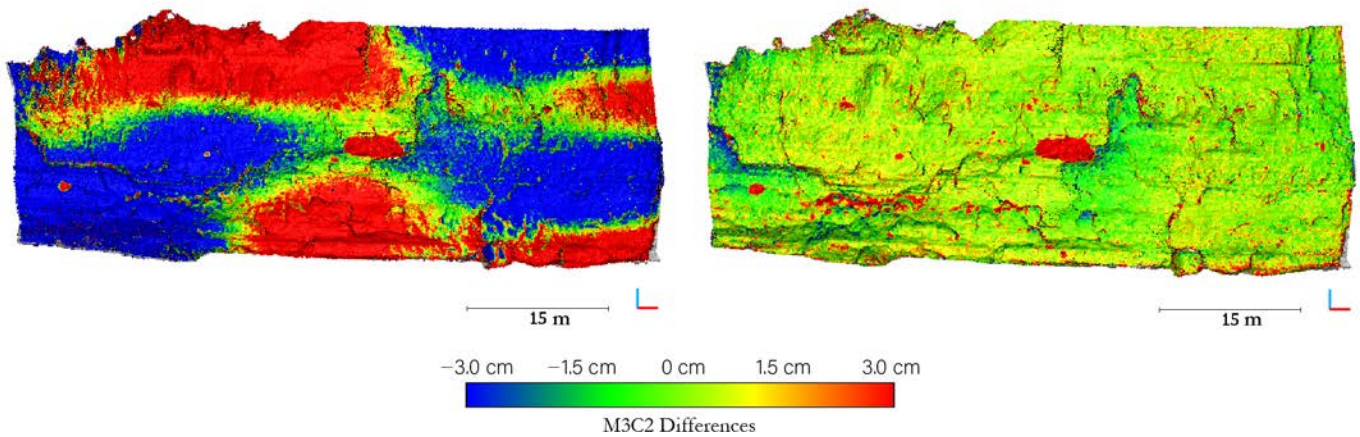


Figure IV.17. 3D comparison using the classical workflow and the MEMI workflow between 09 November 2019 and 19 January 2020. The same comparison has been rendered twice, but using a different colour/threshold scale; **a)** and **b)** show the comparisons using the classic and MEMI workflows respectively with a treshold value of 30 cm (values below 30 cm are shown in green-yellow); **c)** and **d)** show the comparisons using the respective workflows with a treshold value of 3 cm.

The results shown in **Figure IV.17** are very relevant evidence of the improvement obtained by applying the MEMI workflow. **Figure IV.17c** is particularly significant, as it clearly shows how the geometries constructed with the classical method are significantly different from each other. In contrast, in **Figure IV.17d**, using the same geometries (MEMI Workflow), much smaller comparison limits are obtained, showing a greater amount of information (rockfalls in red, and pre-failure deformation in blue).

However, it should be noted that the result obtained by the classical method is also valid. The difference between the geometries makes it difficult to obtain low comparison thresholds (a necessary condition for emulating LiDAR data), but this does not mean that the comparisons are erroneous. As shown in **Figure IV.17a**, large rockfalls can be correctly identified. It is only a problem in terms of “scale” and deformation detection limits.

10.3 Granada-Alhambra – DSLR System

10.3.1 Rockfall monitoring

The DSLR system installed in the Tajo de San Pedro – Granada is the application case that has allowed us to obtain more results. Thanks to the monitoring carried out over 2 years and the commitment made by the Patronato de la Alhambra y el Generalife to prepare biannual reports, we have been able to process a large number of data and consequently obtain numerous rockfalls.

Figure IV.18 show all the rockfalls detected during this research. Each colour corresponds to the following periods: 07/2019-11/2019 (orange), 11/2019-11/2020 (purple) and 11/2020 – 05/2021 (green). This result is very useful to highlight the significant rockfall activity that occurs in the Tajo de San Pedro and it allows us to observe how the distribution of rockfalls is homogeneous both temporally and spatially. In addition, it demonstrates the impossibility of detecting rockfalls in areas where there is vegetation (white gaps).

The result shown in **Figure IV.18** was obtained using the DSLR systems installed in the Tajo de San Pedro, applying the MEMI workflow and carrying out a manual filtering of the rockfalls (semi-automated processing).

Thanks to the long observation period, multiple results can be obtained in the same way as with other monitoring strategies. Examples of that are i) **Figure IV.19**, showing an intensity distribution of the rockfalls (based only on the number of rockfalls); ii) **Figure IV.20a**, showing a frequency-volume histogram, used to understand the type of activity that occurs on the cliff; and iii) **Figure IV.20b**, which shows the magnitude-frequency distribution that also defines the behaviour of the scarp and is widely used for engineering analysis.

Rockfalls - Granada Alhambra

- 07/2019 vs 11/2019 (107 days) - 22 Rockfalls
- 11/2019 vs 11/2020 (355 days) - 67 Rockfalls
- 11/2020 vs 05/2021 (207 days) - 46 Rockfalls

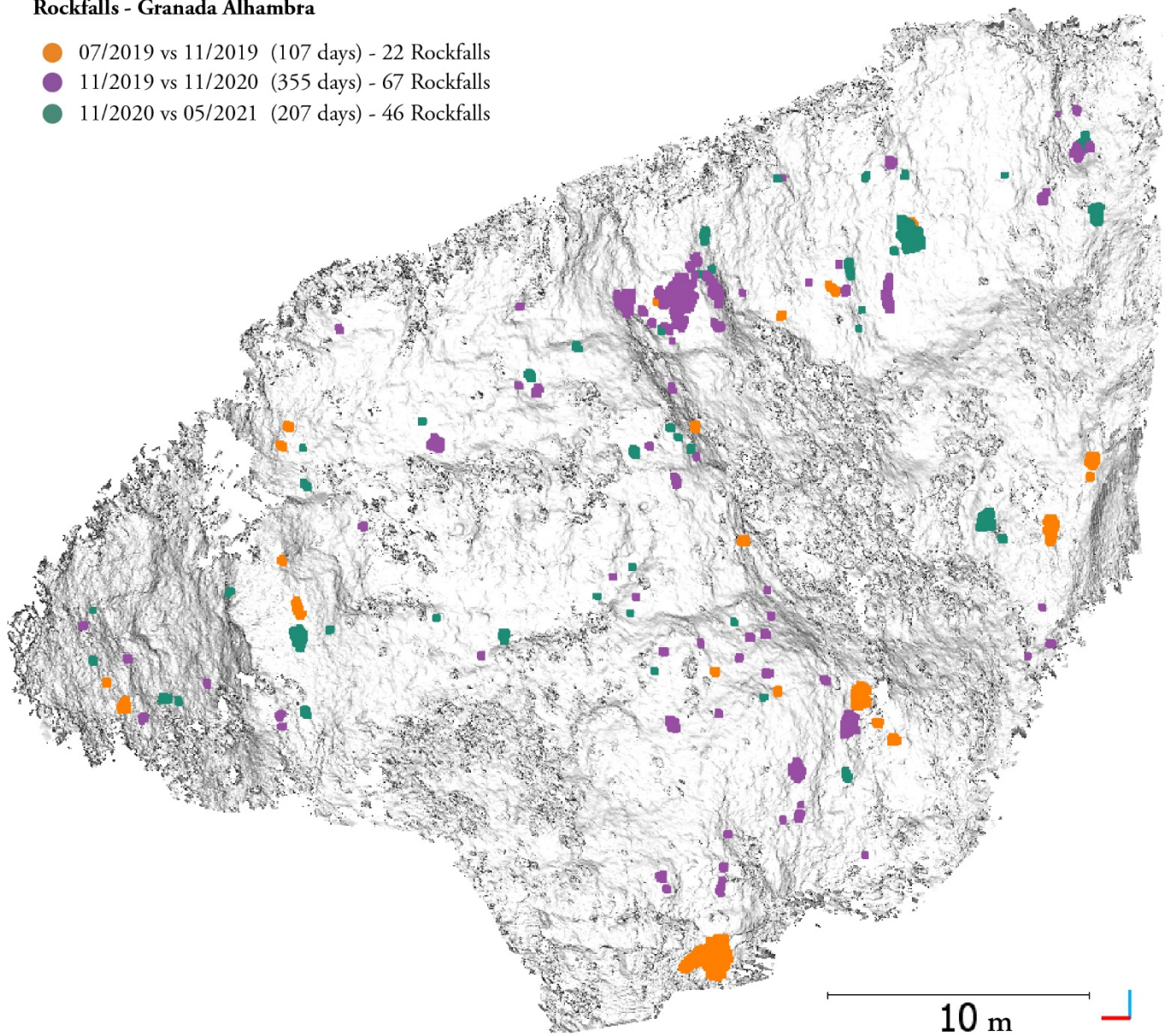


Figure IV.18. Rockfalls identified in the Tajo de San Pedro (Granada). Each colour identifies a different observation period. In total, 135 rockfalls have been identified over 669 days. The size of the rockfall markers has been increased to facilitate their visualisation.

Rockfall Density - Granada Alhambra

From 07/2019 to 11/2020 (462 days)

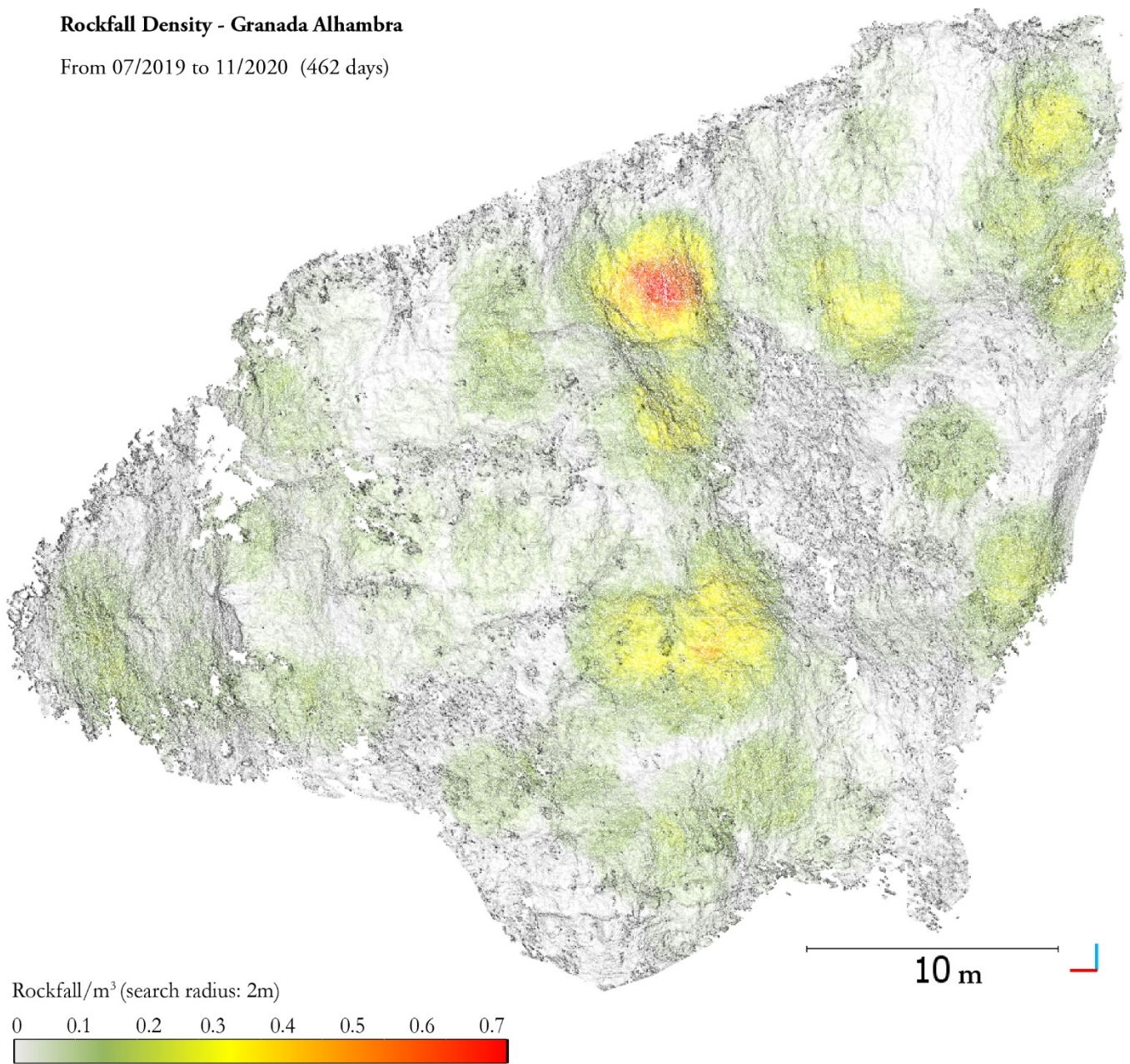


Figure IV.19. Visualisation of the rockfall density distribution. The areas with warm colours show a higher concentration in the number of rockfalls during the 462-day observation period. The areas where no landslides are identified can be clearly visualised. These areas correspond to vegetation. A sphere of radius 2 metres has been used to count the number of rock falls per cubic metre.

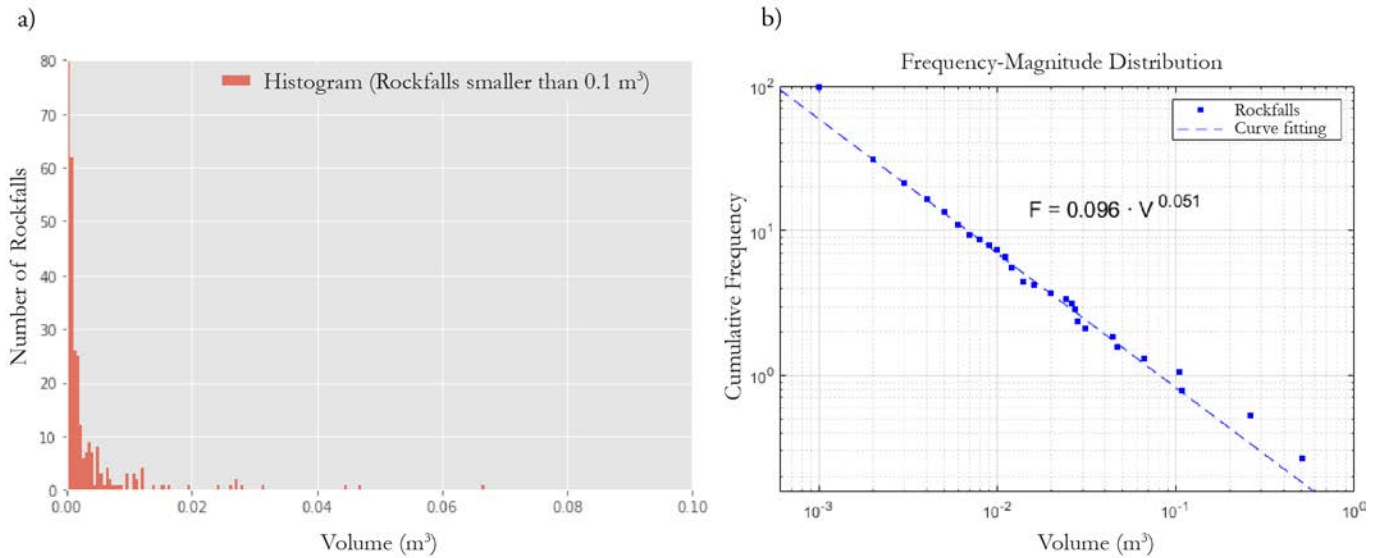


Figure IV.20. Results obtained from the monitoring of rockfalls over a period of 669 days. **a)** Histogram of the distribution of rockfalls. Here we can see that most of the rockfalls are of small magnitude. **b)** Frequency-Magnitude distribution. The equation fitted to the number of rockfalls allows to characterize the behaviour of the Tajo de San Pedro cliff.

10.3.2 Automatic rockfall monitoring

Given the difficulty of processing the data from the Tajo de San Pedro, the automatic monitoring system based on Machine Learning algorithms has been applied in this study area. **Figure IV.10b** (page 211) shows the confusion matrix obtained for the best training performed with the Random Forest classification algorithm. Using the same trained model, **Figure IV.21** shows the result of applying the generated ML model to the validation data (**Figure IV.9a**).

This dataset consists of 68 clusters, randomly selected (38 rockfalls and 30 wrong clusters), and has not been part of the ML training process. The result is shown in different colours: i) Rockfalls correctly identified by the ML model, 89% success rate (in purple); ii) Wrong clusters (not rockfalls) correctly identified by the model, 97% success rate (in blue). iii) False positives, clusters identified as rockfalls that are simply wrong clusters. iv) False negatives, clusters that are rockfalls, but the ML model has identified as wrong clusters.

ML - Granada Alhambra

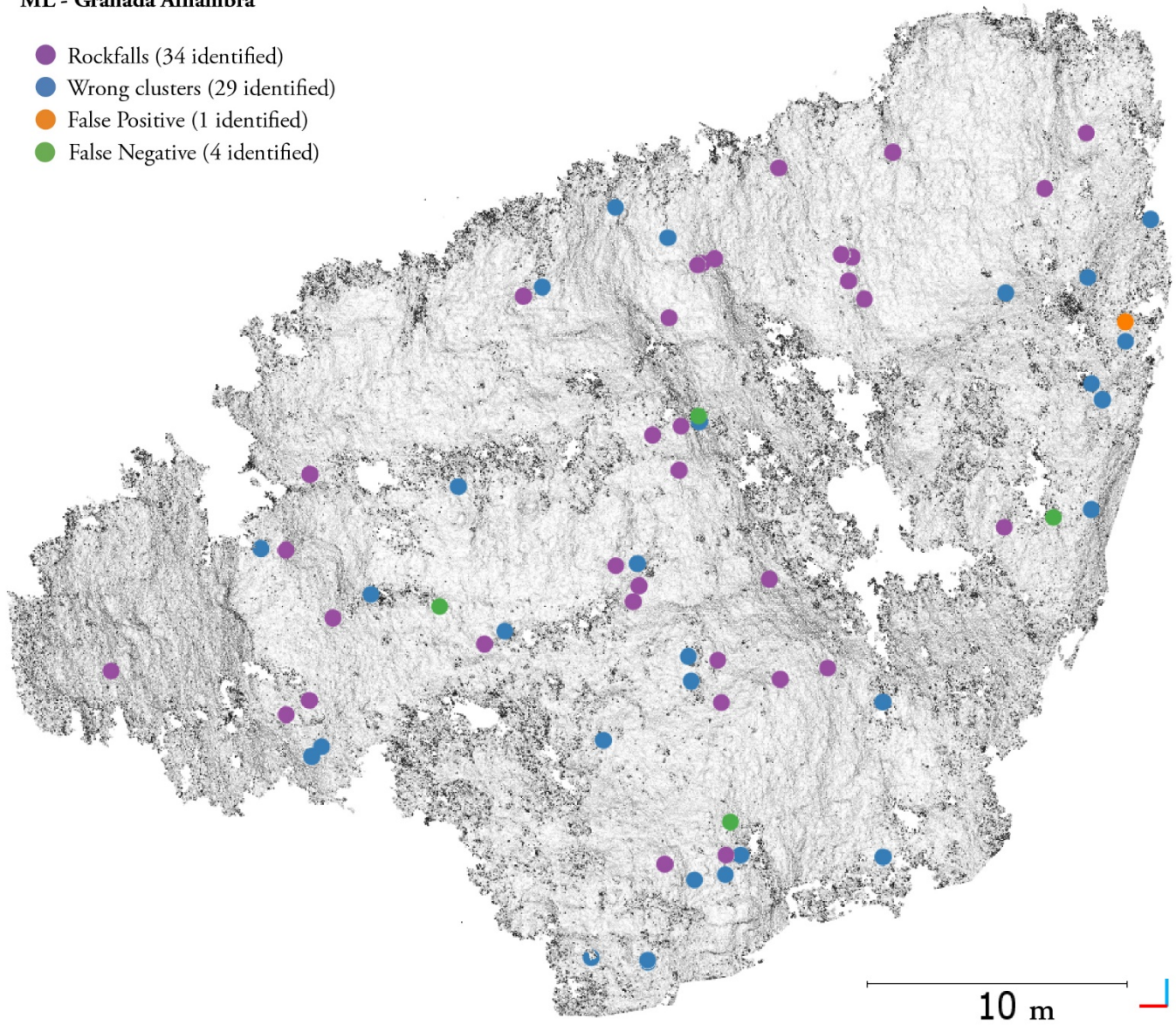


Figure IV.21. Result obtained after automatically processing (with Machine Learning algorithm) 68 clusters in the Tajo de San Pedro. Purple colour shows the correctly identified rockfalls. Blue colour shows the wrong clusters correctly identified. Orange dot show a false positive, a cluster identified as a rockfall by the algorithm that is not a rockfall and the colour green identifies the false negatives, clusters identified as wrong clusters but which are rockfalls.

The aim of this chapter is to outline the limitations and opportunities of the application cases for rockfall detection previously described. In the absence of a real scientific analysis of the results obtained in this section, it is not possible to discuss them. However, the author considers it interesting to point out the limitations and possibilities that are observed in the results for the rockfall monitoring.

11.1 Rockfall monitoring workflow

The workflow developed in this research (updated from the RISK-NAT workflow) for the identification of rockfalls works well in controlled environments. The experiences of Abellán (2009) and Royán (2015) show that it is an effective method for detecting rockfalls from point clouds. The transition in the technology of data acquisition does not present a major problem. The point clouds obtained by the photogrammetric systems created in this research and processed using the developed algorithms have a quality comparable to LiDAR in the same working environments. This is supported by the results obtained in the accuracy estimation and by the results reported previously, which show that it has been possible to monitor the rockfalls and obtain the usual by-products in the same way as before with terrestrial LiDAR, but at a much lower cost.

In addition, the inclusion of the new algorithms allows for faster processing and no dependence on privately licenced software. For this purpose, the use of the M3C2 distance calculation in CloudCompare rather than the Polyworks method, as well as the change of programming language from MATLAB to Python represent considerable advances.

From field work conducted on the cliffs under study, it is difficult to identify differences between LiDAR data and photogrammetric data. The only notable difference lies in the vegetation modelling. While LiDAR allows a perfect modelling of the vegetation, the photogrammetric model generates a dome effect that covers all the vegetation. This makes it difficult to identify the vegetation using geometric criteria. Unlike the LiDAR data used by

RISKNAT, the possibility of working with real RGB data for each point provided by photogrammetry helps us to discern vegetation. And it allows the generation of new image-based algorithms for filtering vegetation.

11.2 Workflow automation

The main limitation of all the developments presented in this thesis is the management of the large amount of data that can be obtained. Although it is possible to work with a high temporal frequency (this entails analysing data captures with monthly frequencies), the systems developed in this thesis have the capacity to obtain data several times a day. This data collection capability has been a novelty in the RISKNAT research group.

For this reason, neither the rockfall identification workflow nor the workstations/servers were prepared to handle such a large amount of data on a daily basis. Thus, in the final part of this thesis, a complete automation of the process has been carried out.

The automation of the process should make it possible to eliminate human intervention throughout the whole process of obtaining rockfalls. By achieving this goal, it is possible to have a system running in the background and obtaining daily rockfall analysis in an automatic way.

However, in the automation process we have encountered a major limitation, which is the identification of clusters created by errors (wrong clusters) that do not represent any rockfall. Whether the source of the data is LiDAR or photogrammetric, the workflow causes non-rockfall clusters, so the identification of rockfalls was always carried out manually when processing with monthly frequencies.

At the end of this thesis, different solutions have been tried in order to overcome this limitation. Since no perfect solution has been found, the author wished to give an account of all tested options and their limitations, since some approaches have generated valuable new knowledge that points the way to possible future research. However, none of these methods have been tested critically enough, and they are presented in this thesis only because

the author believes that this dissertation is the ideal place to present all the work done in order to facilitate future work.

The most promising method is the use of Machine Learning. Unlike other strategies, this strategy does not limit any of the parameters. The automatic ML method was used on the Tajo de San Pedro cliff because it was the most challenging. The presence of a lot of vegetation that has not been filtered out, together with a photogrammetric model with certain weaknesses, make it a good candidate for Machine Learning algorithms.

The results obtained are encouraging and should be understood as an initial approximation of the method. The main limitation we have found in working with Machine Learning algorithms is the lack of data. In order to correctly train intelligence algorithms that can discern between a false cluster and a rockfall, a large amount of previously classified input data is needed.

Moreover, this classification should be revised as using mislabelled training data impairs the performance of the algorithm, and some of the results obtained may indicate that some manually identified rockfalls are not really rockfalls.

To improve the ML algorithms, new parameters could be introduced for the classification, for example, the volume of each cluster. This has not been introduced in this experiment due to the high computational cost of calculating the volume of all clusters.

Given the complexity of the data, it is likely that the decision tree structures are not sufficiently suitable for binary cluster classification. For this reason, a logical evolution would be to transform the Machine Learning system by a Deep Learning binary classification neural network.

A final consideration is the very difficult challenge of achieving a fully automated system capable of identifying 100% of rockfalls without error. There will always be a compromise to be made between automation capability and the number of false positives tolerated. The advances shown in this thesis have the potential to greatly improve such a decision, as it demonstrates that an automatic process with a high success rate can be achieved.

11.3 Application cases

The application cases provided in the previous chapter demonstrate the different possibilities for rockfall monitoring. All the data used to generate the results of the previous section have been obtained from the photogrammetric systems developed and processed with the new algorithms shown in this thesis. Although the significance of these rockfalls has not been explored in geological terms, the reader can get a good idea of the potential of fixed photogrammetric systems operating in an automated way for geohazard monitoring.

Together with the scripts and codes, the systems have succeeded in identifying rockfalls and pre-failure deformation. The capability of being fixed time-lapse systems allows this monitoring to be conducted on a sub-daily frequency. Allowing to obtain new correlations (e.g., daily rainfall or temperature) that are difficult to obtain with classical monitoring methods using a longer observation time. Allowing 4D geohazard analysis.

However, these real working experiences have also shown us that outdoor systems are sensitive to weather conditions and that more robust systems are needed to obtain long observation time series.

The examples given provide a solid answer to the initial question posed in this thesis. Yes, it is possible to monitor rockfalls with fixed time-lapse photogrammetric systems instead of expensive LiDAR. However, in order to obtain a similar level of accuracy, processing algorithms and workflows must be applied, and the photographic captures must be carried out in a controlled and specific manner for each study area.

This answer is supported by the results shown in the **Chapter 10**, which show different rockfalls identified using a threshold value of 3 cm (the same used with LiDAR data by Abellán (2009) and Royán (2015)). These examples show how, in addition to large rockfalls (100 m³), minor rockfalls (smaller than 0.1 m³), which are the most common, have also been identified. In addition, similar to the experiences of these authors, pre-failure deformation has also been identified in large blocks, which, although not analysed in depth, give us an idea of the potential of the method.

Section V

GLOBAL SUMMARY

CHAPTER 12 – SUMMARY OF THE DISCUSSIONS

CHAPTER 13 – CONCLUDING REMARKS



Chapter 12

Summary of the Discussion

12

This chapter presents a general discussion of all the research conducted in this thesis. The aim of this chapter, which is mandatory, is to connect all the partial discussions detailed throughout the thesis in order to justify the work done. Partial discussions associated with each photogrammetric system (**Chapter 6**) and each method, PCStacking in **Chapter 7** and MEMI in **Chapter 8**, have already been addressed. Furthermore, a brief consideration about the rockfall monitoring has previously been provided in **Chapter 11**.

In addition to the summary of what has already been presented in previous chapters, the author wishes to make a few brief overall observations which, taken together, represent a general discussion of the research.

12.1 Summary of the discussion

Can rockfall monitoring be carried out using fixed-camera photogrammetric systems in a similar way to terrestrial LiDAR (TLS)? This is the question that was posed at the outset of this dissertation. After all the many pages devoted to technical explanations, expositions of methods, tests and discussions, the answer is clearly in the affirmative, and the author considers that all the research undertaken in this dissertation justifies this response.

Throughout this dissertation we have presented photogrammetric systems designed ad hoc to obtain the necessary data for monitoring. This task, outside the basic knowledge of the geosciences, posed a major challenge that has been successfully overcome.

In general terms, the systems have fulfilled their objective of capturing data at high temporal frequency and sending it remotely to servers. However, it is necessary to point out that all systems have suffered from failures, most of which are associated with the inefficiency of the system due to the severe climatic conditions of the study areas.

Solutions such as the photogrammetric systems developed, could have been purchased commercially. However, their high price and their lack of flexibility for adaptation to the

study areas, as well as the task of programming them in accordance with our research, demonstrate that the decision to develop them ourselves was the right one. However, a review of the design of these systems may be necessary in order to make them more stable. It is the author's wish that any new system generated in this way will make the most of the lessons (both good and bad) learned in this field.

These photogrammetric systems, discussed in greater depth in **Chapter 6** form the basis of this thesis. From their testing at laboratory level (**Figure II.1**) to their implementation in real study areas (**Figure III.2, Figure III.5, Figure III.8**), the use of these systems has been transversal in all the developed methodologies. It would have been difficult to achieve the overall improvements in the identification of rockfalls if the photogrammetric systems presented in this thesis had not been performed correctly.

The use of the most basic systems, known as RasPi systems (**Section 3.3**), has revealed the need to generate post-processing algorithms in order to eliminate the geometric error generated by low-cost photogrammetric models. This algorithm, called PCStacking (**Chapter 4**), makes it possible to obtain more consistent models with very low-cost systems.

The discussion of the PCStacking algorithm is detailed in **Section 7.4**. While this algorithm has shown good performance, it still requires a lot of input data (about 10 models to get a good result) and is also very time consuming. Nevertheless, the results obtained are very good and enable very low-cost systems to be used efficiently for rockfall monitoring.

Although the development of this system was interrupted during the thesis in order to focus on high-definition systems, the author finds it very satisfying to have been able to develop both the very low-cost system and an associated algorithm that yields better 3D comparisons.

The generation of a set of very low-cost photogrammetric system plus a data processing algorithm to obtain a better quality of model comparison, together constitute a very substantial contribution to the community. This strategy removes the financial barrier that many surveillance strategies involve, and may lead to the expansion of these systems in the community without being hampered by the need for a large investment.

The use of high-definition systems has entailed a great responsibility. These systems require a higher investment in equipment and a higher level of programming. Nevertheless, during the course of the thesis it has been possible to generate two high-resolution systems; the HRCam system (**Section 3.4**) and the DSLR system (**Section 3.5**). These systems are subject to greater failures than the RasPi system. This is due to both the complexity of the installation and the metal boxes used. On the other hand, the quality of the photogrammetric models obtained is much higher, enabling better quality rockfall monitoring.

The development of the MEMI algorithm (**Chapter 5**) has been the key element for facilitating the use of photogrammetry for rockfall monitoring. Thanks to the MEMI algorithm, direct comparisons of photogrammetric models can be obtained without the need to i) install ground control points (GCP) on the wall. ii) perform camera calibrations, and iii) use alignment algorithms.

All these published advances contribute to higher quality 3D change detection (**Sections 7.2** and **8.2** discusses the improvements achieved). These improvements benefit numerous scientific disciplines. As an example, this thesis discusses its use in rockfall monitoring, but it can be used in many other fields of geoscience and engineering.

The results obtained are comparable to those traditionally obtained with LiDAR. The slight differences are discussed in **Section 8.2**. However, the great novelty provided by the use of these photogrammetric systems, such as HRCam or DSLR, is the ease with which large amounts of data can be obtained. For this reason, it has been necessary to change the traditional way of working.

These new working methods (**Chapter 9**), although they are not fully completed in this thesis, enable rockfall monitoring to be addressed in an automatic way. While all automation processes invariably present a challenge for researchers, this automation is crucial for managing all the data that photogrammetric systems can capture with a very high temporal resolution. As previously mentioned, automation will hardly allow for a 100% secure identification. For this reason, models will have to be improved, trained and made more robust in order to increase the percentage of positive results. It is necessary to achieve a good compromise between the automation of the whole process and the quality of the results.

This strategy still needs to be further developed and has the potential of being an unprecedented breakthrough in rockfall monitoring with a low-cost approach without sacrificing quality.

Regarding the cohesion of the research, the algorithms presented cannot be understood without the systems developed, and in the same way, the algorithms could not have been developed without the systems. Thus, the justification of the different phases of the research is entirely logical and should be understood as a linear evolution of the scientific method. First the instrumentation has been generated, then the data has been acquired, afterwards the processing strategies have been developed and finally the rockfall monitoring results have been obtained. Although the rockfall results part requires future development in order to achieve more consistent results.

12.2 Global consideration

As described at the beginning of this dissertation, the monitoring of natural phenomena has been conducted over time. As new technological opportunities have opened the way to the development of new working methods, so the monitoring of natural phenomena has evolved.

Based on a more **social objective** (sometimes overlooked), the rapid spread of digital photogrammetry, facilitated by its low cost and user-friendliness, the democratisation of natural phenomena monitoring has become a reality. For this reason, the development of very low-cost systems will play an important role in the expansion of this technology. Thanks to the sharing of knowledge throughout the community, these advances will help to extend monitoring to those places where it was not possible before, either because the cost of access was too high or because remote access made it unfeasible.

In addition, the development of high-resolution systems is necessary for identifying the limits of technology. It is by reaching these limits that science advances and better solutions are generated. These solutions, which in the case of this thesis have been developed in real risk areas, have the ultimate goal of improving the life of the community.

Consequently, the author believes that the opportunities generated by photogrammetric monitoring systems for rockfall monitoring are of great significance for society, since a better knowledge of the danger undoubtedly leads to a greater capacity to protect against it, and therefore to a reduction in risk and a safer life for all.

Regarding the **technological objective** extensively described in these chapters, solving the challenge of dealing with large amounts of data and obtaining the results in an optimal and automatic way constitute an unprecedented step forward in the monitoring of rockfalls in near-real time, as well as enabling the evolution of monitoring from 3D to 4D.

The author considers that the contributions made in this thesis represent a considerable advance in this regard, from the establishment of the systems (hardware) to the development of the workflows (software). All the advances developed in this thesis are especially relevant to the general objectives described above (democratising technology and advancing in near-real time and 4D monitoring). Moreover, they are capable of providing the basis for future research and progress towards the achievement of the overall objectives.

12.3 Further research

Based on the limitations discussed in the previous chapters, future work can be carried out on the basis of the work developed in this thesis.

Photogrammetric systems must be improved; as mentioned above, they suffer from different failures detected throughout the course of this thesis. For this reason, approaching photogrammetric systems from an engineering-electronic perspective may give rise to the creation of much more robust devices with a lower error rate.

The possibility of improving the configurations of photogrammetric systems also exists. With more time and resources, camera locations and the quality of the images taken can be improved; older cameras can be upgraded; better lenses can be used, and more camera locations can be added to the system. All these improvements will undoubtedly have a beneficial impact on monitoring capability.

RasPi systems also have potential for improvement. Further research is needed on the generation of very low-cost systems that allow monitoring at a reasonable cost. In addition, specific actions such as improving the photographic lenses would provide better quality at a similarly lower cost.

In relation to RasPi systems, comparisons should be made to obtain their range of reliability. These comparisons can be made synthetically by analysing known rockfalls (controlled volume) or by comparing the system with LiDAR data. This comparison is necessary in order to estimate the accuracy of the system with respect to a real reference.

High resolution photogrammetric systems also need to be improved at the internal programming level. The interaction between cameras (we have worked with three different brands: Sony, Nikon, and Canon) and the control unit are not user-friendly and may lead to system errors.

Optimisation of the PCStacking algorithm will be a very interesting aspect of future work. It is a very time-consuming algorithm, and its integration with point cloud software such as CloudCompare would be a very interesting contribution to the community.

Rockfall monitoring can be improved in many aspects. Future work should be done to obtain more accurate identifications. This work could address both the photogrammetric process for eliminating errors prior to comparisons and methods in cluster classification and filtering. In this respect, fields such as Machine Learning or Deep Learning still have a long way to go.

Finally, there is extensive work to be done on the geological aspect. Further work is needed to identify as accurately as possible (eliminating false positives) all the rock falls and pre-fault deformations that have occurred during this time, in order to provide data to improve the knowledge and behaviour of the areas studied. This information would also provide the possibility of comparison with other monitoring methods (seismic or LiDAR). In addition, the higher temporal frequency of observation opens up a world of possibilities to study, correlate and better understand rockfall phenomena.

Chapter 13

Concluding Remarks

13

13.1 Photogrammetric Systems

Three different photogrammetric systems have been developed over the course of this research. This development has entailed the design, assembly, and installation in the respective study areas. Each photogrammetric system has been developed to operate in a remote way, which means programmable, solar-powered and with data transmission capabilities.

Two different concepts have been used to develop the systems. The first was to make very low-cost systems (about 150€) by sacrificing photographic quality. This system is called the **RasPi system** and has been installed in the experimental study area of the RISKAT research group located in Puigcercós (Catalonia, NE Spain). The **RasPi system** has been used to obtain low-resolution photogrammetric models. Thanks to the creation of advanced algorithms (**PCStacking**) it has been possible to detect rockfalls and pre-failure deformation.

The second concept consisted of generating systems with commercial cameras. In this case, the cost of each photogrammetric system is higher (about 2,000€), but as a result higher quality photogrammetric model have been obtained. Two autonomous time-lapse still photogrammetric systems were developed using conventional cameras controlled by microcontrollers.

On the one hand, the **HRCam** photogrammetric system has been installed in Puigcercós, in the same location as the **RasPi system**, while the **DSLR** system has been installed in the study area of the Tajo de San Pedro, on the slope of the Alhambra (Granada).

Thanks to the creation of a workflow (**MEMI Workflow**) adapted to the monitoring systems obtained, it has been possible to carry out important monitoring campaigns, identifying both landslides and precursor deformation. The results of this monitoring can be compared with those obtained by LiDAR. In addition, it is possible to carry out observations at a very high temporal frequency.

13.2 PCStacking (Publication I)

This section presents an algorithm for increasing precision in the comparison of point clouds (PCs) obtained through Multi-View Stereo photogrammetry. This method, called Point Cloud Stacking (**PCStacking**), refers to the process of taking photographs, as well as the data processing and post-processing of the information to generate enhanced PCs. This section, published in a paper, describes the application of the method using both synthetic PCs specially developed to emulate photogrammetric models, and a real case study with photogrammetric PCs obtained using a very low-cost time-lapse camera system.

The results show a reduction of more than 50% of the error, increasing the precision in both experiments, and validating the proposed approach under different conditions. In more detail, the 25th and 75th percentiles were progressively reduced with both the synthetic data and the actual photogrammetric models from ± 3.2 cm to ± 1.4 cm, and from ± 1.5 cm to ± 0.5 cm, respectively. The resulting enhancement means that relatively low-cost strategies could be used in place of more expensive systems, but the proposed algorithm can also be used to repeat TLS scenarios in order to increase the signal-to-noise ratio. The proposed approach may constitute a step forward for high precision monitoring of both natural processes (landslides, glaciers, riverbeds, erosion, etc.) and man-made scenarios (structural monitoring of buildings, tunnels, beams, dams, etc.) using low-cost time-lapse camera systems.

13.3 MEMI Workflow (Publication II)

This section presents the MEMI workflow developed in this thesis. It has been carried out in order to obtain higher quality comparisons when using photogrammetric systems. The comparison made with the classic, multi-epoch single-imagery (MESI) and multi-epoch multi-imagery (**MEMI**) workflows shows that the workflow developed in this article leads to significant improvements in the construction of photogrammetric models.

The improvements demonstrated in this paper yield models with a greater geometric coherence between them, without the need for complex camera calibrations, post-process alignments or the use of GCPs. The MEMI workflow reduced the error up to a factor of 2 in the comparison accuracy (2.83 cm with the classic workflow vs 1.54 cm with the proposed

approach). The proposed enhancement is very relevant when performing studies based on change detection processes. The published pipeline reduces the deformation thresholds used to determine if changes have occurred.

13.4 Rockfall Monitoring

To achieve rockfall monitoring, the entire historical workflow of the RISKNAT group has first been adapted to a new programming language (from private licensing MATLAB to open-source Python code). The workflow has then been adapted to introduce the improvements in the processing algorithms (both the improvements made by myself such as MEMI workflow and by external authors such as M3C2 3D comparison).

Finally, all the programming software has been developed to make the photogrammetric monitoring system work automatically, linking all the steps in the photogrammetric processing to obtain the rockfall identification, thereby achieving complete automation from the image acquisition to the calculation of the volume of rockfalls. In addition, due to the need to improve the automation of the rockfall monitoring process to avoid wrong classification, different algorithms to improve cluster filtering are also presented in this thesis. These filters range from simple parametric variations to the application of complex Machine Learning methods.

To conclude, this thesis presents three real examples of photogrammetric monitoring systems based on fixed time-lapse cameras. Thanks to the data acquired by these systems and the improvement and automation of the rockfall identification algorithms, it has been possible to carry out rockfall monitoring in a similar way to other monitoring strategies.

The advances presented in this thesis represent unprecedented progress in the creation of true low-cost early warning systems that can operate in at-risk areas. All the solutions developed in this thesis (which are published under CC BY-SA 4.0 - Free Cultural Works licence) have the ultimate ambition of approaching monitoring systems to society, democratizing their use and making society safer and more resilient to natural disasters.

Section VI

REFERENCES

REFERENCES - OVERALL REFERENCES



References

Overall References

R

- Abancó, C.**, Hürlimann, M., Fritschi, B., Graf, C., & Moya, J. (2012). Transformation of ground vibration signal for debris-flow monitoring and detection in alarm systems. *Sensors*, 12(4), 4870–4891. <https://doi.org/10.3390/s120404870>
- Abellán, A.** (2009). Improvements in our understanding of rockfall phenomenon by Terrestrial Laser Scanning. In *Dissertation* (Issue July).
- Abellán, A.**, Calvet, J., Vilaplana, J. M., & Blanchard, J. (2010). Detection and spatial prediction of rockfalls by means of terrestrial laser scanner monitoring. *Geomorphology*, 119(3–4), 162–171. <https://doi.org/10.1016/j.geomorph.2010.03.016>
- Abellán, A.**, Jaboyedoff, M., Oppikofer, T., & Vilaplana, J. M. (2009). Detection of millimetric deformation using a terrestrial laser scanner: Experiment and application to a rockfall event. *Natural Hazards and Earth System Science*, 9(2), 365–372. <https://doi.org/10.5194/nhess-9-365-2009>
- Abellán, A.**, Oppikofer, T., Jaboyedoff, M., Rosser, N. J., Lim, M., & Lato, M. J. (2014). Terrestrial laser scanning of rock slope instabilities. *Earth Surface Processes and Landforms*, 39(1), 80–97. <https://doi.org/10.1002/esp.3493>
- Abellán, A.**, Vilaplana, J. M., Calvet, J., García-Sellés, D., & Asensio, E. (2011). Rockfall monitoring by Terrestrial Laser Scanning - Case study of the basaltic rock face at Castellfollit de la Roca (Catalonia, Spain). *Natural Hazards and Earth System Science*, 11(3), 829–841. <https://doi.org/10.5194/nhess-11-829-2011>
- Abellán, A.**, Vilaplana, J. M., & Martínez, J. (2006). Application of a long-range Terrestrial Laser Scanner to a detailed rockfall study at Vall de Núria (Eastern Pyrenees, Spain). *Engineering Geology*, 88(3–4), 136–148. <https://doi.org/10.1016/j.enggeo.2006.09.012>
- Agisoft.** (2021). *Agisoft Metashape User Manual: Professional Edition, Version 1.7.*
- Agisoft LLC.** (2018). *Metashape Python Reference, Release 1.6.0* (pp. 1–199). https://www.agisoft.com/pdf/metashape_python_api_1_6_0.pdf
- Agisoft LLC.** (2020). *Agisoft Metashape Professional Edition* (1.6.2 build 10247). <https://www.agisoft.com/>
- Aha, D. W.**, Kibler, D., & Albert, M. K. (1991). Instance-based learning algorithms. *Machine Learning*, 6(1). <https://doi.org/10.1007/bf00153759>

- Akiyama, T. S.,** Marcato Junior, J., Gonçalves, W. N., Bressan, P. O., Eltner, A., Binder, F., & Singer, T. (2020). DEEP LEARNING APPLIED to WATER SEGMENTATION. *International Archives of the Photogrammetry, Remote Sensing and Spatial Information Sciences - ISPRS Archives*, 43(B2). <https://doi.org/10.5194/isprs-archives-XLIII-B2-2020-1189-2020>
- Allen, S.,** & Huggel, C. (2013). Extremely warm temperatures as a potential cause of recent high mountain rockfall. *Global and Planetary Change*, 107, 59–69. <https://doi.org/10.1016/j.gloplacha.2013.04.007>
- Anderson, K.,** Westoby, M. J., & James, M. R. (2019). Low-budget topographic surveying comes of age: Structure from motion photogrammetry in geography and the geosciences. *Progress in Physical Geography*, 43(2), 163–173. <https://doi.org/10.1177/0309133319837454>
- Angeli, M. G.,** Pasuto, A., & Silvano, S. (2000). A critical review of landslide monitoring experiences. *Engineering Geology*, 55(3), 133–147. [https://doi.org/10.1016/S0013-7952\(99\)00122-2](https://doi.org/10.1016/S0013-7952(99)00122-2)
- Artese, S.,** Lerma, J. L., Zagari, G., & Zinno, R. (2016). *The survey, the representation and the structural modeling of a dated bridge*. <https://doi.org/10.4995/arqueologica8.2016.3559>
- Atzeni, C.,** Barla, M., Pieraccini, M., & Antolini, F. (2015). Early Warning Monitoring of Natural and Engineered Slopes with Ground-Based Synthetic-Aperture Radar. *Rock Mechanics and Rock Engineering*, 48(1), 235–246. <https://doi.org/10.1007/s00603-014-0554-4>
- Azañón, J. M.,** Azor, A., Booth-Rea, G., & Torcal, F. (2004). Small-scale faulting, topographic steps and seismic ruptures in the Alhambra (Granada, southeast Spain). *Journal of Quaternary Science*, 19(3), 219–227. <https://doi.org/10.1002/jqs.838>
- Azañón, J. M.,** Rodríguez-Peces, M. J., García-Mayordomo, J., & Justo, J. L. (2011). Fallas Activas Y Sismicidad En Las Partes Altas De La Ciudad De Granada : Comportamiento Dinámico De La Formación. *4º Congreso Nacional de Ingeniería Sísmica*, 1–7.
- Azzoni, A.,** la Barbera, G., & Zaninetti, A. (1995). Analysis and prediction of rockfalls using a mathematical model. *International Journal of Rock Mechanics and Mining Sciences & Geomechanics Abstracts*, 32(7), 709–724. [https://doi.org/10.1016/0148-9062\(95\)00018-C](https://doi.org/10.1016/0148-9062(95)00018-C)
- Baker, S.,** & Matthews, I. (2004). Lucas-Kanade 20 years on: A unifying framework. *International Journal of Computer Vision*, 56(3), 221–255. <https://doi.org/10.1023/B:VISI.0000011205.11775.fd>

- Barlow, J.**, Lim, M., Rosser, N., Petley, D., Brain, M., Norman, E., & Geer, M. (2012). Modeling cliff erosion using negative power law scaling of rockfalls. *Geomorphology*, 139–140, 416–424. <https://doi.org/10.1016/j.geomorph.2011.11.006>
- Bartonek, D.**, & Buday, M. (2020). Problems of creation and usage of 3D model of structures and theirs possible solution. *Symmetry*, 12(1), 1–13. <https://doi.org/10.3390/SYM12010181>
- Bin, W.**, Hai-bin, Z., & Bin, L. (2018). Detection of Faint Asteroids Based on Image Shifting and Stacking Method. *Chinese Astronomy and Astrophysics*, 42(3), 433–447. <https://doi.org/10.1016/j.chinastron.2018.09.007>
- Blanch, X.**, Abellán, A., & Guinau, M. (2020). Point Cloud Stacking: A Workflow to Enhance 3D Monitoring Capabilities Using Time-Lapse Cameras. *Remote Sensing*, 12(8), 1240. <https://doi.org/10.3390/rs12081240>
- Blanch, X.**, Eltner, A., Guinau, M., & Abellán, A. (2021). Multi-Epoch and Multi-Imagery (MEMI) Photogrammetric Workflow for Enhanced Change Detection Using Time-Lapse Cameras. *Remote Sensing*, 13(8), 1460. <https://doi.org/10.3390/rs13081460>
- Blanch, X.**; Abellán, A.; Guinau, M. (2019). Rockfall monitoring at a high-temporal rate using cost-effective photogrammetric systems. Geophysical Research Abstracts. Vol. 21. Número 11591-2. European Geosciences Union (EGU). <https://meetingorganizer.copernicus.org/EGU2019/EGU2019-11591-2.pdf>
- Blanchard, J.**, Calvet, J., Abellán, A., García-Sellés, D., Khazaradze, G., & Vilaplana, J. M. (2008). Estudio del escarpe de coronación del deslizamiento de Puigcerçós mediante Láser Escáner Terrestre. Conca de Tremp, Catalunya. *Geo-Temas*, 10, 1389–1392.
- Bradski, G.** (2000). The OpenCV Library. *Dr Dobbs Journal of Software Tools*. <https://doi.org/10.1111/0023-8333.50.s1.10>
- Breiman, L.** (2001). Random forests. *Machine Learning*, 45(1). <https://doi.org/10.1023/A:1010933404324>
- Brodu, N.**, & Lague, D. (2012). 3D terrestrial lidar data classification of complex natural scenes using a multi-scale dimensionality criterion: Applications in geomorphology. *ISPRS Journal of Photogrammetry and Remote Sensing*, 68(1), 121–134. <https://doi.org/10.1016/j.isprsjprs.2012.01.006>
- Brunier, G.**, Fleury, J., Anthony, E. J., Gardel, A., & Dussouillez, P. (2016). Close-range airborne Structure-from-Motion Photogrammetry for high-resolution beach morphometric surveys: Examples from an embayed rotating beach. *Geomorphology*, 261, 76–88. <https://doi.org/10.1016/J.GEOMORPH.2016.02.025>

- Buill, F.,** Núñez, M. A., & Rodríguez, J. J. (2003). *Fotogrametría analítica* (Primera edición). Edicions de la Universitat Politècnica de Catalunya, SL. <http://hdl.handle.net/2099.3/36694>
- Buill, F.,** Núñez-Andrés, M. A., Lantada, N., & Prades, A. (2016). Comparison of Photogrammetric Techniques for Rockfalls Monitoring. *IOP Conference Series: Earth and Environmental Science*, 44(4). <https://doi.org/10.1088/1755-1315/44/4/042023>
- Capes, R.,** & Teeuw, R. (2017). On safe ground? Analysis of European urban geohazards using satellite radar interferometry. *International Journal of Applied Earth Observation and Geoinformation*, 58. <https://doi.org/10.1016/j.jag.2017.01.010>
- Cardenal, J.,** Mata, E., Delgado, J., Hernandez, M. a, & Gonzalez, A. (2008). Close Range Digital Photogrammetry Techniques Applied To Landslides Monitoring. *The International Archives of the Photogrammetry, Remote Sensing and Spatial Information Sciences.*, Vol. XXXVI(May 2014), 235–240.
- Castellazzi, G.,** D’Altri, A. M., Bitelli, G., Selvaggi, I., & Lambertini, A. (2015). From laser scanning to finite element analysis of complex buildings by using a semi-automatic procedure. *Sensors (Switzerland)*, 15(8). <https://doi.org/10.3390/s150818360>
- Castillo, C.,** Pérez, R., James, M. R., Quinton, J. N., Taguas, E. v., & Gómez, J. A. (2012). Comparing the accuracy of several field methods for measuring gully erosion. *Soil Science Society of America Journal*, 76(4), 1319–1332. <https://doi.org/10.2136/sssaj2011.0390>
- Cataogue, S.,** Infrastructure, F. O. R., To, R., Scale, L., Hazard, F. O. R., & On, A. (2013). *Slope Inventory for Rockfall Hazard Assessment*.
- Chen, Y.,** & Medioni, G. G. (1992). Object modelling by registration of multiple range images. *Image and Vision Computing*, 10(3), 145–155. [https://doi.org/https://doi.org/10.1016/0262-8856\(92\)90066-C](https://doi.org/https://doi.org/10.1016/0262-8856(92)90066-C)
- Choi, R. Y.,** Coyner, A. S., Kalpathy-Cramer, J., Chiang, M. F., & Peter Campbell, J. (2020). Introduction to machine learning, neural networks, and deep learning. *Translational Vision Science and Technology*, 9(2). <https://doi.org/10.1167/tvst.9.2.14>
- CloudCompare.** (2021). (*version 2.11*) ([GPL software]; p. Retrieved from <http://www.cloudcompare.org/>). <https://www.danielgm.net/cc/>
- Cook, K. L.** (2017). An evaluation of the effectiveness of low-cost UAVs and structure from motion for geomorphic change detection. *Geomorphology*, 278, 195–208. <https://doi.org/10.1016/j.geomorph.2016.11.009>

- Cook, K. L.,** & Dietze, M. (2019). Short Communication: A simple workflow for robust low-cost UAV-derived change detection without ground control points. *Earth Surface Dynamics Discussions*, 1–15. <https://doi.org/10.5194/esurf-2019-27>
- Copons, R.,** & Vilaplana, J. M. (2008). Rockfall susceptibility zoning at a large scale: From geomorphological inventory to preliminary land use planning. *Engineering Geology*, 102(3–4), 142–151. <https://doi.org/10.1016/j.enggeo.2008.03.020>
- Copons, R.,** Vilaplana, J. M., Corominas, J., Altimir, J., & Amigó, J. (2012). Rockfall Risk Management in High-Density Urban Areas. The Andorran Experience. In *Landslide Hazard and Risk*. <https://doi.org/10.1002/9780470012659.ch23>
- Corominas, J.,** & Alonso, E. (1984). Inestabilidad de laderas en el Pirineo catalán. In *Ponencias y comunicaciones - ETSICCP-UPC C.1 - C.53*.
- Corominas, J.,** Moya, J., Lloret, A., Gili, J. A., Angeli, M. G., Pasuto, A., & Silvano, S. (2000). Measurement of landslide displacements using a wire extensometer. *Engineering Geology*, 55(3), 149–166. [https://doi.org/10.1016/S0013-7952\(99\)00086-1](https://doi.org/10.1016/S0013-7952(99)00086-1)
- Crosta, G. B.,** & Agliardi, F. (2003). Failure forecast for large rock slides by surface displacement measurements. *Canadian Geotechnical Journal*, 40(1), 176–191. <https://doi.org/10.1139/t02-085>
- Cruden, D. M.,** & Varnes, D. J. (1996). *Cruden, D. M., Varnes, D. J., 1996, Landslide Types and Processes, Transportation Research Board, U. S. National Academy of Sciences, Special Report, 247: 36-75. January 1996, 36–75.*
- Cuevas, J. L.** (1992). Estratigrafía del “Garumniense” de la Conca de Tremp. Prepirineo de Lérida. *Acta Geológica Hispánica*, 27(1–2), 95–108.
- Derron, M. H.,** & Jaboyedoff, M. (2010). LIDAR and DEM techniques for landslides monitoring and characterization. *Natural Hazards and Earth System Science*, 10(9), 1877–1879. <https://doi.org/10.5194/nhess-10-1877-2010>
- Dewez, T. J. B.,** Rohmer, J., Regard, V., & Cnudde, C. (2016). Probabilistic coastal cliff collapse hazard from repeated terrestrial laser surveys: case study from Mesnil Val (Normandy, northern France). *Journal of Coastal Research*, 65(65), 702–707. <https://doi.org/10.2112/si65-119.1>
- Dias-Da-Costa, D.,** Valença, J., & Júlio, E. N. B. S. (2011). Laboratorial test monitoring applying photogrammetric post-processing procedures to surface displacements. *Measurement: Journal of the International Measurement Confederation*, 44(3), 527–538. <https://doi.org/10.1016/j.measurement.2010.11.014>

- El-Din Fawzy, H.** (2015). The accuracy of mobile phone camera instead of high resolution camera in digital close range photogrammetry. In *International Journal of Civil Engineering and Technology (IJCIET)* (Vol. 6, Issue 1). www.jifactor.com
- Elias, M., Eltner, A., Liebold, F., & Maas, H. G.** (2020a). Assessing the influence of temperature changes on the geometric stability of smartphone-and raspberry Pi cameras. *Sensors (Switzerland)*, 20(3). <https://doi.org/10.3390/s20030643>
- Eltner, A., Bressan, P. O., Akiyama, T., Gonçalves, W. N., & Marcato Junior, J.** (2021). Using Deep Learning for Automatic Water Stage Measurements. *Water Resources Research*, 57(3). <https://doi.org/10.1029/2020WR027608>
- Eltner, A., Elias, M., Sardemann, H., & Spieler, D.** (2018). Automatic Image-Based Water Stage Measurement for Long-Term Observations in Ungauged Catchments. *Water Resources Research*, 54(12), 10,362-10,371. <https://doi.org/10.1029/2018WR023913>
- Eltner, A., Kaiser, A., Abellán, A., & Schindewolf, M.** (2017). Time lapse structure-from-motion photogrammetry for continuous geomorphic monitoring. *Earth Surface Processes and Landforms*, 42(14), 2240–2253. <https://doi.org/10.1002/esp.4178>
- Eltner, A., Kaiser, A., Castillo, C., Rock, G., Neugirg, F., & Abellán, A.** (2016). Image-based surface reconstruction in geomorphometry-merits, limits and developments. *Earth Surface Dynamics*, 4(2), 359–389. <https://doi.org/10.5194/esurf-4-359-2016>
- Eltner, A., & Schneider, D.** (2015). Analysis of Different Methods for 3D Reconstruction of Natural Surfaces from Parallel-Axes UAV Images. *Photogrammetric Record*, 30(151), 279–299. <https://doi.org/10.1111/phor.12115>
- Eltner, A., & Sofia, G.** (2020). Structure from motion photogrammetric technique. *Developments in Earth Surface Processes*, 23(January), 1–24. <https://doi.org/10.1016/B978-0-444-64177-9.00001-1>
- Erismann, T. H., & Abele, G.** (2001). Dynamics of Rockslides and Rockfalls. *Dynamics of Rockslides and Rockfalls*. <https://doi.org/10.1007/978-3-662-04639-5>
- Ester, M., Kriegel, H. P., Sander, J., & Xu, X.** (1996). A Density-Based Algorithm for Discovering Clusters in Large Spatial Databases with Noise. *Kdd*, 96(34), 226–231. <https://doi.org/10.1016/B978-044452701-1.00067-3>
- Fanos, A. M., Pradhan, B., Alamri, A., & Lee, C.-W.** (2020). Machine Learning-Based and 3D Kinematic Models for Rockfall Hazard Assessment Using LiDAR Data and GIS. *Remote Sensing*, 12(11), 1755. <https://doi.org/10.3390/rs12111755>
- Feng, L., Pazzi, V., Intrieri, E., Gracchi, T. & Gigli, G.** (2020). Joint detection and classification of rockfalls in a microseismic monitoring network, *Geophysical Journal*

- Ferrero, A. M.**, Forlani, G., Roncella, R., & Voyat, H. I. (2009). Advanced geostructural survey methods applied to rock mass characterization. *Rock Mechanics and Rock Engineering*, 42(4), 631–665. <https://doi.org/10.1007/s00603-008-0010-4>
- Feurer, D.**, & Vinatier, F. (2018). Joining multi-epoch archival aerial images in a single SfM block allows 3-D change detection with almost exclusively image information. *ISPRS Journal of Photogrammetry and Remote Sensing*, 146(December), 495–506. <https://doi.org/10.1016/j.isprsjprs.2018.10.016>
- Furukawa, Y.**, Curless, B., Seitz, S. M., & Szeliski, R. (2010). Towards internet-scale multi-view stereo. *Proceedings of the IEEE Computer Society Conference on Computer Vision and Pattern Recognition*, 1434–1441. <https://doi.org/10.1109/CVPR.2010.5539802>
- Furukawa, Y.**, & Ponce, J. (2010). Accurate, dense, and robust multiview stereopsis. *IEEE Transactions on Geoscience and Remote Sensing*, 32(8), 1362–1376. <https://doi.org/10.1109/TPAMI.2009.161>
- Gabrieli, F.**, Corain, L., & Vettore, L. (2016). A low-cost landslide displacement activity assessment from time-lapse photogrammetry and rainfall data: Application to the Tessina landslide site. *Geomorphology*, 269, 56–74. <https://doi.org/10.1016/j.geomorph.2016.06.030>
- Gaffey, C.**, & Bhardwaj, A. (2020). Applications of unmanned aerial vehicles in cryosphere: Latest advances and prospects. *Remote Sensing*, 12(6). <https://doi.org/10.3390/rs12060948>
- Gallach, X.** (2012). Estudi de susceptibilitat de caiguda de roques a la paret del Monestir de Montserrat a partir de la inspecció d'indicadors d'inestabilitat i d'anàlisi SIG. 32.
- Garcia, M.** (2021). Identificació i ponderació dels paràmetres necessaris per a la detecció automàtica de desprendiments rocosos a partir de models fotogramètrics.
- García-Sellés, D.**, Falivene, O., Arbués, P., Gratacos, O., Tavani, S., & Muñoz, J. A. (2011). Supervised identification and reconstruction of near-planar geological surfaces from terrestrial laser scanning. *Computers and Geosciences*, 37(10), 1584–1594. <https://doi.org/10.1016/j.cageo.2011.03.007>
- Ghorbanzadeh, O.**, Blaschke, T., Gholamnia, K., Meena, S., Tiede, D., & Aryal, J. (2019). Evaluation of Different Machine Learning Methods and Deep-Learning Convolutional Neural Networks for Landslide Detection. *Remote Sensing*, 11(2), 196. <https://doi.org/10.3390/rs11020196>

- Giacomini, A.**, Thoeni, K., Santise, M., Diotri, F., Booth, S., Fityus, S., & Roncella, R. (2020). Temporal-Spatial Frequency Rockfall Data from Open-Pit Highwalls Using a Low-Cost Monitoring System. *Remote Sensing*, 12(15), 2459. <https://doi.org/10.3390/rs12152459>
- Gigli, G.**, Morelli, S., Fornera, S., & Casagli, N. (2014). Terrestrial laser scanner and geomechanical surveys for the rapid evaluation of rock fall susceptibility scenarios. *Landslides*, 11(1), 1–14. <https://doi.org/10.1007/s10346-012-0374-0>
- Gili, J. A.**, Moya, J., Corominas, J., Crosetto, M., & Monserrat, O. (2021). Past, present and future monitoring at the vallcebre landslide (Eastern pyrenees, spain). *Applied Sciences (Switzerland)*, 11(2), 1–22. <https://doi.org/10.3390/app11020571>
- Gómez-Gutiérrez, Á.**, de Sanjosé-Blasco, J. J., Lozano-Parra, J., Berenguer-Sempere, F., & de Matías-Bejarano, J. (2015). Does HDR pre-processing improve the accuracy of 3D models obtained by means of two conventional SfM-MVS software packages? The case of the corral del veleta rock glacier. *Remote Sensing*, 7(8), 10269–10294. <https://doi.org/10.3390/rs70810269>
- gPhoto2.** Digital Camera software. (2021, April). GPhoto2. <http://gphoto.org/>
- Grêt, A.**, Snieder, R., Aster, R. C., & Kyle, P. R. (2005). Monitoring rapid temporal change in a volcano with coda wave interferometry. *Geophysical Research Letters*, 32(6), 1–4. <https://doi.org/10.1029/2004GL021143>
- Guidi, G.**, Gonizzi, S., & Micoli, L. L. (2014). Image pre-processing for optimizing automated photogrammetry performances. *ISPRS Annals of the Photogrammetry, Remote Sensing and Spatial Information Sciences*, 2(5), 145–152. <https://doi.org/10.5194/isprsannals-II-5-145-2014>
- Guzzetti, F.**, Carrara, A., Cardinali, M., & Reichenbach, P. (1999). Landslide hazard evaluation: a review of current techniques and their application in a multi-scale study, Central Italy. *Geomorphology*, 31(1–4), 181–216. [https://doi.org/10.1016/S0169-555X\(99\)00078-1](https://doi.org/10.1016/S0169-555X(99)00078-1)
- Hungr, O.**, Leroueil, S., & Picarelli, L. (2014). The Varnes classification of landslide types, an update. *Landslides*, 11(2), 167–194. <https://doi.org/10.1007/s10346-013-0436-y>
- Hürlimann, M.**, Abancó, C., Moya, J., Raimat, C., & Luis-Fonseca, R. (2011). Debris-Flow Monitoring Stations in the Eastern Pyrenees . Description of Instrumentation , First Experiences and Pre- Liminary Results. *Italian Journal of Engineering Geology and Environment*, 553–562. <https://doi.org/10.4408/IJEGE.2011-03.B-061>
- Iglhaut, J.**, Cabo, C., Puliti, S., Piermattei, L., O’Connor, J., & Rosette, J. (2019). Structure from Motion Photogrammetry in Forestry: a Review. In *Current Forestry Reports* (Vol. 5, Issue 3). <https://doi.org/10.1007/s40725-019-00094-3>

- Jaboyedoff, M.**, Demers, D., Locat, J., Locat, A., Locat, P., Oppikofer, T., Robitaille, D., & Turmel, D. (2009). Use of terrestrial laser scanning for the characterization of retrogressive landslides in sensitive clay and rotational landslides in river banks. *Canadian Geotechnical Journal*, 46(12), 1379–1390. <https://doi.org/10.1139/t09-073>
- Jaboyedoff, M.**, & Derron, M.-H. (2005). Hazard assessment within an Integrated Risk Assessment Process for Landslides (IRAPL). *Landslide Risk Management - Proceedings of the International Conference on Landslide Risk Management, Vancouver, Canada, on CD*(January), 7.
- Jaboyedoff, M.**, Oppikofer, T., Abellán, A., Derron, M. H., Loye, A., Metzger, R., & Pedrazzini, A. (2012). Use of LIDAR in landslide investigations: A review. *Natural Hazards*, 61(1), 5–28. <https://doi.org/10.1007/s11069-010-9634-2>
- James, M. R.**, & Quinton, J. N. (2014). Ultra-rapid topographic surveying for complex environments: The hand-held mobile laser scanner (HMMS). *Earth Surface Processes and Landforms*, 39(1), 138–142. <https://doi.org/10.1002/esp.3489>
- James, M. R.**, & Robson, S. (2012). Straightforward reconstruction of 3D surfaces and topography with a camera: Accuracy and geoscience application. *Journal of Geophysical Research: Earth Surface*, 117(3), 1–17. <https://doi.org/10.1029/2011JF002289>
- James, M. R.**, & Robson, S. (2014). Mitigating systematic error in topographic models derived from UAV and ground-based image networks. *Earth Surface Processes and Landforms*, 39(10), 1413–1420. <https://doi.org/10.1002/esp.3609>
- James, M. R.**, Robson, S., d'Oleire-Oltmanns, S., & Niethammer, U. (2017). Optimising UAV topographic surveys processed with structure-from-motion: Ground control quality, quantity and bundle adjustment. *Geomorphology*, 280, 51–66. <https://doi.org/10.1016/j.geomorph.2016.11.021>
- James, M. R.**, Robson, S., & Smith, M. W. (2017). 3-D uncertainty-based topographic change detection with structure-from-motion photogrammetry: precision maps for ground control and directly georeferenced surveys. *Earth Surface Processes and Landforms*, 42(12), 1769–1788. <https://doi.org/10.1002/esp.4125>
- Janeras, M.**, Jara, J. A., López, F., Marturià, J., Royán, M. J., Vilaplana, J. M., Aguasca, A., Fàbregas, X., Cabranes, F., & Gili, J. A. (2015). Using several monitoring techniques to measure the rock mass deformation in the Montserrat Massif. *IOP Conference Series: Earth and Environmental Science*, 26(1). <https://doi.org/10.1088/1755-1315/26/1/012030>
- Javernick, L.**, Brasington, J., & Caruso, B. (2014). Modeling the topography of shallow braided rivers using Structure-from-Motion photogrammetry. *Geomorphology*, 213, 166–182. <https://doi.org/10.1016/j.geomorph.2014.01.006>

- Justo, J. L.**, Azañón, J. M., Azor, A., Saura, J., Durand, P., Villalobos, M., Morales, A., & Justo, E. (2008). Neotectonics and slope stabilization at the Alhambra, Granada, Spain. *Engineering Geology*, 100(3–4), 101–119. <https://doi.org/10.1016/j.enggeo.2007.12.007>
- Justo, J. L.**, Saura, J., Castro, D., Azañón, M., Durand, P., Morales, A., Vázquez, N., & Justo, E. (2009). Restauración del Tajo de San Pedro en La Alhambra de Granada. Aspectos de cálculo. *Informes de La Construcción*, 61(514), 81–92. <https://doi.org/10.3989/ic.05.001>
- Kaiser, A.**, Neugirg, F., Rock, G., Müller, C., Haas, F., Ries, J., & Schmidt, J. (2014). Small-scale surface reconstruction and volume calculation of soil erosion in complex moroccan Gully morphology using structure from motion. *Remote Sensing*, 6(8), 7050–7080. <https://doi.org/10.3390/rs6087050>
- Karpatne, A.**, Ebert-Uphoff, I., Ravela, S., Babaie, H. A., & Kumar, V. (2019). Machine Learning for the Geosciences: Challenges and Opportunities. *IEEE Transactions on Knowledge and Data Engineering*, 31(8), 1544–1554. <https://doi.org/10.1109/TKDE.2018.2861006>
- Khazaradze, G.**, Guinau, M., Blanch, X., Abellán, A., Tapia, M., Furdada, G., & Suriñach, E. (2020). Multidisciplinary studies of the Puigcerçós historical landslide in the Catalan Pyrenees. *Geophysical Research Abstracts*, 22, 7796. <https://meetingorganizer.copernicus.org/EGU2020/EGU2020-7796.html?pdf>
- Khazaradze, G.**, Guinau, M., Blanch, X., Abellán, A., Vilaplana, J. M., Royán, M., Tapia, M., Roig, P., Furdada, G., & Suriñach, E. (2019). Puigcerçós: a natural laboratory to study landslides and rockfalls in the Catalan Pyrenees. Multi-Scale Analysis of Slopes under Climate Change. *A Cross-Disciplinary Workshop - MUSLOC*.
- Khazaradze, G.**, Qamar, A., & Dragert, H. (1999). Tectonic deformation in western Washington from continuous GPS measurements. *Geophysical Research Letters*, 26(20), 3153–3156. <https://doi.org/10.1029/1999GL010458>
- Khazaradze, G.**, Vasquez, S., López, R., Guinau, M., Calvet, J., Vilaplana, J. M., Blanch, X., Tapia, M., Roig, P., & Suriñach, E. (2017). Fracture and slope stability monitoring at Puigcerçós landslide (Catalonia, Spain). *Geophysical Research Abstracts*, 19(16599), 40828. <https://doi.org/10.13140/RG.2.2.29512.32002>
- Knight, J.**, Keiler, M., & Harrison, S. (2012). Impacts of Recent and Future Climate Change on Natural Hazards in the European Alps. In *Climate Forcing of Geological Hazards*. <https://doi.org/10.1002/9781118482698.ch10>
- Kogelnig, A.**, Suriñach, E., Vilajosana, I., Hübl, J., Sovilla, B., Hiller, M., & Dufour, F. (2011). On the complementariness of infrasound and seismic sensors for monitoring snow avalanches. *Natural Hazards and Earth System Science*, 11(8), 2355–2370. <https://doi.org/10.5194/nhess-11-2355-2011>

- Krautblatter, M., & Moser, M.** (2009). A nonlinear model coupling rockfall and rainfall intensity based on a four year measurement in a high Alpine rock wall (Reintal, German Alps). *Natural Hazards and Earth System Science*, 9(4). <https://doi.org/10.5194/nhess-9-1425-2009>
- Kromer, R.,** Hutchinson, D. J., Lato, M. J., Gauthier, D., & Edwards, T. (2015). Identifying rock slope failure precursors using LiDAR for transportation corridor hazard management. *Engineering Geology*, 195, 93–103. <https://doi.org/10.1016/j.enggeo.2015.05.012>
- Kromer, R.,** Rowe, E., Hutchinson, J., Lato, M., & Abellán, A. (2018). Rockfall risk management using a pre-failure deformation database. *Landslides*, 15(5). <https://doi.org/10.1007/s10346-017-0921-9>
- Kromer, R.,** Abellán, A., Hutchinson, D. J., Lato, M., Edwards, T., & Jaboyedoff, M. (2015). A 4D filtering and calibration technique for small-scale point cloud change detection with a terrestrial laser scanner. *Remote Sensing*, 7(10), 13029–13058. <https://doi.org/10.3390/rs71013029>
- Kromer, R.,** Walton, G., Gray, B., Lato, M., & Group, R. (2019). Development and Optimization of an Automated Fixed-Location Time Lapse Photogrammetric Rock Slope Monitoring System. *Remote Sensing*, 11(16), 1890. <https://doi.org/10.3390/rs11161890>
- Kurczynski, P., & Gawiser, E.** (2010). A simultaneous stacking and deblending algorithm for astronomical images. *Astronomical Journal*, 139(4), 1592–1599. <https://doi.org/10.1088/0004-6256/139/4/1592>
- Lague, D.,** Brodu, N., & Leroux, J. (2013). Accurate 3D comparison of complex topography with terrestrial laser scanner: Application to the Rangitikei canyon (N-Z). *ISPRS Journal of Photogrammetry and Remote Sensing*, 82, 10–26. <https://doi.org/10.1016/j.isprsjprs.2013.04.009>
- Lato, M. J.,** Bevan, G., & Fergusson, M. (2012). Gigapixel imaging and photogrammetry: Development of a new long range remote imaging technique. *Remote Sensing*, 4(10), 3006–3021. <https://doi.org/10.3390/rs4103006>
- Lato, M. J., & Vöge, M.** (2012). Automated mapping of rock discontinuities in 3D lidar and photogrammetry models. *International Journal of Rock Mechanics and Mining Sciences*, 54, 150–158. <https://doi.org/10.1016/j.ijrmms.2012.06.003>
- Lato, M.,** Kemeny, J., Harrap, R. M., & Bevan, G. (2013). Rock bench: Establishing a common repository and standards for assessing rockmass characteristics using LiDAR and photogrammetry. *Computers and Geosciences*, 50, 106–114. <https://doi.org/10.1016/j.cageo.2012.06.014>

- Lim, M.**, Petley, D. N., Rosser, N. J., Allison, R. J., Long, A. J., & Pybus, D. (2005). Combined Digital Photogrammetry and Time-of-Flight Laser Scanning for Monitoring Cliff Evolution. *The Photogrammetric Record*, 20(110), 109–129. <https://doi.org/10.1111/j.1477-9730.2005.00315.x>
- Lim, M.**, Rosser, N. J., Allison, R. J., & Petley, D. N. (2010). Erosional processes in the hard rock coastal cliffs at Staithes, North Yorkshire. *Geomorphology*, 114(1–2), 12–21. <https://doi.org/10.1016/j.geomorph.2009.02.011>
- Lin, D.**, Grundmann, J., & Eltner, A. (2019). Evaluating Image Tracking Approaches for Surface Velocimetry With Thermal Tracers. *Water Resources Research*, 55(4), 3122–3136. <https://doi.org/10.1029/2018WR024507>
- Liu, G.**, Fomel, S., Jin, L., & Chen, X. (2009). Stacking seismic data using local correlation. *Geophysics*, 74(3). <https://doi.org/10.1190/1.3085643>
- Liu, W.**, Wang, C., Zang, Y., Lai, S. H., Weng, D., Sian, X., Lin, X., Shen, X., & Li, J. (2019). Ground camera images and UAV 3D model registration for outdoor augmented reality. *26th IEEE Conference on Virtual Reality and 3D User Interfaces, VR 2019 - Proceedings*. <https://doi.org/10.1109/VR.2019.8797821>
- Lowe, D. G.** (2004). Distinctive image features from scale-invariant keypoints. *International Journal of Computer Vision*, 60(2), 91–110. <https://doi.org/10.1023/B:VISI.0000029664.99615.94>
- Lowe, D. G.** (1999). Object recognition from local scale-invariant features. *Proceedings of the IEEE International Conference on Computer Vision*, 2. <https://doi.org/10.1109/iccv.1999.790410>
- Lucas, B. D.**, & Kanade, T. (1981). *Iterative Image Registration Technique With an Application To Stereo Vision*. 2, 674–679.
- Luhmann, T.**, Fraser, C., & Maas, H. G. (2016). Sensor modelling and camera calibration for close-range photogrammetry. *ISPRS Journal of Photogrammetry and Remote Sensing*, 115, 37–46. <https://doi.org/10.1016/j.isprsjprs.2015.10.006>
- Maiwald, F.**, Vietze, T., Schneider, D., Henze, F., Münster, S., & Niebling, F. (2017). Photogrammetric analysis of historical image repositories for virtual reconstruction in the field of digital humanities. *International Archives of the Photogrammetry, Remote Sensing and Spatial Information Sciences - ISPRS Archives*, 42(2W3), 447–452. <https://doi.org/10.5194/isprs-archives-XLII-2-W3-447-2017>
- Malamud, B. D.**, Turcotte, D. L., Guzzetti, F., & Reichenbach, P. (2004). Landslide inventories and their statistical properties. *Earth Surface Processes and Landforms*, 29(6), 687–711. <https://doi.org/10.1002/esp.1064>

- Mallalieu, J.**, Carrivick, J. L., Quincey, D. J., Smith, M. W., & James, W. H. M. (2017). An integrated Structure-from-Motion and time-lapse technique for quantifying ice-margin dynamics. *Journal of Glaciology*, *63*(242), 937–949. <https://doi.org/10.1017/jog.2017.48>
- Manconi, A.**, Kourkouli, P., Caduff, R., Strozzi, T., & Loew, S. (2018). Monitoring surface deformation over a failing rock slope with the ESA sentinels: Insights from Moosfluh instability, Swiss Alps. *Remote Sensing*, *10*(5). <https://doi.org/10.3390/rs10050672>
- Matas, G.**, Lantada, N., Corominas, J., Gili, J. A., Ruiz-Carulla, R., & Prades, A. (2017). RockGIS: a GIS-based model for the analysis of fragmentation in rockfalls. *Landslides*, *14*(5), 1565–1578. <https://doi.org/10.1007/s10346-017-0818-7>
- Mazzanti, P.**, & Brunetti, A. (2010). Assessing rockfall susceptibility by Terrestrial SAR Interferometry. *Proceedings of the Mountain Risks International Conference, Firenze, Italy, 24-26 November 2010*, 109–114. http://www.nhazca.it/wp-content/uploads/2011/06/mazzantibrunetti_mountain_risk_rev.pdf
- McGuire, B.**, & Maslin, M. (2012). Climate Forcing of Geological Hazards. In *Climate Forcing of Geological Hazards*. <https://doi.org/10.1002/9781118482698>
- McKean, J.**, & Roering, J. (2004). Objective landslide detection and surface morphology mapping using high-resolution airborne laser altimetry. *Geomorphology*, *57*(3–4). [https://doi.org/10.1016/S0169-555X\(03\)00164-8](https://doi.org/10.1016/S0169-555X(03)00164-8)
- Meidow, J.**, Usländer, T., & Schulz, K. (2018). Obtaining as-built models of manufacturing plants from point clouds. *At-Automatisierungstechnik*, *66*(5). <https://doi.org/10.1515/auto-2017-0133>
- Micheletti, N.**, Chandler, J. H., & Lane, S. N. (2015). Investigating the geomorphological potential of freely available and accessible structure-from-motion photogrammetry using a smartphone. *Earth Surface Processes and Landforms*, *40*(4), 473–486. <https://doi.org/10.1002/esp.3648>
- Michoud, C.**, Abellán, A., Baillifard, F.-J., Demierre, J., Derron, M.-H., Jaboyedoff, M., Jakubowski, J., & May-Delasoie, F. (2012). The structurally-controlled rockslide of Barmasse (Valais, Switzerland): structural geology, ground-based monitoring and displacement vs. rainfall modeling. *EGU General Assembly Conference Abstracts*, *14*, 2914.
- Michoud, C.**, Carrea, D., Costa, S., Derron, M. H., Jaboyedoff, M., Delacourt, C., Maquaire, O., Letortu, P., & Davidson, R. (2015). Landslide detection and monitoring capability of boat-based mobile laser scanning along Dieppe coastal cliffs, Normandy. *Landslides*, *12*(2), 403–418. <https://doi.org/10.1007/s10346-014-0542-5>

- Mölg, N., & Bolch, T.** (2017). Structure-from-motion using historical aerial images to analyse changes in glacier surface elevation. *Remote Sensing*, 9(10). <https://doi.org/10.3390/rs9101021>
- MP Antenna.** (2019). *SECTOR 120-2.4GHZ Datasheet*.
- Nesbit, P. R., & Hugenholtz, C. H.** (2019). Enhancing UAV-SfM 3D model accuracy in high-relief landscapes by incorporating oblique images. *Remote Sensing*, 11(3). <https://doi.org/10.3390/rs11030239>
- Nex, F., & Remondino, F.** (2014). UAV for 3D mapping applications: A review. In *Applied Geomatics* (Vol. 6, Issue 1). <https://doi.org/10.1007/s12518-013-0120-x>
- Nouwakpo, S. K., Wetz, M. A., & McGwire, K.** (2016). Assessing the performance of structure-from-motion photogrammetry and terrestrial LiDAR for reconstructing soil surface microtopography of naturally vegetated plots. *Earth Surface Processes and Landforms*, 41(3), 308–322. <https://doi.org/10.1002/esp.3787>
- Ntregka, G. & Quintero.** (2013). Photogrammetric exploitation of hdr images for cultural heritage documentation. *ISPRS Annals of the Photogrammetry, Remote Sensing and Spatial Information Sciences*, 2(5/W1), 209–214. <https://doi.org/10.5194/isprsannals-II-5-W1-209-2013>
- Núñez, A., Buill, F., Regot, J., & de Mesa, A.** (2012). Generation of virtual models of cultural heritage. *Journal of Cultural Heritage*, 13(1), 103–106. <https://doi.org/10.1016/j.culher.2011.06.004>
- On, M., Howell, J. A., Enge, H. D., & Kurz, T. H.** (2008). Terrestrial laser scanning in geology: data acquisition, processing and accuracy considerations. In *Journal of the Geological Society* (Vol. 165). <http://pubs.geoscienceworld.org/jgs/article-pdf/165/3/625/2791581/625.pdf>
- Oppikofer, T., Jaboyedoff, M., & Keusen, H. R.** (2008). Collapse at the eastern Eiger flank in the Swiss Alps. *Nature Geoscience*, 1(8), 531–535. <https://doi.org/10.1038/ngeo258>
- Pan, B.** (2018). Digital image correlation for surface deformation measurement: Historical developments, recent advances and future goals. *Measurement Science and Technology*, 29(8). <https://doi.org/10.1088/1361-6501/aac55b>
- Parente, L., Chandler, J. H., & Dixon, N.** (2019). Optimising the quality of an SfM-MVS slope monitoring system using fixed cameras. *Photogrammetric Record*, 34(168), 408–427. <https://doi.org/10.1111/phor.12288>
- Pech-Pacheco, J. L., Cristóbal, G., Chamorro-Martínez, J., & Fernández-Valdivia, J.** (2000). Diatom autofocusing in brightfield microscopy: A comparative study. *Proceedings -*

International Conference on Pattern Recognition, 15(3), 314–317.
<https://doi.org/10.1109/icpr.2000.903548>

Pedregosa, F., Varoquaux, G., Gramfort, A., Michel, V., Thirion, B., Grisel, O., Blondel, M., Prettenhofer, P., Weiss, R., Dubourg, V., Vanderplas, J., Passos, A., Cournapeau, D., Brucher, M., Perrot, M., & Duchesnay, É. (2011). Scikit-learn: Machine learning in Python. *Journal of Machine Learning Research*, 12.

Pertuz, S., Puig, D., & Garcia, M. A. (2013). Analysis of focus measure operators for shape-from-focus. *Pattern Recognition*, 46(5), 1415–1432.
<https://doi.org/10.1016/j.patcog.2012.11.011>

Petrie, G., & Toth, C. (2008). Introduction to Laser Ranging, Profiling, and Scanning. *Topographic Laser Ranging and Scanning, April*, 1–28.
<https://doi.org/10.1201/9781420051438.ch1>

Python Core Team. (2015). *Python: A dynamic, open source programming language*. Python Software Foundation. <https://doi.org/10.1109/8.121596>

Quinlan, J. R. (1986). Induction of Decision Trees. *Machine Learning*, 1(1).
<https://doi.org/10.1023/A:1022643204877>

Rabatel, A., Deline, P., Jaillet, S., & Ravanel, L. (2008). Rock falls in high-alpine rock walls quantified by terrestrial lidar measurements: A case study in the Mont Blanc area. *Geophysical Research Letters*, 35(10), 1–5. <https://doi.org/10.1029/2008GL033424>

Raspberry Pi Foundation. (2016). *Raspberry Pi 3 Model B*.
<https://www.raspberrypi.org/products/raspberry-pi-3-model-b/>

Reyes-Carmona, C., Barra, A., Galve, J. P., Monserrat, O., Pérez-Peña, J. V., Mateos, R. M., Notti, D., Ruano, P., Millares, A., López-Vinielles, J., & Azañón, J. M. (2020). Sentinel-1 DInSAR for monitoring active landslides in critical infrastructures: The case of the rules reservoir (Southern Spain). *Remote Sensing*, 12(5), 1–22.
<https://doi.org/10.3390/rs12050809>

Riquelme, A. J., Abellán, A., Tomás, R., & Jaboyedoff, M. (2014). A new approach for semi-automatic rock mass joints recognition from 3D point clouds. *Computers and Geosciences*, 68, 38–52. <https://doi.org/10.1016/j.cageo.2014.03.014>

Riquelme, A. J., Tomás, R., & Abellán, A. (2016). Characterization of rock slopes through slope mass rating using 3D point clouds. *International Journal of Rock Mechanics and Mining Sciences*, 84, 165–176. <https://doi.org/10.1016/j.ijrmms.2015.12.008>

Roig-Lafon, P. (2021). *Identification of snow avalanche release areas and flow characterization based on seismic data studies*.

- Romeo, S.**, di Matteo, L., Kieffer, D. S., Tosi, G., Stoppini, A., & Radicioni, F. (2019). The use of gigapixel photogrammetry for the understanding of landslide processes in alpine terrain. *Geosciences (Switzerland)*, 9(2). <https://doi.org/10.3390/geosciences9020099>
- Roncella, R.**, Forlani, G., Fornari, M., & Diotri, F. (2014). Landslide monitoring by fixed-base terrestrial stereo-photogrammetry. *ISPRS Annals of the Photogrammetry, Remote Sensing and Spatial Information Sciences*, 2(5), 297–304. <https://doi.org/10.5194/isprsannals-II-5-297-2014>
- Rose, N. D.**, & Hungr, O. (2007). Forecasting potential rock slope failure in open pit mines using the inverse-velocity method. *International Journal of Rock Mechanics and Mining Sciences*, 44(2), 308–320. <https://doi.org/10.1016/j.ijrmms.2006.07.014>
- Rosser, N.**, Petley, D. N., Lim, M., Dunning, S. A., & Allison, R. J. (2005). Terrestrial laser scanning for monitoring the process of hard rock coastal cliff erosion. *Quarterly Journal of Engineering Geology and Hydrogeology*, 38(4), 363–375. <https://doi.org/10.1144/1470-9236/05-008>
- Rosser, N.**, Lim, M., Petley, D., Dunning, S., & Allison, R. (2007). Patterns of precursory rockfall prior to slope failure. *Journal of Geophysical Research: Earth Surface*, 112(4). <https://doi.org/10.1029/2006JF000642>
- Rothery, D. A.**, Francis, P. W., & Wood, C. A. (1988). Volcano monitoring using short wavelength infrared data from satellites. *Journal of Geophysical Research*, 93(B7), 7993–8008. <https://doi.org/10.1029/JB093iB07p07993>
- Rowley, T.**, Ursic, M., Konsoer, K., Langendon, E., Mutschler, M., Sampey, J., & Pocwiardowski, P. (2020). Comparison of terrestrial lidar, SfM, and MBES resolution and accuracy for geomorphic analyses in physical systems that experience subaerial and subaqueous conditions. *Geomorphology*, 355, 107056. <https://doi.org/10.1016/j.geomorph.2020.107056>
- Royán, M. J.** (2015). *Caracterización y predicción de desprendimientos de rocas mediante LiDAR Terrestre*. <http://diposit.ub.edu/dspace/handle/2445/68667?mode=full#.YTShwYIH6w.mendley>
- Royán, M. J.**, Abellán, A., Jaboyedoff, M., Vilaplana, J. M., & Calvet, J. (2014). Spatio-temporal analysis of rockfall pre-failure deformation using Terrestrial LiDAR. *Landslides*, 11(4), 697–709. <https://doi.org/10.1007/s10346-013-0442-0>
- Royán, M. J.**, Abellán, A., & Vilaplana, J. M. (2015). Progressive failure leading to the 3 December 2013 rockfall at Puigcerçós scarp (Catalonia, Spain). *Landslides*, 12(3), 585–595. <https://doi.org/10.1007/s10346-015-0573-6>

- Ruiz-Carulla, R.**, Corominas, J., & Mavrouli, O. (2017). A fractal fragmentation model for rockfalls. *Landslides*, 14(3), 875–889. <https://doi.org/10.1007/s10346-016-0773-8>
- Santise, M.**, Thoeni, K., Roncella, R., Sloan, S. W., & Giacomini, A. (2017). Preliminary tests of a new low-cost photogrammetric system. *International Archives of the Photogrammetry, Remote Sensing and Spatial Information Sciences - ISPRS Archives*, 42(2W8), 229–236. <https://doi.org/10.5194/isprs-archives-XLII-2-W8-229-2017>
- Santos, A.**, Martínez, J. M., & Salinas, J. (1994). Caracterización geotécnica de las condiciones de cimentación de los edificios y estabilidad de las laderas del conjunto monumental de la Alhambra de Generalife. *Revista Digital Del Cedex*, (96 SE-Artículos). <http://ingenieriacivil.cedex.es/index.php/ingenieria-civil/article/view/1019>
- Sartori, M.**, Baillifard, F., Jaboyedoff, M., & Rouiller, J.-D. (2010). Kinematics of the 1991 Randa rockslides (Valais, Switzerland). *Natural Hazards and Earth System Science*, 3(5), 423–433. <https://doi.org/10.5194/nhess-3-423-2003>
- Schwalbe, E.**, & Maas, H.-G. (2017). Determination of high resolution spatio-temporal glacier motion fields from time-lapse sequences. *Earth Surface Dynamics Discussions*, May, 1–30. <https://doi.org/10.5194/esurf-2017-33>
- Selvakumaran, S.**, Plank, S., Geiß, C., Rossi, C., & Middleton, C. (2018). Remote monitoring to predict bridge scour failure using Interferometric Synthetic Aperture Radar (InSAR) stacking techniques. *International Journal of Applied Earth Observation and Geoinformation*, 73(July), 463–470. <https://doi.org/10.1016/j.jag.2018.07.004>
- Severance, C.** (2013). Eben upto: Raspberry Pi. *Computer*, 46(10). <https://doi.org/10.1109/MC.2013.349>
- Simeoni, L.**, & Mongiovi, L. (2007). Inclinometer Monitoring of the Castelrotto Landslide in Italy. *Journal of Geotechnical and Geoenvironmental Engineering*, 133(6), 653–666. [https://doi.org/10.1061/\(asce\)1090-0241\(2007\)133:6\(653\)](https://doi.org/10.1061/(asce)1090-0241(2007)133:6(653))
- Smith, M. W.**, Carrivick, J. L., & Quincey, D. J. (2015). Structure from motion photogrammetry in physical geography. *Progress in Physical Geography*, 40(2), 247–275. <https://doi.org/10.1177/0309133315615805>
- Stumpf, A.**, Malet, J. P., Allemand, P., Pierrot-Deseilligny, M., & Skupinski, G. (2015). Ground-based multi-view photogrammetry for the monitoring of landslide deformation and erosion. *Geomorphology*, 231, 130–145. <https://doi.org/10.1016/j.geomorph.2014.10.039>
- Sturzenegger, M.**, Yan, M., Stead, D., & Elmo, D. (2007). Application and limitations of ground-based laser scanning in rock slope characterization. *Proceedings of the 1st Canada-*

US Rock Mechanics Symposium - Rock Mechanics Meeting Society's Challenges and Demands, 1(May 2016), 29–36. <https://doi.org/10.1201/noc0415444019-c4>

- Suriñach, E.**, Tapia, M., Roig, P., & Blanch, X. (2018). On the effect of the ground seismic characteristics in the estimation of mass movements based on seismic observation. In *Geophys. Res. Abstract* (Vol. EGU8479, p. 20).
- Tannant, D.** (2015). Review of Photogrammetry-Based Techniques for Characterization and Hazard Assessment of Rock Faces. *International Journal of Geohazards and Environment*, 1, 76–87. <https://doi.org/10.15273/ijge.2015.02.009>
- Tarolli, P.** (2014). High-resolution topography for understanding Earth surface processes: Opportunities and challenges. In *Geomorphology* (Vol. 216). <https://doi.org/10.1016/j.geomorph.2014.03.008>
- Tavani, S.**, Granado, P., Riccardi, U., Seers, T., & Corradetti, A. (2020). Terrestrial SfM-MVS photogrammetry from smartphone sensors. *Geomorphology*, 367. <https://doi.org/10.1016/j.geomorph.2020.107318>
- Technical, E. E. A.** (2010). Mapping the impacts of natural hazards and technological accidents in Europe An overview of the last decade. In *Technical report No 132010* (Issue 13).
- Telletxea, B.**, Tapia, M., Guinau, M., Royán, M. J., Roig Lafon, P., Blanch, X., Khazaradze, G., Suriñach, E., Furdada, G., Garcia-Sellés, D., Abellán, A., and Vilaplana, J. M. (2021): Identification and characterization of rockfalls using seismic signals, LiDAR, and imagery. Advances on real-time detection, EGU General Assembly 2021, online, 19–30 <https://doi.org/10.5194/egusphere-egu21-13149>
- Teltonika Networks.** (2021). *RUT950-Datasheet*. <https://teltonika-networks.com/downloads/en/rut950/RUT950-Datasheet.pdf>
- Terzaghi, K.** (1962). Stability of steep slopes on hard unweathered rock. *Geotechnique*, 12(4). <https://doi.org/10.1680/geot.1962.12.4.251>
- Teza, G.**, Atzeni, C., Balzani, M., Galgaro, A., Galvani, G., Genevois, R., Luzi, G., Mecatti, D., Noferini, L., Pieraccini, M., Silvano, S., Uccelli, F., & Zaltron, N. (2008). Ground-based monitoring of high-risk landslides through joint use of laser scanner and interferometric radar. *International Journal of Remote Sensing*, 29(16), 4735–4756. <https://doi.org/10.1080/01431160801942227>
- Teza, G.**, Marcato, G., Pasuto, A., & Galgaro, A. (2015). Integration of laser scanning and thermal imaging in monitoring optimization and assessment of rockfall hazard: a case history in the Carnic Alps (Northeastern Italy). *Natural Hazards*, 76(3), 1535–1549. <https://doi.org/10.1007/s11069-014-1545-1>

- Tonini, M.,** & Abellán, A. (2014). Rockfall detection from terrestrial LiDAR point clouds: A clustering approach using R. *Journal of Spatial Information Science*, 8(8), 95–110. <https://doi.org/10.5311/josis.2014.8.123>
- Travelletti, J.,** Delacourt, C., Allemand, P., Malet, J. P., Schmittbuhl, J., Toussaint, R., & Bastard, M. (2012). Correlation of multi-temporal ground-based optical images for landslide monitoring: Application, potential and limitations. *ISPRS Journal of Photogrammetry and Remote Sensing*, 70, 39–55. <https://doi.org/10.1016/j.isprsjprs.2012.03.007>
- Travelletti, J.,** Oppikofer, T., Delacourt, C., Malet, J.-P. P., & Jaboyedoff, M. (2008). Monitoring landslide displacements during a controlled rain experiment using a long-range terrestrial laser scanning (TLS). *International Archives of the Photogrammetry, Remote Sensing and Spatial Information Sciences - ISPRS Archives*, 37(May 2014), 485–490.
- Triggs, B.,** McLauchlan, P. F., Hartley, R. I., & Fitzgibbon, A. W. (2000). Bundle adjustment – a modern synthesis. *Lecture Notes in Computer Science (Including Subseries Lecture Notes in Artificial Intelligence and Lecture Notes in Bioinformatics)*, 1883. https://doi.org/10.1007/3-540-44480-7_21
- UUGear WittyPi3.** (2021, April 1). <http://www.uugear.com/Product/Witty-Pi-3-Rev1-Realtime-Clock-and-Power-Management-for-Raspberry-Pi/>.
- Varnes, D.** (1978). Slope Movement Types and Processes. *Special Report*, 176, 11–33.
- Verma, A. K.,** & Bourke, M. C. (2019). A method based on structure-from-motion photogrammetry to generate sub-millimetre-resolution digital elevation models for investigating rock breakdown features. *Earth Surface Dynamics*, 7(1), 45–66. <https://doi.org/10.5194/esurf-7-45-2019>
- Vidal, L. M.** (1881). Nota acerca de los hundimientos ocurridos en la Cuenca de Tresp (Lérida) en Enero de 1881. In *Boletín de la Comisión del Mapa Geológico de España VIII* (pp. 113–129).
- Volkwein, A.,** Schellenberg, K., Labiouse, V., Agliardi, F., Berger, F., Bourrier, F., Dorren, L. K. A., Gerber, W., & Jaboyedoff, M. (2011). Rockfall characterisation and structural protection - A review. *Natural Hazards and Earth System Science*, 11(9), 2617–2651. <https://doi.org/10.5194/nhess-11-2617-2011>
- Voltaic Systems.** (2021). <https://voltaicsystems.com/>
- Walter, M.,** Schwaderer, U., & Joswig, M. (2012). Seismic monitoring of precursory fracture signals from a destructive rockfall in the Vorarlberg Alps, Austria. *Natural Hazards and Earth System Science*, 12(11), 3545–3555. <https://doi.org/10.5194/nhess-12-3545-2012>

- Westoby, M. J.**, Brasington, J., Glasser, N. F., Hambrey, M. J., & Reynolds, J. M. (2012). “Structure-from-Motion” photogrammetry: A low-cost, effective tool for geoscience applications. *Geomorphology*, 179, 300–314. <https://doi.org/10.1016/j.geomorph.2012.08.021>
- Whalley, W. B.** (1984). Rockfalls. In D. Brunsden (Ed.), *Slope Instability* (pp. 217–256).
- Wilkinson, M. W.**, Jones, R. R., Woods, C. E., Gilment, S. R., McCaffrey, K. J. W., Kokkalas, S., & Long, J. J. (2016). A comparison of terrestrial laser scanning and structure-from-motion photogrammetry as methods for digital outcrop acquisition. *Geosphere*, 12(6), 1865–1880. <https://doi.org/10.1130/GES01342.1>
- Williams, J. G.**, Rosser, N. J., Hardy, R. J., Brain, M. J., & Afana, A. A. (2018). Optimising 4-D surface change detection: An approach for capturing rockfall magnitude-frequency. *Earth Surface Dynamics*, 6(1), 101–119. <https://doi.org/10.5194/esurf-6-101-2018>
- Woith, H.**, Daskalopoulou, K., Zimmer, M., Fischer, T., Vlček, J., Trubač, J., Rosberg, J. E., Vylita, T., & Dahm, T. (2020). Multi-Level Gas Monitoring: A New Approach in Earthquake Research. *Frontiers in Earth Science*, 8(October), 1–6. <https://doi.org/10.3389/feart.2020.585733>
- Wooster, M. J.**, & Rothery, D. A. (1997). Thermal monitoring of Lascar Volcano, Chile, using infrared data from the along-track scanning radiometer: A 1992-1995 time series. *Bulletin of Volcanology*, 58(7), 566–579. <https://doi.org/10.1007/s004450050163>
- WP/WLI.** (1995). A suggested method for describing the rate of movement of a landslide. *Bulletin of the International Association of Engineering Geology*, 52(1), 75–78. <https://doi.org/10.1007/BF02602683>
- Wu, Z.**, Ni, M., Hu, Z., Wang, J., Li, Q., & Wu, G. (2019). Mapping invasive plant with UAV-derived 3D mesh model in mountain area—A case study in Shenzhen Coast, China. *International Journal of Applied Earth Observation and Geoinformation*, 77. <https://doi.org/10.1016/j.jag.2018.12.001>
- Yilmaz, A.**, Javed, O., & Shah, M. (2006). Object tracking: A survey. In *ACM Computing Surveys* (Vol. 38, Issue 4). <https://doi.org/10.1145/1177352.1177355>
- Yilmaz, H. M.**, Yakar, M., Gulec, S. A., & Dulgerler, O. N. (2007). Importance of digital close-range photogrammetry in documentation of cultural heritage. *Journal of Cultural Heritage*, 8(4), 428–433. <https://doi.org/10.1016/j.culher.2007.07.004>
- Zhang, C.**, Bastian, J., Shen, C., van den Hengel, A., & Shen, T. (2013). Extended depth-of-field via focus stacking and graph cuts. *2013 IEEE International Conference on Image Processing, ICIP 2013 - Proceedings*, 1272–1276. <https://doi.org/10.1109/ICIP.2013.6738262>

Zoumpikas, T., Puig, A., Salamó, M., García Sellés, D., Blanco Nuñez, L., & Guinau Sellés, M. (2021). *An intelligent framework for end-to-end rockfall detection*. <http://diposit.ub.edu/dspace/handle/2445/178934#.YUEls1p-JMU.mendeley>

Zvelebil, J., & Moser, M. (2001). Monitoring based time-prediction of rock falls: Three case-histories. *Physics and Chemistry of the Earth, Part B: Hydrology, Oceans and Atmosphere*, 26(2), 159–167. [https://doi.org/10.1016/S1464-1909\(00\)00234-3](https://doi.org/10.1016/S1464-1909(00)00234-3)

Section VII

APPENDICES

APPENDIX A – SCRIPTS AND ALGORITHMS

APPENDIX B – PUBLICATION I (REMOTE SENSING)

APPENDIX C – PUBLICATION II (REMOTE SENSING)

```
from tensorflow.keras.models import load_model
from SegNet import *
from utils import *

print('Tensorflow version: ', tf.__version__)
print('Keras version: ', tf.keras.__version__)

# Load the storage model
#model = load_model('./models/SegNet_t1.h5')
model = load_model(r'C:\Users\XBG-KIWA\Documents\06_RESOURCES\')

#main_parameters
TRAIN_DIR = './data/train'
VAL_DIR = './data/val'
TEST_DIR = './data/test'
IMG_SIZE = 512

#load images and masks -> resize and normalise
train_images, train_masks = create_datasets(TRAIN_DIR, IMG_SIZE)
val_images, val_masks = create_datasets(VAL_DIR, IMG_SIZE)
test_images, test_masks = create_datasets(TEST_DIR, IMG_SIZE)
```

Appendix A

Scripts and algorithms

A

Scan or click on the code to visit the GitHub repository or the Elsevier authorization for the use of the **Figure I.7**



RasPi System scripts



HRCam System scripts



DSLR System scripts



PCStacking algorithm



MEMI workflow



XBGRockfall Software



Machine Learning



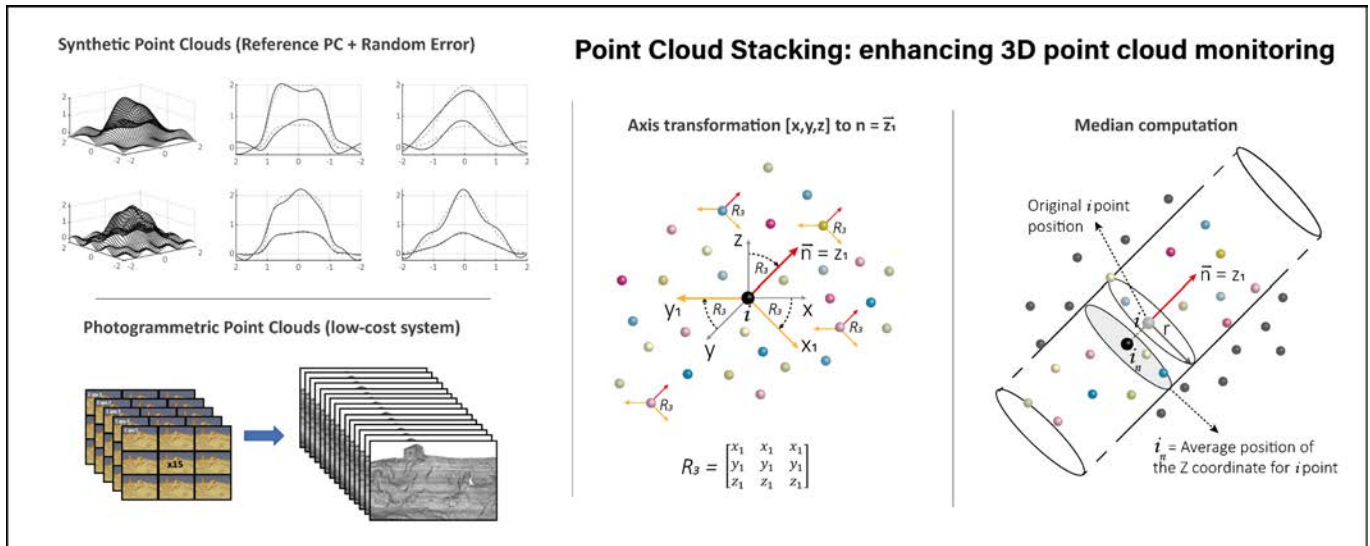
Elsevier Authorisation

Appendix B

Publication I (Remote Sensing)



GRAPHICAL ABSTRACT





remote sensing

an Open Access Journal by MDPI

Indexed in:
EI Compendex

CITESCORE
6.6
SCOPUS

IMPACT
FACTOR
4.848

CERTIFICATE OF PUBLICATION

Certificate of publication for the article titled:
Point Cloud Stacking: A Workflow to Enhance 3D Monitoring Capabilities Using Time-Lapse Cameras

Authored by:
Xabier Blanch; Antonio Abellan; Marta Guinau

Published in:
Remote Sens. 2020, Volume 12, Issue 8, 1240



Academic Open Access Publishing
since 1996

Basel, January 2022

Article

Point Cloud Stacking: A Workflow to Enhance 3D Monitoring Capabilities Using Time-Lapse Cameras

Xabier Blanch ^{1,*}, Antonio Abellan ^{2,3} and Marta Guinau ¹

¹ RISKNAT Research Group, GEOMODELS Research Institute, Faculty of Earth Sciences, Universitat de Barcelona, 08028 Barcelona, Spain; mguinau@ub.edu

² Institute of Applied Geosciences, School of Earth and Environment, University of Leeds, Leeds LS2 9JT, UK; a.abellan@leeds.ac.uk

³ Center for Research on the Alpine Environment (CREALP), Sion, CH-1950 Valais, Switzerland

* Correspondence: xabierblanch@ub.edu

Received: 25 March 2020; Accepted: 10 April 2020; Published: 13 April 2020



Abstract: The emerging use of photogrammetric point clouds in three-dimensional (3D) monitoring processes has revealed some constraints with respect to the use of LiDAR point clouds. Oftentimes, point clouds (PC) obtained by time-lapse photogrammetry have lower density and precision, especially when Ground Control Points (GCPs) are not available or the camera system cannot be properly calibrated. This paper presents a new workflow called Point Cloud Stacking (PCStacking) that overcomes these restrictions by making the most of the iterative solutions in both camera position estimation and internal calibration parameters that are obtained during bundle adjustment. The basic principle of the stacking algorithm is straightforward: it computes the median of the Z coordinates of each point for multiple photogrammetric models to give a resulting PC with a greater precision than any of the individual PC. The different models are reconstructed from images taken simultaneously from, at least, five points of view, reducing the systematic errors associated with the photogrammetric reconstruction workflow. The algorithm was tested using both a synthetic point cloud and a real 3D dataset from a rock cliff. The synthetic data were created using mathematical functions that attempt to emulate the photogrammetric models. Real data were obtained by very low-cost photogrammetric systems specially developed for this experiment. Resulting point clouds were improved when applying the algorithm in synthetic and real experiments, e.g., 25th and 75th error percentiles were reduced from 3.2 cm to 1.4 cm in synthetic tests and from 1.5 cm to 0.5 cm in real conditions.

Keywords: time-lapse photogrammetry; multi-view stereo; 3D point clouds; 3D stacking; change detection; rock slope monitoring

1. Introduction

The acquisition of point clouds (PCs) using photogrammetric techniques for three-dimensional (3D) modelling of natural surfaces has increased significantly in recent years [1,2]. The ease of acquiring images, as well as the low cost of the whole system (devices to take images and processing software) has democratized access to photogrammetric data and ensures greater accessibility compared to LiDAR (Light Detection and Ranging) PCs. Spurred on by this accessibility more and more data are being acquired and consequently more natural surfaces are being reconstructed and investigated [2,3].

Different algorithms have been recently developed for the treatment of LiDAR PCs [4–6] and especially TLS (Terrestrial Laser Scanner) data [7–12], entailing a wider use of PCs acquired by photogrammetric systems in several geoscience fields [2,3,13]. Examples include: a classification algorithm using a multi-scale dimensionality criterion called “CARactérisation de NUages de POints (CANUPO)” [9]; the geomorphological change detection algorithm “Multi-scale Model to Model Cloud

Comparison (M3C2)" [14] and a four-dimensional (4D) workflow for detecting changes in PCs [11] or [15]. Notably, the work by Kromer et al. [11] proposed computing the median distances of a series of point clouds acquired at different time steps and with respect to a fixed reference, extending the M3C2 algorithm [14] to 4D. Kromer et al. [11] and Lague et al. [14] obtained a better level of detection on PC comparison by minimizing point scattering around a central value, they do not improve the PC *per se*. Although these algorithms were originally developed with the aim of improving results by taking into account the properties and errors of LiDAR datasets, they can be used with PCs captured using different sensors (LiDAR, sonar, etc.); nevertheless, the particular characteristics of photogrammetric data such as non-linear and time-variant errors require the development of new methodologies specifically designed to overcome the constraints of this technique. Interestingly, improving PC quality by stacking multiple low-quality datasets as those generated using time-lapse cameras has not been explored yet.

1.1. Photogrammetry vs. LiDAR 3D Point Cloud Errors

The transformation of digital images into photogrammetric PCs using the technique called Structure from Motion (SfM) consists of estimating the three-dimensional position of points in the space defined from two-dimensional (2D) images [3,16]. Nowadays, both commercial and open-source software products are available for this purpose [17]. In addition to the SfM algorithms, these suites incorporate different tools and utilities to improve the quality of the processing such as the masking of images, the automatic detection of markers, the refinement of camera calibration and the filtering of points based on their quality.

Since the SfM technique is based on iterations of various processes during the bundle adjustment, the obtained PC is a possible solution among many possible results. The quality of the generated PC depends both on the number of homologous points identified and on the quality of the bundle adjustment [18]. For this reason, any repeatability analysis carried out using different images of the same site implies the generation of photogrammetric models with significantly different geometries due to the different random solutions in both camera position estimation and internal calibration parameters. These geometric differences, which can be called **geometric errors**, will be more or less significant depending on the quality of the homologous points and the bundle adjustment, which depends on the quality of the photographs.

This type of error contrasts strongly with the errors that are obtained in the LiDAR PCs. LiDAR, whose operation is extensively described in Petrie and Toth [19] and Jaboyedoff et al. [6], generates geometrically consistent models; however, due to its operation, the PCs obtained have a random Gaussian noise distributed along all points [11]. This dispersion, called **random error**, was easily solved and was the theoretical basis of the development of many algorithms for the processing of LiDAR data [14,20].

Several studies have shown that the use of photogrammetric techniques does not result in a particular loss of accuracy with respect to LiDAR PCs [16,21–23]. It should be noted, however, that these studies are mostly based on large-scale or detailed laboratory analyses in which hundreds of photographs and numerous control points were used to generate the models. It is well known that the accuracy of LiDAR data depends mainly on the device used to acquire the data. In contrast, the accuracy of the photogrammetric data depends on many other factors such as the camera setup, the weather conditions and the sharpness of the acquired images.

1.2. Landslide Monitoring Using Photogrammetry

The use of digital photogrammetry for landslide monitoring has evolved considerably over the past few years. Photogrammetric monitoring methods can be divided into those using a single camera position plus Digital Image Correlation (DIC) techniques [24] to detect changes between two images captured at different times [25,26], and those that use images taken from different positions (multi-view methods) [27]. One advantage of these photogrammetric techniques is that, in addition to the analysis

of current changes, they allow old deformations to be studied by scanning analogue photographs taken before the development of the methodology [28].

Model comparisons and difference calculations can be obtained from: (a) one-dimensional (1D) values resulting from topographic sections extracted from Digital Terrain Models (DTM) [28]; (b) 2D displacements in the image plane obtained using DIC methods [26]; (c) in 3D from the comparison of PCs obtained by SfM techniques [27]; and (d) the 4D analysis based on multi-temporal PC comparisons [29].

As mentioned by Gabrieli et al. [25], it is possible to obtain 3D information of the displacement of a landslide with a single camera, using complex DIC methods and a reference DTM. Even so, several factors, such as the orientation of the deformation and the range and the magnitude of the movement, have a decisive effect on the accuracy of the results. In addition, classical DIC is strongly influenced by changes in illumination [30] and normally assumes that the main deformation field is parallel to the internal camera coordinate system, which is not always the case. Thus, the deformation field should be subsequently ortho-rectified using a DTM (e.g., Travelletti et al. [26]).

The use of methods based on multi-view techniques for the study of landslides also carries some limitations, as described in Tannant [31] and Cardenal et al. [27]. These studies can be approached from two different angles. The first consists of obtaining a large number of images from different camera positions to provide algorithms with a large amount of data. The second strategy consists of implementing 4D monitoring by using photogrammetric systems with fixed cameras. In this case, the number of images is limited as it depends directly on the number of cameras installed. These workflows allow the generation of 3D models with a high temporal (sub-daily) frequency, allowing detailed monitoring of deformation, as well as 4D analysis.

The most recent studies in the field of geosciences [29,32] emphasize the importance of two key elements of the SfM process to obtain good quality results. The first is the need to perform lens calibration to obtain the internal parameters of the camera. These parameters, some of which are highly sensitive, allow the elimination of radial and tangential distortion, correcting the deformations of the resulting models. The second element consists of positioning ground control points (GCP) in order to estimate the fit of the models to the real surface. James et al. [33] developed tools to optimize SfM processes by analyzing the parameters that allow better ground control quality. They processed the output of ground control point and point precision analyses using Monte Carlo approaches. These improvements allow the calculation of 3D uncertainty-based topographic change from precision maps. Santise et al. [34] tried to improve the photogrammetric models by reducing the image noise from a three-image merge (see Section 1.3). Additionally, Parente et al. [18] demonstrated an improvement in monitoring quality when a fixed-camera approach was adopted, even with a poor camera calibration procedure. However, there are no algorithms or workflows available to improve the photogrammetric models via the modification of the calculated PCs based on error reduction strategies.

Although several authors have emphasized the importance of using GCP and lens calibration [2,33], in some contexts, such as landslide monitoring, this is impossible due to the unfeasibility of installing targets such as GCP on inaccessible slopes. In addition, obtaining calibration parameters fixed in time is difficult on a high frequency (time-lapse) basis in a fixed area and in remote locations. These limitations, combined with the reduced number of images obtained by fixed camera systems, imply a reduction in the quality of the resulting models compared to those obtained with TLS.

Based on the above, the accuracy and resolution of photogrammetry-derived PCs are strongly controlled not only by internal characteristics (instrument specifications) but also by external considerations (range, number and setup of stations, deformation magnitude, etc.). While TLS is thought to provide a more robust data set compared with SfM, no single technology is universally best suited to all situations because of the wide variety of fieldwork setup and instrumental considerations [35]. On the one hand, the limited number of stations and subsequent occlusions in TLS-derived PCs have been highlighted as one of the main TLS limitations [36]. On the other hand, loss of fine-scale details due to rounding off or over-smoothing of the SfM-derived surfaces on sharp outcrop corners has been observed by several authors (e.g., Wilkinson et al. [35] and Nouwakpo [37]).

Compared to TLS, digital photogrammetry is considered a low-cost landslide monitoring system [2,3,23,38]. In addition, the cost of photographic devices (700 €–3000 €) can be considerably reduced by using very low-cost photographic sensor and lens combinations (50 €), thus producing very low-cost monitoring systems. These systems are based on combinations of photographic microsensors (3.76×2.74 mm) and low-quality lenses associated with small microcomputers that are designed to obtain, process and store the images acquired. These systems are designed essentially to operate autonomously and in remote areas [34] (see Section 2.3.2.). These configurations are used because they are easy to obtain, easy to program and can be installed in active areas without concerns about damage due to their low cost. However, the use of these devices implies a lower quality of the photogrammetric models due to the low resolution of the sensor, as well as the poor quality of the lenses. For this reason, when very low-cost photogrammetric systems are used, new methodologies to improve the quality of the photogrammetric models are required, such as the one presented in this article.

1.3. Techniques for Image Stacking (2D)

Using 2D stacking algorithms to enhance digital imagery is a common strategy in several disciplines such as astronomy, computer-vision and microscopy; recent examples of astronomical image processing include successful attempts to increase the signal-to-noise ratio (SNR) [39] and the combination of different wavelengths to de-noise imagery of celestial bodies [40]. Image stacking strategies using photographs taken at different f-stops or with the focus point on different parts of the subject (aka “f-stop stacking” or “focus stacking,” respectively) have also been used to extend the depth of field of the composite images in order to overcome blurriness [41]. In addition, various 2D stacking strategies have been tested to derive high quality imagery from a series of 2D photographs, leading to considerable improvements in photogrammetric models, e.g., when using super-resolution images [42]. On the contrary, stacking 2D images under specific conditions might not always entail noteworthy increases in SNR, as reported by Santise et al. [34].

Similarly, diverse image stacking techniques are commonly employed when using satellite Interferometric Synthetic-Aperture Radar (InSAR) techniques to monitor ground deformation, as recently reported by Selvakumaran et al. [43]. Indeed, atmospheric noise is filtered when using these strategies, leading to a higher SNR and a more accurate DinSAR time series as pointed out by Manconi [30]. In the same way, 2D stacking plays an important role in other fields such as Seismic Data Processing, improving the overall SNR and overall quality of seismic data [44]. Although several publications describing stacking techniques on 2D matrices were found in the literature, no other publications dealing with the improvement of 3D objects (e.g., PCs) were identified during our literature review.

1.4. Aim and Objectives

The aim of this manuscript is to present and validate a workflow to enhance the monitoring capabilities of time-lapse camera systems by stacking individual 3D point clouds generated from Multi View Stereo (MVS) photogrammetry.

The proposed workflow allows the accuracy of the individual PC to be improved by getting the most out of the iterative solutions obtained during the bundle adjustment process, a key step in the MVS photogrammetry workflow. More specifically, bundle adjustment resolves an indeterminate system with a larger number of unknowns than equations (intrinsic and extrinsic camera parameters vs. number of cameras/perspectives respectively), thus, multiple solutions in the form of PCs satisfying these equations are possible. Since the average value in a local coordinate system of the “range” coordinate converges for a large enough size sample (i.e., total number of PCs), a gain in precision can be obtained by stacking and averaging this value on the individual PC, allowing the correction of individual geometric aberrations, as shown below.

The proposed workflow was tested using a synthetic point cloud, created using mathematical functions that attempted to emulate the photogrammetric models, and data collected from a rock cliff

located in Puigcercós (Catalonia, NE Spain), using very low-cost photogrammetric systems specially developed for this experiment. This work demonstrates that the proposed workflow is especially well-suited for improving precision when a high temporal sampling procedure can be set up or when low-cost time-lapse camera systems are being used, or both.

2. Materials and Methods

2.1. PCStacking Workflow

2.1.1. Automatic 3D Reconstruction from Time-Lapse Camera Systems

Structure from Motion photogrammetry with multi-view stereo (SfM-MVS) reconstruction was used to generate 3D point clouds from time-lapse camera systems by: (a) Finding correspondence between images through the identification of key features (tie points) in two or more images as homologous points, using a Scale Invariant Feature Transform (SIFT) algorithm [45]. This process is scale, lighting and orientation invariant for all photographs, in order to account for different camera locations and zoom; (b) Estimating the interior and exterior orientation parameters, including the position of each time-lapse system, as well as its orientation and their distortion parameters that satisfy the equations of the “bundle adjustment.” This iterative process consists of minimizing the squared Euclidean distance between the coordinates of each point and its re-projection in each of the iterations, in order to progressively refine the value of each of these parameters. This process was carried out in Agisoft Metashape software (2019 Agisoft). A more detailed description of the SfM-MVS procedure can be seen in Westoby et al. [3]. The SfM workflow results in a sparse PC containing the three-dimensional location of a series of key points in a local coordinate system, together with an estimate of the interior and exterior orientation parameters for each image. This allows calculation of the depth maps of the model in order to reconstruct a dense PC using stereo multi-view algorithms such as PMVS2 (Patch-based MultiView Stereo) [46], CMVS (Clustering Views for MultiView Stereo) [47] and other algorithms integrated in commercial software (e.g., Agisoft Metashape).

2.1.2. Point Cloud Stacking Algorithm

The proposed workflow makes the most of the different solutions generated iteratively during the bundle adjustment and is based, on the one hand, on optimal data collection using time-lapse camera systems and, on the other hand, on an algorithm that generates an enhanced PC from a series of stacked PCs. The proposed method of data collection differs from classic photogrammetry in that, for each of the camera positions, multiple and successive images are captured, in synchrony with the other cameras. This allows the generation of different approximate solutions (Point Clouds) that serve as input data in the PCStacking algorithm. Each individual PC is then stacked and processed in order to generate an enhanced 3D model as the output (Figure 1).

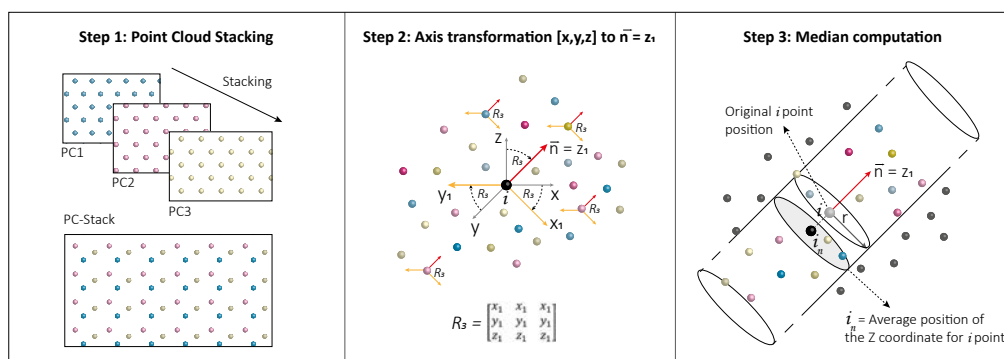


Figure 1. The three steps developed by the Point Cloud Stacking algorithm. Step 1: All points are stored in the PC-Stack cloud. Step 2: Coordinates system change. Step 3: Point averaging on the normal axis.

The main steps of the algorithm are (Figure 1): (1) point cloud stacking, (2) local axis transformation and (3) median computation along the normal vector. More specifically, all the individual PCs are stored in a single point cloud (“PC-Stack”) in the first step. Then, a Principal Component Analysis (PCA) is used to transform the global coordinate system to a local coordinate system, so that the third principal component on this orthogonal transformation (rotation and translation) would be defined as the local normal vector. Finally, the algorithm averages the third eigenvalue along the third eigenvector on each point of PC-Stack using the median operator. For practical purposes, this local vector can also be computed with a cylinder of radius r and infinite length in the local normal direction. An extra-dense PC is obtained as a result, where all points have the averaged (median) coordinate for a local subset of points. The overall principle of the proposed algorithm is quite straightforward: point cloud precision can be enhanced by increasing the sample size in order to compensate for systematic errors in a large enough number of datasets, although this does not improve accuracy. The main steps of the Algorithm 1 can be found in the pseudo-code below:

Algorithm 1 PCStacking is

```

1   Start
2   get the number of Point Clouds ( $m$ ) from a designated folder
3   load  $m$  Point Clouds into the workspace
4   merge all Point Clouds into a single matrix (PC-Stack)           [step 1]
5   input search radius value ( $r_1$ )
6   for each Point in PC-Stack
7       create a subset1 of PC-Stack inside  $r_1$ , with coordinates ( $x,y,z$ )
8       apply axes transformation (PCA), being normal vector  $\rightarrow Z_1$  axes   [step 2]
9       compute median value of the subset1 along eigen vectors ( $X, Y, Z$ )   [step 3]
10      end
11      output the mean coordinates of the stacked Point Cloud
12  End
  
```

2.2. Experimental Design (I): Synthetic Test

2.2.1. Synthetic Point Clouds Creation

A synthetic test space formed by PCs that emulate the errors observed in **Photogrammetric Point Clouds** (Phot-PC) was performed, in order to assess the PCStacking algorithm. In the first instance, a regular perfect surface (without any geometric error) was created using Equation (1). This surface is considered the **Reference Point Cloud** (Ref-PC):

$$z_{\text{Ref-PC}} = 2e^{-x^2-y^6} \quad (1)$$

Then, two different errors are added into the synthetic function, modifying the position of their points in order to simulate the typical errors in photogrammetric data. The first error added is based on a function that keeps the X and Y coordinates but adds a deviation in Z (Equation (2)). This Z deviation is generated using sinusoidal functions because the differences in each point must be related to the previous one. The goal of this process is to generate a geometric error with a solution of continuity avoiding random errors. The values $\{x,y,z\}$ in Equation (2) correspond to the coordinates of the points in the Ref-PC and the parameters $\{A,f,d_1,d_2\}$ are calculated randomly using predefined ranges. That means the synthetic test suite generates a different error (z_{sin}) in each iteration (Figure 2):

$$z_{\text{sin}} = A * \sin((x \cdot f) + d_1) \cdot \sin((y \cdot f) + d_2) \quad (2)$$

The result of Equation (2) is added directly to the Z coordinate in Ref-PC, obtaining a PC with deformations along the Z axis, which can be considered as the geometric error inherent to

the photogrammetric models (see Section 1.1). The second error added to the Ref-PC is a random Gaussian distribution error. This error, similar to the one inherent to LiDAR PCs, has little presence in photogrammetric models. However, it is introduced in order to avoid totally regular surfaces. This error is entered into the three coordinates and is defined as x_{disp} , y_{disp} and z_{disp} . Finally, the **Synthetic Point Cloud** (Synt-PC) is obtained from the sum of the Ref-PC coordinates, the geometric deformation obtained by the sinusoidal function (Equation (2)) and the Gaussian scattering errors (Equations (3)–(5)):

$$x_{\text{Synt-PC}} = x_{\text{Ref-PC}} + x_{\text{disp}} \quad (3)$$

$$y_{\text{Synt-PC}} = y_{\text{Ref-PC}} + y_{\text{disp}} \quad (4)$$

$$z_{\text{Synt-PC}} = z_{\text{Ref-PC}} + z_{\text{sin}} + z_{\text{disp}} \quad (5)$$

The first row of Figure 2 shows the original Ref-PC created with Equation (1) without errors. The first column shows the random functions generated by the sinusoidal function (Equation (2)) and the second column shows the sum of this function with the Ref-PC. The third and fourth columns display cross-sections showing the geometric differences of the resulting PCs with respect to the Ref-PC.

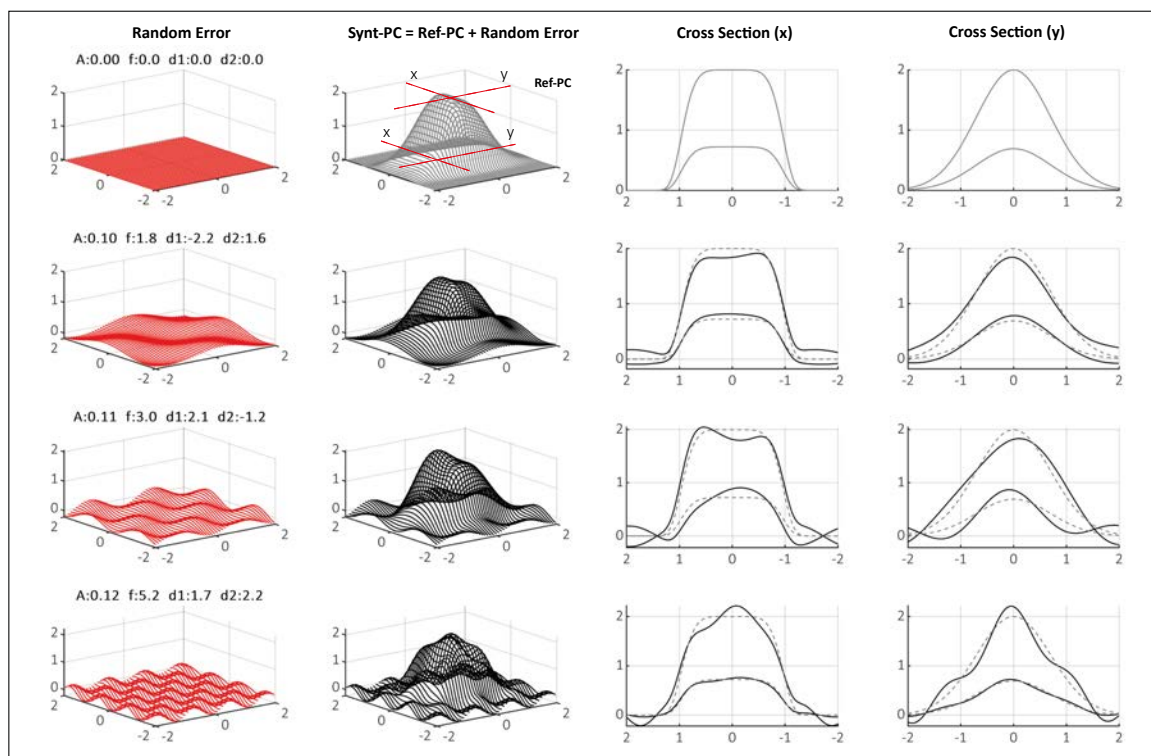


Figure 2. Functions developed to create the Synthetic Point Clouds (Synt-PC) First row: Function without error, representing the reference PC (Ref-PC) (Equation (1)). Rows (2 to 4): Synthetic functions created with errors based on random parameters (Equation (2)). Columns (left to right): Error function; sum of Ref-PC + Error function, X cross-section, Y cross-section. Dotted lines correspond to the Ref-PC and continuous lines to the Synt-PC.

As the PCStacking algorithm needs different simultaneous photogrammetric models to obtain an **Enhanced Point Cloud** (Enh-PC), 20 random functions were generated, and 20 different Gaussian scattering errors were calculated in order to obtain 20 Synt-PC. This allowed analysis of the performance of the PCStacking algorithm, as well as the sensitivity of the method.

These 20 Synt-PCs emulate the different simultaneous photogrammetric models that would later be generated using real photographs. Figure 3 shows the X and Y cross-sections of five of these Synt-PCs as well as a comparison between two of them using the M3C2 algorithm [14] in

CloudCompare software [48]. This comparison was carried out to verify whether or not the differences between different Synt-PCs resembled the differences between two real photogrammetric models (see Section 2.3.3.).

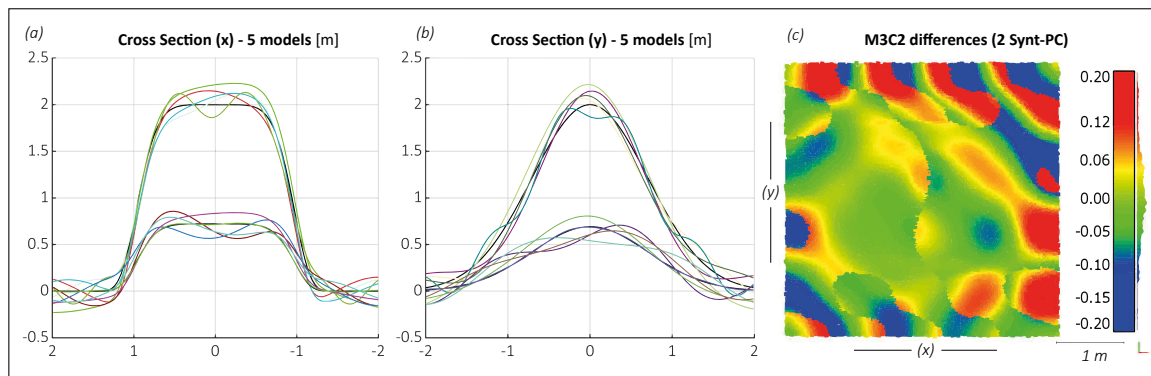


Figure 3. (a) X cross-sections of 5 Synt-PC (each color corresponds to a different Synt-PC), the black line corresponds to the sections of the Ref-PC. (b) Y cross-sections of 5 Synt-PC (each color corresponds to a different Synt-PC), the black line corresponds to the sections of the Ref-PC. (c) Distribution of differences between two Synt-PC computed by M3C2.

2.2.2. PCStacking Application

After obtaining the 20 Synt-PCs, the following workflow was designed to test the PCStacking method. This involved applying the PCStacking algorithm to the 20 Synt-PCs to obtain the Enh-PC_n (n being the number of Synt-PCs considered). The resulting Enh-PC_n was then compared with the Ref-PC. The Synt-PCs were introduced into the algorithm in an incremental way, from two to 20 Synt-PCs. Then, each Enh-PC_n was compared with the Ref-PC in order to assess the performance of the designed method, as well as its sensitivity to the number of Synt-PCs introduced.

PCStacking test summary:

- Design a Reference PC (Ref-PC)
- Create 20 Synthetic PCs (Synt-PC)
- Application of the PCStacking algorithm: ($n \rightarrow 2:20$)
 - o Input: n Synthetic PCs (Synt-PC)
 - o Output: Enhanced PC (Enh-PC_n)
 - o Comparison between the Enhanced PCs (Enh-PC_n) and the Reference PC (Ref-PC)
- Analysis of computed differences

The Enh-PC_n vs. Ref-PC comparison was carried out using the Point to Mesh algorithm to avoid the influence of statistical averaging of the results using other comparison methods such as the M3C2 algorithm [14]. In this case, the conversion of the Ref-PC into a mesh does not introduce errors because the Ref-PC is a regular surface. For this reason, the distances obtained in the comparison correspond to the real distance between each point of the Enh-PC_n and the synthetic surface computed from the Ref-PC. The performance of the developed method was evaluated through the statistical values of the differences between Enh-PC_n and Ref-PC, assuming that an improvement means achieving an Enh-PC_n more and more similar to the Ref-PC. Thus, the differences obtained in the comparison must tend to zero.

2.2.3. Redundancy Test

Due to the use of random parameters to produce the Synt-PCs, the workflow explained in the previous section was repeated 20 times. Therefore, 400 (20×20) different Synt-PCs were calculated to

test the PCStacking method, covering a large number of possibilities and providing more consistent results. In each iteration, the standard deviation corresponding to each Enh-PC_n vs. Ref-PC comparison was calculated. As this process was repeated 20 times in an iterative way, 20 standard deviation values were obtained for each Enh-PC_n vs. Ref-PC comparison. This procedure allowed us to evaluate whether the described method works independently of the random parameters introduced to produce the Synt-PC. This redundancy test was carried out because in some tests the random values of the Synt-PC were too low, which resulted in a Synt-PCs with little error that generated a much improved Enh-PCs. With the generation of 400 Synt-PCs and the computation of the standard deviation of the 400 comparisons (Ref-PC vs. Enh-PC1:2020 times) the median values showed the real range of the PCStacking algorithm.

2.3. Experimental Design (II): 3D Reconstruction of a Rocky Cliff

To observe the performance of the PCStacking algorithm using real data, a test was performed with images obtained by using a photogrammetric system of very low-cost fixed time-lapse cameras on a rock cliff situated in Puigcerçós (Catalonia, NE Spain).

2.3.1. Pilot Study Area

The images used for the test were captured from Puigcerçós cliff (Catalonia, NE Spain). This rock face (123 m long and 27 m high) is the result of a large rototranslational landslide [49] that occurred at the end of the 19th century [50,51] (Figure 4a). The structure of the area (Figure 4b), together with its high rockfall activity and low risk (due to lack of exposed elements) make it an ideal study area for the development of methodologies such as the TLS point cloud processing methods described by Royán et al., Abellan et al. and Tonini et al. [8,52–54].

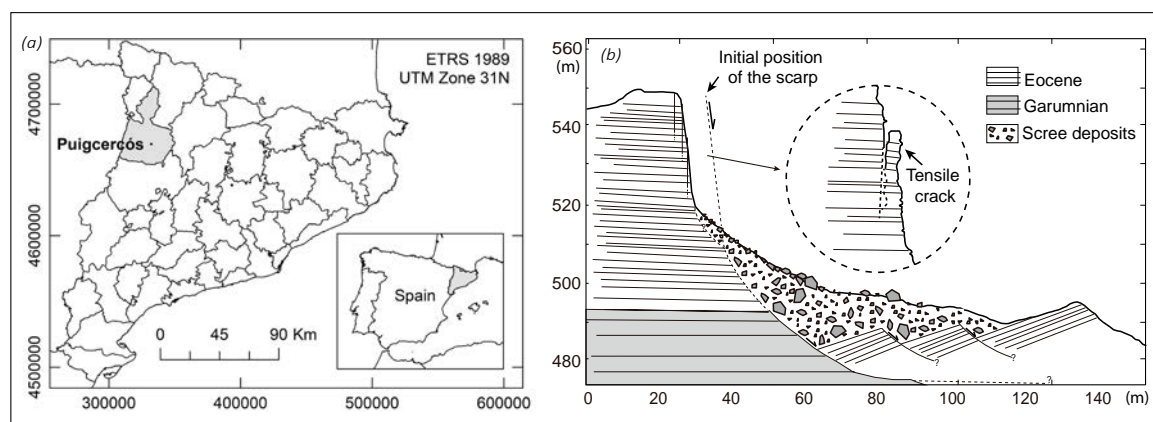


Figure 4. (a) Puigcerçós location (Pallars Jussà—Catalonia—NE Spain). (b) Geomorphological scheme of the Puigcerçós cliff and main rockfall mechanism (modified from Royán et al. [8]).

2.3.2. Field Setup and Data Acquisition

The acquisition of data was carried out using a low-cost photogrammetric system developed ad-hoc for this study. The system consists of five photographic modules and a data transmission module. Each photographic module is composed of a Sony IMX219PQ photographic sensor of 8 megapixels and 1/4" format assembled on a commercial Raspberry Pi Foundation Camera Module V2 board that is characterized by a 3.04-mm focal length lens (29 mm equivalent in 35 mm format) and a maximum aperture of f/2.0. These sensors are controlled by a Raspberry Pi Zero W, a small microcomputer produced by Raspberry Pi Foundation. This computer takes the images and stores and transmits the data to the servers. A solar panel (10 W) and a battery (4500 mAh) are used to power each module. In order to manage the energy source, as well as to carry out the functions of the timer, the commercial board Witty Pi 2 by UUGear is used as a real-time clock and for power management (Figure 5). All these components can be assembled for less than 150 €. Thanks to the remote transmission system based on

a 4G WiFi data network and to the solar charging system, the system has very low maintenance costs. The distribution of five photogrammetric modules in five different positions allows the acquisition of daily photogrammetric models of the cliff, inferring a very high temporal frequency of monitoring of rockfalls and deformations.

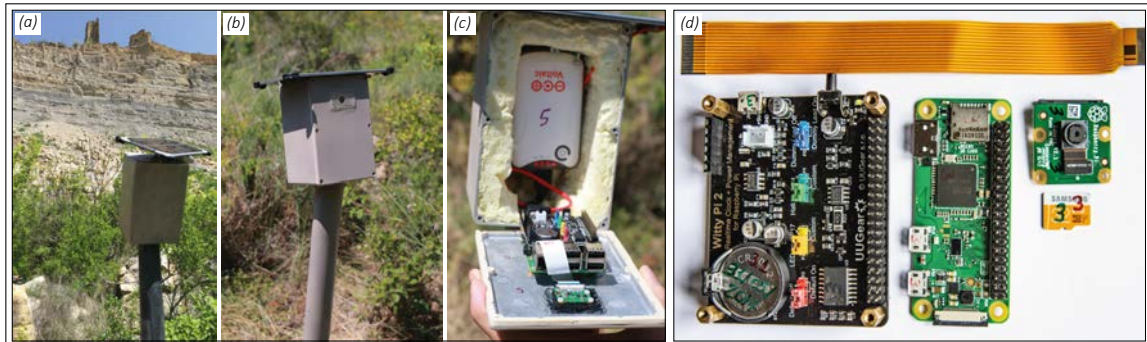


Figure 5. Low-cost photogrammetric systems developed ad-hoc for rockfall monitoring on the Puigercós cliff. (a,b,c) Images of the installation on the Puigercós cliff. (d) Main electronic components (left to right): WittyPi2, Raspberry Pi Zero W, Raspberry Camera Module v2 and MicroSD card.

The quality of the point clouds produced by this low-cost system is theoretically lower than that obtained using commercial cameras, due to the size of the sensor, the low resolution and the quality of the lens. Consequently, the resulting photogrammetric models are not high quality. This system is thus ideal as a case study to monitor the performance of the PCStacking method and to evaluate its ability to generate higher quality photogrammetric models.

Since there is no ideal surface of the terrain that corresponds to the Ref-PC in the synthetic test, the algorithm was tested by comparing the two models acquired on consecutive days (February 25 and 26, 2019) from an area without any activity. Due to the non-activity and therefore the non-existence of movement, we assume that the difference between the models must be zero.

2.3.3. Point Cloud Reconstruction

The system developed on Puigercós was configured to capture 15 images in the same photo burst synchronized in the five installed cameras. From these 15 photographs captured by each camera, 15 different photogrammetric models of the same moment in time were reconstructed using Agisoft Metashape (2019 Agisoft). To improve the software's calculation process, different tools such as zone masking, cutting out working areas and optimizing camera positions were used. The results were always obtained at the highest quality, both in the calculation of homologous points and the dense point cloud (PC).

Due to the large size of the rockface and the requirement to work in an area without deformation, we have carried out the test in a specific zone. This truncated rectangle has a size of 12.5 m × 10 m and an area of approximately 100 m². The computational cost to perform the entire process for a given radius in this small area is around 60 minutes to generate the 3D models with Agisoft Metashape and 70 minutes to apply the PCStacking algorithm. These times have been achieved with a commercial medium-high performance equipment (Intel(R) Core(TM) i9—7900X up to 4.30 GHz, 64GB RAM and NVIDIA GeForce GTX 1080 Ti). The raw point clouds obtained by the Metashape software are composed by approximately 150,000 points.

As the test was carried out on two consecutive days, a total of 30 **Photogrammetric Point Clouds** (Photo-PC) were generated. The calculated models were aligned and scaled with a reference LiDAR to produce metric values for comparison. Figure 6a shows the X and Y cross-sections of four Photo-PCs. It demonstrates the correct alignment of the models but shows clearly different surfaces due to the poor quality of the acquisition system.

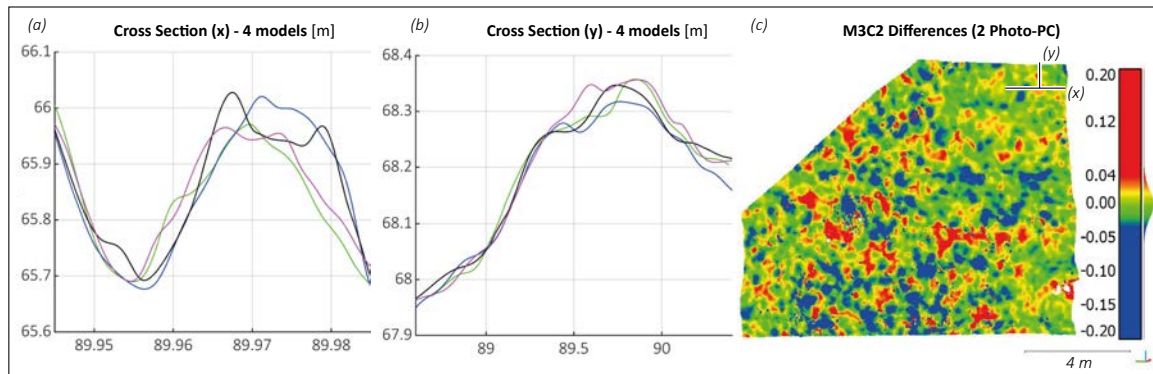


Figure 6. (a) X cross-sections of four Photo-PCs generated using five images (each color corresponds to a different Photo-PC). (b) Y cross-sections of four Photo-PCs generated using five images (each color corresponds to a different Photo-PC). (c) Distribution of differences of two Photo-PCs computed by M3C2. (x) and (y) shows the cross section represented in (a) and (b).

The differences between two PCs, computed using the M3C2 algorithm [14] (Figure 6b), are randomly distributed due to the different geometries generated in the photogrammetric reconstruction process.

3. Results

3.1. Synthetic Test

The histograms of the differences between the Enh-PC_n and the Ref-PC (Figure 7a) provide a quantitative assessment of the improvement achieved with the PCStacking algorithm. The increase in the number of input models (Synt-PCs) resulted in a better fit between Enh-PC_n and Ref-PC.

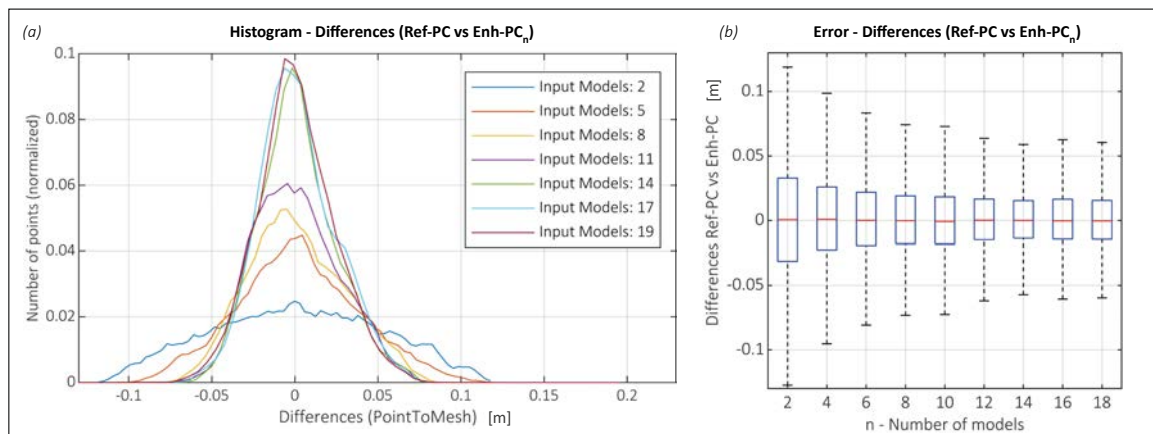


Figure 7. Results from the application of the PCStacking algorithm with synthetic data. (a) Histogram of the differences between the Enh-PC_n and the Ref-PC. Each colored line represents a different number of Synt-PCs introduced into the PCStacking algorithm. (b) Boxplot with the errors of the differences obtained in the different comparisons (Enh-PC_n vs. Ref-PC).

The boxplot in Figure 7b illustrates the distribution of the differences calculated from the comparisons between Enh-PC_n vs. Ref-PC. The boxplot depicts a decrease in the errors when more inputs were used. The 25th and 75th percentiles progressively reduced to 50% after using 18 models. Specifically, the percentiles were progressively reduced from ± 3.2 cm to ± 1.4 cm after using the PCStacking algorithm with 18 models. Likewise, the minimums and maximums shown in the boxplot also showed a reduction close to 50%. The comparisons between Enh-PC_n vs. Ref-PC in the redundancy test (Figure 8a) reveal a considerable reduction of the standard deviation when increasing the number

of models introduced. The average standard deviations of the comparisons of all iterations decreased from 4.9 cm to 1.8 cm when 20 PC were used.

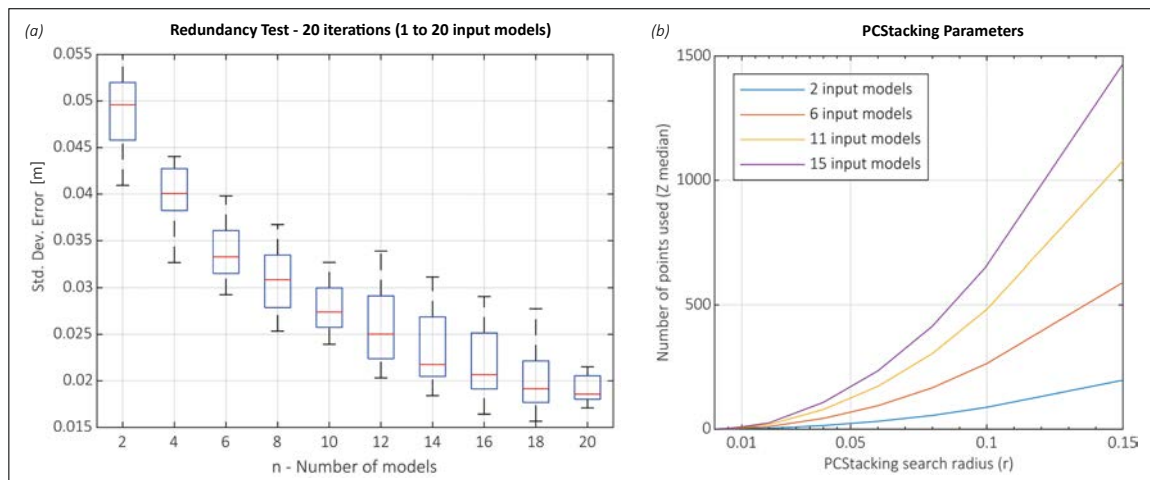


Figure 8. (a) Evolution of the standard deviation of the comparison Enh-PC_n vs. Ref-PC in the redundancy test. The standard deviation decreased from 4.9 cm to 1.8 cm. A total of 400 Synt-PCs were used to compute this plot. (b) Number of averaged points according to the search radius (r). Each colored line represents a different number of Synt-PCs introduced into the PCStacking algorithm.

The quartile bars (Figures 7b and 8a) demonstrate non-constant values because in some iterations the Synt-PCs may have much more error than in others. As an example, in Figure 7b, the 75th percentile bar belonging to the input of 16 Synt-PCs is larger (1.4 cm) than the one belonging to the input of 14 Synt-PCs (1.3 cm). This random distribution of error is the main reason for carrying out the iterative test.

One effect of using the PCStacking method is that the result obtained (Enh-PC_n) accumulates all the points of the different Synt-PCs used, producing both a more accurate and denser Enh-PC. The plot in Figure 8b depicts the number of points available to average the Z coordinate, which depends on the number of Synt-PCs used as input data and on the search radius defined. This value is a great indicator of when the algorithm has enough input points to compute the new Z coordinate.

Using this parameter as a filter, those points that were averaged using a smaller number of points were removed from the Enh-PC. For this research, all points in the Enh-PC that were averaged using less than as many points as Synt-PCs introduced, were removed. In this way, this filter easily allows the removal of points in some Enh-PC that are not generally in all Synt-PCs, such that unrepresentative points produced during the reconstruction of the model are removed.

3.2. 3D Reconstruction on a Rocky Cliff

The process for evaluating the algorithm using real images taken on 25th and 26th February 2019 involved: (a) Calculation of the Enh-PC_{n=2:15} from the February 25th PCs; (b) Calculation of the Enh-PC_{n=2:15} from the February 26th PCs; (c) Point to mesh comparison (in CloudCompare) between a February 25th Photo-PC and a February 26th Photo-PC without applying any enhancement algorithm; and (d) Point to mesh comparison (in CloudCompare) between all Enh-PC_(2:15)^{25 feb} vs. Enh-PC_(2:15)^{26 feb}. The outputs from these comparisons are the distances in metric values existing between the two models studied. Given that between 25th and 26th February 2019 there was no change in the analyzed cliff, the expected difference in an ideal case must be zero.

The results obtained are shown in Figure 9, which is analogous to Figure 7. The histogram of the values obtained in the comparison (25th February vs. 26th February) (Figure 9a) demonstrates that the precision of the values increases when more models are added to the algorithm (the differences tend to zero). Moreover, Figure 9b shows a decrease in the 25th and 75th percentiles of almost 70%.

Values decreased from ± 1.5 cm for a simple comparison to ± 0.5 cm when comparing the $\text{Enh-PC}_{15}^{25 \text{ feb}}$ vs. $\text{Enh-PC}_{15}^{26 \text{ feb}}$.

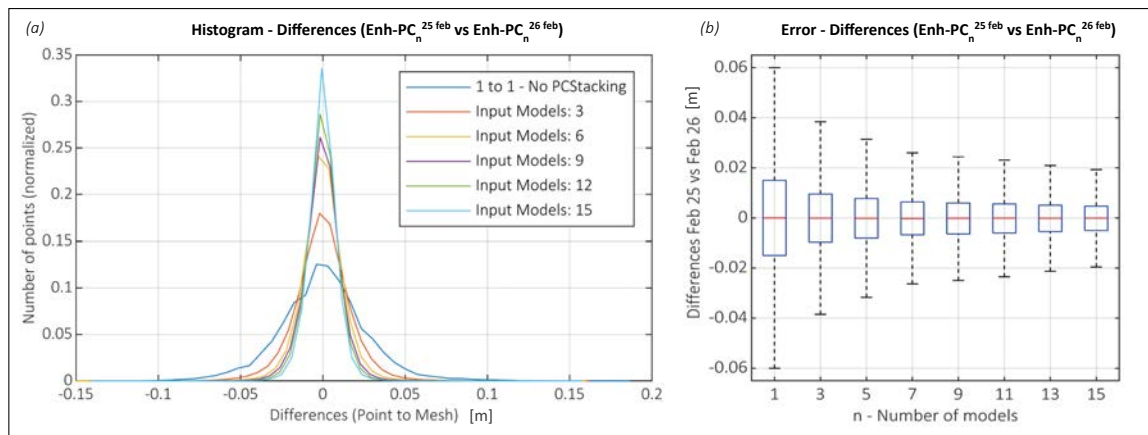


Figure 9. Results from the application of the PCStacking algorithm to real images. (a) Histogram of the differences between the $\text{Enh-PC}_n^{25 \text{ feb}}$ and $\text{Enh-PC}_n^{26 \text{ feb}}$. Each colored line represents a different number of PCs introduced into the PCStacking algorithm. (b) Error of the differences obtained in the different comparisons ($\text{Enh-PC}_n^{25 \text{ feb}}$ vs. $\text{Enh-PC}_n^{26 \text{ feb}}$).

Figure 10 depicts the sensitivity of the algorithm from the input parameters of the code. The plot in Figure 10a shows the standard deviation obtained in the comparisons made by M3C2 [14] between $\text{Enh-PC}_n^{25 \text{ feb}}$ and $\text{Enh-PC}_n^{26 \text{ feb}}$. Each plotted line represents different parameters in the search radius (r) of the PCStacking algorithm (Section 2.1 and Figure 1). Note that for the smaller radius ($r = 0.1$ cm) the algorithm does not produce any improvement, because as in the synthetic test (Figure 8b), the small search radius does not provide enough points to average the Z coordinate in the direction of the normal.

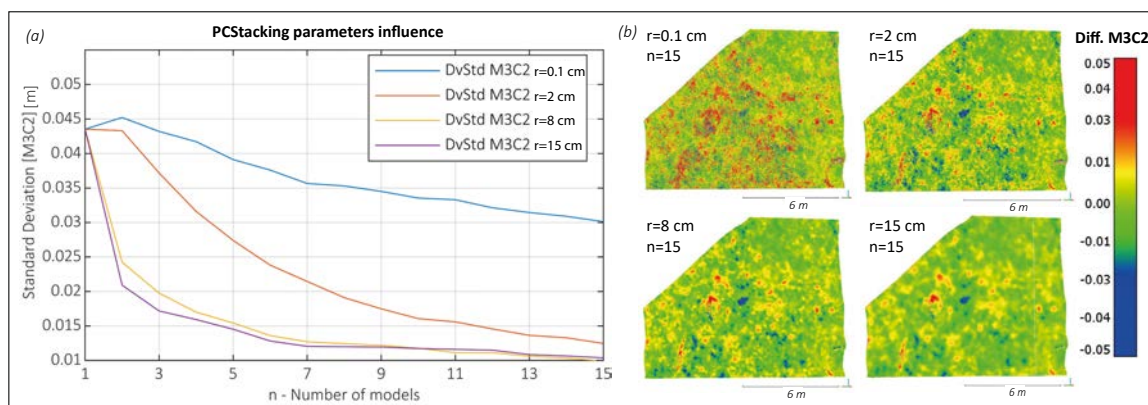


Figure 10. Influence of the search radius (r) on the PCStacking results. (a) Standard deviation of the $\text{Enh-PC}_n^{25 \text{ feb}}$ vs. $\text{Enh-PC}_n^{26 \text{ feb}}$ comparison. (b) Comparisons between $\text{Enh-PC}_{15}^{25 \text{ feb}}$ and $\text{Enh-PC}_{15}^{26 \text{ feb}}$ for different search radii (r).

When the search radius is larger the algorithm has more points to average, resulting in a decrease in the standard deviation of the comparisons. The images in Figure 10b show the comparisons using the M3C2 algorithm between $\text{Enh-PC}_{15}^{25 \text{ feb}}$ and $\text{Enh-PC}_{15}^{26 \text{ feb}}$ for the different search radii described.

Since the proposed algorithm involves averaging the Z coordinate along the normal axis at each point, obtaining the normals at each point in the correct way is critical. As discussed in Lague et al. [14], the roughness of the surface makes the calculation of normals dependent on the scale at which it is performed. Thus, calculating normals using inappropriate scales means that the averaging is not done in the right direction. Consequently, the efficiency of the algorithm decreases considerably.

In the case of the Synth-PC the normals were calculated using the CloudCompare software. However, for the real case of the Puigcercós Cliff, the normals were computed automatically using Agisoft Metashape software (2019 Agisoft) (see Section 4. Discussion).

4. Discussion

4.1. Synthetic Test vs. Real Data

The cross-sections obtained from the synthetic point clouds (Synt-PCs) (Figure 3a) and real photogrammetric models (Photo-PC) (Figure 7a) are very similar. Likewise, the random distribution of the error obtained in a comparison of two Synt-PCs (Figure 3b) is similar to that obtained from real data (Photo-PC) (Figure 6b). The use of random parameters in the sinusoidal function allows the generation of different PCs with errors that are geometrically consistent in each iteration. This is important because in the reconstruction of models obtained using low-cost photogrammetric systems, surfaces with different geometries are always generated even though the input photographs are captured at the same time. The result of using the described functions (Equations (1) and (2)) together with the random parameters (Equations (3)–(5)) generated synthetic PCs with a similar pattern to that of photogrammetric models.

Despite the above mentioned observations, the comparison between two Synth-PCs using the M3C2 algorithm [14] (Figure 3b) depicts some repeatability in the distribution of the differences, while the pattern of the comparison between two Photo-PCs (Figure 6b) is absolutely random. This is because Synth-PCs were created by the sinusoidal function (Equation (2)), which is periodic. Even so, we believe that this conceptual dissimilarity in the distribution of the differences does not affect the PCStacking method trials proposed in this paper.

To sum up, the synthetic study suite designed to test the PCStacking algorithm worked well and the generated PCs are comparable to PCs obtained from low-cost photogrammetric models. Thus, this methodology based on the generation of synthetic functions can be extrapolated to the synthetic study of different PC improvement algorithms.

4.2. The PCStacking Method

The results of the assessment of the PCStacking workflow reveal a significant improvement in the precision of the enhanced point clouds. This advance was observed with both synthetic and photogrammetric PCs. In the synthetic case the initial error of the comparison was larger (± 3.2 cm) and the reduction occurred more progressively while introducing a greater number of Synt-PCs to the algorithm, reaching ± 1.4 cm in the Enh-PC₁₈ comparison (Figure 7). In contrast, real photogrammetric models had a smaller comparison error that ranged from ± 1.5 cm to ± 0.5 cm when 15 PCs were used. In this case, 50% reduction in error was achieved when using only five PCs (Figure 9). This is because: (a) the synthetic PCs were designed with a higher geometric error with a distribution dependent on random parameters (see Equation (2)); and (b) the errors in the real photogrammetric PCs are not homogeneous and tend to be concentrated in areas where the software has more difficulty identifying homologous points. Consequently, synthetic data has larger and more distributed errors, thus, the algorithm needs more input point clouds to reduce the error. Even so, the algorithm succeeded in reducing the errors in both the synthetic test and the real case, and the number of PCs used was sufficient to stabilize the error reduction.

Concerning data acquisition, the application of the algorithm using only one image per camera position (classic capture scheme), instead of a set of images as in this study, would reduce its efficiency considerably. The use of different simultaneous images captured in the same burst means that each model is built on the basis of a totally different point identification process and bundle adjustment. This is because the intrinsic errors of the photographic sensors will always generate differences between the images, despite the short time between shots. Consequently, SfM algorithms produce different geometries generating slightly different models. The averaging of these differences through

the PCStacking algorithm improves the precision of the PCs obtained from images captured using low-cost systems.

The results of the redundancy test applied to Synt-PCs reveal that the developed code is robust. The goal of this test is to eliminate any possibility of associating the improvement with the use of low random values for the generation of the Synt-PCs. As shown in Figure 8a the standard deviation of the 20 iterations performed progressively decreased as the number of input models increased. The differences in the error bars are related to the randomness of the parameters contemplated in Equation (2) to introduce the random error to the Synt-PCs. Thus, some iterations produce Synt-PC with errors greater than others. This results in point averaging between point clouds with greater dispersion, thus augmenting the error in the comparison Enh-PC_n vs. Ref-PC.

The considerable increase in the number of averaged points shown in Figure 8b is due to two key parameters: (1) the number of input PCs and (2) the PCStacking search radius. Therefore, these two parameters control the quality of the result (Figure 10). For this reason, in a real situation, a sensitivity study to determine the parameters that would improve the results is required.

4.3. Current Limits and Margins for Improvement

As shown in Figures 7–9, the improvement obtained by the application of the PCStacking method was not linear. In addition, Figure 10a reveals that a sensitivity study of the parameters used is required because, depending on the point density of the input data, the algorithm will start working optimally from a certain search radius. The use of a very large search radius may end up involving excessive smoothing of the Z coordinate. However, the use of a very small search radius will not provide enough information for the PCStacking algorithm to perform point averaging.

The reduction in error (Figure 10a) observed when using a 0.1 cm radius (extremely small) was due to the effect of the densification of the PCStacking algorithm and the averaging of the M3C2 algorithm. In our work, the PCStacking algorithm, with a radius of 0.1 cm, did not average any value because the density of points was too low to include more than one point. Thus, the Enh-PC obtained can be considered the same as if all the input Photo-PCs had been merged without any processing. Since the search radius of the M3C2 for the comparison was the same for all analyses (1 cm), the use of the M3C2 resulted in a reduction in the error as more input Photo-PC were introduced. If the PCStacking algorithm did not have the property of densifying the PC for the 0.1 cm search radius, there would have been no improvement. In order to identify the improvements produced by the PCStacking algorithm, the comparisons between Enh-PCs and Ref-PC in the synthetic test, and between Enh-PC_n^{25 feb} and Enh-PC_n^{26 feb} in the real case test, were calculated using the Point to Mesh comparison algorithm. Since the application of this algorithm does not produce any improvement by itself, the error reduction shown in Figures 4 and 9 can be associated with the PCStacking algorithm. On the other hand, when a real representation of the distribution of differences between two PCs was needed (Figures 3, 8 and 10), the M3C2 algorithm was used, since this allows better visualization of the results as well as discrimination between positive and negative values of the differences obtained.

Another important consideration before applying the method is the correct determination of the normals for each point. As cited in Lague et al. [14], miscalculation of normals will result in poor adjustment of the method. Since the normals must be calculated based on a search radius, taking into account the roughness of each surface, it is necessary to find the best fit between both the method and the radius to obtain an optimal result with the PCStacking algorithm. However, the normals calculated directly by the digital photogrammetry software are sufficiently well-computed to allow the PCStacking algorithm to work properly.

Although the results presented show an interesting improvement in the field of point clouds, due to the differences in the errors of the photogrammetric models with respect to the LiDAR data explained in the introduction, the efficiency of the PCStacking algorithm will not be equivalent with the LiDAR data. Even so, the algorithm has not been tested with other acquisition systems. Thus, the performance of the algorithm in point clouds obtained with other technologies has not been

verified yet. If the proper computation of the normals cannot be guaranteed, the PCStacking method can be applied by modifying part of the algorithm. Instead of averaging only the Z coordinate in the direction of the normal, it will be necessary to average all the coordinates $\{x,y,z\}$ in the direction of the respective normals. In this case, exploratory tests showed that the method also produced better PCs but with greater surface smoothness.

Another discussion point is the computational cost of applying the algorithm. Digital photogrammetry software generates, at its highest quality, very dense PCs that easily exceed millions of points. Because the PCStacking algorithm is based on the introduction (and accumulation) of different PCs, the workspaces can easily exceed tens of millions of points. Since Z-coordinate averaging is done point-to-point, the computational cost is high. Nevertheless, the PCStacking algorithm can also be used in low performance computers by simply subsampling the original PCs. Therefore, a necessary improvement of the method will involve optimizing the calculation. This optimization could be achieved using dedicated PC library methods that significantly speed up the process as well as the use of PC fractionation methods.

5. Conclusions

This article presents a workflow to increase the precision in the comparison of PCs obtained through Multi-View Stereo photogrammetry. This method, called Point Cloud Stacking (PCStacking), refers to the process of taking photographs, as well as the data processing and post-processing of the information to generate enhanced PCs. This paper describes the application of the method using both synthetic PCs specially developed to emulate photogrammetric models and a real case study, with photogrammetric PCs obtained using a very low-cost time-lapse camera system. The results showed a reduction of more than 50% of the error, increasing the precision in both experiments, and validating the proposed approach under different conditions. In more detail, the 25th and 75th percentiles were progressively reduced with both the synthetic data and the actual photogrammetric models from ± 3.2 cm to ± 1.4 cm, and from ± 1.5 cm to ± 0.5 cm respectively. The resulting enhancement means that relatively low-cost strategies could be used in place of more expensive systems, but the proposed algorithm can also be used to repeat TLS scenarios in order to increase the signal-to-noise ratio. The proposed approach might constitute a step forward for high precision monitoring of both natural processes (landslides, glaciers, riverbeds, erosion, etc.) and man-made scenarios (structural monitoring of buildings, tunnels, beams, dams, etc.) using low-cost time-lapse camera systems.

Author Contributions: Algorithm conceptualization and methodology: X.B. and A.A.; software: X.B.; formal analysis: X.B., A.A. and M.G.; investigation: X.B., A.A. and M.G.; validation: X.B., A.A. and M.G. writing—original draft preparation, X.B.; writing—review and editing A.A. and M.G.; visualization: X.B.; supervision, A.A. and M.G. All authors have read and agreed to the published version of the manuscript.

Funding: The presented study was supported by the PROMONTEC Project (CGL2017-84720-R) funded by the Ministry of Science, Innovation and Universities (MICINN-FEDER). The first author (X. Blanch) was supported by an APIF grant funded by the University of Barcelona and the second author (A. Abellán) was supported by the European Union's Horizon 2020 research and innovation programme under a Marie Skłodowska-Curie fellowship (grant agreement no. 705215).

Acknowledgments: The authors thank the ORIGENS UNESCO Global Geopark for granting permission to work in Puigcercós rock cliff and the reviewers and the editor for the valuable comments and suggestions that contributed to the improvement of the present manuscript.

Conflicts of Interest: The authors declare no conflict of interest.

References

1. Dewez, T.J.B.; Rohmer, J.; Regard, V.; Cnudde, C. Probabilistic coastal cliff collapse hazard from repeated terrestrial laser surveys: Case study from Mesnil Val (Normandy, northern France). *J. Coast. Res.* **2016**, *65*, 702–707. [[CrossRef](#)]
2. Eltner, A.; Kaiser, A.; Castillo, C.; Rock, G.; Neugirg, F.; Abellán, A. Image-based surface reconstruction in geomorphometry—merits, limits and developments. *Earth Surf. Dyn.* **2016**, *4*, 359–389. [[CrossRef](#)]

3. Westoby, M.J.; Brasington, J.; Glasser, N.F.; Hambrey, M.J.; Reynolds, J.M. “Structure-from-Motion” photogrammetry: A low-cost, effective tool for geoscience applications. *Geomorphology* **2012**, *179*, 300–314. [[CrossRef](#)]
4. Riquelme, A.J.; Abellán, A.; Tomás, R.; Jaboyedoff, M. A new approach for semi-automatic rock mass joints recognition from 3D point clouds. *Comput. Geosci.* **2014**, *68*, 38–52. [[CrossRef](#)]
5. Derron, M.H.; Jaboyedoff, M. LIDAR and DEM techniques for landslides monitoring and characterization. *Nat. Hazards Earth Syst. Sci.* **2010**, *10*, 1877–1879. [[CrossRef](#)]
6. Jaboyedoff, M.; Oppikofer, T.; Abellán, A.; Derron, M.H.; Loye, A.; Metzger, R.; Pedrazzini, A. Use of LIDAR in landslide investigations: A review. *Nat. Hazards* **2012**, *61*, 5–28. [[CrossRef](#)]
7. García-Sellés, D.; Falivene, O.; Arbués, P.; Gratacos, O.; Tavani, S.; Muñoz, J.A. Supervised identification and reconstruction of near-planar geological surfaces from terrestrial laser scanning. *Comput. Geosci.* **2011**, *37*, 1584–1594. [[CrossRef](#)]
8. Royán, M.J.; Abellán, A.; Jaboyedoff, M.; Vilaplana, J.M.; Calvet, J. Spatio-temporal analysis of rockfall pre-failure deformation using Terrestrial LiDAR. *Landslides* **2014**, *11*, 697–709. [[CrossRef](#)]
9. Brodu, N.; Lague, D. 3D terrestrial lidar data classification of complex natural scenes using a multi-scale dimensionality criterion: Applications in geomorphology. *ISPRS J. Photogramm. Remote Sens.* **2012**, *68*, 121–134. [[CrossRef](#)]
10. Abellán, A.; Vilaplana, J.M.; Calvet, J.; García-Sellés, D.; Asensio, E. Rockfall monitoring by Terrestrial Laser Scanning—Case study of the basaltic rock face at Castellfollit de la Roca (Catalonia, Spain). *Nat. Hazards Earth Syst. Sci.* **2011**, *11*, 829–841. [[CrossRef](#)]
11. Kromer, R.A.; Abellán, A.; Hutchinson, D.J.; Lato, M.; Edwards, T.; Jaboyedoff, M. A 4D filtering and calibration technique for small-scale point cloud change detection with a terrestrial laser scanner. *Remote Sens.* **2015**, *7*, 13029–13058. [[CrossRef](#)]
12. Jaboyedoff, M.; Demers, D.; Locat, J.; Locat, A.; Locat, P.; Oppikofer, T.; Robitaille, D.; Turmel, D. Use of terrestrial laser scanning for the characterization of retrogressive landslides in sensitive clay and rotational landslides in river banks. *Can. Geotech. J.* **2009**, *46*, 1379–1390. [[CrossRef](#)]
13. Smith, M.W.; Carrivick, J.L.; Quincey, D.J. Structure from motion photogrammetry in physical geography. *Prog. Phys. Geogr.* **2015**, *40*, 247–275. [[CrossRef](#)]
14. Lague, D.; Brodu, N.; Leroux, J. Accurate 3D comparison of complex topography with terrestrial laser scanner: Application to the Rangitikei canyon (N-Z). *ISPRS J. Photogramm. Remote Sens.* **2013**, *82*, 10–26. [[CrossRef](#)]
15. Williams, J.G.; Rosser, N.J.; Hardy, R.J.; Brain, M.J.; Afana, A.A. Optimising 4-D surface change detection: An approach for capturing rockfall magnitude-frequency. *Earth Surf. Dyn.* **2018**, *6*, 101–119. [[CrossRef](#)]
16. James, M.R.; Robson, S. Straightforward reconstruction of 3D surfaces and topography with a camera: Accuracy and geoscience application. *J. Geophys. Res. Earth Surf.* **2012**, *117*, 1–17. [[CrossRef](#)]
17. Eltner, A.; Schneider, D. Analysis of Different Methods for 3D Reconstruction of Natural Surfaces from Parallel-Axes UAV Images. *Photogramm. Rec.* **2015**, *30*, 279–299. [[CrossRef](#)]
18. Parente, L.; Chandler, J.H.; Dixon, N. Optimising the quality of an SfM-MVS slope monitoring system using fixed cameras. *Photogramm. Rec.* **2019**, *34*, 408–427. [[CrossRef](#)]
19. Petrie, G.; Toth, C. Introduction to Laser Ranging, Profiling, and Scanning. In *Topographic Laser Ranging and Scanning*; Shan, J., Toth, C.K., Eds.; CRC Press/Taylor & Francis: London, UK, 2008; pp. 1–28.
20. Abellán, A.; Jaboyedoff, M.; Oppikofer, T.; Vilaplana, J.M. Detection of millimetric deformation using a terrestrial laser scanner: Experiment and application to a rockfall event. *Nat. Hazards Earth Syst. Sci.* **2009**, *9*, 365–372. [[CrossRef](#)]
21. Kaiser, A.; Neugirg, F.; Rock, G.; Müller, C.; Haas, F.; Ries, J.; Schmidt, J. Small-scale surface reconstruction and volume calculation of soil erosion in complex moroccan Gully morphology using structure from motion. *Remote Sens.* **2014**, *6*, 7050–7080. [[CrossRef](#)]
22. Castillo, C.; Pérez, R.; James, M.R.; Quinton, J.N.; Taguas, E.V.; Gómez, J.A. Comparing the accuracy of several field methods for measuring gully erosion. *Soil Sci. Soc. Am. J.* **2012**, *76*, 1319–1332. [[CrossRef](#)]
23. Javernick, L.; Brasington, J.; Caruso, B. Modeling the topography of shallow braided rivers using Structure-from-Motion photogrammetry. *Geomorphology* **2014**, *213*, 166–182. [[CrossRef](#)]
24. Pan, B. Digital image correlation for surface deformation measurement: Historical developments, recent advances and future goals. *Meas. Sci. Technol.* **2018**, *29*, 1–32. [[CrossRef](#)]

25. Gabrieli, F.; Corain, L.; Vettore, L. A low-cost landslide displacement activity assessment from time-lapse photogrammetry and rainfall data: Application to the Tessina landslide site. *Geomorphology* **2016**, *269*, 56–74. [[CrossRef](#)]
26. Travelletti, J.; Delacourt, C.; Allemand, P.; Malet, J.P.; Schmittbuhl, J.; Toussaint, R.; Bastard, M. Correlation of multi-temporal ground-based optical images for landslide monitoring: Application, potential and limitations. *ISPRS J. Photogramm. Remote Sens.* **2012**, *70*, 39–55. [[CrossRef](#)]
27. Stumpf, A.; Malet, J.P.; Allemand, P.; Pierrot-Deseilligny, M.; Skupinski, G. Ground-based multi-view photogrammetry for the monitoring of landslide deformation and erosion. *Geomorphology* **2015**, *231*, 130–145. [[CrossRef](#)]
28. Cardenal, J.; Mata, E.; Delgado, J.; Hernandez, M.A.; Gonzalez, A. Close Range Digital Photogrammetry Techniques Applied To. *Int. Arch. Photogramm. Remote Sens. Spat. Inf. Sci.* **2008**, *XXXVI*, 235–240.
29. Kromer, R.; Walton, G.; Gray, B.; Lato, M.; Group, R. Development and Optimization of an Automated Fixed-Location Time Lapse Photogrammetric Rock Slope Monitoring System. *Remote Sens.* **2019**, *11*, 1890. [[CrossRef](#)]
30. Manconi, A.; Kourkouli, P.; Caduff, R.; Strozzi, T.; Loew, S. Monitoring surface deformation over a failing rock slope with the ESA sentinels: Insights from Moosfluh instability, Swiss Alps. *Remote Sens.* **2018**, *10*, 672. [[CrossRef](#)]
31. Tannant, D. Review of Photogrammetry-Based Techniques for Characterization and Hazard Assessment of Rock Faces. *Int. J. Geohazards Environ.* **2015**, *1*, 76–87. [[CrossRef](#)]
32. Eltner, A.; Kaiser, A.; Abellan, A.; Schindewolf, M. Time lapse structure-from-motion photogrammetry for continuous geomorphic monitoring. *Earth Surf. Process. Landf.* **2017**, *42*, 2240–2253. [[CrossRef](#)]
33. James, M.R.; Robson, S.; d'Oleire-Oltmanns, S.; Niethammer, U. Optimising UAV topographic surveys processed with structure-from-motion: Ground control quality, quantity and bundle adjustment. *Geomorphology* **2017**, *280*, 51–66. [[CrossRef](#)]
34. Santise, M.; Thoeni, K.; Roncella, R.; Sloan, S.W.; Giacomini, A. Preliminary tests of a new low-cost photogrammetric system. *Int. Arch. Photogramm. Remote Sens. Spat. Inf. Sci. -ISPRS Arch.* **2017**, *42*, 229–236. [[CrossRef](#)]
35. Wilkinson, M.W.; Jones, R.R.; Woods, C.E.; Gilment, S.R.; McCaffrey, K.J.W.; Kokkalas, S.; Long, J.J. A comparison of terrestrial laser scanning and structure-from-motion photogrammetry as methods for digital outcrop acquisition. *Geosphere* **2016**, *12*, 1865–1880. [[CrossRef](#)]
36. Sturzenegger, M.; Yan, M.; Stead, D.; Elmo, D. Application and limitations of ground-based laser scanning in rock slope characterization. In Proceedings of the 1st Canada—U.S. Rock Mechanics Symposium, Simon Fraser University, Burnaby, BC, Canada, 27–31 May 2007; Volume 1, pp. 29–36.
37. Nouwakpo, S.K.; Wetz, M.A.; McGwire, K. Assessing the performance of structure-from-motion photogrammetry and terrestrial LiDAR for reconstructing soil surface microtopography of naturally vegetated plots. *Earth Surf. Process. Landf.* **2016**, *41*, 308–322. [[CrossRef](#)]
38. Verma, A.K.; Bourke, M.C. A method based on structure-from-motion photogrammetry to generate sub-millimetre-resolution digital elevation models for investigating rock breakdown features. *Earth Surf. Dyn.* **2019**, *7*, 45–66. [[CrossRef](#)]
39. Bin, W.; Hai-bin, Z.; Bin, L. Detection of Faint Asteroids Based on Image Shifting and Stacking Method. *Chin. Astron. Astrophys.* **2018**, *42*, 433–447. [[CrossRef](#)]
40. Kurczynski, P.; Gawiser, E. A simultaneous stacking and deblending algorithm for astronomical images. *Astron. J.* **2010**, *139*, 1592–1599. [[CrossRef](#)]
41. Zhang, C.; Bastian, J.; Shen, C.; Van Den Hengel, A.; Shen, T. Extended depth-of-field via focus stacking and graph cuts. In Proceedings of the 2013 IEEE International Conference on Image Processing, Melbourne, Australia, 15–18 September 2013; pp. 1272–1276.
42. Lato, M.J.; Bevan, G.; Fergusson, M. Gigapixel imaging and photogrammetry: Development of a new long range remote imaging technique. *Remote Sens.* **2012**, *4*, 3006–3021. [[CrossRef](#)]
43. Selvakumaran, S.; Plank, S.; Geiß, C.; Rossi, C.; Middleton, C. Remote monitoring to predict bridge scour failure using Interferometric Synthetic Aperture Radar (InSAR) stacking techniques. *Int. J. Appl. Earth Obs. Geoinf.* **2018**, *73*, 463–470. [[CrossRef](#)]
44. Liu, G.; Fomel, S.; Jin, L.; Chen, X. Stacking seismic data using local correlation. *Geophysics* **2009**, *74*, V43–V48. [[CrossRef](#)]

45. Lowe, D.G. Distinctive image features from scale-invariant keypoints. *Int. J. Comput. Vis.* **2004**, *60*, 91–110. [[CrossRef](#)]
46. Furukawa, Y.; Ponce, J. Accurate, dense, and robust multiview stereopsis. *IEEE Trans. Pattern Anal. Mach. Intell.* **2010**, *32*, 1362–1376. [[CrossRef](#)] [[PubMed](#)]
47. Furukawa, Y.; Curless, B.; Seitz, S.M.; Szeliski, R. Towards internet-scale multi-view stereo. In Proceedings of the 2010 IEEE Computer Society Conference on Computer Vision and Pattern Recognition, San Francisco, CA, USA, 13–18 June 2010; pp. 1434–1441.
48. Girardeau-Montaut, D. CloudCompare (version 2.x; GPL software), EDF R&D, Telecom ParisTech. Available online: <http://www.cloudcompare.org/> (accessed on 20 January 2020).
49. Hungr, O.; Leroueil, S.; Picarelli, L. The Varnes classification of landslide types, an update. *Landslides* **2014**, *11*, 167–194. [[CrossRef](#)]
50. Vidal, L.M. Nota acerca de los hundimientos ocurridos en la Cuenca de Tremp (Lérida) en Enero de 1881. In *Boletín de la Comisión del Mapa Geológico de España VIII*; Madrid, Spain, 1881; pp. 113–129.
51. Corominas, J.; Alonso, E. Inestabilidad de laderas en el Pirineo catalán. *Ponen. y Comun.* **1984**. ETSICCP-UPC C.1–C.53.
52. Abellán, A.; Calvet, J.; Vilaplana, J.M.; Blanchard, J. Detection and spatial prediction of rockfalls by means of terrestrial laser scanner monitoring. *Geomorphology* **2010**, *119*, 162–171. [[CrossRef](#)]
53. Royán, M.J.; Abellán, A.; Vilaplana, J.M. Progressive failure leading to the 3 December 2013 rockfall at Puigcercós scarp (Catalonia, Spain). *Landslides* **2015**, *12*, 585–595. [[CrossRef](#)]
54. Tonini, M.; Abellan, A. Rockfall detection from terrestrial LiDAR point clouds: A clustering approach using R. *J. Spat. Inf. Sci.* **2014**, *8*, 95–110. [[CrossRef](#)]



© 2020 by the authors. Licensee MDPI, Basel, Switzerland. This article is an open access article distributed under the terms and conditions of the Creative Commons Attribution (CC BY) license (<http://creativecommons.org/licenses/by/4.0/>).

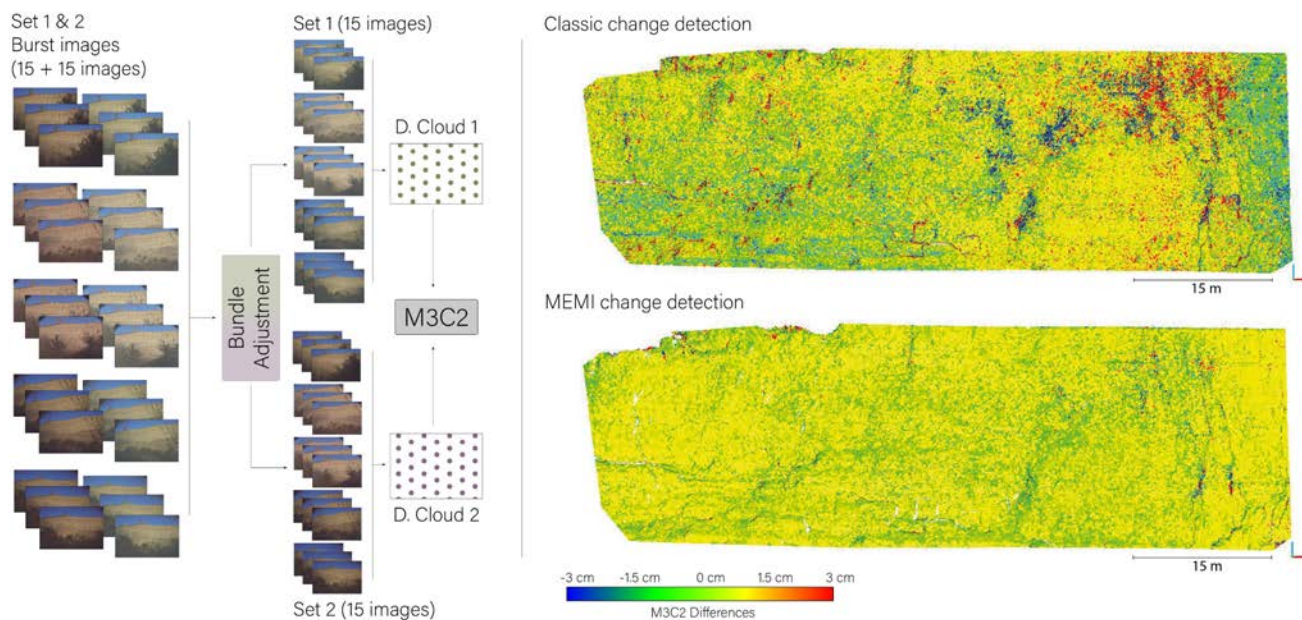
Appendix C

Publication II (Remote Sensing)



GRAPHICAL ABSTRACT

Multi-Epoch and Multi-Imagery (MEMI) Workflow



remote sensing
an Open Access Journal by MDPI

Indexed in:
EI Compendex

CITESCORE
6.6
SCOPUS

IMPACT
FACTOR
4.848

CERTIFICATE OF PUBLICATION

Certificate of publication for the article titled:
Multi-Epoch and Multi-Imagery (MEMI) Photogrammetric Workflow for Enhanced Change
Detection Using Time-Lapse Cameras

Authored by:
Xabier Blanch; Anette Eltner; Marta Guinau; Antonio Abellan

Published in:
Remote Sens. 2021, Volume 13, Issue 8, 1460

MDPI Academic Open Access Publishing
since 1996

Basel, January 2022



Article

Multi-Epoch and Multi-Imagery (MEMI) Photogrammetric Workflow for Enhanced Change Detection Using Time-Lapse Cameras

Xabier Blanch ^{1,*} , Anette Eltner ² , Marta Guinau ¹ and Antonio Abellan ^{3,4}

¹ RISKINAT Research Group, GEOMODELS Research Institute, Faculty of Earth Sciences, Universitat de Barcelona, 08028 Barcelona, Spain; mguinau@ub.edu

² Institute of Photogrammetry and Remote Sensing, Technische Universität Dresden, 01069 Dresden, Germany; anette.eltner@tu-dresden.de

³ Center for Research on the Alpine Environment (CREALP), Sion, CH1950 Valais, Switzerland; antonio.abellan@crealp.vs.ch

⁴ Institute of Applied Geosciences, School of Earth and Environment, University of Leeds, Leeds LS2 9JT, UK

* Correspondence: xabierblanch@ub.edu

Abstract: Photogrammetric models have become a standard tool for the study of surfaces, structures and natural elements. As an alternative to Light Detection and Ranging (LiDAR), photogrammetry allows 3D point clouds to be obtained at a much lower cost. This paper presents an enhanced workflow for image-based 3D reconstruction of high-resolution models designed to work with fixed time-lapse camera systems, based on multi-epoch multi-images (MEMI) to exploit redundancy. This workflow is part of a fully automatic working setup that includes all steps: from capturing the images to obtaining clusters from change detection. The workflow is capable of obtaining photogrammetric models with a higher quality than the classic Structure from Motion (SfM) time-lapse photogrammetry workflow. The MEMI workflow reduced the error up to a factor of 2 when compared to the previous approach, allowing for M3C2 standard deviation of 1.5 cm. In terms of absolute accuracy, using LiDAR data as a reference, our proposed method is 20% more accurate than models obtained with the classic workflow. The automation of the method as well as the improvement of the quality of the 3D reconstructed models enables accurate 4D photogrammetric analysis in near-real time.

Keywords: time-lapse photogrammetry; multi-view stereo; 3D point clouds; change detection; rockslope monitoring; Multi-Epoch and Multi-Imagery (MEMI)



Citation: Blanch, X.; Eltner, A.; Guinau, M.; Abellan, A. Multi-Epoch and Multi-Imagery (MEMI) Photogrammetric Workflow for Enhanced Change Detection Using Time-Lapse Cameras. *Remote Sens.* **2021**, *13*, 1460. <https://doi.org/10.3390/rs13081460>

Academic Editor: Roland Perko

Received: 24 March 2021

Accepted: 7 April 2021

Published: 9 April 2021

Publisher's Note: MDPI stays neutral with regard to jurisdictional claims in published maps and institutional affiliations.



Copyright: © 2021 by the authors. Licensee MDPI, Basel, Switzerland. This article is an open access article distributed under the terms and conditions of the Creative Commons Attribution (CC BY) license (<https://creativecommons.org/licenses/by/4.0/>).

1. Introduction

Structure from Motion (SfM) photogrammetry is a technique used to reconstruct 3D models from unregistered, overlapping image sets. This approach is a low-cost and flexible surveying tool that can be considered as an alternative to techniques such as Light Detection and Ranging (LiDAR) that usually require high-cost equipment.

Due to advances in the processing techniques of digital photogrammetry and computer vision, results comparable to LiDAR can be achieved under specific circumstances, i.e., capturing 3D data with great precision and high quality [1]. The large number of publications in the last five years using point clouds calculated with image-based 3D reconstruction to analyse and monitor objects and surfaces, for example building structures [2–5] or natural surfaces [6–10], confirm the popularisation of the use of this technique [11].

1.1. Basic Principles of SfM Photogrammetric Systems

Basic principles of SfM photogrammetry are widely described in previous publications such as [9,10,12,13]. The principal idea relies on estimating point positions in 3D (object space) from corresponding points on 2D surfaces (image space). The workflow can be performed in different software, both commercial and open source [8]. Some of these suites,

such as Agisoft Metashape, allow for automation of the processing chain using scripts via API. Hence, the usual pre-processing steps used to reconstruct 3D models such as image masking, marker detection or filtering of outlier points can be automated.

Capturing the overlapping images to calculate 3D models can be considered from two data acquisition perspectives, either using a set of stationary cameras pointing at the object of interest or using a single camera moving around the object of interest, i.e., fixed and mobile systems, respectively. Fixed systems compute the 3D model with images always taken from the same position with a unique camera for each. Therefore, the photogrammetric processing is based on limited camera perspectives. This has consequences for the reliability of the image-based 3D reconstruction. Micheletti et al. [14] demonstrated that by providing an adequate spatial distribution of the image network geometry, acceptable accuracies can be achieved even using small image sets. However, they considered one camera for all images, which is not the case for stationary setups. In contrast to capturing the images with a single camera, where only one set of interior parameters have to be estimated (i.e., principle length, principle point, and distortion parameters), each new camera entails considering additional interior camera parameters because the physical properties are different for each camera [15]. Considering these challenges of fixed systems, Kromer et al. [16] were able to achieve detection limits between 2–3 cm, in the ranges required for monitoring prefailure deformation on slopes with only five stationary cameras.

Besides the geometric considerations of the imaging network, using fixed systems entails further difficulties regarding the operation of these systems in an autonomous manner. In this regard, a communication network has to be provided to transmit the data or to check the system status. Furthermore, a sufficient energy supply is required. Despite these constraints, fixed camera stations for SfM photogrammetry are growing in the field of geoscience monitoring and the last year has seen publications on a fixed rockfall monitoring system developed with low-cost cameras published by Blanch et al. [13], an array of cameras used to study rock slope hazards on a road published by Kromer et al. [16] and an autonomous terrestrial stereo-pair photogrammetric monitoring system developed to observe rockfalls in mining environments published by Giacomini et al. [17].

Mobile systems such as UAVs bring greater flexibility. Large sets of photographs can be acquired from a single camera, allowing for a larger number of observations from several perspectives for the bundle block adjustment. This increase in input data allows for more reliable photogrammetric models. Verma and Bourke [18], for example, used more than 50 photographs at close range (<2 m) to obtain sub-millimetre-resolution models of rock faces using calibrated error evaluation chart. In addition, the ability to extend the mobile system by mounting a camera onto an Unmanned Aerial Vehicle (UAV) allows areas and perspectives to be reached that are difficult to reach on foot [19]. Commercial ready-to-fly solutions have led to an increase in the use of aerial photogrammetry in recent years [8,20–24]. On the contrary, the inability to take pictures both from the same exact position (as in a fixed system) and at a high temporal frequency makes it difficult to use algorithms and workflows based on the redundant use of image bursts created to obtain higher quality models [13] as we will see in this paper, although experience with multi-epoch imagery workflows such as [1,25] demonstrates a certain capacity for improvement with mobile systems.

SfM photogrammetry is considered a low-cost approach compared to other methods of terrain observation [9]. However, the cost of photogrammetric systems varies widely depending on their configuration. Mid to High-cost systems (>1.000 EUR) are composed of commercial solutions using cameras and devices with large sensors of high resolution. These cameras, usually DSLR or mirrorless full frame cameras (43 mm sensor diagonal), can obtain images of more than 24 mega pixels. They have high sensitivity photoreceptors, produce very little digital noise and hence possess exceptional image quality with a high capacity to extract information from dark and bright areas due to the high dynamic range of these images. Furthermore, these cameras can use high-quality fixed lenses that enable the capture of images with very little distortion and great sharpness, which is advantageous

for obtaining high quality models [8]. There have been several studies implementing photogrammetric systems with commercial, high-quality cameras [16,26–28]. However, one limitation of these kinds of devices in fixed camera systems is their cost and the large amount of data that needs to be transferred remotely, as the size of each image can reach more than 30 MB.

Other than that, low-cost photogrammetric solutions involve the use of very simple photographic systems (less than a hundred euros). These systems are based on uncoupled camera modules controlled by single-board computers, such as Raspberry Pi [29], or microcontrollers, such as Arduino (open-source) systems. These cameras are associated with photographic sensor diagonals of less than 16 mm with resolutions that vary between 5 and 12 mega pixels. To reduce costs, they are equipped with low-quality plastic lenses that usually result in strong distortions. The quality of the images obtained with these cameras, revealing low sharpness and high digital noise, are the main constraint for their application in 3D measurement tasks [13]. However, low-cost solutions are easy to implement and simple to program. In addition, these systems are ideal for installation at sites exposed to destructive phenomena such as flash floods or mass movements. Various examples of low-cost photogrammetry implementations can be found in the field of geosciences [13,30–32].

1.2. Improvements of SfM Photogrammetric Workflows

Strategies to obtain improved SfM photogrammetric models are required, especially in scenarios that entail the use of fixed and low-cost camera systems. These improvements can be implemented at different stages of the SfM photogrammetric workflow. Regarding the data collection stage, studies have been carried out to investigate the impact of using High Dynamic Range (HDR) images instead of conventional photographs to reconstruct 3D models in the fields of cultural heritage documentation [33] and geomorphic change detection [34]. Other studies have examined the use of high-resolution photographs (gigapixel) [35,36]. Furthermore, attempts have been made to enhance SfM photogrammetric models by stacking images in order to reduce the noise from digital cameras [31], although with inconclusive results.

Several studies have focused on improving the SfM photogrammetric results by pre-processing of the input data, such as enhancing the image quality [37] as well as pre-defining calibration parameters and adjusting the imaging network configuration. For instance, James and Robson [38] mitigated systematic errors common for UAV models [8] by obtaining additional convergent images to enhance the strength of the image network geometry [39]. Furthermore, it is important to retrieve suitable lens calibration parameters [39], which is especially the case for consumer grade cameras that usually exhibit stronger distortions. More recently, Elias et al. [40] carried out a study to estimate the effect of temperature changes on low-cost camera sensors, highlighting the importance of also considering the temporal stability of cameras, especially during long-term observations.

Another focus has been on improvement of the SfM workflow itself to obtain 3D models with the highest possible quality, allowing for multi-epoch imagery change detection. The differences between these methods depend both on the characteristics of the object to be studied and on the possibility of automating processes and locating ground control points. Verna and Bourke [18] presented a method that is capable of obtaining sub-millimetre accurate small-scale digital elevation models at close range. Another setup developed by Kromer et al. [16] enabled the detection of rockfalls automatically from time-lapse imagery. Eltner et al. [41] introduced a time-lapse SfM photogrammetry workflow that enabled the almost continuous detection of soil surface changes with millimetre accuracy. The methodology proposed by Feurer and Vinater [25] improves SfM photogrammetry-derived 3D models by joining imagery from different points in time during image matching and 3D reconstruction. This has the advantage that systematic errors might be spatially consistent over time and therefore negligible during change detection. This methodology was put into practice by Cook and Dietze [1].

Finally, methodological proposals have been made to improve the results, regardless of the pre-processing and workflow used. For instance, the PCStacking (i.e., point cloud stacking) algorithm developed by Blanch et al. [13] improves the 3D models using subsequent photogrammetric reconstruction solutions for images shot over a short time interval. Another recently developed strategy to enable more reliable change detection involves the introduction of precision maps by James et al. [42]. Together with the M3C2 tool from Lague et al. [43], the strategy allows change detection results to be obtained with information about the significance of the measured change.

The research presented in this paper proposes a new automatic pipeline to obtain improved 3D models using fixed time-lapse cameras. The methodology is based on a fully automatic workflow of the whole data acquisition and processing routine, from capturing images remotely with various cameras to performing change detection. This study proposes a new method that allows the calculation of photogrammetric models with high spatial frequency, high temporal resolution and high accuracy, therefore achieving higher quality in automatic change detection.

2. Materials and Methods

2.1. Pilot Study Area

The system was developed on the Puigcercós cliff (Catalonia, NE Spain) (Figure 1a), which is part of the Orígens UNESCO Global Geopark. The rock face (123 m long and 27 m high) is the result of a large rototranslational landslide [44] that occurred at the end of the 19th century [45,46]. The structure of the zone (Figure 1b), its high rockfall activity and low risk (due to lack of exposed elements) have made it an ideal area to develop methodologies such as the detection and spatial prediction of rockfalls by means of Terrestrial Laser Scanner (TLS) [47], the clustering approach workflow for rockfall detection [48], the spatio-temporal analysis of rockfalls pre-failure deformation [49,50] and the enhanced workflow PCStacking described by Blanch et al. [13]. In addition to studies related to rockfall monitoring, the site is an ideal natural laboratory for developing new observational techniques in the field of geosciences [51] such as the estimation of mass movements based on seismic observation [52] and the use of GPS data to study the fractures and slope stability [53].

2.2. Equipment

Images for the image-based reconstruction of high-resolution point clouds were taken by a photogrammetric system developed ad hoc for the Puigcercós pilot study area. The system consists of five camera modules, a data transmission module (Figure 2) and a workstation. Images were taken by the camera modules fixed at five locations in close proximity to each other (Figure 1c) on small elevations on one of the transverse ridges created by the ancient landslide. The average distance between the camera modules is 30 m and the distance to the main rock face of the cliff is around 100 m. The maximum distance between the transmission module and the camera modules is about 130 m. Each camera module consists of a high-performance commercial camera with a fixed lens, a microcomputer with RTC (Real Time Clock), an external WiFi antenna, a battery and a solar panel. These modules were mounted in dustproof and waterproof metal enclosures (Figure 2).

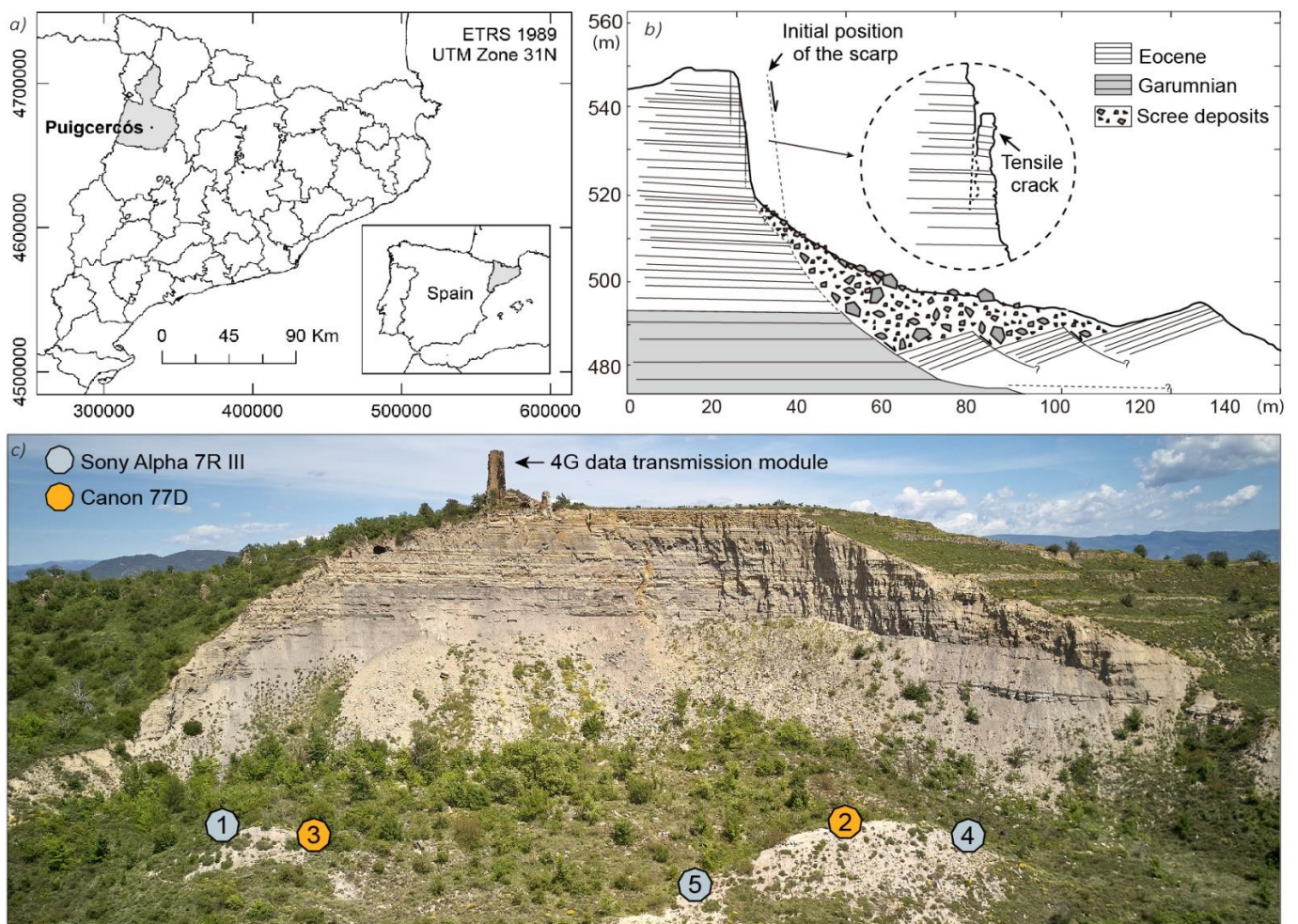


Figure 1. (a) Puigcercós location in Pallars Jussà region, Catalonia, NE Spain. (b) Geomorphological scheme of the Puigcercós cliff and main rockfall mechanism (modified from Royán et al. [49]). (c) Distribution of the camera modules in front of the Puigcercós cliff.

Three of the five modules use a full-frame (35.9×24 mm) mirrorless Sony Alpha 7R III with a resolution of 42.4 MPx (pixel pitch of $4.51 \mu\text{m}$). These cameras are equipped with a 35 mm f/2.8 lens. The other two systems use a DSLR camera Canon 77D with a cropped sensor APS-C (22.3×14.9 mm) and with a resolution of 24.2 MPx (pixel pitch of $3.72 \mu\text{m}$). The Canon cameras are equipped with a pancake 24 mm f/2.8 lens. The use of a 24 mm lens on an APS-C cropped sensor generates the same field of view as using a 35 mm full frame lens. Sony and Canon modules are alternatively positioned in the study area (Figure 1c). The theoretical depth error for this camera setup, assuming a stereo-classic case and error free camera parameter estimations, amounts to 2.3 cm [9]. However, higher accuracies can be expected because five instead of two cameras capture the same area of interest with slightly convergent perspectives.

The microcomputer used is a Raspberry Pi 3 Model B+ [29] from Raspberry Pi Foundation. It is in charge of scheduling data acquisition, capturing the images, transmitting the data and managing the battery of the devices. A commercial board Witty Pi 2 from UUGear is used as a real-time clock and power management system for Raspberry Pi 3, and to manage voltage differences and schedule the system. Finally, a solar panel (20 W) and an AGM battery (7000 mAh) make each module autonomous in terms of power (Figure 1b).

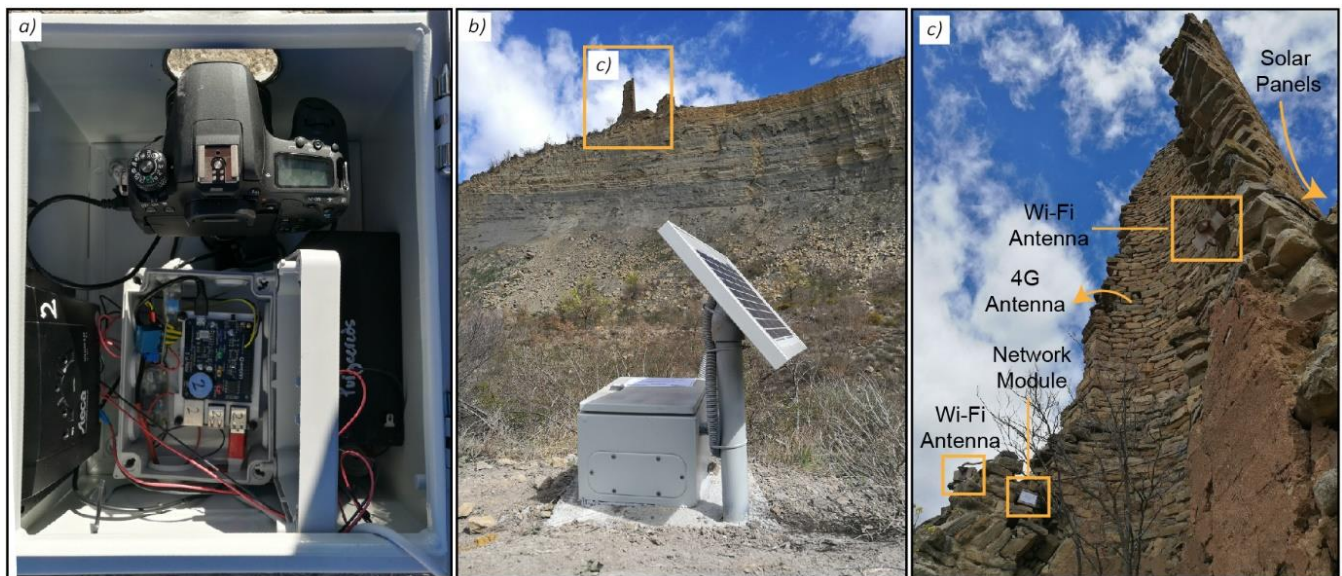


Figure 2. Components of the photogrammetric system mounted at Puigcercós. (a) Internal view of the camera module composed of a Canon 77D camera and the auxiliary control system. (b) External view of a camera module in front of the Puigcercós cliff. (c) Installation site of the 4G data transmission module on the upper part of the rock cliff. The two sectorial Wi-Fi antennas, the router module and the battery can be seen in the tower.

A 4G transmission module is based on a 50 dB 4G unidirectional antenna, a Teltonika RUT950 router and two 10 dB WIFI sectorial antennas (Figure 1c) that project the network from the top of the cliff to the area where the camera modules are installed (see Section 2.2). Again, a solar panel and an AGM battery supply power to these devices.

The last part of the photogrammetric system is the workstation/server. This computer is in charge of performing server functions by receiving and storing the images. Furthermore, the workstation performs the entire workflow fully automatically to eventually obtain the high-resolution photogrammetric models and their change detection map. The workstation in this study consisted of commercial components of a medium–high range with an Intel(R) Core(TM) i9-7900X processor of up to 4.30 GHz, with 64 GB of RAM and a NVIDIA GeForce GTX 1080 Ti graphics card.

2.3. Data Acquisition

Images were obtained at a sub-daily frequency for 4D analysis of the rockfalls. The camera modules captured four images in a burst mode three times per day. Thus, three times four images were taken from five camera modules, resulting in 60 images of the Puigcercós cliff every 24 hours. The images were taken at 9 a.m., 1 p.m. and 6 p.m., although the most-used images were taken at 6 p.m. to avoid shadows on the escarpment. All images are obtained in JPG format using the highest possible quality. The focus point is set manually, and the exposure time is automatically calculated according to the aperture, set at $f/11$ to obtain an acceptable depth of field. The configuration of the photogrammetric system can be easily modified to increase the acquisition of images on a more exhaustive daily basis. The scripts of the photogrammetric system that allow for scheduling, capturing and sending the images remotely to the server were developed using the open-source Python programming language (version 3.7) [54]. The images were transmitted daily to the workstation where, after server storage, the automatic photogrammetric processing of the images was activated to obtain the 3D models to carry out change detection, also automatically.

LiDAR data was acquired as the reference dataset. The data was obtained with the ILRIS-3D-Optech TLS (Terrestrial Laser Scanner). This high precision device allows the generation of a point cloud (2.500 points/s) with the 3-D coordinates (X, Y, Z) of each point

with an accuracy of 7 mm when scanning at a distance of 100 m, according to the manufacturer's specifications. The standard deviation of the instrumental and methodological error was defined as 1.68 cm at an average distance of 150 m by Abellan et al. [47] and derived from this parameter, the change detection threshold for the scanning distance of the Puigcercós cliff was defined as 3.0 cm by Royan et al. [49] The TLS data was captured in October 2019.

2.4. From 2D to 4D—Workflow for Automatic Change Detection with Time-Lapse Imagery

To highlight the improvements made in this study, the methodology is divided into three sections: (1) Workflow part I, which refers to the tools developed for automatic pre-processing of data; (2) Workflow part II, which focuses on the improved photogrammetric workflow to acquire time-lapse 3D data, called multi-epoch multi-imagery (MEMI); and (3) Workflow part III, which introduces an automated change detection approach demonstrated at Puigcercós (Figure 3). These three steps are part of a whole working pipeline that allows change detection models to be obtained automatically from the different images, as described below.

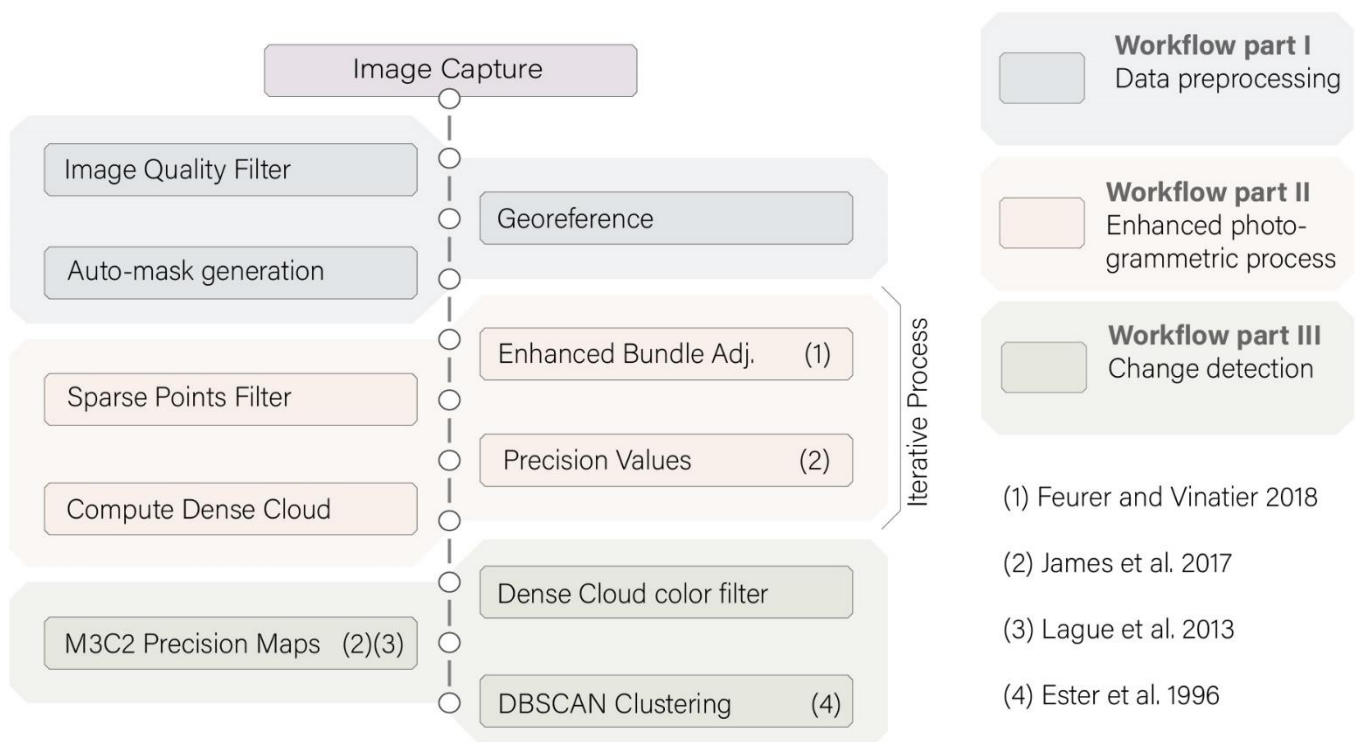


Figure 3. 4D pipeline designed for the automatic analysis of rockfalls in Puigcercós. The colours represent different parts of the process grouped according to their description in the manuscript.

2.4.1. Data Pre-Processing (Workflow Part I)

Data pre-processing is essential because images were not captured under controlled environmental conditions. Image quality and data acquisition geometry change due to lack of maintenance, excess humidity, presence of fog, changing lighting conditions, vegetation growth, temperature changes and small variations in camera positions because of impacts, animals or metal dilations during the long-term observation period. Data pre-processing is particularly important because the success of the following stages strongly depends on the quality of the input data.

Several tools have been developed to perform data editing steps that users usually need to do when preparing data for photogrammetric processing. These steps utilize

techniques from computer vision and image analysis to enable geometric georeferenced models of maximum quality. The developed tools comprise:

- (a) **Image Quality Filter.** The cliff is located in a mountainous area where fog, snow and heavy rainfall are frequent, making the use of quality filters mandatory. Images are filtered based on an image quality estimation made with the Open CV library [55]. The applied function is a Laplacian variation [56,57]. If images are not sharp enough due to unfavourable environmental conditions, the time-lapse photogrammetry processing workflow is stopped at this step.
- (b) **Georeference.** This tool allows one to determine if the cameras have changed their position, based on a reference image [58]. Although the camera systems are fixed to the ground, camera movements are possible, e.g., due to temperature changes, wind or animals. Also, changes in the interior camera geometry are likely due to heating and cooling of the housing [40,59]. In this study we used the Lucas–Kanade method [60,61], also implemented in OpenCV, which has been shown to be suitable for tracking targets in geoscience applications [62]. It is used to track control points, assigned in a reference image, in the target image. To ensure good georeferencing Ground Control Points (GCPs) are located in the images, thus providing their 2D coordinates, their corresponding 3D coordinates are assigned in object space. In this study, the real-world coordinates of GCPs were extracted from a TLS point cloud of the escarpment and were assigned manually by correlating TLS points with image pixels. The precision of this approach of GCP retrieval is discussed in Section 4.3.
- (c) **Auto-mask generation.** During the image-based 3D reconstruction steps a mask was applied to calculate a dense, high-resolution, large data volume point cloud only for the area of interest. Thus, the images are masked to the area of interest in their field of view. Due to changes in the camera geometry these masks need to be updated. The tracked GCPs allow calculation of the parameters of a perspective transformation to warp the binary masks from the reference images to the targeted images according to their movements.

2.4.2. Enhanced Photogrammetric Process (Workflow Part II)

The second part of the presented workflow is an advancement of the photogrammetric workflow described in Feurer and Vinatier [25] and Cook and Dietze [1]. In these studies, it was referred to as the time-SIFT or multi-epoch imagery workflow. We will use the acronym MESI (Multi-Epoch Single-Imagery) to refer to this workflow. Furthermore, an enhanced workflow was introduced that exploits the redundancy of images due to bursts of captured images from the fixed time-lapse camera setup for the multi-temporal analysis (Figure 4), and this is referred to as Multi-Epoch Multi-Imagery (MEMI).

In the classic time-lapse SfM photogrammetry workflow two separate bundle adjustments are performed to reconstruct the image geometry and the sparse point cloud, which refers to the 3D coordinates of the tie points [41]. Each bundle adjustment is done with the individual photos of the single epochs, i.e., individually for set 1 and set 2 (Figure 4a). In each set there is only one image from each camera. Eventually, the dense point clouds are obtained after each bundle adjustment. These point clouds are geo-referenced in a local, scaled coordinate system via GCPs extracted from the LiDAR scan. However, due to errors, e.g., during their tracking in the images, alignment errors between the point clouds are possible, which is partly compensated for by ICP-type (Iterative Closest Point) algorithms [63].

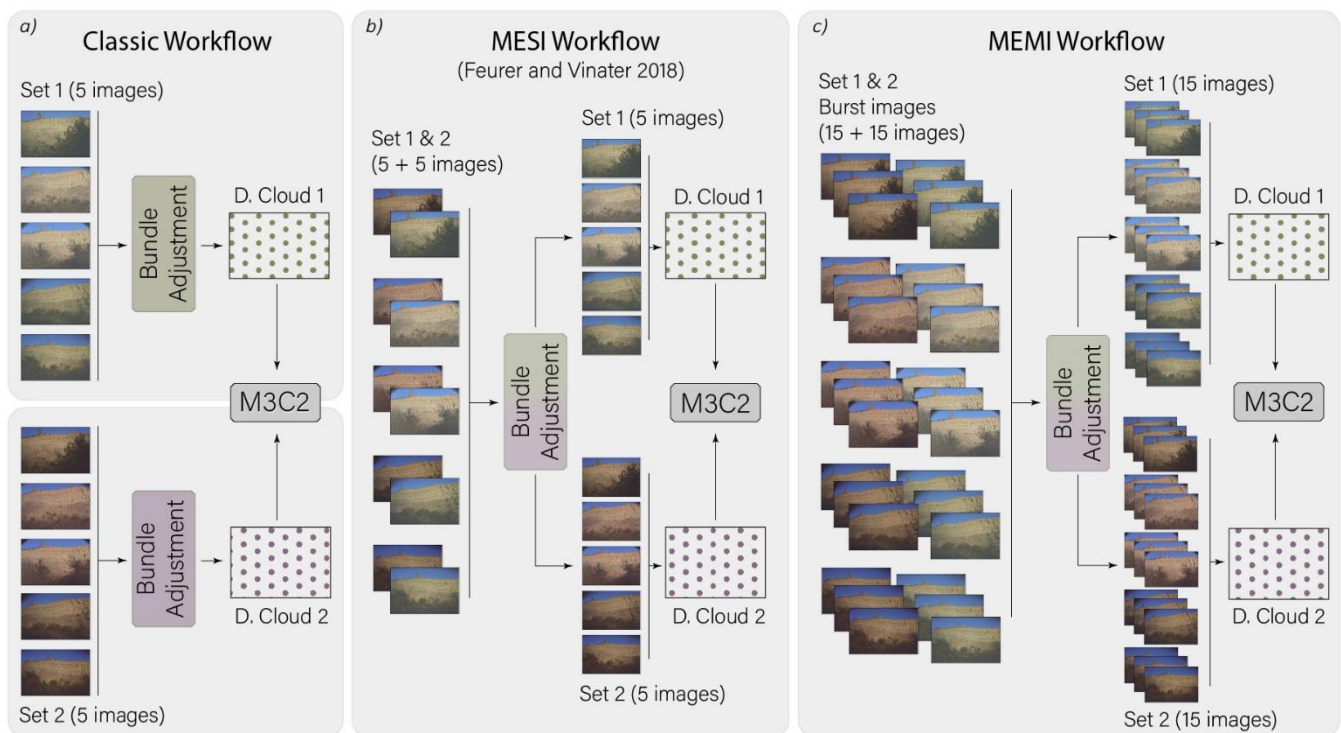


Figure 4. Three different SfM photogrammetry workflows to calculate multi-temporal point clouds for change detection. The colour shading denotes images obtained at different time epochs. (a) The classic workflow corresponds to the standard SfM photogrammetric approach. (b) The multi-epoch imagery workflow (MESI) adopts the method defined by Feurer and Vinatier [25], i.e., joining images from multi-epochs during image matching and bundle adjustment. (c) The Multi-Epoch Multi-Imagery (MEMI) workflow considers (additionally to b) redundant image bursts from each epoch.

For the MESI workflow the method described in Feurer and Vinatier [25] and Cook and Dietze [1] is implemented, performing image matching using data from different time epochs. The time-SIFT approach is described as “joining multi-epoch images in a single block” [25]. The result of the bundle adjustment using MESI is a sparse point cloud that contains tie points matched across overlapping frames from different points in time (Figure 4b). Only one bundle adjustment is performed to calculate sparse 3D point clouds, merging image Set 1 and Set 2. Consequently, spatially correlated systematic errors typical for SfM photogrammetry [42] are assumed to display similar magnitudes across the epochs and therefore are mitigated during change detection after differencing of point clouds. The bundle adjustment with merged multi-epoch single images also has the advantage that the observation number increases strongly (several thousand more image points) while only a few additional unknowns (14 for each camera, i.e., exterior and interior camera orientation parameters) are introduced, increasing the reliability of the estimated parameters. After estimating the camera parameters, the images are separated again into the original sets to calculate the two dense point clouds using only images from the same epoch. The computed dense models do not require further alignment because they were already aligned in the same coordinate system during the bundle adjustment, considering the across-epoch tie points.

Besides the multi-epoch merging of images during 3D reconstruction, the improvements due to capturing bursts of photographs during one point in time shown in Blanch et al. [13] were also implemented in this study. Thus, image bursts from each epoch and multi epoch imagery were combined. The dense point clouds were computed in the automatic multi-epoch multi-imagery (MEMI) workflow using more than one image per camera location (Figure 4c). Therefore, each dense point cloud was created using 15 images (per epoch) instead of five as in the classic and MESI workflow. This resulted in two dense point clouds, but for the MEMI approach each one was calculated with the

burst of images taken during different epochs. Again, the clouds share the geo-reference and spatially correlated errors (calculated from all 30 images in the bundle adjustment). This enables good alignment to enhance the detection of changes between models. However, this approach only works if stable areas are large enough within the field of view of the cameras. This workflow was implemented using Agisoft Metashape Pro (version 1.6.6) [64] software and was automated using the available Python API (version 1.6.4) [65]. In line with previous work [16], a further processing step was integrated into the automatic workflow. To improve the accuracy of the 3D reconstruction a filter, based on a reprojection error and reconstruction uncertainty, was applied to the sparse point cloud after the bundle adjustment (Figure 3) to reduce outliers.

The last step of the automatic photogrammetric process involved a workflow introduced by James et al. [42] (Figure 3) to export sparse point coordinate precision estimates from Metashape [42]. Given the sensitivity of the precision parameters an iterative bundle adjustment was performed until the precision values of the control points and the tie points stabilized. The sparse point precision was used to calculate 3-D precision maps [42]. These precision maps improve the level of detection (LoD) estimation because instead of considering a uniform value for the entire point cloud, a LoD is calculated considering the spatially correlated errors from the 3D reconstruction [42].

2.4.3. Change Detection (Workflow Part III)

The final step of the introduced 4D pipeline, after reconstructing multi-temporal 3D models of high quality, is automatic change detection. First, a colour filter was applied to the dense point cloud to remove shadowed areas because in this study the shaded areas were not correctly calculated and therefore led to errors in the detection of changes [65].

Afterwards, the M3C2 algorithm [43], integrated into the software CloudCompare (version 2.11) [66], was used to calculate the model differences between different epochs considering the precision maps option [42]. The point cloud difference calculation resulted in a new point cloud with an additional scalar containing the metric distances between the compared dense clouds. Thereby, the DBSCAN algorithm [67] was used to automatically extract clusters of points that had difference values above a threshold and a minimum number of neighbours within a certain distance. The use of this methodology for LiDAR point clouds is explained in detail in Tonini and Abellan [48]. As a result of the application of the clustering algorithm, a new point cloud was generated that only contained points that match the characteristics required to be part of a change cluster.

The introduced automated enhanced workflow for change detection from photogrammetric models ends at this point. The provision of the source-code enables the workflow to be implemented and adapted according to the individual applications and their specific analytical requirements.

Due to automation, the 4D pipeline presented in this study obtains multi-temporal 3D point clouds from the automatically captured input data with all the changes identified ready for further analysis.

2.5. Performance Assessment

To assess the performance of the three different approaches, the classic approach, MESI and MEMI were compared for a period when no changes occurred. Three tests were designed to assess the relative accuracy of change detection, to evaluate the interior point cloud precision and to determine the absolute point cloud accuracies by comparing the point clouds to each other and to an independent LiDAR reference.

2.5.1. Relative Accuracy of Detected Changes

The three workflows described in Figure 4 were performed with the same input data to observe potential differences between the resulting change detection models, and to assess the accuracy of change detection, without considering absolute errors of change. To enable

the evaluation of absolute accuracies of change detection independent TLS measurements from the same time period would be needed [1].

In order to analyse the relative accuracy, two different tests were performed. The input data for each test consists of a burst of images captured by each of the five camera modules on two consecutive days. Due to the use of images from contiguous dates, with no obvious changes in the area of interest, it is possible to assess the performance of the multi-temporal change detection because no changes should be visible in the final change map. For the first test, the images considered were taken on 8 and 13 November 2019. Due to the setup configuration at that time, bursts of three images were captured by each of the five camera modules. The second test was performed using images captured on the 23rd and 24th of May 2020. As a result of a system improvement, the second test benefitted from a higher burst, with four images captured by each of the five camera modules.

To assess in more detail the improvement in change detection due to the increased number of images from each burst, an additional evaluation was performed, using the MEMI workflow, but with a burst of two images instead of a burst of four. The MEMI workflow using only two images is referred to as the mild MEMI workflow (Figure 5a), whereas the enhanced workflow that implements all (i.e., four) images is referred to as the full MEMI workflow (Figure 5b).

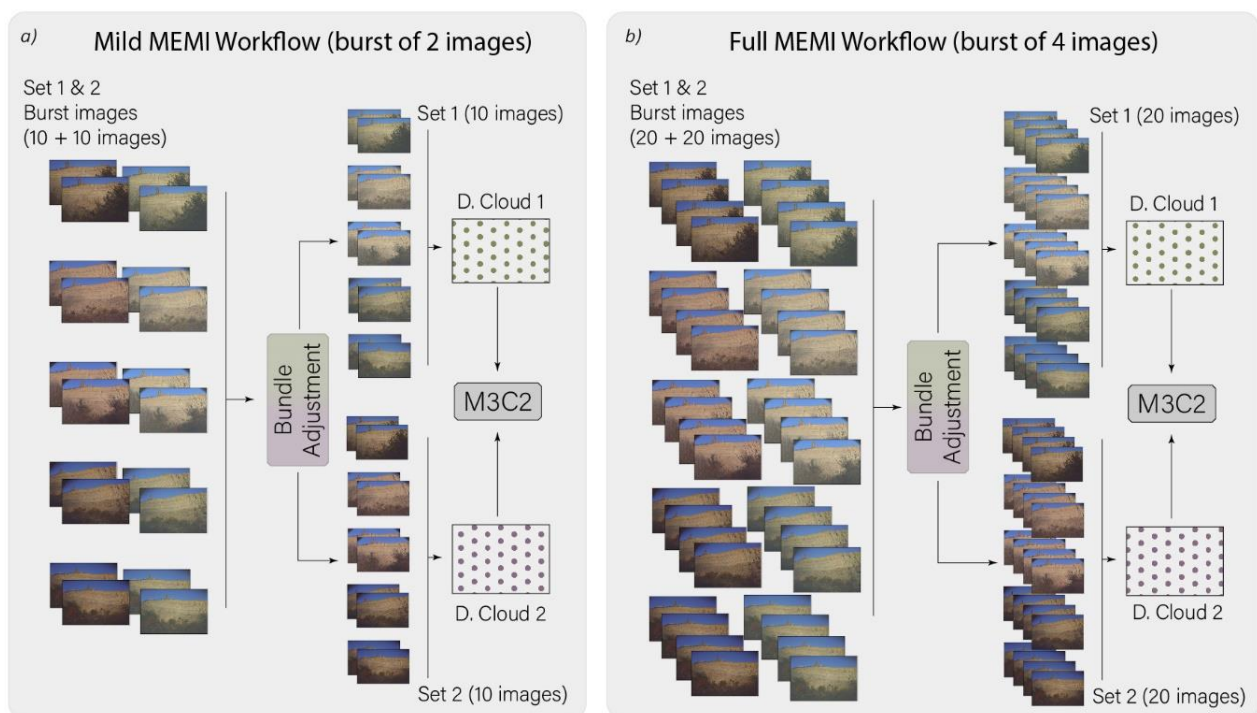


Figure 5. (a) Mild MEMI workflow created for the change detection evaluation. (b) Full MEMI workflow created using all images available.

Comparison of the resulting 3D point cloud differences from the three workflows was carried out using the M3C2 from Lague et al. [43], implemented in the CloudCompare software. All comparisons (classic, MESI, mild MEMI and full MEMI) were performed using the same software configurations and images taken from the same modules at the same time but introducing more images from each burst the more complex the workflow. No filter was applied nor were any of the sparse point clouds considered differently. Although we used the same GCPs to geo-reference the images in all workflows, the point clouds obtained in the classic workflow needed to be aligned using the ICP algorithm [63] because set 1 and set 2 did not share exactly the same camera orientation due to the separate bundle adjustments.

2.5.2. Interior Precision of the Point Clouds

As well as considering the relative accuracy of change detection [1], we also assessed the interior precision of the retrieved 3D point clouds [1] with a test using the precision estimation algorithms described in James et al. [42]. The approach (Figure 6) allowed us to quantify the performance of the time-lapse SfM methods in a different way than the change detection test, presenting the spatial distribution of errors in terms of precision in centimetres and using a LiDAR TLS to retrieve ground control. For this test we used the images corresponding to November 8 and 13 because they were the most similar to the LiDAR TLS scan performed on October 2019. In 2019 the photogrammetric systems were not optimized to obtain bursts of four images, so the results presented were obtained using only bursts of three images, and with no separation into mild and full MEMI. Following the approach proposed by James et al. [42], the precision estimation values ($\sigma_x \sigma_y \sigma_z$) were estimated for each point of the sparse cloud. With a simple interpolation process, the precision estimation values ($\sigma_x \sigma_y \sigma_z$) were transferred from the sparse cloud points to the dense cloud points.

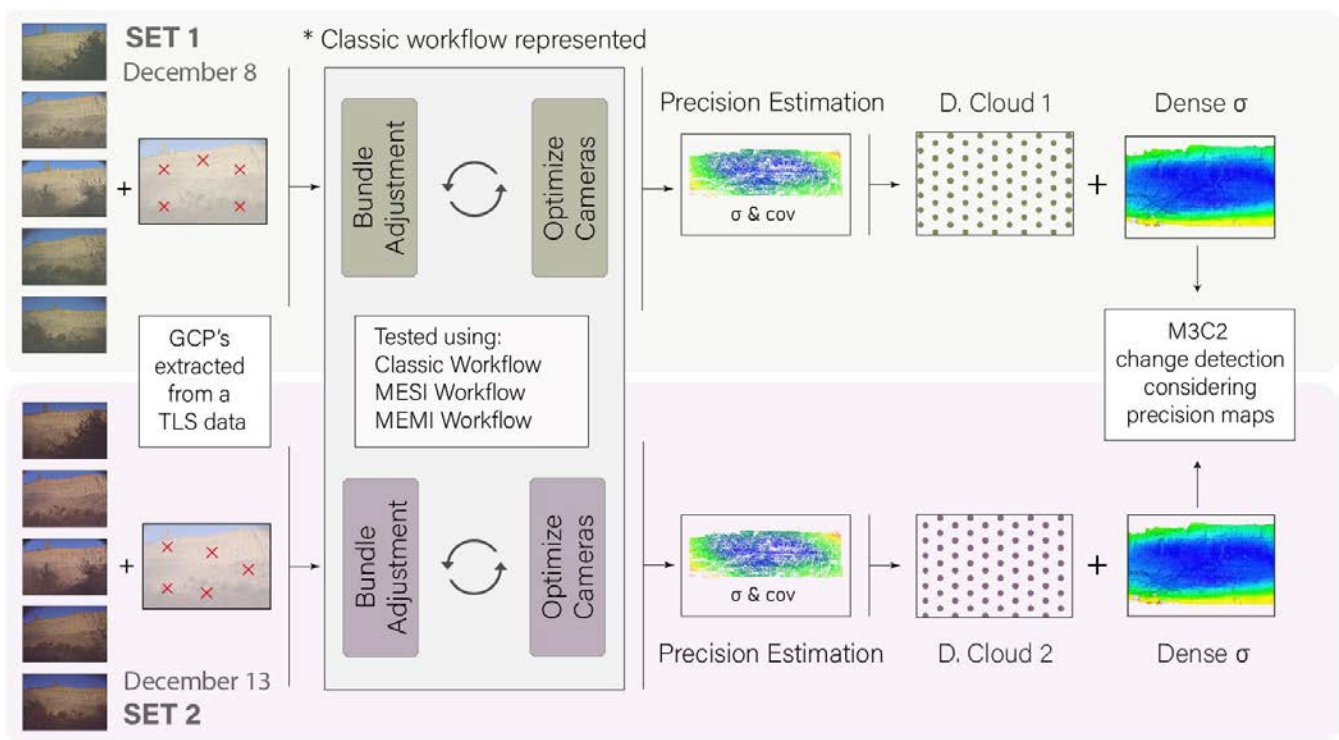


Figure 6. Precision estimation to only detect significant changes. The 4D pipeline illustrated here comprises the classic workflow. The MESI and the MEMI workflow were also evaluated.

2.5.3. Absolute Accuracy of a Single Point Cloud

In order to determine the performance of the time-lapse SfM algorithms in terms of absolute accuracy, the final performance assessment consisted of comparing the photogrammetric models to LiDAR data. It was assumed that the LiDAR data represent a reference geometry, so the smaller the differences between the LiDAR and the photogrammetric models, the higher the absolute accuracy of them.

Due to the interval between the captured LiDAR data (October 2019) and the first captured photogrammetric data (November 2019), and the high number of rockfalls affecting the cliff, the period between datasets included several changes. In order to avoid eliminating the errors and smoothing of the results, the detected rockfalls were not eliminated for

the absolute accuracy test. Therefore, this assessment does not represent a non-deformation scenario between the LiDAR data and the photogrammetric models.

3. Results

3.1. Relative Accuracy of Detected Changes

The differences between the two models of two consecutive days resulting from the MEMI workflow tended mostly to zero (Figures 7 and 8), whereas the classic and MESI workflow revealed higher deviations, with the largest values measured with the former approach.

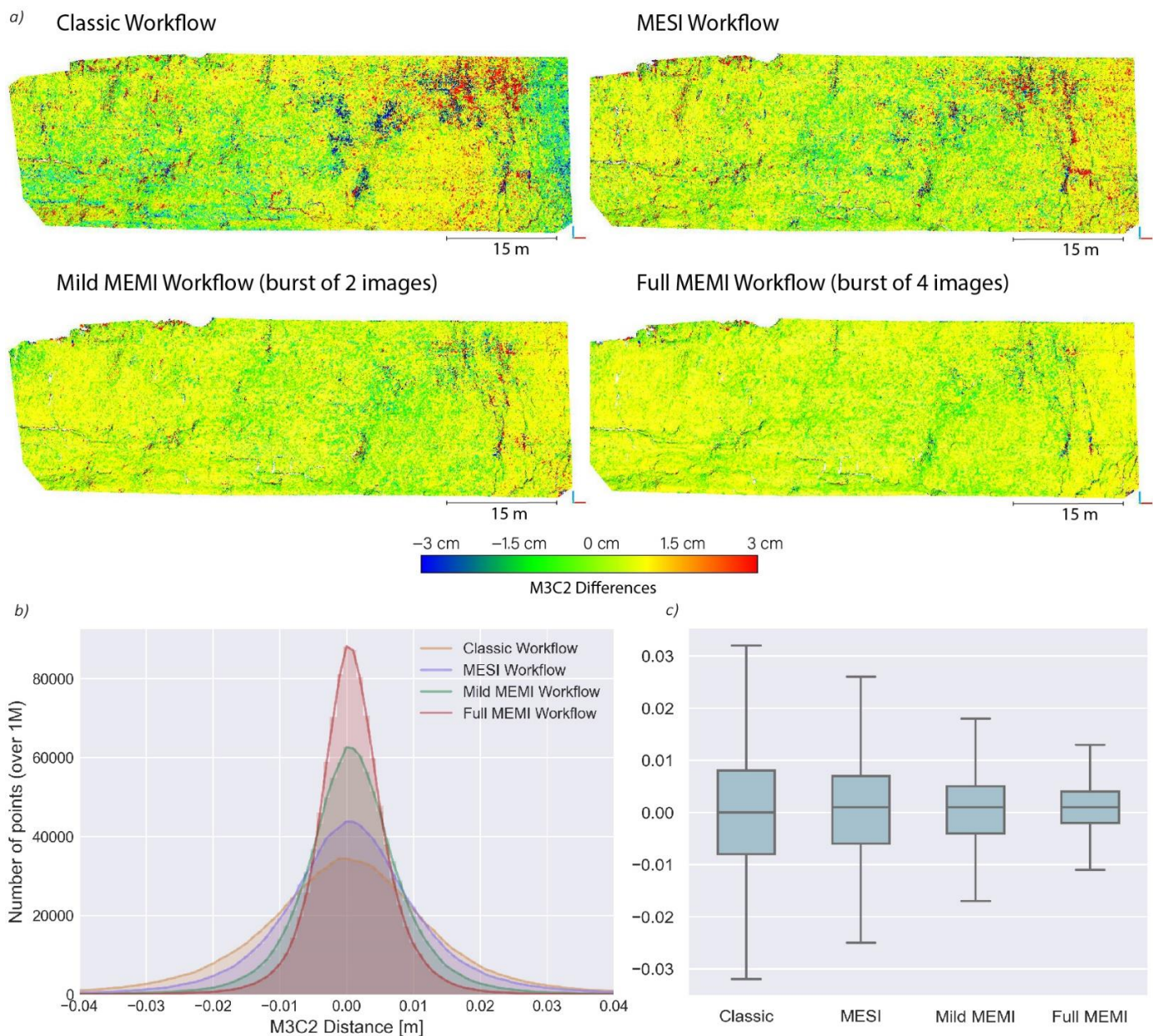


Figure 7. (a) Graphic representation of the differences between the models of 23 and 24 May, according to the workflow used. The four models are represented using the same colour scale. (b) Histogram with the M3C2 results. (c) Error bar plot with the dispersion of the values obtained in each comparison.

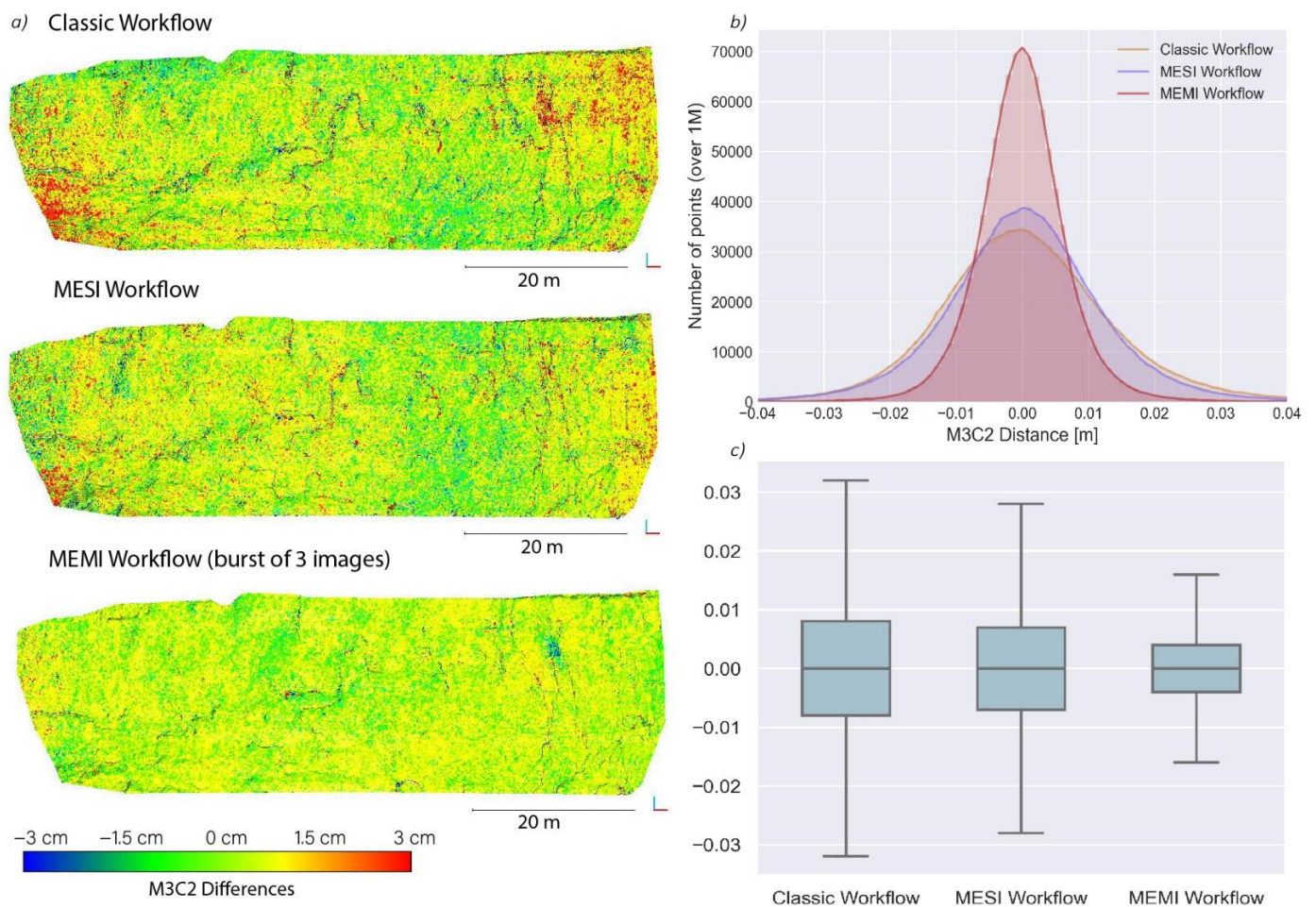


Figure 8. (a) Graphic representation of the differences between the models of November 8 and 13, according to the workflow used. The three models are represented with the same colour scale. (b) Histogram with the M3C2 results. (c) Error bar plot with the dispersion of the values obtained in each comparison.

This can be observed in the maps of differences (Figure 7a) and in the histograms (Figure 7b) obtained using the May 2020 images. The smallest differences between the two compared days were achieved with the MEMI workflow using four images (full MEMI workflow). The standard deviation of the M3C2 differences decreased by 50%, from 3.37 cm in the classic workflow to 1.68 cm in the full MEMI workflow. The boxplots (Figure 7c) also highlight the increase in performance from classic to full MEMI, showing that both the average difference and the range of differences decreased.

The computational cost of each workflow as well as the main characteristics of the obtained models are described in Table 1.

Figure 8 also shows the M3C2 distance maps for the three different workflows (classic, MESI, MEMI), using the images captured in November 2019 to assess the relative accuracy of the point clouds (Figure 8a). The measured change detection with the MEMI workflow showed the lowest range of differences with respect to the other methods (Figure 8a). In addition, the histograms (Figure 8b) show a considerable reduction in the standard deviation of the differences (nearly 50%) when using MEMI, decreasing from 2.83 cm with the classic workflow to 1.54 cm with the MEMI workflow (Table 2).

Table 1. Main parameters of the point clouds and M3C2 results obtained in May 2020 test.

	Classic Workflow	MESI Workflow	Mild MEMI Workflow	Full MEMI Workflow
Tie points	55,106	67,950	177,451	217,619
Matching time	20 s	1 min 6 s	3 min 30 s	8 min 53 s
Matching memory	4.85 GB	4.90 GB	5.18 GB	5.07 GB
Alignment time	4 s	27 s	2 min 41 s	6 min 2 s
Dense Point Cloud (points)	11,432,934	11,336,012	10,453,432	11,101,038
Depth map time	23 s	31 s	1 min 30 s	4 min 32 s
Dense Cloud time	35 s	36 s	59 s	1 min 51 s
Mean M3C2 distance (mm)	−0.55	1.01	1.03	0.78
St. Dev M3C2 (cm)	3.37	3.00	2.22	1.68

Table 2. Main parameters of the point clouds and M3C2 results obtained in November 2019 test.

	Classic Workflow	MESI Workflow	MEMI Workflow
Tie points	39,953	89,681	204,939
Matching time	18 s	1 min 3 s	8 min 36 s
Matching memory	4.86 GB	4.87 GB	5.13 GB
Alignment time	4 s	31 s	5 min 56 s
Dense Point Cloud (points)	11,263,507	11,242,875	10,961,212
Depth map time	36 s	431 s	5 min 52 s
Dense Cloud time	39 s	39 s	1 min 55 s
Mean M3C2 distance (mm)	0.87	0.47	0.09
St. Dev M3C2 (cm)	2.83	2.45	1.54

3.2. Interior Precision of the Point Clouds

Figure 9 show the results obtained from the precision estimation test using the November 2019 images. Figure 9a shows the distribution of σ_y , which is the most important parameter for change detection in this study as it is the direction of highest deformation (depth direction). The results of the MEMI workflow show that precisions between 0 and 3 cm were concentrated in the central zone of the area of interest. Thus, this zone demonstrated the best photogrammetric reconstruction performance.

With increasing distance from the central region (of highest image overlap) the precisions decreased in a spatial, radial-symmetric pattern. Similar patterns, but with higher magnitudes of precision, were identified in the MESI workflow. Such high values of σ_y were not obtained in the classic workflow, as shown in the error boxplots (Figure 9b). In general, the estimated precision of change detection was considerably higher with the MEMI workflow when compared to the classic and MESI approaches. The use of MEMI reduced both the error values as well as the range of these values along the escarpment, reaching σ_x and σ_z values below 2 cm (Table 3).

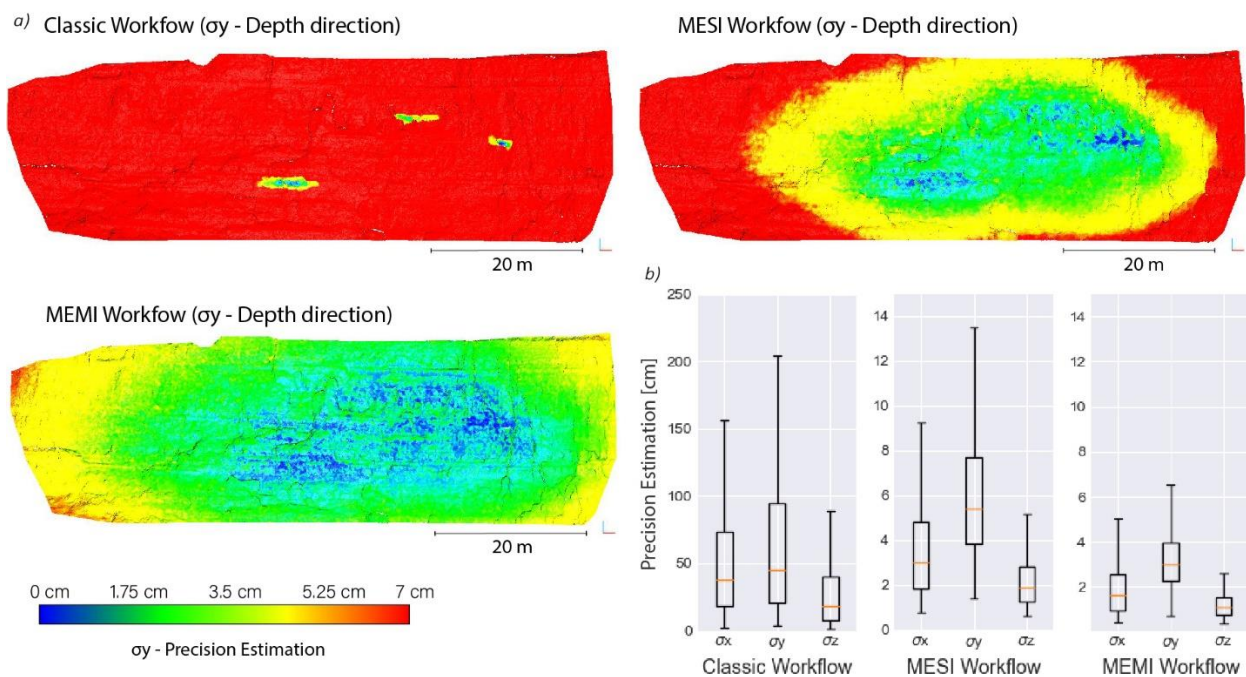


Figure 9. (a) Results obtained from the precision estimation test, considering the distribution of σ_y (depth direction). (b) Error boxplots of the range of the precision estimations (note the different scale on the y axis).

Table 3. Main results obtained in the precision estimation test.

	Classic Workflow	MESI Workflow	MEMI Workflow
σ_x (mean)	37.5 cm	3.0 cm	1.7 cm
σ_y (mean)	44.8 cm	5.4 cm	3.0 cm
σ_z (mean)	15.5 cm	1.9 cm	1.1 cm

3.3. Absolute Accuracy of a Single Point Cloud

Figure 10 shows the M3C2 results obtained in the comparison of the three approaches described in Figure 4 in comparison to a reference LiDAR dataset. Figure 10a illustrates a small part of the cliff with the results of the M3C2 comparisons. Three images are represented using the same colour map.

We observed that the MEMI vs. LiDAR data results showed lower random errors and that the detected rockfalls were better represented than in the classic or MESI results. In general, non-deformation zones (yellow and green) predominated in the MEMI comparison with respect to the other approaches. However, it should be noted that the best comparison was not error-free either, as very small clusters with false deformation were identified.

Due to the presence of rockfalls, the absolute standard deviation parameter does not represent a correct accuracy parameter. For this reason, Figure 10b shows the relative variation of the standard deviation with respect to the best comparison (MEMI vs. LiDAR data). The standard deviation of the M3C2 comparison increased by 19% when using the MESI algorithm and by 24% when using the classic workflow. Also, the graph in Figure 9b shows how the comparison with the highest points (97% of the points) within the range of ± 10 cm was the one made using the MEMI approach. The other workflows had lower values (close to 96%) which means that more points were in the range above ± 10 cm.

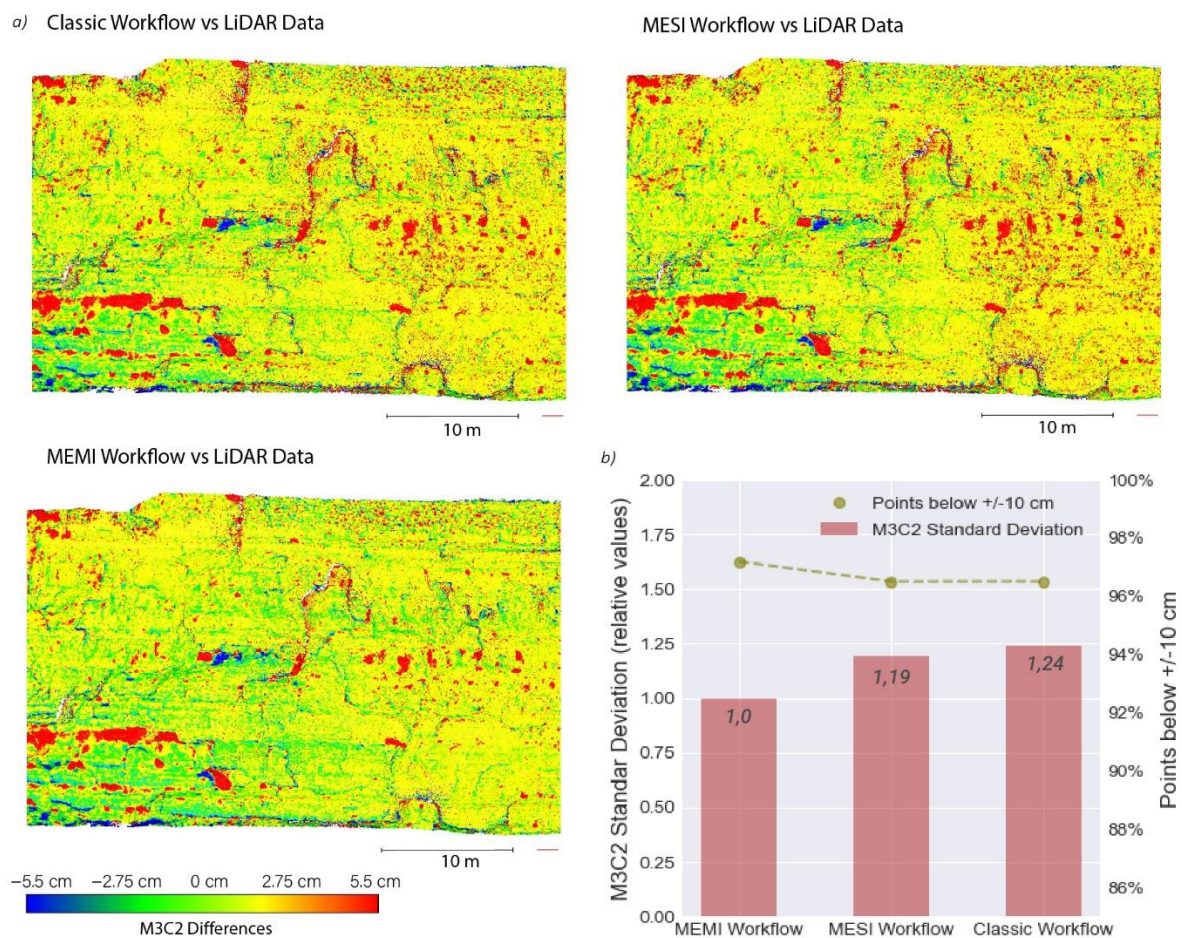


Figure 10. (a) Graphic representation of the differences between the LiDAR data (October 2019) and photogrammetry models (November 2019), according to the workflow used. The three models are represented with the same colour map. The larger red clusters indicate rockfalls that occurred during the comparison period. (b) Bar plot showing the relative M3C2 standard deviation of the comparisons.

4. Discussion

4.1. Automated and Multi-Epoch Multi-Imagery (MEMI) Workflow

The results presented in this paper demonstrate a significant improvement in the methodology used to obtain automatic photogrammetric models using time-lapse cameras. The use of new methodologies such as the multi-epoch imagery (MESI) workflow already represents a considerable improvement in photogrammetric models as described in Feurer and Vinatier [25] and Cook and Dietze [1]. However, the multi-epoch multi-imagery (MEMI) workflow proposed in this paper allowed us to obtain photogrammetric models with greater geometric consistency and less error in the change detection comparison. So the comparison accuracy [1] was increased.

The main limitation of the pipeline presented in this paper is that it requires simultaneous photographs from the same locations during two different periods. So, it cannot be applied to images obtained by UAV, manual systems or historical pictures. A system of fixed cameras is required for the proper performance of the system. Although the cameras are installed in fixed systems of concrete the acquired images are not identical because there are variations in sensor position due to vibration, wind or temperature change, which is why it is necessary to apply automatic algorithms that allow one to track and obtain automatic GCP.

It should be noted that the results obtained in all performance assessments were obtained automatically using the entire pipeline proposed herein. The automation of

the process increases the capacity for analysis and allows the data to be processed in a constant way in a server without the attention of an operator. And it overcomes one of the main limitations that exist when working with a great deal of data, which is being overwhelmed by the large amount of data. Overcoming this limitation is critical to 4D change detection work.

Focusing on the photogrammetric workflow presented in this paper we can define the enhanced workflow as a method for fixed cameras in which no lens calibration is required. Many articles have previously described the need for correct lens calibration. The results obtained using the classic method and MESI workflow reveal how part of the errors obtained have a dome effect classically associated with poor characterization of the intrinsic parameters of the camera. The MEMI workflow eliminates these errors thanks to the better characterization of the intrinsic parameters in the automatic lens calibration process performed by the photogrammetric software. All results have been obtained without any initial parameters developed based on a camera pre-calibration.

This improvement is possibly due to the redundancy of input data when solving the automatic calibration. However, the working method does not succeed in eliminating the classic limitations that all photogrammetric processes have. The quality of the model obtained decreases as we approach the extremes of the model because the photographic coverage of these points is more precarious. Also, in the shaded or poorly resolved areas of the images we find problems when making the photogrammetric reconstruction. The use of advanced methods does not end with the classic limitations of photogrammetry such as the loss of quality at the ends of the model but helps to mitigate its effects.

Despite the above limitations, the workflow presented allows the comparison of photogrammetric models with a better quality than using the classic method and allows work without lens calibration and without control points. These improvements simplify and facilitate the use of photogrammetric systems, especially in dangerous areas where it is impossible to reach the study area. A clear example of the application of this method is rockfall monitoring where it is impossible to access the cliff to install control points due to the danger of rockfall.

The results obtained in this study allow us to show both the improvements obtained using the multi-epoch single-imagery (MESI) workflow and the more advanced workflow multi-epoch multi-imagery (MEMI) developed in this work. The use of MESI workflows leads to an increase in accuracy and precision due to the fact that the spatial error behaviour is mitigated during change detection (i.e., by subtracting models and thus errors). Multi-imagery (from the same point in time) leads to increased accuracy and precision as the photons hit the sensor with a normal distribution and therefore slightly different image features are subsequently detected (leading to slightly different models); therefore, the more images the greater the consistency obtained in the bundle adjustment and consequently the higher the accuracy and precision. The synthesis of these two enhancement concepts is what produces the improvements we obtained for photogrammetric tracking systems from fixed time-lapse camera systems.

However, it should be noted that further work is needed to correctly identify which mechanism provides the best results. The use of proprietary software that works as a black box precludes us observing exactly which part of the processing is affected by the use of multi-imagery. Although the improvement in the results obtained is evident, why the use of multi-imagery has an impact on the results cannot be perfectly explained using our research.

4.2. Relative Accuracy of Detected Changes

One of the methods used in this paper to present the workflow improvements is a change detection analysis between photogrammetric models obtained on consecutive days. Working with photographs obtained on consecutive (or almost consecutive) days allows us to assume that there are no significant differences between the models and consequently

that the change detection comparison should be close to 0. Moreover, this type of comparison allows us to quickly determine the errors that occur in the reconstruction process.

For this publication, two change detection tests were performed. The first test used the best possible data, using a burst of images of four photographs from two consecutive days in May 2020. The second test used the earliest available images (and closest to TLS data) captured on two close dates in November 2019. In this configuration only bursts of three photos were available. The M3C2 method, widely used in the quantification of differences in photogrammetric models, was used to eliminate non-representative deformation errors in comparisons of two point clouds.

In both tests (Figures 7 and 8) we can see graphically how the differences obtained tended to zero when we used a MEMI workflow. These graphic observations were corroborated by the analysis of histograms. Both histograms showed that the classic workflow accumulated fewer points near zero with a greater dispersion of differences. On the other hand, the MEMI workflow accumulated many more points near the zero-deformation value and produced histograms with a lower dispersion of values. The evolution of these values can also be observed in the error bar plot of Figure 7c and Figure 8c. Figure 7c shows that when using the MEMI workflow with a burst of two images per position (mild MEMI workflow) the results obtained contained smaller geometric errors than when using the classic method or the multi-epoch single-imagery described by Feurer and Vinatier [25].

The results shown in Figures 7 and 8 were obtained from different input data. Both figures show how the comparison accuracy improved with the pipeline presented in this article, reaching M3C2 standard deviations of around 1.5 cm. The improvement in the comparison accuracy is a relevant factor since it allows one to reduce the threshold in the detection of changes, increasing the ability to identify changes in the photogrammetric models studied. However, both figures also show how in the areas farthest from the centre there is a tendency to accumulate errors. These errors were mitigated in the more complex workflows, but they did not disappear. This suggests that these are areas where the identification of homologous points is poor, and the reconstruction of the model does not achieve the same quality.

In future works, it would be of great interest to test the performance of the MEMI algorithm in scenarios with larger differences between captures in order to determine whether the accuracies obtained in non-deformation scenarios are valid in scenarios where there are significant changes.

4.3. Interior Precision of the Point Clouds

In order to determine the interior precision of the point clouds, GCP was used to quantify precision at the real scale. However, the working method presented in this paper does not necessarily require control points since the resulting models for comparison share the same location of cameras and are perfectly positioned between them. It is interesting to note that the use of this workflow eliminates the tedious alignment process between point clouds. Because we work with fixed cameras, we can use GPS to obtain the location of each sensor, allowing the photogrammetric software to provide a georeferenced model without the need to use GCP control points, or we can align the locations with georeferenced data. However, the use of GCP allows better georeferencing as well as the possibility of implementing control points.

To calculate the precision we took advantage of the methodology developed by James et al. [42], which allowed us to obtain precision parameters from the control points that were used in the model. In the graphic visualization (Figure 9a) we can see the evolution of σ_y (parameters that indicate the precision in the direction of the deformation). Obtaining these values is subject to the precision of the GCPs introduced in the bundle adjustment phase. It should be remembered that for this work the GCPs were extracted from the local coordinates of a LiDAR TLS 3D model, so the precision obtained in the GCP extraction was not particularly high.

However, we are publishing these results with the intention of showing the progression of the estimation precision within the different workflows, as the same GCPs were used for all cases. We do not wish to focus on the absolute results, but rather on the fact that the comparison is relevant in relative terms. For this reason, Figure 9b shows how values were reduced considerably as more complex workflows were used.

Although obtaining the coordinates of the control points must be done in a more robust way, achieving precision values of less than 2 centimetres on the x and z axes and close to 3 centimetres on the y axis is remarkable. This precision estimation test represents a good way of expressing the improvement in real precision obtained using the MEMI workflow shown in this study.

4.4. Absolute Accuracy of a Single Point Cloud

The results obtained in the comparison of the different photogrammetric workflows with a LiDAR point cloud confirm the improvement that the MEMI workflow represents. It should be noted that the results do not show a perfect non-deformation comparison because there was a one-month difference between the LiDAR acquisition and the photogrammetric models.

This temporal gap is the reason why, in the comparison, in addition to obvious erroneous clusters, obvious rockfalls were identified as shown in Figure 10a. It should also be noted that the identification of rockfalls was much more reliable in the MEMI comparison than in the other workflows tested.

Due to the presence of rockfalls, the absolute values obtained are not representative of the absolute accuracy of the method. For this reason, the results are expressed in relative terms (Figure 10b). Both the graphical comparison and the relative quantification of the M3C2 standard deviation demonstrate that the use of the MEMI workflow substantially improves the absolute accuracy.

The use of multi-temporal multi-imaging algorithms minimizes the geometric error, yielding a 3D model much more similar to the one obtained by LiDAR (perfect in geometric terms). Furthermore, the improvement in absolute accuracy was due to the use of multi-images, as the differences between the classic workflow and the MEMI were not as clear. However, future work in which LiDAR data and photographs can be obtained simultaneously (non-deformation between LiDAR model and photogrammetric model) will allow the absolute accuracy of the different working methods proposed in this research to be achieved in a much more robust way.

5. Conclusions

Five autonomous fixed photogrammetric time-lapse systems were developed using conventional cameras controlled by microcontrollers. These systems allow photogrammetric models to be obtained and sent autonomously and with a high-temporal resolution (sub-daily basis) allowing 4D analysis. The comparison made with the classic, multi-epoch single-imagery (MESI) and multi-epoch multi-imagery (MEMI) workflows shows that the workflow developed in this article leads to significant improvements in the construction of photogrammetric models. The improvements demonstrated in this paper yield models with a greater geometric coherence between them without the need for complex camera calibrations, post-process alignments or the use of GCPs. The MEMI workflow reduced the error up to a factor of 2 in the comparison accuracy (2.83 cm with the classic workflow vs. 1.54 cm with the proposed approach). The proposed enhancement is very relevant when performing studies based on change detection processes. The published pipeline reduces the deformation thresholds used to determine if changes have occurred. Finally, our work shows the possibility of automating the entire workflow without any user intervention, demonstrating that there is the possibility of developing automatic systems for control and monitoring of surfaces via the use of photogrammetric systems.

Author Contributions: Algorithm conceptualization and methodology: X.B., A.E.; software: X.B., A.E.; formal analysis: X.B., A.E., M.G. and A.A., investigation: X.B., A.E., M.G. and A.A., validation: X.B., A.E. M.G. and A.A. writing—original draft preparation, X.B.; writing—review and editing A.E., M.G., A.A.; visualization: X.B.; supervision, A.E., M.G. and A.A. All authors have read and agreed to the published version of the manuscript.

Funding: The presented study was supported by the PROMONTEC Project (CGL2017-84720-R) funded by the Ministry of Science, Innovation and Universities (MICINN-FEDER). The first author (X. Blanch) was supported by an APIF grant funded by the University of Barcelona and the second author (A. Abellán) was supported by the European Union’s Horizon 2020 research and innovation programme under a Marie Skłodowska-Curie fellowship (grant agreement no. 705215). Anette Eltner was funded by the DFG (EL 926/3-1).

Data Availability Statement: The data (image sets) that support the findings of this study are available from the corresponding author, upon reasonable request.

Acknowledgments: The authors would like to thank Mike James for his help and support in the precision estimation results, the ORIGENS UNESCO Global Geopark for granting permission to work on Puigcercós rock cliff and the reviewers and the editor for the valuable comments and suggestions that contributed to the improvement of the present manuscript.

Conflicts of Interest: The authors declare no conflict of interest.

References

1. Cook, K.L.; Dietze, M. Short communication: A simple workflow for robust low-cost UAV-derived change detection without ground control points. *Earth Surf. Dyn. Discuss.* **2019**, *1*–15. [[CrossRef](#)]
2. Bartonek, D.; Buday, M. Problems of creation and usage of 3D model of structures and their possible solution. *Symmetry* **2020**, *12*, 181. [[CrossRef](#)]
3. Meidow, J.; Usländer, T.; Schulz, K. Obtaining as-built models of manufacturing plants from point clouds. *At-Automatisierungstechnik* **2018**, *66*. [[CrossRef](#)]
4. Artese, S.; Lerma, J.L.; Zagari, G.; Zinno, R. The survey, the representation and the structural modeling of a dated bridge. In Proceedings of the 8th International Congress on Archaeology, Computer Graphics, Cultural Heritage and Innovation, Valencia, Spain, 5–7 September 2016; Universitat Politècnica de Valencia: Valencia, Spain, 2016.
5. Castellazzi, G.; D’Altri, A.M.; Bitelli, G.; Selvaggi, I.; Lambertini, A. From laser scanning to finite element analysis of complex buildings by using a semi-automatic procedure. *Sensors* **2015**, *15*, 8360. [[CrossRef](#)] [[PubMed](#)]
6. Jaboyedoff, M.; Oppikofer, T.; Abellán, A.; Derron, M.H.; Loye, A.; Metzger, R.; Pedrazzini, A. Use of LIDAR in landslide investigations: A review. *Nat. Hazards* **2012**, *61*, 5–28. [[CrossRef](#)]
7. Abellán, A.; Oppikofer, T.; Jaboyedoff, M.; Rosser, N.J.; Lim, M.; Lato, M.J. Terrestrial laser scanning of rock slope instabilities. *Earth Surf. Process. Landf.* **2014**, *39*, 80–97. [[CrossRef](#)]
8. Eltner, A.; Schneider, D. Analysis of different methods for 3D reconstruction of natural surfaces from parallel-axes UAV images. *Photogramm. Rec.* **2015**, *30*, 279–299. [[CrossRef](#)]
9. Eltner, A.; Kaiser, A.; Castillo, C.; Rock, G.; Neugirg, F.; Abellán, A. Image-based surface reconstruction in geomorphometry—merits, limits and developments. *Earth Surf. Dyn.* **2016**, *4*, 359–389. [[CrossRef](#)]
10. Westoby, M.J.; Brasington, J.; Glasser, N.F.; Hambrey, M.J.; Reynolds, J.M. “Structure-from-Motion” photogrammetry: A low-cost, effective tool for geoscience applications. *Geomorphology* **2012**, *179*, 300–314. [[CrossRef](#)]
11. Anderson, K.; Westoby, M.J.; James, M.R. Low-budget topographic surveying comes of age: Structure from motion photogrammetry in geography and the geosciences. *Prog. Phys. Geogr.* **2019**, *43*, 163–173. [[CrossRef](#)]
12. James, M.R.; Robson, S. Straightforward reconstruction of 3D surfaces and topography with a camera: Accuracy and geoscience application. *J. Geophys. Res. Earth Surf.* **2012**, *117*, 1–17. [[CrossRef](#)]
13. Blanch, X.; Abellán, A.; Guinau, M. Point cloud stacking: A workflow to enhance 3D monitoring capabilities using time-lapse cameras. *Remote Sens.* **2020**, *12*, 1240. [[CrossRef](#)]
14. Micheletti, N.; Chandler, J.H.; Lane, S.N. Investigating the geomorphological potential of freely available and accessible structure-from-motion photogrammetry using a smartphone. *Earth Surf. Process. Landf.* **2015**, *40*, 473–486. [[CrossRef](#)]
15. Eltner, A.; Sofia, G. Structure from motion photogrammetric technique. *Dev. Earth Surf. Process.* **2020**, *23*, 1–24. [[CrossRef](#)]
16. Kromer, R.; Walton, G.; Gray, B.; Lato, M.; Group, R. Development and optimization of an automated fixed-location time lapse photogrammetric rock slope monitoring system. *Remote Sens.* **2019**, *11*, 1890. [[CrossRef](#)]
17. Giacomini, A.; Thoeni, K.; Santoni, M.; Diotri, F.; Booth, S.; Fityus, S.; Roncella, R. Temporal-spatial frequency rockfall data from open-pit highwalls using a low-cost monitoring system. *Remote Sens.* **2020**, *12*, 2459. [[CrossRef](#)]
18. Verma, A.K.; Bourke, M.C. A method based on structure-from-motion photogrammetry to generate sub-millimetre-resolution digital elevation models for investigating rock breakdown features. *Earth Surf. Dyn.* **2019**, *7*, 45–66. [[CrossRef](#)]

19. Gaffey, C.; Bhardwaj, A. Applications of unmanned aerial vehicles in cryosphere: Latest advances and prospects. *Remote Sens.* **2020**, *12*, 948. [CrossRef]
20. Tannant, D. Review of photogrammetry-based techniques for characterization and hazard assessment of rock faces. *Int. J. Geohazards Environ.* **2015**, *1*, 76–87. [CrossRef]
21. Nesbit, P.R.; Hugenholtz, C.H. Enhancing UAV-SfM 3D model accuracy in high-relief landscapes by incorporating oblique images. *Remote Sens.* **2019**, *11*, 239. [CrossRef]
22. Nex, F.; Remondino, F. UAV for 3D mapping applications: A review. *Appl. Geomat.* **2014**, *6*, 1–15. [CrossRef]
23. Liu, W.; Wang, C.; Zang, Y.; Lai, S.H.; Weng, D.; Sian, X.; Lin, X.; Shen, X.; Li, J. Ground camera images and UAV 3D model registration for outdoor augmented reality. In Proceedings of the 26th IEEE Conference on Virtual Reality and 3D User Interfaces, VR 2019, Osaka, Japan, 23–27 March 2019.
24. Wu, Z.; Ni, M.; Hu, Z.; Wang, J.; Li, Q.; Wu, G. Mapping invasive plant with UAV-derived 3D mesh model in mountain area—A case study in Shenzhen Coast, China. *Int. J. Appl. Earth Obs. Geoinf.* **2019**, *77*. [CrossRef]
25. Feurer, D.; Vinatier, F. Joining multi-epoch archival aerial images in a single SfM block allows 3-D change detection with almost exclusively image information. *ISPRS J. Photogramm. Remote Sens.* **2018**, *146*, 495–506. [CrossRef]
26. Parente, L.; Chandler, J.H.; Dixon, N. Optimising the quality of an SfM-MVS slope monitoring system using fixed cameras. *Photogramm. Rec.* **2019**, *34*, 408–427. [CrossRef]
27. Roncella, R.; Forlani, G.; Fornari, M.; Diotri, F. Landslide monitoring by fixed-base terrestrial stereo-photogrammetry. *ISPRS Ann. Photogramm. Remote Sens. Spat. Inf. Sci.* **2014**, *2*, 297–304. [CrossRef]
28. Motta, M.; Gabrieli, F.; Corsini, A.; Manzi, V.; Ronchetti, F.; Cola, S. Landslide Displacement Monitoring from Multi-Temporal Terrestrial Digital Images: Case of the Valoria Landslide Site. In *Landslide Science and Practice*; Margottini, C., Canuti, P., Sassa, K., Eds.; Springer: Berlin/Heidelberg, Germany, 2013; Volume 2, pp. 73–78.
29. Raspberry Pi Foundation. Raspberry Pi 3 Model B. 2016. Available online: <https://www.raspberrypi.org/> (accessed on 1 April 2020).
30. Eltner, A.; Elias, M.; Sardemann, H.; Spieler, D. Automatic image-based water stage measurement for long-term observations in ungauged catchments. *Water Resour. Res.* **2018**, *54*, 10362–10371. [CrossRef]
31. Santise, M.; Thoeni, K.; Roncella, R.; Sloan, S.W.; Giacomini, A. Preliminary tests of a new low-cost photogrammetric system. *Int. Arch. Photogramm. Remote Sens. Spat. Inf. Sci. ISPRS Arch.* **2017**, *42*, 229–236. [CrossRef]
32. Mallalieu, J.; Carrivick, J.L.; Quincey, D.J.; Smith, M.W.; James, W.H.M. An integrated structure-from-motion and time-lapse technique for quantifying ice-margin dynamics. *J. Glaciol.* **2017**, *63*, 937–949. [CrossRef]
33. Ntregka, A.; Georgopoulos, A.; Quintero, M.S. Photogrammetric exploitation of hdr images for cultural heritage documentation. *ISPRS Ann. Photogramm. Remote Sens. Spat. Inf. Sci.* **2013**, *2*, 209–214. [CrossRef]
34. Gómez-Gutiérrez, Á.; de Sanjosé-Blasco, J.J.; Lozano-Parra, J.; Berenguer-Sempere, F.; de Matías-Bejarano, J. Does HDR pre-processing improve the accuracy of 3D models obtained by means of two conventional SfM-MVS software packages? The case of the corral del veleta rock glacier. *Remote Sens.* **2015**, *7*, 10269–10294. [CrossRef]
35. Romeo, S.; di Matteo, L.; Kieffer, D.S.; Tosi, G.; Stoppini, A.; Radicioni, F. The use of gigapixel photogrammetry for the understanding of landslide processes in alpine terrain. *Geosciences* **2019**, *9*, 99. [CrossRef]
36. Lato, M.J.; Bevan, G.; Fergusson, M. Gigapixel imaging and photogrammetry: Development of a new long range remote imaging technique. *Remote Sens.* **2012**, *4*, 3006–3021. [CrossRef]
37. Guidi, G.; Gonizzi, S.; Micoli, L.L. Image pre-processing for optimizing automated photogrammetry performances. *ISPRS Ann. Photogramm. Remote Sens. Spat. Inf. Sci.* **2014**, *2*, 145–152. [CrossRef]
38. James, M.R.; Robson, S. Mitigating systematic error in topographic models derived from UAV and ground-based image networks. *Earth Surf. Process. Landf.* **2014**, *39*, 1413–1420. [CrossRef]
39. Luhmann, T.; Fraser, C.; Maas, H.G. Sensor modelling and camera calibration for close-range photogrammetry. *ISPRS J. Photogramm. Remote Sens.* **2016**, *115*, 37–46. [CrossRef]
40. Elias, M.; Eltner, A.; Liebold, F.; Maas, H.G. Assessing the influence of temperature changes on the geometric stability of smartphone-and raspberry Pi cameras. *Sensors* **2020**, *20*, 643. [CrossRef] [PubMed]
41. Eltner, A.; Kaiser, A.; Abellan, A.; Schindewolf, M. Time lapse structure-from-motion photogrammetry for continuous geomorphic monitoring. *Earth Surf. Process. Landf.* **2017**, *42*, 2240–2253. [CrossRef]
42. James, M.R.; Robson, S.; Smith, M.W. 3-D uncertainty-based topographic change detection with structure-from-motion photogrammetry: Precision maps for ground control and directly georeferenced surveys. *Earth Surf. Process. Landf.* **2017**, *42*, 1769–1788. [CrossRef]
43. Lague, D.; Brodu, N.; Leroux, J. Accurate 3D comparison of complex topography with terrestrial laser scanner: Application to the Rangitikei canyon (N-Z). *ISPRS J. Photogramm. Remote Sens.* **2013**, *82*, 10–26. [CrossRef]
44. Hungr, O.; Leroueil, S.; Picarelli, L. The Varnes classification of landslide types, an update. *Landslides* **2014**, *11*, 167–194. [CrossRef]
45. Vidal, L.M. Nota acerca de los hundimientos ocurridos en la Cuenca de Tremp (Lérida) en Enero de 1881. In *Boletín de la Comisión del Mapa Geológico de España VIII*; Imprenta Y Fundición de Manuel Tello: Madrid, Spain, 1881; pp. 113–129.
46. Corominas, J.; Alonso, E. Inestabilidad de laderas en el Pirineo catalán. *Ponen. Comun. ETSICCP-UPC C.1 C.53* **1984**.
47. Abellán, A.; Calvet, J.; Vilaplana, J.M.; Blanchard, J. Detection and spatial prediction of rockfalls by means of terrestrial laser scanner monitoring. *Geomorphology* **2010**, *119*, 162–171. [CrossRef]

48. Tonini, M.; Abellan, A. Rockfall detection from terrestrial LiDAR point clouds: A clustering approach using R. *J. Spat. Inf. Sci.* **2014**, *8*, 95–110. [[CrossRef](#)]
49. Royán, M.J.; Abellán, A.; Jaboyedoff, M.; Vilaplana, J.M.; Calvet, J. Spatio-temporal analysis of rockfall pre-failure deformation using Terrestrial LiDAR. *Landslides* **2014**, *11*, 697–709. [[CrossRef](#)]
50. Royán, M.J.; Abellán, A.; Vilaplana, J.M. Progressive failure leading to the 3 December 2013 rockfall at Puigercós scarp (Catalonia, Spain). *Landslides* **2015**, *12*, 585–595. [[CrossRef](#)]
51. Khazaradze, G.; Guinau, M.; Blanch, X.; Abellan, A.; Vilaplana, J.M.; Royan, M.; Tapia, M.; Roig, P.; Furdada, G.; Suriñach, E. Puigercós: A natural laboratory to study landslides and rockfalls in the Catalan Pyrenees. Multi-scale analysis of Slopes under climate change. A cross-disciplinary work. *MUSLOC* **2019**.
52. Khazaradze, G.; Guinau, M.; Blanch, X.; Abellán, A.; Tapia, M.; Furdada, G.; Suriñach, E. Multidisciplinary studies of the Puigercós historical landslide in the Catalan Pyrenees. *Geophys. Res. Abstr.* **2020**, *22*, 7796.
53. Suriñach, E.; Tapia, M.; Roig, P.; Blanch, X. On the effect of the ground seismic characteristics in the estimation of mass movements based on seismic observation. *Geophys. Res. Abstr.* **2018**, *EGU8479*, 20.
54. Python Core Team. Python: A Dynamic, Open Source Programming Language. Python Software Foundation. 2020. Available online: <https://www.python.org/> (accessed on 1 April 2020).
55. Bradski, G. The OpenCV Library. *Dr Dobbs J. Softw. Tools* **2000**. [[CrossRef](#)]
56. Pech-Pacheco, J.L.; Cristóbal, G.; Chamorro-Martínez, J.; Fernández-Valdivia, J. Diatom autofocusing in brightfield microscopy: A comparative study. *Proc. Int. Conf. Pattern Recognit.* **2000**, *15*, 314–317. [[CrossRef](#)]
57. Pertuz, S.; Puig, D.; Garcia, M.A. Analysis of focus measure operators for shape-from-focus. *Pattern Recognit.* **2013**, *46*, 1415–1432. [[CrossRef](#)]
58. Yilmaz, A.; Javed, O.; Shah, M. Object tracking: A survey. *ACM Comput. Surv.* **2006**, *38*, 13-es. [[CrossRef](#)]
59. Schwalbe, E.; Maas, H.-G. Determination of high resolution spatio-temporal glacier motion fields from time-lapse sequences. *Earth Surf. Dyn. Discuss.* **2017**, 1–30. [[CrossRef](#)]
60. Lucas, B.D.; Kanade, T. Iterative image registration technique with an application to stereo vision. In Proceedings of the 7th International Joint Conference on Artificial Intelligence (IJCAI), Vancouver, BC, Canada, 24–28 August 1981; Volume 2, pp. 674–679.
61. Baker, S.; Matthews, I. Lucas-Kanade 20 years on: A unifying framework. *Int. J. Comput. Vis.* **2004**, *56*, 221–255. [[CrossRef](#)]
62. Lin, D.; Grundmann, J.; Eltner, A. Evaluating image tracking approaches for surface velocimetry with thermal tracers. *Water Resour. Res.* **2019**, *55*, 3122–3136. [[CrossRef](#)]
63. Chen, Y.; Medioni, G.G. Object modelling by registration of multiple range images. *Image Vis. Comput.* **1992**, *10*, 145–155. [[CrossRef](#)]
64. Agisoft Metashape Professional Edition (Version 1.6.6). Software. 2020. Available online: <http://www.agisoft.com/downloads/installer/> (accessed on 1 April 2020).
65. Agisoft LLC. *Metashape Python Reference, Release 1.6.0*; Agisoft LLC: Petersburg, Russia, 2018; pp. 1–199.
66. CloudCompare (Version 2.11). 2021. Available online: <http://www.cloudcompare.org/> (accessed on 1 April 2020).
67. Ester, M.; Kriegel, H.P.; Sander, J.; Xu, X. A density-based algorithm for discovering clusters in large spatial databases with noise. *Kdd* **1996**, *96*, 226–231. [[CrossRef](#)]



UNIVERSITAT DE
BARCELONA

Facultat de Ciències
de la Terra

RISKNAT
RISCOS NATURALS



geomodels
Institut de recerca

